SURFACE MORPHOLOGY AND ORDERING IN SIDE-CHAIN LIQUID CRYSTAL DIBLOCK AND HOMOPOLYMER ULTRATHIN FILMS

By

Jung-Sheng Wu

Bachelor of Science, Chemical Engineering
National Taiwan University, Taipei, Taiwan, R.O.C., 1992

Master of Science, Chemical Engineering
National Taiwan University, Taipei, Taiwan, R.O.C., 1994

Submitted to the Department of Chemical Engineering
in Partial Fulfillment of the Requirements for the Degree of

DOCTOR OF PHILOSOPHY IN CHEMICAL ENGINEERING

at the

MASSACHUSETTS INSTITUTE OF TECHNOLOGY

June 2002

Signature of Author:______________________________
Department of Chemical Engineering
March 2002

Certified By:______________________________
Paula T. Hammond, Joseph P. Mares Associate Professor
Thesis Supervisor

Accepted By:______________________________
Daniel Blankschtein, Professor
Chairman, Committee on Graduate Students

Surface Morphology and Ordering in Side-Chain Liquid Crystal Diblock and Homopolymer Ultrathin Films

by

Jung-Sheng Wu

Submitted to the Department of Chemical Engineering
in Partial Fulfillment of the Requirements for the Degree of
Doctor of Philosophy in Chemical Engineering

Abstract

Microphase-separated morphologies of side-chain liquid crystal (LC) diblock copolymers have been examined as substrate-supported thin films. The film thicknesses ranged from 0.5 to 10 times the block copolymer period (L_o). These novel materials are of interest because they exhibit self-oriented electro-optical properties in the bulk state, and may exhibit interesting field dependent nanometer-scale ordering as thin films. A primary challenge in taking advantage of these properties involves the fundamental understanding and control of the nano-domain morphology, which is strongly affected by the substrate, block copolymer properties, and LC alignment within the domains.

In these studies, an amorphous side-chain LC diblock polymer system has been synthesized containing a side-chain mesogen with a chiral alkyl end. Experiments were conducted using Atomic Force Microscopy, Transmission Electron Microscopy, and X-ray Specular Reflectometry, to determine the complex surface morphology. Contact angle measurements and angle-resolved X-ray Photoelectron Spectrometry were also conducted to determine LC orientation at different interfaces. From this information, final models of complex morphologies were derived for different block copolymer compositions, including lamellar, cylindrical, and new smectic-bilayered morphologies.

To better understand the ordering of the LC mesogen at different interfaces, LC homopolymer films were studied. LC anchoring was planar at the substrate, but homeotropic at the air interface due to exposure of the non-polar mesogen tail. Block copolymer thin films were then examined for compositions ranging from 40% to 85% weight fraction of the LC block. Due to the wetting properties of the LC diblock copolymer, novel LC terraces were observed on the top surfaces corresponding to single smectic layer spacing. For diblock thin films, both blocks coexist at the air surfaces to form a mixed surface. Hybrid morphologies, consisting of both symmetrical and anti-symmetrical wettings, were noted for the lamellar morphology with film thicknesses between 0.5 and $1.5L_o$. The surface properties are determined by LC orientation, which depends on the film thickness. Homeotropic anchoring of the smectic LC mesogens at the air interface was observed in both the homopolymer and the block copolymers, resulting in smectic terraces on the top surfaces of the films. In thicker films, when the influence of the substrate was decreased, the lamellar orientation was found to undergo a transition from parallel stacking near the substrate to perpendicular arrangement at the air surface. Effects of annealing and solvent exposure on the resulting thin-film behavior were also addressed.

Thesis Supervisor: Professor Paula T. Hammond
Joseph P. Mares Associate Professor

Dedication

This thesis is dedicated to:

my parents, Tsun-Hsien Wu and Hsiu-Chin Huang
for their overwhelming love and support
over the years

and my wife, Peiwen Fang,
whose love, courage, company, and smile
have always been invaluable to me

Acknowledgement

The completion of this thesis work would have been impossible without the assistance and guidance I have received from many people.

First and foremost, I would especially like to thank Professor Paula T. Hammond, who advised and supported me through this research. Her openness to the new ideas gives me a lot of freedom to approach many new interesting fields. I appreciated her patience to teach me to become independent in research. I acknowledge my thesis committee members: Professors Paul Laibinis, Anne Mayes, and Thomas Russell. I also acknowledge the Program in Polymer Science and Technology (PPST).

My collaborators have contributed enormously in this work. Dr. Wen-Yue Zheng developed the synthesis of these LC diblock copolymers. Special thanks go to Dr. Mitch Anthamatten, for his diligent efforts in the bulk morphological study. Dr. Michael J. Fasolka helped me in the analysis of diblock copolymer thin film morphologies. I would like to thank all those who assisted me in various instruments: Dr. Libby Shaw (AR-XPS and AFM), Mr. Mike Frongillo (TEM), Dr. Yuan Lu (XPS, Harvard), Dr. Carl Miller (AR-XPS, Raytheon), and Dr. Sushil Satija (XSR, NIST).

I would like to thank each of the members of the Hammond research group for the friendship and support in these years: Wen-Yue Zheng, Jyotsna Iyer, Sarah Clark, Aaron Moment, Bindu Nair, Cathy Santini, Dave Dewit, Mitch Anthamatten, Mark Johnson, Xueping Jiang, Dean DeLongchamp, Yongwoo Lee, LaRuth McAfee, LaShanda James-Korley, Shoshana Gourdin, Greg Pollock, Haipeng Zheng, Illsoon Lee, Mike Berg, Heejae Kim, Hiroaki Tokuhisa, Kristoffer Stokes, Juhyun Park, and Marianne Terrot. Thank my classmate, Thanh-nga Tran.

I would like to thank Fang-Tsuay and Yi-Jen for their encouragement and teaching during these years. Special thanks go to Ruey-Jin for her lovely accompany, especially these two months. I offer my thanks to Ting-Ting and Chao-Yang for kindly hosting me in last two months.

Finally, I wholeheartedly thank my family back in Taiwan for their unconditional support, encourage, and love: my parents, sister, brother, and wife.

Table of Contents

List of Figures

List of Tables

Chapter 1

Introduction and Background

1.1 INTRODUCTION

A diblock copolymer consists of two chemically different polymer chains bonded together as a single macromolecule. Incompatible blocks can be covalently joined through synthesis, and the unfavorable contacts between dissimilar blocks can lead to phase-segregated nanostructures.[1-4] Phase segregation of high molecular weight diblock copolymers is spontaneous after reaching thermal equilibrium. Recent investigations of block copolymers confined in thin films have established a base of knowledge and have promoted numerous applications.[4,5] Ultrathin films of diblock copolymers have properties strongly dependent on surface properties, such as roughness,[6] chemical structure,[7] and surface tension.[8,9] Self-arrangement of the surface morphology and the thin film structure will occur to minimize the total free energy.

Side-chain liquid crystal (LC) block copolymers are a new class of materials, which combine the ordering phenomena of block copolymers and liquid crystals.[10-20] These systems consist of an LC mesophase nested within a larger block copolymer mesophase. Key issues include the relative orientation and wetting behavior of the block copolymer morphology and the LC layers. It is well known that these block copolymers impart electro-optic effects in phase-segregated morphologies.[21-23] Phase segregation also enables these materials to have a greater mechanical cohesive strength, which cannot be achieved in low molar mass LCs. Recently, the effects of interfaces and confinement on LC behavior have been investigated with increasing interest by numerous researchers. Both the substrate and interfaces play important roles in determining LC behavior. The stability and type of LC ordering may also be influenced by surfaces. An understanding of the LC thin film morphologies of these materials could lead to interesting approaches to surface modification, such as electro- or photo-switchable wetting properties, unique thin film membranes, or smart coatings.

In order to control and take advantage of these unique material properties of LC diblock copolymers, it is necessary to understand the interactions between all constitutive parts of these materials in an ultrathin film environment; the LC moiety, the polymer backbone, the air-interface, and the substrate-interface all play intricate and balancing roles in determining the lowest free energy structure. The surface morphology of LC diblock copolymer thin films encompasses the interplay between two different levels of order – order between individual LC mesogens, and order between microphase-segregated domains – both of which may be influenced by energy and ordering effects at the substrate surface or air interface. To investigate the possibility of forming micro-domain structures on surfaces, I explored the ordering behavior of nanometer-scale ultrathin films of side-chain LC block copolymers spun cast onto silicon substrates. An unusual stepped morphology was observed due to configurational frustration induced by the incommensurability between the block copolymer morphological domain periodicity (L_o), the smectic LC period (s_o), and the film thickness.

1.2 THESIS OBJECTIVES

1.2.1 Motivation

Side-chain LC diblock polymers present a number of interesting applications, such as polymer electronics, data storage, display device, adhesives, and nonlinear optical devices; consequently, the interest in bulk polymer morphologies and ordering of LC block copolymer systems has increased greatly in recent years.[24] Despite the interest in the solid-state properties of these materials, there have only been a few reports of their behavior as ultrathin films on surfaces.[6,9,25-27] Surface segregation of fully amorphous block copolymer thin films produces interesting nanostructures, which are the basis for chemical patterning, lithography, or textured surfaces.[7,28-33] A base of knowledge has been established in the formation of thin films of amorphous block copolymers, which serves to direct these applications.[34-37] On the other hand, the surface morphology of LC diblock copolymer thin films encompasses the interplay between two different levels of ordering (the block copolymer period and the LC smectic layer), both of which may be influenced by energy and ordering effects at the substrate surface and air interface. These systems consist of an LC mesogen nested within a larger mesophase, and the relative orientation and wetting behavior of the block copolymer and LC smectic layer are at issue. An understanding of the thin film morphologies of these materials could lead to interesting approaches to surface modification, such as electro- or photo-switchable wetting properties, unique thin film membranes, or smart coatings.

Block copolymers can self-assemble into well-ordered microphase morphologies with dimensions on the molecular scale.[1,3,4] This unique feature has attracted attention for applying natural nano-scale structures, such as patterns. However, grain size usually limits the usage of block copolymers. Several methods are possible to increase the grain size and reduce the number of grain boundaries, such as substrate confinement, and alignment with external fields. The side-chain LC diblock copolymer combines the advantages of both block copolymer nano-domains and LC ordering, and opens a new field of material design. The formation of large domains in LC-containing diblock copolymers are facilitated because the LC molecules have a natural tendency to pack together and to be aligned easily by external fields. In thin films, a fundamental understanding of morphology and LC spatial orientation is the key to controlling grain boundaries and approaching applications.

The surface phase segregation of LC block copolymers can lead to unique applications. As discussed, the block copolymer can phase-segregate into specific known morphologies, such as hexagonally packed cylinders or lamellae, and the presence of LC groups as pendant side-chains promotes both mesogenic and morphological alignment. One possibility is to create alignable nano-patterns at the surface using side-chain LC diblock copolymers. Electric or magnetic fields could then be used to tune the optical properties of the patterned regions, making these materials useful as microshutters, rewritable memory storage devices, potential membranes, or templates for further materials deposition or synthesis.

Hammond *et al.* [10-14,38] has synthesized and characterized a series of LC diblock polymers, and investigated their bulk morphology. In this thesis, I have examined ultrathin film morphologies obtained with these block copolymers, in order to foster future applications. The LC diblock thin film morphology is more complicated than general diblock copolymer thin films because of LC ordering. As the film becomes thinner, surface and interface effects dominate the morphology. LC ordering may govern the behavior of thin films. In addition, the alignment of LC mesogens can be controlled by outside environments and molecular-level mesogen design.

I have investigated how LC alignment is affected by the confinement of the substrate, air interface, and block interfaces in this thesis. The effects of temperature are also examined. I am also interested in studying the interplay among different levels of ordering, such as diblock copolymer micro-domains ($L_o \sim 20$ nm) and LC mesophase alignment ($s_o \sim 3$ nm). Block copolymer domains can induce LC orientation and the LC phase can influence block morphology. In addition, LC anchoring has significant effects on the surface morphologies. The scope of this research has focused on understanding LC diblock copolymer thin film behavior and building a systematic approach for future studies. In particular, the goal of this thesis is to explore the different thin film morphologies of side-chain LC diblock copolymers supported by a substrate, and the LC alignment created at different interfaces.

1.2.2. Thesis Structure

This thesis consists of six chapters. Three main phases of morphological studies, including the homopolymer, lamellar diblock copolymers, and high LC-ratio diblock copolymers, are described in three different chapters. Chapter One provides the introduction, motivation, and objective of this research. The remainder of this chapter covers the basic concepts and previous works related to this study.

Chapter Two is entitled, 'Design, Synthesis, and Characterization'. These materials were synthesized and characterized in a separate study by Zheng [10-12] and Anthamatten.[13,14,39] For the ease of reference, details of these procedures are included in Chapter Two. This section describes the materials and experimental methods in detail, such as the material properties, substrate properties, thin film formation, and characterization tools. Further information on the experimental instruments, operating parameters, and sample preparation methods used, as well as related experimental theories, are also included in this chapter.

In Chapter Three, the alignment of LC side-chain smectic homopolymers is discussed. In order to demonstrate LC alignment, I chose LC homopolymers as a model system. Several surface-analysis tools are used to detect the depth profile. Molecular simulations are also used to determine the stable conformations. LC alignment in thin films can be systematically studied and identified by both theoretical and experimental approaches. The LC homopolymer system is helpful for understanding more complex LC diblock systems.

An analysis of the morphology of substrate supported lamellar diblock copolymer thin films is found in Chapter Four. I present experimental observations and explain the LC lamellar thin film morphology with a proposed model. I found that LC anchoring can strongly affect the surface morphologies. All data, from techniques, such as X-ray Photoelectron Spectroscopes (XPS), Atomic Force Microscopy (AFM), and Transmission Electron Microscopy (TEM), are carefully analyzed. The discussion focuses on the formation of LC terraces at the air interface. Factors influencing the thin film morphology, such as solvent vapor and annealing, are discussed. This study can be applied to other LC diblock copolymers and other thin film morphologies.

Chapter Five, 'Morphologies of High LC Ratio Thin Films: Cylinder and Smectic Bilayers', is divided into two sections and focuses on high LC-volume fraction diblock copolymers. The first section discusses the thin film morphology of a cylindrical diblock copolymer. The second section deals with the morphology of smectic bilayered thin films. The resulting morphologies are compared with the LC homopolymer study to understand the block interface effects. Only a small amount of secondary block (PS block phase-segregated in high LC ratio diblock samples) will change the morphology. The theories and methods explained in Chapter Four are applied.

Finally, Chapter Six summarizes all results and presents a conclusion. Additionally, Chapter Six suggests directions for future efforts in the field of LC diblock copolymer thin films.

1.3 BACKGROUND

1.3.1 Diblock copolymer basics

Recently, block copolymers have attracted much attention, due to their special properties and applications, such as in adhesives, compatibilizers, and, emulsifiers.[1,3] It is well known that most block copolymers form ordered morphologies, as a consequence of the incompatibility of the constituent polymer blocks. Block immiscibility causes spontaneous phase separation. Molecular connectivity forces phase separation to occur on molecular length scales and produces periodic, uniformly ordered, tens of nm-sized micro-domains – e.g., alternating lamellae, hexagonally-packed cylinders, and body-centered-cubic-packed spheres, etc. – as shown in Figure 1.1a.

Many morphological variations have been observed in block copolymers, including bicontinuous phases, the presence of multiple morphologies at phase boundaries, and defect structures, e.g., modulated-layer and perforated layer phases.[40-46] Figure 1.1b shows the block periodicity of lamellar and cylindrical diblock copolymers.

Properties of diblock copolymers can be well controlled by designing constituent polymers. Morphological structures of block copolymers are determined predominantly by thermodynamics, while polymer blends are basically controlled by kinetics. Consequently, the morphologies are more stable and are not influenced by different process conditions. Moreover, the block copolymer morphology can be influenced by external forces, including shear flow,[47,48] surface interactions,[49] electric fields,[28,29,50-52] and magnetic fields.[53-55] Shear flow is usually used to orient to bulk melt samples, but it cannot be used for ultrathin films due to the higher energy barriers of the substrate.

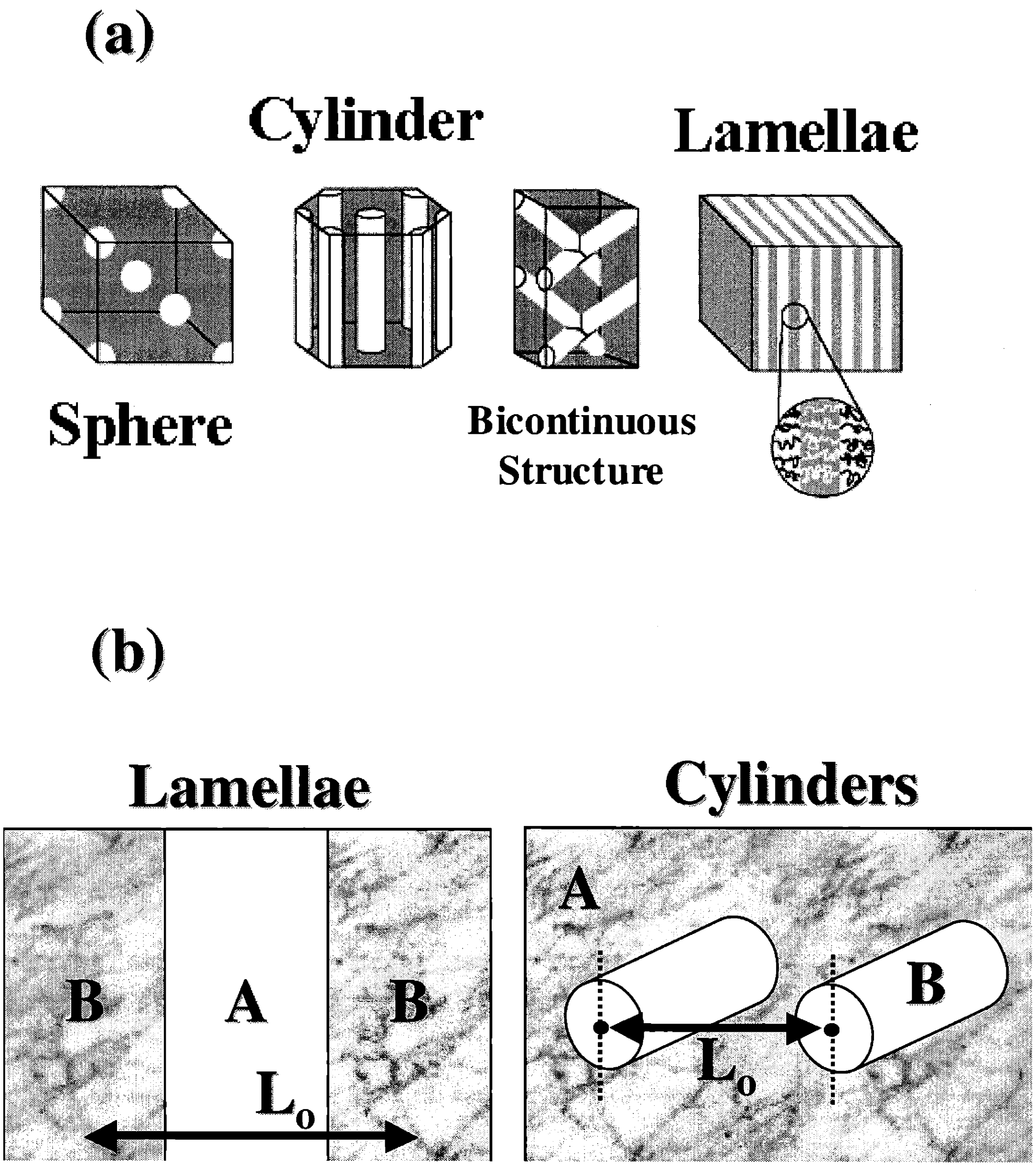

Figure 1.1: (a) Common morphologies of diblock copolymers with different block ratios; (b) the definition of block periodicity (L_o) of lamellar and cylindrical diblock copolymers.

The presence and type of equilibrium microstructures of a microphase-separated diblock copolymer melt can be predicted using mean-field theory [56-59] and is influenced by four key parameters.[1-3,60] The first factor is the number of statistical segments (N). High molecular weight (MW) polymers differ from small molecules in three ways, including elastic free energy contribution upon deformation of the polymer coils, slow relaxation times of macromolecules, and long-range steric effects. The second factor is the Flory-Huggins segmental interaction parameter (χ_{AB}), which denotes the degree of immiscibility of two polymers. The quantity χN is used as the principal determinant of the degree of microphase separation. Phase segregation occurs if the criteria $(\chi_{AB} N) > (\chi_{AB} N)_{\text{critical}}$ is satisfied, where "critical" denotes the critical value of the spinodal curve. The third factor is the conformational asymmetry parameter (ε), which accounts for differences in persistence length and inter-segmental interactions between the two blocks. This parameter controls how these two blocks fill their respective domains. The last factor is the volume fraction of the minor block ($f = (N_A / (N_A + N_B))$). The volume fraction determines the particular morphology for bulk diblock copolymers when $(\chi_{AB} N) > (\chi_{AB} N)_{\text{critical}}$. The most common morphologies observed in block copolymers as a fraction of volume fractions (f) are summarized in Table 1.1 below. If the poly-dispersities of both blocks are narrow, spheres and cylinders order onto regular lattices.

Table 1.1: Possible diblock morphologies at different block ratios.

f	**Possible Morphologies**
0~21%	Body-centered-cubic-packed spheres
21~33%	Hexagonally packed cylinders
33~37%	Cubic 3D, Bicontinuous cubic (Ia3d or Pn3m symmetry), Double gyroid or Double diamond
37~50%	One-dimensional stacks of lamellae
50%	Lamellae

Morphology is one of the most dominant factors in determining block copolymer properties. Nanometer scale domains determine the mechanical and reactive behaviors. Most block copolymers form ordered, phase-segregated morphologies through block immiscibility. Phase segregation, when confined by different boundary conditions, such as in a thin film environment, may yield interesting new morphological arrangements.

1.3.2 Diblock copolymer thin films - Basics

Thin film properties of block copolymers on surfaces have attracted much interest recently.[61] The surface constraint and thin film confinement can have enormous effects on polymer configurations and phase behavior. Russell, Anastasiadis, Satija *et al.* [62-69] reported the study of surface morphology on confined polymers and polystyrene-b-poly(methyl methacrylate) diblock copolymer brushes. They used off-specular X-ray scattering, neutron reflectivity (NR), neutron scattering, small-angle neutron scattering, and TEM to study the polymer thin film morphology and the influence of the film thickness on the order-disorder transition. Bates *et al.* [36,70,71] studied diblock copolymers in a confined geometry by NR, TEM, and AFM, and observed the confinement-induced morphological changes occurring in close proximity to the order-disorder-transition temperature of the block copolymer. Krausch *et al.* [72] investigated the adsorption of polystyrene-b-poly(vinyl pyridine) diblock copolymer on surfaces from selective solvents, and observed highly regular two-dimensional arrays of spherical surface micelles.

Nanostructures and patterns can form by the self-assembly of block domains. With good control over micro-domain orientation, these nm-scale patterns can be transferred to other materials. Lamellar growth, defect annihilation, and LC packing are slow processes in substrate-supported thin film environments compared to diblock copolymers in the bulk state. The slow kinetics may influence the final morphology. Several researchers have tried to form larger domains in thin films by using kinetic effects on patterned substrates, [31,73-75] or using an electric field to align morphologies.[29,50-52,76]

Lamellar thin film wetting structure

Isotropic lamellar diblock copolymer films usually form a macromolecular stack parallel to the surface, with a period, L_o, equal to the thickness of an ABBA sequence. There are two possible arrangements in supported lamellar diblock copolymer thin films as shown in Figure 1.2.[77,78] The thickness of this ordered film must belong to a discrete spectrum of allowed values, d_n, where $d_n = (n+½) L_o$, or $d_n = n L_o$, depending on the interfacial segregation behavior of the blocks.

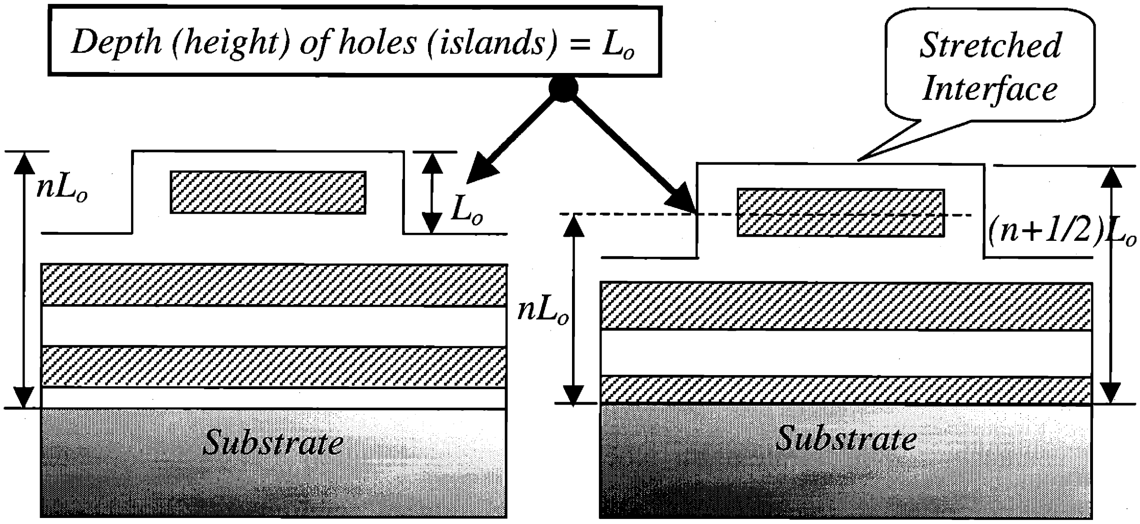

Symmetric wetting

- One block wets both surfaces.
- Thickness = $n L_o$

Anti-symmetric wetting

- Preferential affinity.
- Thickness = $(n+1/2) L_o$

Figure 1.2: Wetting behavior of lamellar diblock copolymer thin films.

For symmetric wetting films, one block must wet both surfaces. If the average film thickness ($d_n < t < d_{n+1}$) is incommensurate with an integral multiple of the block periodicity (L_o), the system will separate into coexisting domains of thickness d_n and d_{n+1}.[77,78] Holes or islands with L_o height will spontaneously nucleate and grow on the surface to maintain a phase segregated block structure. For anti-symmetric wetting films, each block wets a different surface. Hole or island structures are then observed if the average film thickness is not equal to $(n + ½) L_o$.

Thin Film Morphology for thicknesses less than L_o

For film thickness (t) below the bulk equilibrium period (L_o), the diblock copolymer morphology is frustrated by a competition of several factors, including strong surface interactions, slow kinetics, and the "bulk" driving force towards a morphology with the nature period L_o. Fasolka and Mayes [7] performed simulations and experiments on diblock copolymer films thinner than L_o. Different morphologies were observed while self-consistent field calculations [79] were used to minimize the interfacial energy and to maintain the natural block periodicity.

Figure 1.3 shows various wetting structures and an example of its phase diagrams for a diblock copolymer from Fasolka.[7] Figure 1.3a shows that diblock copolymers prefer symmetric wetting in which the B block is favored to cover both the substrate and air interface. Four possible morphologies are shown, including the full surface-parallel lamellae (FL, $t \approx L_o$), the surface-parallel half-lamellae (HL, $t \approx ½L_o$), the hybrid structure (HY, $t < ½L_o$), and the perpendicular lamellae (PL, $t < ½L_o$). FL and HL are surface-parallel morphologies. Here, the flat A-B interfaces minimize the unfavorable contact between blocks, while maintaining the diblock copolymer's periodicity. HY and PL are surface-perpendicular morphologies in which the B block perforates the A block (white) layer with $½L_o$ width. PL also keeps the equilibrium L_o spacing. Carvalho *et al.* [80] also reported the perpendicular lamellar morphology in diblock copolymer thin films. Figure 1.3b [7] shows two models of anti-symmetric wetting. The air favors the A block (white) and the silicon substrate favors the B block (black). Instead of HY and PL structures, the anti-symmetric hybrid morphology (AHY, $t \approx L_o$) and one and an half lamellae (3/2 FL) are shown.

Figure 1.3c [7] shows the phase diagram of both symmetric and anti-symmetric diblock copolymer films. In this figure, R is defined as the affinity (S) of the block B (black color) with air to that with the silicon substrate ($R = \frac{S^B_{air}}{S^B_{substrate}}$). At R = ±1, the affinity of the block B with air is equal to the affinity with the substrate, while the affinity with the substrate is far larger at R = 0. Different morphologies are displayed at different thicknesses (t / L_o) and R (relative affinity of B to air and the substrate). While

R > 0, the thin film performs symmetric wetting. FL structure dominates the thicker films ($t/L_o > 0.6$). HY and PL structures are only observed at lower thickness and high R. While R < 0, the thin film performs the anti-symmetric wetting structure. HL structure dominates most of the thicknesses. 3/2FL and AHY structures show at t/L_o close to one, where the film thickness is incommensurate with $(n + ½) L_o$.

Possible Applications of Ordered Diblock Copolymer Thin Films

Fasolka and Mayes [32] studied the ultrathin film morphology of polystyrene-b-poly (n-butyl methacrylate) (PS-PnBMA) on both flat and corrugated silicon oxide substrates. In order to increase the configurational entropy, the lamella might adopt a perpendicular orientation at a thickness less than half lamellae.[37,81] However, complete perpendicular orientation would result in a large energy loss at the substrate, because of the interaction of PnBMA with the substrate. The resulting compromise morphology consists of semi-columns of PnBMA that perforate through the PS layer to increase the overall configurational entropy of the system, while maintaining a layer of PnBMA at the substrate.

Block copolymer nano-scale patterns can be used as a mask for lithography as illustrated by Park [30,31], Harrison [82], and Li.[75] The pattern can be transferred to a substrate by selectively etching of one block chemically. Alternately, the block copolymer domains can serve as a template for decoration with nanoparticles, even metals. Shibauchi *et al.* [83] reported the magnetic properties of well-ordered ultra-high density ($1.25*10^{12}$ per in²) arrays of vertically oriented high-aspect-ratio cobalt nano-rods having a 14 nm diameter. The arrays were fabricated by electro-deposition within the pores of a nanoscale template derived from films of diblock copolymers. Cheng and Ross [84] also reported the formation of single-domain cobalt dot arrays with high magnetic particle density, patterned over large areas (e.g., 10 cm diameter wafers) fabricated by self-assembled block copolymer lithography as a template. Jeoung *et al.* [85] developed a novel approach to highly ordered and modular nano-electrode arrays using block copolymer self-assembly.

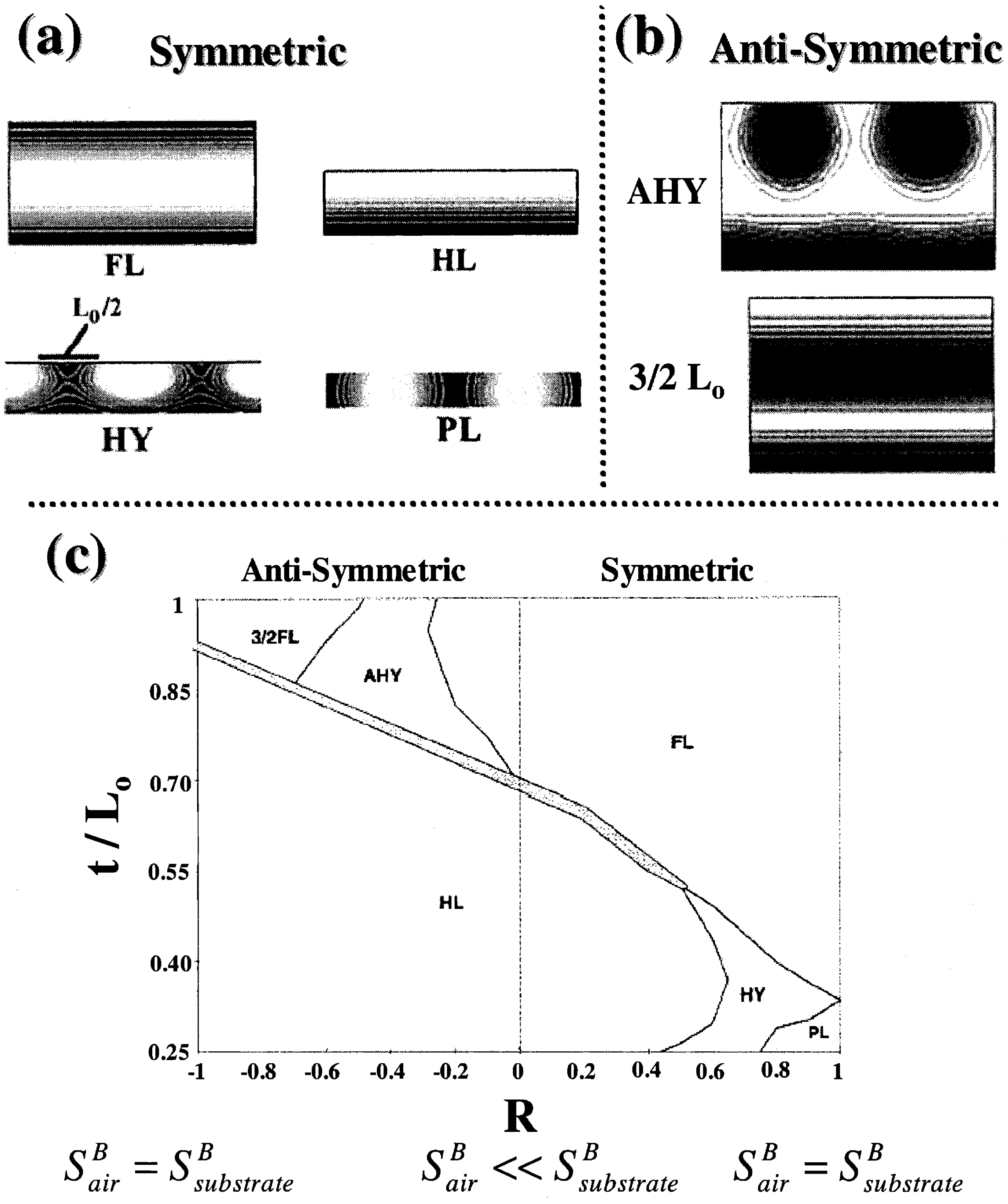

Figure 1.3: Possible thin film morphologies of diblock copolymers of different thicknesses from SCF simulation (a) symmetric wetting; (b) anti-symmetric wetting; (c) phase diagram for both wetting conditions.

1.3.3 Diblock copolymer thin films – Morphology Control

Electric field alignment and substrate modification can serve as approaches to create larger uniform domains. Both approaches can be used to control the block copolymer morphologies.

Electric field alignment of diblock copolymer thin films

Morkved,[29,86,87] Mansky,[51] and Thurn-Albrecht [52,76,88] used an electric field to align diblock copolymer domains. Electric fields have been shown to orient nanoscopic domains effectively in thin PS-b-PMMA asymmetric cylindrical diblock copolymer films. The threshold field strength is independent of film thickness (for films of 10-30 μm thickness) and can be described by the difference in interfacial energies of the components. Morkved *et al.* [29] studied the aligned cylindrical phase of diblock copolymer films in the region between electrodes directly using TEM. In the central gap region, cylinders formed parallel to each other, with few defects. Outside the central gap, cylinders followed the curvature of field lines. The effects of an external electric field on the equilibrium properties of lamellar and cylindrical assemblies in confined diblock copolymers were also studied theoretically.[28] After using controlled interfacial interactions and electric fields to manipulate the orientation of the morphology, Russell *et al.* [4] used the aligned block copolymer patterns to generate nano-porous templates as scaffolds for nanoscopic structures. The difference between the values of the polymer-plate interfacial tension for each of the two components was a determining factor for the threshold field strength.[50]

Substrate Modification

Substrate modification is a potential method to create long-range ordering of block copolymer thin films. Segalman *et al.* [89] investigated the long-range order of spherical domain block copolymer films using confined substrates with wells and mesas. RomachandraRao *et al.* [90] focused on the enhancement of diblock copolymer ordering kinetics by annealing films in the presence of supercritical carbon dioxide to enhance long-range ordering.

Random copolymers can be coated onto the substrate to create a neutral surface for both blocks and can enhance perpendicular lamellar morphology. Kellogg *et al.* [37] created a neutral surface by using thin layers of random copolymers. Huang [91,92] and Mansky [93,94] fabricated a neutral surface for PdS-b-PMMA diblock copolymers by coating a thin tunable layer of a random-copolymer (PS-r-PMMA) brush to control the domain orientation. They used neutron reflectivity and small-angle neutron scattering to determine the orientation of the lamellar micro-domains for films with various boundary conditions.[91,93,95] Successive steps of CF_4 reactive ion etching followed by field emission scanning electron microscopy were used to ascertain the orientation of the micro-domains as a function of film depth. The orientation of the lamellar micro-domains was observed to be perpendicular (normal) to the neutral film surface.

Topographically patterned substrates can induce block copolymer morphology. Fasolka [32,96] used topographic patterned substrates to control the diblock copolymer thin film morphology. Rockford *et al.* [97,98] studied the propagation of nano-patterned substrates to template the ordering of a symmetric block copolymer lamellar morphology. They established a striped, chemically heterogeneous surface (with 20 nm wide periodic gold lines) over large areas, where the stripe width is comparable to the size of a polymer molecule. The controlled nanoscale surface interactions affected the subsequent macromolecular ordering and produced a surface-directed morphology.

Heier *et al.* [99] investigated the transfer of a chemical pattern on a substrate into a symmetric diblock copolymer thin film. The substrates had patterns of self-assembled monolayers (SAMs) produced by micro-contact printing on gold. They studied thin diblock copolymer films on chemically heterogeneous surfaces using scanning force microscopy and TEM. They found that the block copolymer was well ordered into lamellae parallel to the substrate over OH-terminated SAMs but that the block copolymer layers on the CH_3-terminated SAMs are frequently oriented perpendicular to the substrate.[100]

Nealey *et al.* [73,101,102] studied the self-assembly of diblock copolymer films on chemically nano-patterned substrates using extreme ultraviolet interferometric lithography. Unexposed regions of their films remained terminated in methyl groups, but exposed regions were modified to oxygen-containing, polar terminal groups. They found that if the substrate period (L_s) was much greater than the bulk lamellar period (L_o), the lamellae oriented parallel to the substrate with symmetric wetting on unexposed regions and anti-symmetric wetting on exposed regions. Moreover, for a surface pattern with L_s close to L_o, the lamellae oriented perpendicular to the substrate and were macroscopically aligned with the surface pattern. These materials can be utilized as nano-templates for nano-fabrication. The experimental data from this study agreed well with simulation results.

Theoretical calculations of diblock copolymer thin film morphology have been published by Kikuchi [103], Binder [103], Walton [81], Matsen [58], Tang [104], and Fredickson. [105,106] Walton [81,107] and Matson [58] have considered the asymmetric boundary conditions of thin diblock films. Pickett [79] and Fasolka [7,96] examined the diblock morphology for film thickness near or beneath L_o. Wang and de Pablo studied Monte Carlo simulations of the morphology of diblock copolymer thin films confined between two homogeneous surfaces,[108,109] between chemically heterogeneous hard surfaces,[110] and between homogeneous and patterned surfaces.[111]

1.3.4 Liquid Crystalline (LC) and LC polymers (LCP)

The liquid crystalline phase is a phase between crystal and liquid states. In the crystal (solid) state, materials exhibit long-range positional and orientational order, and molecules arrange onto three-dimensional lattices. In the liquid state, molecules exhibit only short-range order. The LC state is a liquid-like state that exhibits some degree of long-range orientational order. There are many different kinds of LC ordering, such as nematic, smectic A, smectic C, etc… as shown in Figure 1.4. The name 'nematic' is derived from the Greek word for thread [112]. Nematic order involves only one-dimensional ordering. 'Smectic' is from the Greek word for soap. In smectic phases, not only is there orientational order, but there is also positional order. These molecules are free to move around randomly, but they tend to point along one direction and arrange themselves in layers. In the smectic A phase, the director is perpendicular to the planes, while in the smectic C phase the director tilts at an angle other than 90° to the planes.

There are two different kinds of LC polymers (LCPs), main-chain LCPs and side-chain LCPs. Main-chain LCPs with LC mesogens as part of the backbone have strong mechanical properties, whereas side-chain LCPs have the potential of aligning the LC mesogens under external fields. A side-chain LC polymer is composed of a polymer backbone and LC mesogens attached to this backbone. The structural features of LC mesogens include their high aspect ratio (length / diameter ≥ 6), rigid structural units and linkages, high level of molecular polarization, and low MW symmetry and regularity to reduce the stability of the crystal phase. The LC polymer exhibits a glassy state at temperatures below its glass transition temperature (Tg). In the glassy state, the LC mobility is much lower, and, consequently, LC block copolymers have slow electro-optic and piezo-electric response times.

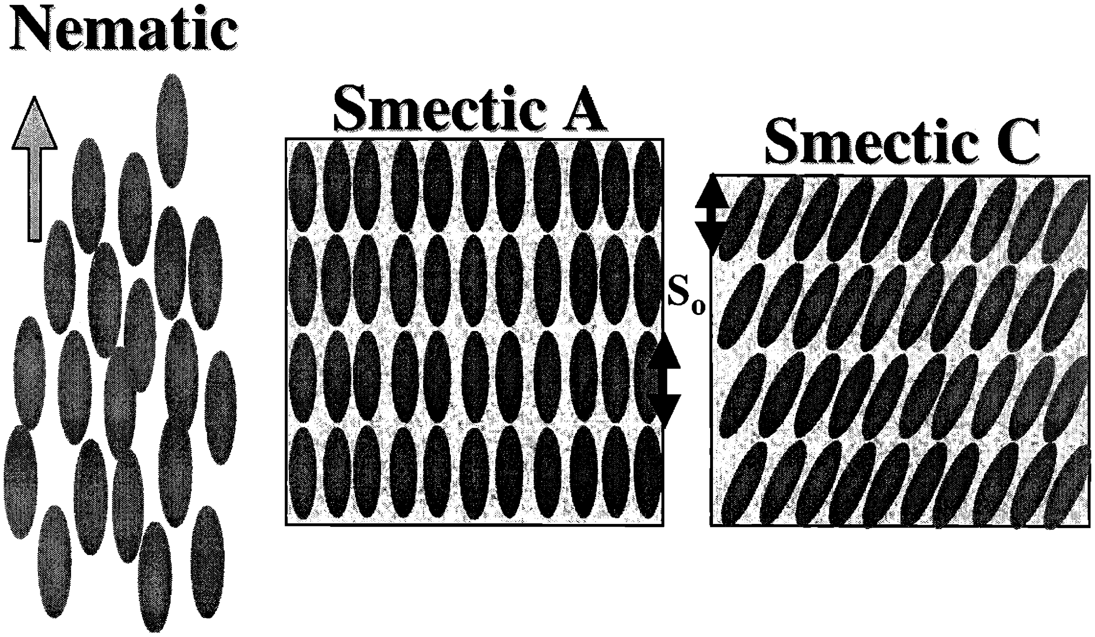

Figure 1.4: Different types of LC ordering.

Zheng and Hammond [10] reported a method to synthesize a series of novel LC diblock copolymers with PS-PMMA backbone and LC side-chain smectic C* layers. The SAXS data and bulk morphologies were examined by Zheng and Anthamatten.[11,13,14] The direction of the LC smectic layer is orthogonal to the direction of the lamellar microphase segregation in the bulk.

Microphase Segregation Criteria for LC Diblock Copolymers

LC block copolymers have two critical temperatures. LC ordering disappears at the LC clearing point (also referred to as the LC clarification temperature, or the LC isotropization temperature, T_{iso}). Above this temperature, the molecules are isotropic and exhibit no long-range order. Phase segregated block copolymers become phase-mixed at what is referred to as the order-disorder transition temperature, or T_{ODT}. For some LC block copolymers T_{ODT} is greater than T_{iso}. For $T < T_{iso}$ and $T < T_{ODT}$, LC mesogens form an ordered mesophase within block copolymer domains. When $T_{iso} < T < T_{ODT}$, there is no LC ordering; however, the polymer blocks are still phase separated. For $T > T_{iso}$ and $T > T_{ODT}$, the blocks are miscible and the polymer shows the isotropic morphology.

LC ordering affects the phase separation of block copolymers.[12,13] The Flory-Huggins (FH) parameter of block copolymers (χ) was modified to the effective FH parameter (χ_{eff}). Microphase segregation occurs when $\chi_{eff}N > (\chi_{eff}N)_{crit}$ where $\chi_{eff} = \chi + \chi_{LC}$. The FH parameter of block copolymers (χ) between two blocks is related to intermolecular segmental interactions in an isotropic melt. For amorphous diblock copolymers, microphase segregation occurs if the product of χN exceeds a critical value. The FH parameter of LC (χ_{LC}) is the additional increment of free energy involved with mixing ordered mesogens and disordered PS chain segments. The effective FH parameter for an LCP (χ_{eff}) is combined with these two factors to represent effective enthalpic and excess entropic effects of mixing. LC ordering can greatly reduce the interaction between the ordered and disordered blocks, thus increasing χ_{eff}, since χ_{LC} is positive. The polymer conformation is the competition between ordering of the LC side chains and coiling of the polymer backbone. When cooling from the isotropic state, if

$\chi N \gg (\chi N)_{crit}$ (above T_{iso}), phase separation occurs at temperatures higher than T_{iso}. LC order forms within the existing phase-segregated domains. If χN is small but close to $(\chi N)_{crit}$, the LC transition can induce phase separation, and block copolymer morphology will be strongly influenced by LC textures.

The mean-field theory by Matsen and Bates [56] predicted a field-induced shift of both transition temperatures and the spinodal point, the suppression of the bcc phase, and the orientational and reorientational phase transitions. Hammond *et al.* [13,14] measured the transition temperatures using small-angle X-ray scattering (SAXS) at different temperatures. When temperature was increased, the small angle peak, which referred to phase separation, also broadened. Le Meur *et al.* [113] reported a shift of the T_{ODT} by a shear. Hammond *et al.* [12] made a series of new side chain LC diblock copolymers and found that the T_{ODT} can be affected by LC isotropization temperature (T_{iso}). For Hammond *et al.*'s [12] lower MW samples at higher LC contents, T_{ODT} and T_{iso} occur at similar temperatures thus suggesting that the LC ordering can induce an order-disorder transition. Furthermore, Hammond *et al.* [12] proved that the PS blocks are incorporated into the LC superstructure forming micrometer-sized focal conic fan structures.

1.3.5 LC polymer thin films

Surface properties have profound influence on polymer thin film applications. The orientation of liquid crystals near a surface is often controlled by a complex balance of long-ranged (elastic) and short-ranged (e.g. chemically-specific) interactions. These interactions are defined by the structure of surfaces over a wide range of length scales (0.1 – 1000 nm).

Wong *et al.* [114] first reported orientational wetting in hybrid liquid crystalline block copolymers thin films. In symmetric diblocks, the copolymer wets the surface with the lamellae perpendicular to the surface. The generic parallel ordering, however, can be restored in asymmetric lamellar diblocks. Nieuwhof and de Jeu [115,116] then reported another side-chain liquid-crystalline polymers from the alternating copolymerization of maleic anhydride and l-olefins carrying biphenyl mesogens. They found that a terminal methoxy group induced a hexatic smectic B mesophase, intermediate terminal alkyl groups induced a smectic E mesophase, and long terminal alkyl groups induced a crystal smectic B mesophase. If the spacer was shorter than the terminal alkyl group, an inter-digitated smectic A mesophase was found in which the terminal alkyl groups overlap. Sentenac *et al.* [117,118] reported a new lamellar morphology of LC diblock copolymer films, in which the amorphous block is similar to the backbone of the LC polymer. Microphase separation and the smectic A phase leads to a terraced film made of alternating amorphous and smectic layers, both parallel to the substrate. Sentenac and de Jeu also studied the structure and fluctuations of freely suspended smectic A and smectic B films using off-specular X-ray diffuse scattering, [119,120] reflectivity, [121-123] optical ellipsometry, [124] and dynamic x-ray scattering.[125] Mach *et al.* [8] studied surface tension in various smectic free-standing films.

Surface properties and LC alignment greatly differ if the end group of the LC mesogen is semi-fluorinated. Ober *et al.* [126,127] synthesized an LC block copolymer with semi-fluorinated side chains, and Kramer *et al.* [126,127] studied the thin film properties. Genzer *et al.* [128,129] used near-edge absorption fine structure (NEXAFS) measurements to probe the molecular orientation of semi-fluorinated mesogens, -$(CH_2)_x(CF_2)_y$-F, which were attached to the polymer backbone and gold substrates. They also used NEXAFS to study the temperature dependence of molecular orientation on the surface for the same polymers;[130] the orientation of the mesogens at the air interface changed abruptly at two temperatures. The lower temperature surface transition occurs close to the temperature of the smectic-B to smectic-A transition, while the higher temperature transition is associated with the bulk LC transition from the smectic-A to the isotropic phase.

In summary of the above literatures, design and synthesis of surfaces with controlled, nanometer-scale topography and well-defined chemical functionality have made possible a new level of control over the anchoring of liquid crystals.

LC Anchoring at the Interface

The total free energy expression of LC anchoring at the interface includes factors of conformational entropy, surface enthalpy, and interfacial energy terms. For example, LC alignment is directly affected by the substrate properties and the surface topography. Moreover, the chemical properties of the LC molecules such as the dielectric constant, dipole, and functional groups are important attributes, which can affect the LC behavior. Hence, by designing different molecular structures, or even by changing the end group of the mesogen, LC alignment can be greatly changed.

There are usually two kinds of LC alignment at the interface: planar and homeotropic, as shown in Figure 1.5. Figure 1.5a shows the planar (or homogeneous, in-plane) texture, where the mesogens are situated parallel to the interface. Coating of long chain polymers on the substrate and stroking in a single direction can create small parallel grooves, all pointing in the same direction, thus inducing the LC planar anchoring. Simply stretching the film in one direction to increase the elastic energy gain can have the same effect. Another method to achieve LC planar anchoring is to evaporate a thin layer of silicon oxide (SiO_2) or metal oxide at an oblique angle (45-80°) onto the surface. Figure 1.5b shows the homeotropic alignment, where the mesogens are perpendicular to the interface. This type of alignment can usually be reached by coating a thin layer of amphiphilic materials on the polar glass substrate with the non-polar end of the coating materials facing the LC layer on the top.

LC alignment would be easy to identify if it was uniform, like Figure 1.5a or Figure 1.5b. However, since both types of alignment can coexist in the same film at different interfaces, the alignment inside the film may not be easy to characterize. Figure 1.5c shows the coexistence of two types of alignment.

Proust *et al.* [131] determined the free energies of adhesion ($W_{A,\text{ advancing}}$ and $W_{R,\text{ receding}}$, where $W = \gamma_L(1+\cos\theta)$) using contact angle experiments. They studied two different nematic LC small molecules (MBBA and LC4) at both homeotropic (H) and planar (P) alignment. The free energy differences ($\Delta W = W_A - W_R = \gamma_L (\cos\theta_A - \cos\theta_R) = \gamma_L \Delta\cos\theta$) for both P and H were calculated and are shown in Table 1.2. They found that ΔW is much smaller for the H structure than the P structure at the nematic phase, but similar at the isotropic phase. This result shows the P structure has a higher adhesion energy difference than H. Therefore, P is more stable. For the same reason, the adhesion free energy difference from the isotropic state to the nematic state is around 2 ergs/cm², which shows the ordered structure is more stable.

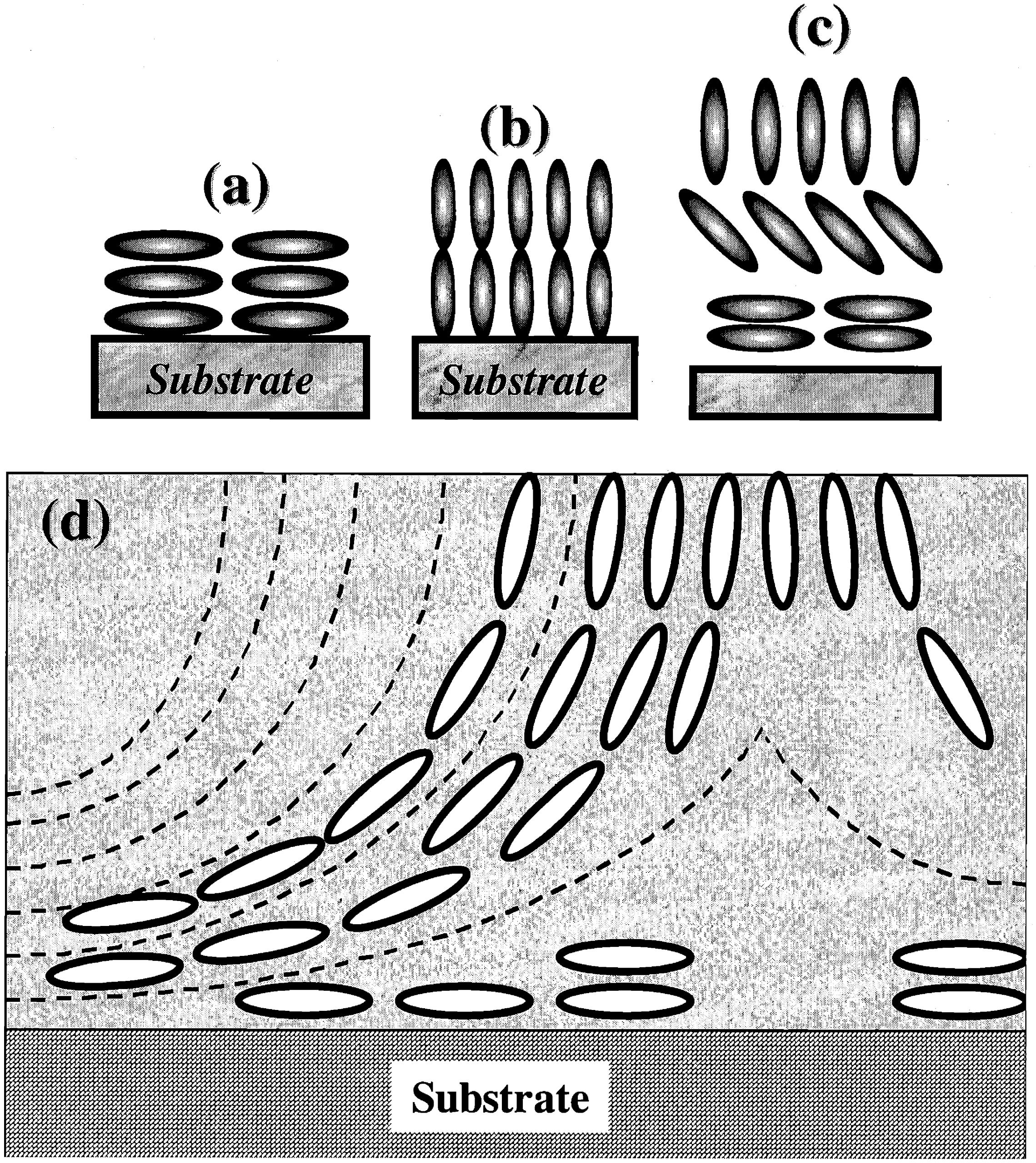

Figure 1.5: Different types of LC alignment at the interface (a) planar anchoring; (b) homeotropic alignment; (c) coexistence of two types of alignment at different interfaces; (d) the schematic plot of LC ordering transition from planar anchoring at the substrate to homeotropic alignment at the air interface.

Table 1.2: Free energy of adhesion differences from Proust *et al.*[120]

(ergs/cm^2)	LC Sample One (MBBA)			LC Sample Two (LC4)		
	H	P	P-H	H	P	P-H
ΔW_N (Nematic)	3	4.5	1.5	2.7	4.5	1.8
ΔW_I (Isotropic)	3	2.8	-0.2	2.7	2.5	-0.2
ΔW_N-ΔW_I	0	1.7		0	2.0	

Figure 1.5d shows the cartoon of the LC orientational transition at two different interfaces. The LC mesogens switch from planar anchoring at the bottom surface to homeotropic anchoring at the top surface. It is difficult to identify where the transition occurs or pinpoint the thickness of the transition zone. In Chapter Three, I use atomic force microscopy, contact angles, angle-resolved X-ray photoelectron spectrometer, and X-ray specular reflectivity to determine LC alignment of LC homopolymers of different thicknesses.

REFERENCES

(1) Allport, DC. *Block copolymers*; Applied Science: London, 1973.
(2) Hamley, IW. *The physics of block copolymers*; Oxford University Press: New York, 1998.
(3) Baltá Calleja, FJ; Roslaniec, Z. *Block copolymers*; Marcel Dekker: New York, 2000.
(4) Russell, TP; Thurn-Albrecht, T; Tuominen, M; Huang, E; Hawker, CJ. *Macromol. Symp.* **2000**, *159*, 77-88.
(5) Russell, TP. *Mater. Sci. Rep.* **1990**, *5*, 171.
(6) Henn, G; Stamm, M; Poths, H; Rucker, M; Rabe, JP. *Physica B* **1996**, *221*, 1-4, 174-184.
(7) Fasolka, MJ; Banerjee, P; Mayes, AM; Pickett, G; Balazs, AC. *Macromolecules* **2000**, *33*, 5702-5712.
(8) Mach, P; Huang, CC; Stoebe, T; Wedell, ED; Nguyen, T; de Jeu, WH; Guittard, F; Naciri, J; Shashidhar, R; Clark, N; Jiang, IM; Kao, FJ; Liu, H; Nohira, H. *Langmuir* **1998**, *14*, 15, 4330-4341.
(9) Figueiredo, P; Geppert, S; Brandsch, R; Bar, G; Thomann, R; Spontak, RJ; Gronski, W; Samlenski, R; Mueller-Buschbaum, P. *Macromolecules* **2001**, *34*, 2, 171-180.
(10) Zheng, WY; Hammond, PT. *Macromol. Rapid Commun.* **1996**, *17*, 11, 813-824.
(11) Zheng, WY; Albalak, R; Hammond, PT. *Macromolecules* **1998**, *31*, 2686-2689.
(12) Zheng, WY; Hammond, PT. *Macromolecules* **1998**, *31*, 3, 711-721.

(13) Anthamatten, M; Hammond, PT. *Macromolecules* **1999**, *32*, 24, 8066-8076.
(14) Anthamatten, M; Zheng, WY; Hammond, PT. *Macromolecules* **1999**, *32*, 15, 4838-4848.
(15) Anthamatten, M; Wu, J-S; Hammond, PT. *Polym. Prepr.* **1999**, *40*, 1, 427-428.
(16) Adams, J; Gronski, W. In *Liquid Crystalline Polymers*; Weiss, R.; Ober, C., Eds.; ACS: Washington DC, 1990.
(17) Chiellini, E; Gallo, G; Angeloni, AS; Laus, M; Bignozzi, MC. *Macromol. Symp.* **1994**, *77*, 349-358.
(18) Mao, G; Wang, J; Clingman, SR; Ober, CK; Chen, JT; Thomas, EL. *Macromolecules* **1997**, *30*, 2556-2567.
(19) Ruokolainen, J; Saariaho, M; Ikkala, O; ten Brinke, G; Thomas, EL; Torkkeli, M; Serimaa, R. *Macromolecules* **1999**, *32*, 1152-1158.
(20) Yamada, M; Iguchi, T; Hirao, A; Nakahama, S; Watanabe, J. *Macromolecules* **1995**, *28*, 50-58.
(21) Meyer, R.B.; Liebert, L.; Strzelecki, L.; Keller, P. *J. Phys. Lett.* **1975**, *36*, 69.
(22) Blackwood, K. M. *Sciencs* **1996**, *273*, 909-912.
(23) Mao, G; Wang, J; Ober, CK; Brehmer, M; O'Rourke, MJ; Thomas, EL. *Chem. Mater.* **1998**, *10*, 6, 1538-1545.
(24) Geil, PH, Ed. *Polymer Single Crystals*: Huntington, NY, 1973.
(25) Mensinger, H; Stamm, M; Boeffel, C. *J. Chem. Phys.* **1992**, *96*, 4, 3183.
(26) Elben, H; Strobl, G. *Macromolecules* **1993**, *26*, 1013.
(27) van der Wielen, MWJ; Stuart, MAC; Fleer, GJ; deBoer, DKG; Leenaers, AJG; Nieuwhof, RP; Marcelis, ATM; Sudholter, EJR. *Langmuir* **1997**, *13*, 17, 4762-4766.
(28) Amundson, K; Helfand, E ; Quan, X; Hudson, SD; Smith, SD. *Macromolecules* **1994**, *27*, 6559.
(29) Morkved, TL; Lu, M; Urbas, AM; Ehrichs, EE; Jaeger, HM; Mansky, P; Russell, TP. *Science* **1996**, *273*, 931-933.
(30) Park, M; Harrison, C; Chaikin, PM ; Register, RA; Adamson, DH. *Science* **1997**, *276*, 1401-1404.
(31) Park, M; Chaikin, PM; Register, RA; Adamson, DH. *Appl. Phys. Lett.* **2001**, *79*, 2, 257-259.
(32) Fasolka, MJ; Harris, DJ; Mayes, AM; Yoon, M ; Mochrie, SGJ. *Phys. Rev. Lett.* **1997**, *79*, 3018.
(33) Wu, J-S; Fasolka, MJ; Hammond, PT. *Macromolecules* **2000**, *33*, 1108-1110.
(34) Mansky, P; Harrison, CK; Register, RA; Chaikin, P; Yao, N. *Appl. Phys. Lett.* **1996**, 2586.
(35) Russell, TP; Menelle, A ; Anastasiadis, SH ; Satija, SK. *Macromolecules* **1991**, *24*, 6263-6269.
(36) Koneripalli, N; Levicky, R; Bates, FS; Ankewer, J; Kaiser, H; Satija, SK. *Langmuir* **1996**, *12*, 6681-6690.
(37) Kellogg, GJ; Walton, DG; Mayes, AM; Lambooy, P; Russell, TP; Gallagher, PD; Satija, SK. *Phys. Rev. Lett.* **1996**, *76*, 14, 2503-2506.
(38) Anthamatten, M; Wu, J-S; Hammond, PT. *Macromolecules* **2001**, *34*, 24, 8574-8579.

(39) Anthamatten, ML. *PhD Thesis: Order in side-chain liquid crystalline diblock copolymers*; MIT: Cambridge, MA, 2001.

(40) Foerster, S; Khandpur, AK; Zhao, J; Bates, FS; Hamley, IW; Ryan, AJ; Bras, W. *Macromolecules* **1994**, *27*, 6922-6935.

(41) Hajduk, DA; Harper, PE; Gruner, SM; Honeker, CC; Kim, G; Thomas, EL; Fetters, LJ. *Macromolecules* **1994**, *27*, 4063.

(42) Hamley, IW; Koppi, KA; Rosedale, JH; Bates, FS; Almdal, K; Mortensen, K. *Macromolecules* **1993**, *26*, 22, 5959-5970.

(43) Hamley, IW; Gehlsen, MD; Khandpur, AK; Koppi, KA; Rosedale, JH; Schulz, MF; Bates, FS; Almdal, K; Mortensen, K. *J. Phys. II France* **1994**, *4*, 2161-2186.

(44) Khandpur, AK; Foerster, S; Bates, FS; Hamley, IW; Ryan, AJ; Bras, W; Almdal, K; Mortensen, K. *Macromolecules* **1995**, *28*, 26, 2796-8806.

(45) Ohta, T; Kawasaki, K. *Macromolecules* **1986**, *19*, 2621-2632.

(46) Thomas, EL; Anderson, DM; Henkee, CS; Hoffman, D. *Nature* **1988**, *334*, 18, 598-601.

(47) Kotaka, T; Okamoto, M; Kojima, A; Kwon, YK; Nojima, S. *Polymer* **2001**, *42*, 3, 1207-1217.

(48) Qiao, L; Winey, KI; Morse, DC. *Macromolecules* **2001**, *34*, 22, 7858-7867.

(49) Tsori, Y; Andelman, D. *J. Chem. Phys.* **2001**, *115*, 4, 1970-1978.

(50) Ashok, B; Muthukumar, M; Russell, TP. *J. Chem. Phys.* **2001**, *115*, 3, 1559-1564.

(51) Mansky, P; DeRouchey, J; Russell, TP; Mays, J; Pitsikalis, M; Morkved, T; Jaeger, H. *Macromolecules* **1998**, *31*, 13, 4399-4401.

(52) Thurn-Albrecht, T; DeRouchey, J; Russell, TP; Jaeger, HM. *Macromolecules* **2000**, *33*, 9, 3250-3253.

(53) Maiti, S; Bag, DS. *Indian J. Chem.* **1995**, *34A*, 673-687.

(54) Firouzi, A; Schaefer, DJ; Tolbert, SH; Stucky, GD; Chmelka, BF. *J. Am. Chem. Soc.* **1997**, *119*, 9466-9477.

(55) Tolbert, SH; Firouzi, A; Stucky, GD; Chmelka, BF. *Science* **1997**, *278*, 264.

(56) Matsen, MW; Barrett, C. *J. Chem. Phys.* **1998**, *109*, 10, 4108-4118.

(57) Matsen, MW; Schick, M. *Macromolecules* **1994**, *27*, 24, 7157-7163.

(58) Matsen, MW. *J. Chem. Phys.* **1997**, *106*, 18, 7781.

(59) Chakraborty, AK; Golumbfskie, AJ. *Annu. Rev. Phys. Chem.* **2001**, *52*, 537-573.

(60) Bates, FS. *PhD Thesis: An investigation of structure and properties in a model set of diblock copolymer-homopolymer blends*, 1982.

(61) Russell, TP. *MRS Bull.* **1996**, *21*, 1, 49-53.

(62) Russell, TP; Karim, A; Mansour, A; Felcher, GP. *Macromolecules* **1988**, *21*, 6, 1890-1893.

(63) Bassereau, P; Brodbreck, D; Russell, TP; Brown, HR; Shull, KR. *Phys. Rev. Lett.* **1993**, *71*, 1716.

(64) Mansky, P; Russell, TP; Hawker, CJ; Mays, J; Cook, DC; Satija, SK. *Phys. Rev. Lett.* **1997**, *79*, 237.

(65) Lambooy, P; Russell, TP; Kellogg, GJ; Mayes, AM; Gallagher, PD; Satija, SK. *Phys. Rev. Lett.* **1994**, *72*, 18, 2899-2902.

(66) Russell, TP; Coulon, G; Deline, VR; Miller, DC. *Macromolecules* **1989**, *22*, 12, 4600-4606.
(67) Anastasiadis, SH; Russell, TP; Satija, SK; Majkrzak, CF. *Phys. Rev. Lett.* **1989**, *62*, 16, 1852-1855.
(68) Anastasiadis, SH; Russell, TP; Satija, SK; Majkrzak, CF. *J. Chem. Phys.* **1990**, *92*, 9, 5677-5691.
(69) Satija, SK; Majkrzak, CF; Russell, TP; Sinha, SK; Sirota, EB ; Hughes, GJ. *Macromolecules* **1990**, *23*, 16, Macromolecules.
(70) Sikka, M ; Singh, N; Bates, FS; Karim, A; Satija, SK; Majkrzak, CF. *J. Phys. II France* **1994**, *2*, 2231.
(71) Singh, N; Kudrle, A; Sikka, M; Bates, FS. *J. Phys. II France* **1995**, *5*, 377.
(72) Meiners, JC; Ritzi, A; Rafailovich, MH; Sokolov, J; Mlynek, J; Krausch, G. *Appl. Phys. A* **1995**, *61*, 519.
(73) Harrison, C; Adamson, DH; Cheng, ZD; Sebastian, JM; Sethuraman, S; Huse, DA; Register, RA; Chaikin, PM. *Science* **2000**, *290*, 5496, 1558-1560.
(74) Harrison, C; Chaikin, PM; Huse, DA; Register, RA; Adamson, DH; Daniel, A ; Huang, E; Mansky, P; Russell, TP; Hawker, CJ; Egolf, DA; Melnikov, IV; Bodenschatz, E. *Macromolecules* **2000**, *33*, 3, 857-865.
(75) Li, RR; Dapkus, PD; Thompson, ME; Jeong, WG; Harrison, C; Chaikin, PM; Register, RA; Adamson, DH. *Appl. Phys. Lett.* **2000**, *76*, 13, 1689-1691.
(76) Schaffer, E; Thurn-Albrecht, T; Russell, TP; Steiner, U. *Nature* **2000**, *403*, 6772, 874-877.
(77) Coulon, G; Collin, B; Ausserre, D; Chatenay, D; Russell, TP. *J. Phys.* **1990**, *51*, 24, 2801-2811.
(78) Maaloum, M; Ausserre, D; Chatenay, D; Coulon, G; Gallot, Y. *Phys. Rev. Lett.* **1992**, *68*, 1575.
(79) Pickett, GT; Balazs, AC. *Macromolecules* **1997**, *30*, 10, 3097-3103.
(80) Carvalho, BL; Thomas, EL. *Phys. Rev. Lett.* **1994**, *73*, 24, 3321-3324.
(81) Walton, DG; Kellogg, GJ; Mayes, AM; Lambooy, P; Russell, TP. *Macromolecules* **1994**, *27*, 6225.
(82) Harrison, C; Park, M; Chaikin, PM; Register, RA; Adamson, DH. *J. Vac. Sci. Technol., B* **1998**, *16*, 2, 544-552.
(83) Shibauchi, T; Krusin-Elbaum, L; Gignac, L; Black, CT; Thurn-Albrecht, T; Russell, TP; Schotter, J; Kastle, GA; Emley, N; Tuominen, MT. *J. Magn. Magn. Mater.* **2001**, *226*, 2, 1553-1554.
(84) Cheng, JY; Ross, CA; Chan, VZH; Thomas, EL; Lammertink, RGH; Vancso, GJ. *Adv. Mater.* **2001**, *13*, 15, 1174.
(85) Jeoung, E; Galow, TH; Schotter, J; Bal, M; Ursache, A; Tuominen, MT; Stafford, CM; Russell, TP; Rotello, VM. *Langmuir* **2001**, *17*, 21, 6396-6398.
(86) Morkved, TL ; Jaeger, HM. *Europhys. Lett.* **1997**, *40*, 643.
(87) Morkved, TL; Lopes, WA; Hahm, J; Sibener, SJ; Jaeger, HM. *Polymer* **1998**, *39*, 16, 3871.
(88) Thurn-Albrecht, T; Steiner, R; DeRouchey, J; Stafford, CM; Huang, E; Bal, M; Tuominen, M; Hawker, CJ; Russell, TP. *Adv. Mater.* **2000**, *12*, 15, 1138-1138.
(89) Segalman, RA; Yokoyama, H; Kramer, EJ. *Adv. Mater.* **2001**, *13*, 15, 1152.

(90) RamachandraRao, VS; Gupta, RR; Russell, TP; Watkins, JJ. *Macromolecules* **2001**, *34*, 23, 7923-7925.
(91) Huang, E; Russell, TP; Harrison, C; Chaikin, PM; Register, RA; Hawker, CJ; Mays, J. *Macromolecules* **1998**, *31*, 22, 7641-7650.
(92) Huang, E; Pruzinsky, S; Russell, TP; Mays, J; Hawker, CJ. *Macromolecules* **1999**, *32*, 16, 5299-5303.
(93) Mansky, P; Russell, TP; Hawker, CJ; Pitsikalis, M; Mays, J. *Macromolecules* **1997**, *30*, 22, 6810-6813.
(94) Mansky, P; Liu, Y; Huang, E; Russell, TP; Hawker, C. *Science* **1997**, *275*, 5305, 1458-1460.
(95) Huang, E; Mansky, P; Russell, TP; Harrison, C; Chaikin, PM; Register, RA; Hawker, CJ; Mays, J. *Macromolecules* **2000**, *33*, 1, 80-88.
(96) Fasolka, MJ. *PhD Thesis: The Morphology and Lateral Patterning of Diblock Copolymer Thin Films*; MIT: Cambridge, MA, 2000.
(97) Rockford, L; Liu, Y; Mansky, P; Russell, TP; Yoon, M; Mochrie, SGJ. *Phys. Rev. Lett.* **1999**, *82*, 12, 2602-2605.
(98) Rockford, L; Mochrie, SGJ; Russell, TP. *Macromolecules* **2001**, *34*, 5, 1487-1492.
(99) Heier, J; Genzer, J; Kramer, EJ; Bates, FS; Walheim, S; Krausch, G. *J. Chem. Phys.* **1999**, *111*, 24, 11101-11110.
(100) Heier, J; Kramer, EJ; Walheim, S; Krausch, G. *Macromolecules* **1997**, *30*, 21, 6610-6614.
(101) Yang, XM; Peters, RD; Nealey, PF; Solak, HH; Cerrina, F. *Macromolecules* **2000**, *33*, 26, 9575-9582.
(102) Peters, RD; Yang, XM; Wang, Q; de Pablo, JJ; Nealey, PF. *J. Vac. Sci. Technol., B* **2000**, *18*, 6, 3530-3534.
(103) Kikuchi, M; Binder, K. *J. Chem. Phys.* **1994**, *101*, 4, 3367-3377.
(104) Tang, WH; Witten, TA. *Macromolecules* **1998**, *31*, 3130-3135.
(105) Fredrickson, GH. *Macromolecules* **1987**, *20*, 2535.
(106) Turner, MS. *Phys. Rev. B: Condens. Matter* **1992**, *69*, 1788.
(107) Shull, KR. *Macromolecules* **1992**, *25*, 2122.
(108) Wang, Q; Nealey, PF; de Pablo, JJ. *Macromolecules* **2001**, *34*, 10, 3458-3470.
(109) Wang, Q; Yan, QL; Nealey, PF; de Pablo, JJ. *J. Chem. Phys.* **2000**, *112*, 1, 450-464.
(110) Wang, Q; Yan, QL; Nealey, PF; de Pablo, JJ. *Macromolecules* **2000**, *33*, 12, 4512-4525.
(111) Wang, Q; Nath, SK; Graham, MD; Nealey, PF; de Pablo, JJ. *J. Chem. Phys.* **2000**, *112*, 22, 9996-10010.
(112) Collings, PJ. *Liquid Crystals - Nature's Delicate Phase of Matter*; Princeton University Press: Princeton, NJ, 1990.
(113) Le Meur, J; Terrisse, J; Schwab, C; Goldzene, J. *J. Phys. Paris, Colloq* **1971**, *5*, 301.
(114) Wong, GCL; Commandeur, J; Fischer, H; de Jeu, WH. *Phys. Rev. Lett.* **1996**, *77*, 5221.
(115) Nieuwhof, RP; Marcelis, ATM; Sudholter, EJR; Picken, SJ; de Jeu, WH. *Macromolecules* **1999**, *32*, 5, 1398-1406.

Dedication

This thesis is dedicated to:

my parents, Tsun-Hsien Wu and Hsiao-Chin Huang
for their overwhelming love and support
over the years

and my wife, Peiwen,
whose love, courage, company, and smile
have always been invaluable to me

Chapter 2

Design, Synthesis, and Characterization

2.1 INTRODUCTORY REMARKS

Ferroelectric liquid crystals (FLC) have attracted much attention since the discovery of surface-stabilized FLC devices capable of switching on nanosecond timescales.[1] Recent advances in FLC's permit their introduction in polymeric liquid crystals by covalently attaching a chiral mesogen onto a polymer backbone with a flexible polymethylene spacer.[2-5] These LC copolymers exhibit the chiral smectic C* phase. Potential applications include electro-optical active devices, optical switching materials, display devices, and optical image storage devices.

The side-chain FLC diblock copolymers used in this thesis were synthesized and characterized by Zheng *et al.* [6] and Anthamatten *et al.*,[7] and examined for their block copolymer morphologies [7-10] and bulk thermotropic LC properties.[6,7,9,10] Previous papers provide the details of these studies, including the material design,[6] synthesis (of the monomer,[7-9] homopolymer,[7-9] and diblock copolymers[7-11]), thermal phase behavior,[6-8,10] morphological behavior,[7-10] orientation behavior with processing,[7,9-11]and simulations.[12]

Thus far, there has been very limited investigation of thin film morphologies of side-chain LC diblock copolymers.[13-19] However, the behavior of these unusual thin films must be better understood, particularly for applications, such as field dependent nano-patterning. Thus, the thin film morphology and LC alignment inside the film are crucial.

A systematic study of the thin film morphology of LC copolymers is described in this thesis.

This chapter will focus on the design, synthesis, and characterization of LC diblock copolymers used in this thesis. Although more detailed accounts of the synthesis of these materials has been reported in separate papers, [6,7] and in the thesis dissertation of Anthamatten,[20] a brief synopsis of the synthesis, and a description of the materials used and the experimental methods will be included. The design criteria of the LC molecules and block copolymer will be described first. Then the synthesis of monomer and polymers, and the characterization will be stated. Substrate effects and cleaning procedures will be also included. Experimental methods with thin film characterization tools will also be described.

2.2 MATERIALS: TARGET MOLECULAR STRUCTURE AND DESIGN CRITERIA

Introduction

A series of LC diblock copolymers was designed in order to study the LC behavior of the diblock copolymer thin films. They combine the advantages of well-defined nanometer domains in block copolymers, and the ordering behavior of the LC phase. Ongoing research in this direction is hindered by two major problems – the formation of large LC domain areas, and the control of natural surface patterns. A few groups have recently reported thin film properties of LC diblock copolymers;[13-19] however, there is a lack of experimental or theoretical understanding of how LC ordering is influenced by the block, air, and substrate interfaces, and the role of the LC phase in determining the ordering of the block copolymer in ultrathin films. For this reason, this thesis presents a new field of study.

Design Criteria

The first criterion for the LC diblock copolymer is that the two blocks must form microphase separated structures at room temperature. When structurally dissimilar blocks are chemically linked together, block polymers can self-assemble into nanometer-scale domains; however, the block components must be sufficiently incompatible to undergo strong segregation to obtain well-ordered copolymer domain. With nanometer scale structures at room temperature, it is possible to study LC behavior in copolymer nano-domains, and the influence of block interfaces on LC alignment.

The chemical structure of the desired LC diblock copolymer consists of two blocks, the glassy amorphous block and the flexible LC-containing block, as shown in Figure 2.1a. The glassy amorphous block provides structural integrity and mechanical strength to the film. Furthermore, the interface between two immiscible blocks can stabilize side-chain LC mesogens. The LC side-chains need to be able to switch easily under external fields (e.g. electric or magnetic field) in order to have good electro-optical properties. For this reason, the LC polymer main chain is chosen to have a glass-transition temperature (Tg) lower than the glass transition of the polystyrene block to increase the mesogen mobility. In the case of this polymer system, the substituted methacrylate has a Tg, which is approximately 40 °C, much lower than the Tg of approximately 100 °C observed for polystyrene. The alkyl spacer between the attached LC mesogen and the polymer backbone can decouple the mesogen from the polymer chain. The spacer length also affects the LC mobility. The chiral group, as shown in Figure 2.1b, at the end of LC mesogen, induces the ferroelectric properties. The end group of the mesogen may play an important role for the thin film surface morphology, and can be modified to achieve different interfacial properties by synthesis. To make the copolymer processible, it should be easily dissolved in general solvents for convenience in processing.

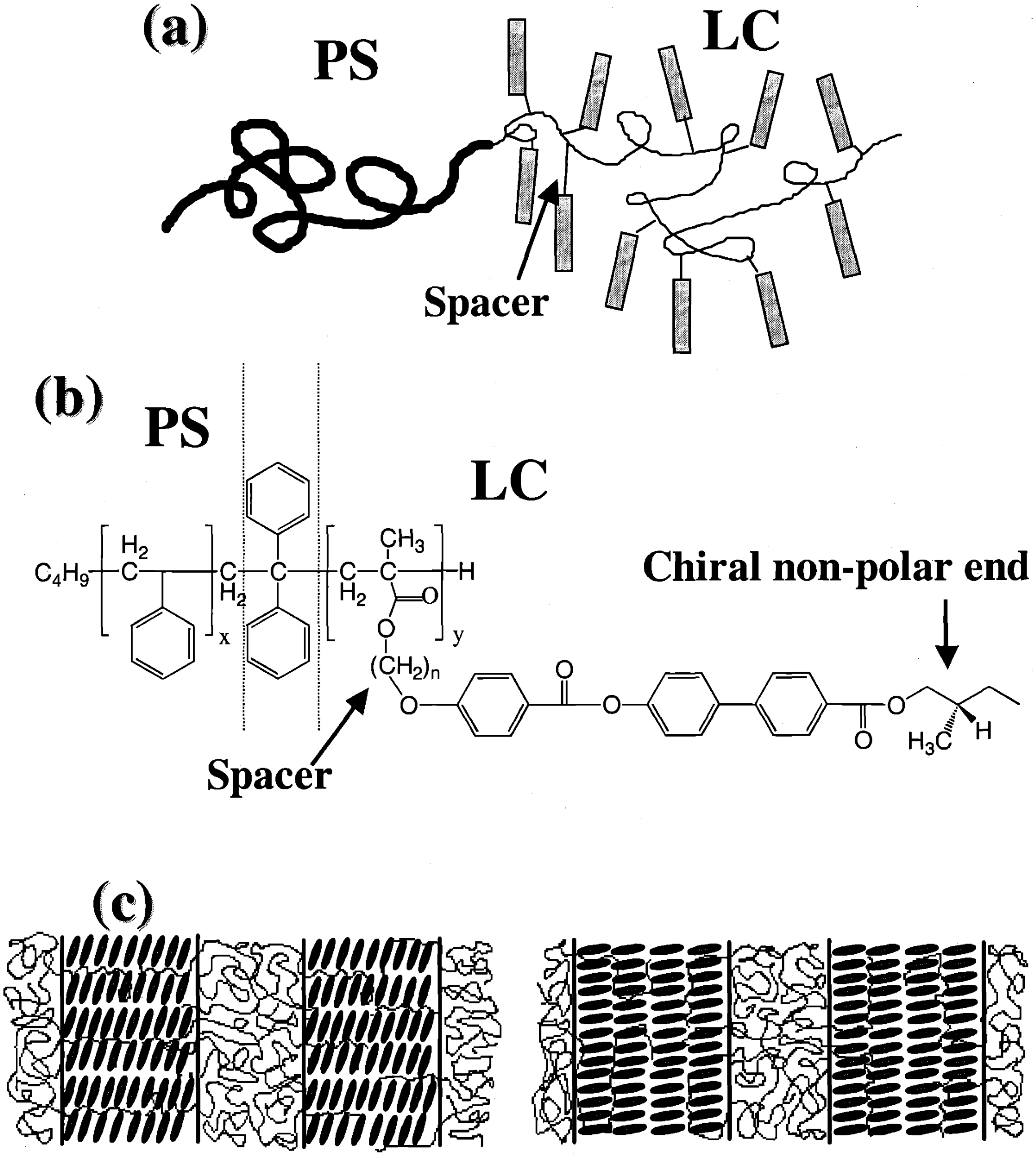

Perpendicular (n = 6) **Parallel (n=10)**

Figure 2.1: (a) Cartoon of side-chain LC diblock copolymer (schematic drawing); (b) Chemical structure of PS-b-PHBPB diblock copolymer; (c) Illustrations of the PS and LC for block interface with perpendicular and parallel smectic ordering. PS, polystyrene. LC, liquid crystal.

Synthetic Method

Direct anionic polymerization was chosen to synthesize this series of LC-containing homopolymer and diblock copolymers. The polymers made using this approach are well defined and mono-dispersed. The other advantage of anionic polymerization is that it can be applied to a number of monomers, making it a flexible approach to changing the non-LC block without major adjustment of the experimental setup and conditions. Furthermore, there is the ability to add an additional block to make triblock copolymers. Finally, the direct polymerization of a liquid crystal monomer ensures complete substitution of side-chain LC mesogens to the polymer backbone.

Target Material

The LC diblock copolymer series investigated in this study, PS-b-PHBPB, is shown in Figure 2.1b. The synthesis and characterization of the monomer, homopolymer, and block copolymer were first synthesized by Zheng and Hammond [6] in our research group. HBPB is a methyl methacrylate monomer with side-chain LC mesogens. The (s)-2-methyl-1-butyl-4'-(((4-hydroxyphenyl)carbonyl)oxy)-1,1'-biphenyl-4-carboxylate mesogens are chemically linked to the main chain with hexyl (n = 6) and decyl (n=10, PDBPB) alkyl spacers. PS-b-PHBPB diblock copolymer, polystyrene, and PHBPB homopolymer are prepared by a sequential anionic polymerization. LC domains exhibit a smectic C* phase with a layer spacing of 3.5 nm, as determined by small angle X-ray scattering (SAXS) in previous studies.[7,8,11]

The PS-b-PHBPB diblock copolymers fit the criteria described above. The details of this serious of diblock copolymers are listed in Section 2.4. They can self-organize into specific nanometer scale morphologies, depending on the relative volume ratio. They are composed of one high Tg block (PS block) to stabilize the domains, and one low Tg block (LC block) for easier LC switching. The mesogen was composed of a chiral non-polar end group, and a flexible spacer controls the mesogen mobility. These characteristics allowed study of LC structures within the block copolymer structure. The system with a shorter spacer (n=6) was chosen to study the thin film morphology, and in this system, the smectic layer was perpendicular to the block interface in bulk morphologies. These LC ultrathin films have several potential applications, such as nano-lithography, nano-structure fabrication, or electro-optical properties.

2.3 SYNTHETIC SCHEME OF MESOGENIC MONOMERS AND BLOCK COPOLYMERS

Zheng [6] in Hammond's group synthesized and fully characterized the LC mesogenic monomer. The PS and LC monomers were then anionic-polymerized sequentially to make diblock copolymers. LC diblock copolymers with various block ratios and LC homopolymer were further prepared by Anthamatten [20] and myself to be used in this study. Figure 2.2 shows the summary of the synthetic scheme. Details of the synthesis and the bulk morphologies are described elsewhere.[6-9,11]

2.3.1 Synthetic Scheme of the LC Mesogenic Monomer ($C_{35}H_{40}O_7$) (5)

4-(6-Hydroxy-(n-hexyl)oxy)benzoic acid ($C_{13}H_{18}O_4$) (1)

p-Hydroxybenzoic acid (0.05 mol, 6.9 g) and KOH (0.11 mol, 6.2 g) were dissolved in 75 mL of ethanol and 10 mL of distilled water with a catalytic amount of KI (0.1 g). The solution was brought to reflux at 105 ºC with the slow addition of 0.06 mol (8.2 g) of 1-hexyl-n-chloro-alcohol. The reaction was refluxed for an additional 12 hours and then cooled to room temperature. Ethanol was removed and the resulting white solid was diluted with 100 mL of distilled water to make it homogeneous. The unreacted n-alkyl alcohol was removed by washing twice with 200 mL of diethyl ether. The aqueous phase was acidified with 6.0 M HCl until pH is 5.0 to produce a white solid. It was then filtered and washed extensively with water. The crude product was recrystallized in the mixture of ethanol: water (9:1). The final yield was about 60% and the structure was confirmed with NMR. White crystals, m.p. 144 °C; ^1H NMR (in $CDCl_3$) chemical shift: 2.2-2.5 [m, 8 secondary H, -(CH_2)-], 4.2 (t, 2 secondary H, -CH_2-O-Ar), 4.8 (t, 2 secondary H, -O-CH_2-), 6.9 and 8.0 (2d, 4 aromatic H).[20]

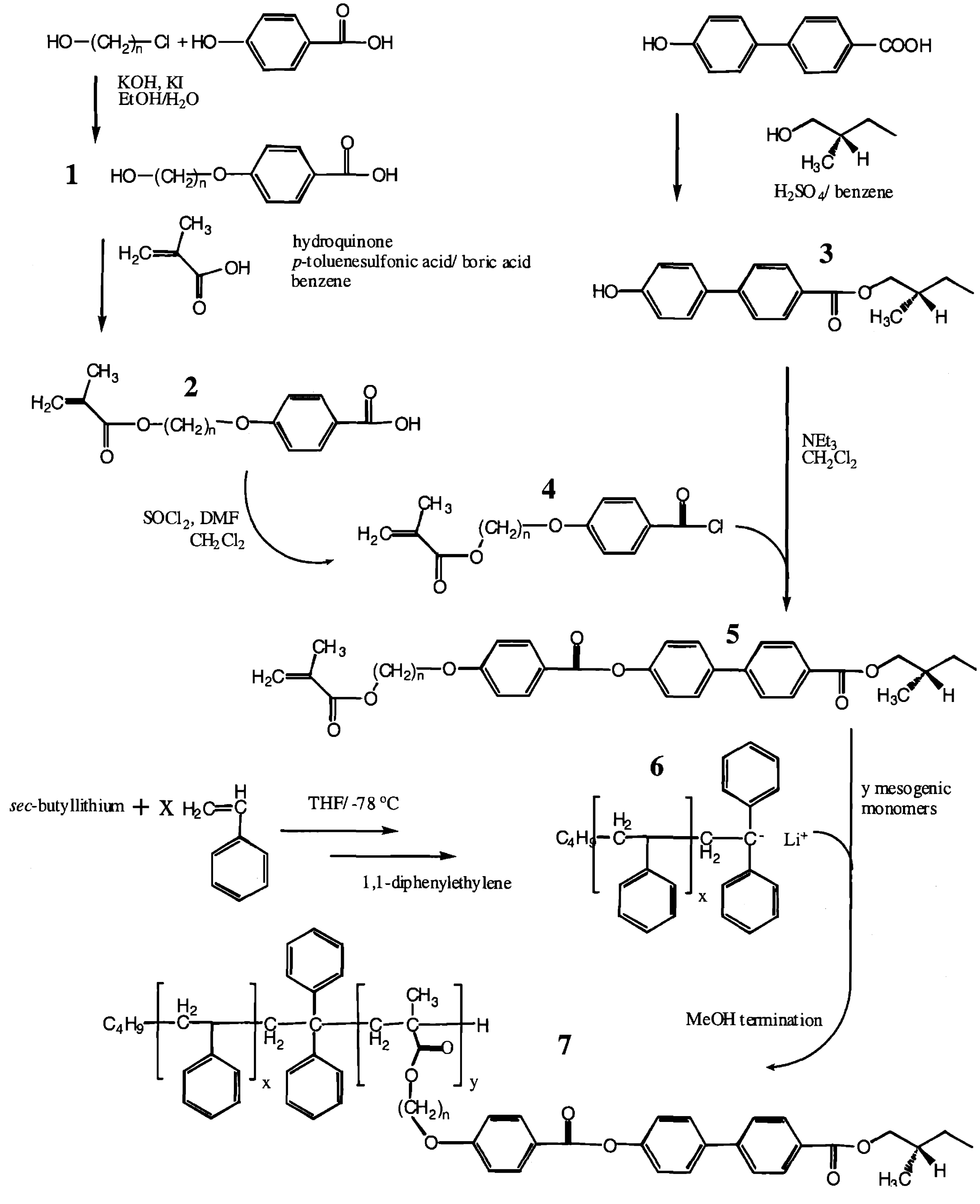

Figure 2.2: Synthetic scheme of the PnBPB monomer and the PS-b-PnBPB diblock copolymer.[20]

4-(6-(Metha-acryloyloxy)hexyloxy)benzoic acid ($C_{17}H_{22}O_5$) (2)

The mixture of **1** (0.017 mol, 4 g), 1 g (0.005 mol) of p-toluene sulfonic acid, 0.65 g (0.006 mol) hydroquinone, 0.1 g (0.002 mol) boric acid, and 16 g (0.186 mol) methacrylic acid was refluxed in 70 mL dried benzene for 48 hours in a Dean-Stark apparatus. The reaction mixture was cooled and diluted with a 3-fold quantity of diethyl ether (200 mL). It was then washed six times with 200 mL warm distillated water to remove excess methacrylic acid. A rotavapor was used to remove the solvent. The product was dissolved in a small amount of acetone (10 mL) and reprecipitated in 600 mL distilled water. The yield is around 100%. The quality of the crude product was sufficient for the following step from NMR. White solid, yield ~80%, m.p. 86 °C; ^1H NMR (in $CDCl_3$) chemical shift: 1.5-1.8 [m, 8 secondary H, $-(CH_2)-$], 1.9 (s, 3 primary H, $=(C-)-CH_3$], 4.0 (t, 2 secondary H, $-CH_2-O-Ar$), 4.2 (t, 2 secondary H), 6.9 and 8.0 (2d, 4 aromatic H).[20]

(S)-2-Methylbutyl 4-hydroxybiphenyl-4'-carboxylate ($C_{18}H_{20}O3$) (3)

4-Hydroxy-4'biphenylcarboxylic acid (12.6 g, 0.06 mol), (S)-2-methyl-1-butanol (20 g, 0.09 mol), and 1 mL of concentrated sulfuric acid were mixed with 150 mL of dry benzene and refluxed for 72 hours in Dean-Stark apparatus until the carboxylic acid component was completely dissolved. Then the cooled mixture was washed with 1% $NaHCO_3$ aqueous solution to a brown clean solution, and dried over $MgSO_4$. The solvent was removed by the rotary evaporator. After two recrystallizations in toluene/hexane solution (1:1), high yields were obtained (~85%). m.p. 105 °C. ^1H NMR (in $CDCl_3$) chemical shift: 1.0 [m, 6 primary H, $-HC(CH_3)-CH_2CH_3$], 1.3 and 1.5 (m, 2 secondary H, $-CH_2CH_3$), 1.8 [m, 1 tertiary H, $-HC(CH_3)-$], 4.1-4.3 (m, 2 secondary H, $-O-CH_2-$), 4.9 (s, 1H, Ar-O-H), 6.9-8.1 (4d, 8 aromatic H).[20]

Methacrylate monomer ($C_{35}H_{40}O_7$) (5)

The acid chloride **4** was first formed by dissolving **2** (5.2 g, 0.017 mol) in 25 mL of dry dichloromethane under nitrogen. Excess thionyl chloride (4 mL) and three drops of

DMF (as a catalyst) were added to the mixture. The mixture was stirred under nitrogen purge for two hours at room temperature. The solvent and excess thionyl chloride were then removed under vacuum resulting in an acid chloride **4**. The acid chloride (4 g, 0.016 mol) was again diluted with dichloromethane (100 mL) and then was added drop-wise to a solution, and 5 mL of triethylamine in 125 mL of dichloromethane. The reaction mixture was stirred for 20 hours at room temperature under nitrogen. Column chromatography using ethyl acetate/ n-hexane (1:3) as the eluent was used to separate the monomer from side products. The monomer was further purified by multiple recrystallizations from dry ethanol and then dried excessively under high vacuum before being used in anionic polymerization. ^{1}H NMR (in $CDCl_3$) is shown in Figure 2.3: chemical shift: 0.9-1.0 [m, 6 primary H, $-HC(CH_3)-CH_2CH_3$], 1.5 and 1.5 (m, 2 secondary H, $-CH_2CH_3$), 1.5-1.8 [m, 8 secondary H, $-(CH_2)-$ and 1 tertiary H, $-HC(CH_3)-$], 1.9 [s, 3 primary H, $=(C-)-CH_3$], 4.0 (t, 2 secondary H, $-CH_2-O-Ar$), 4.2 (t, 2 secondary H), 6.9-8.1 (4d, 8 aromatic H).[20]

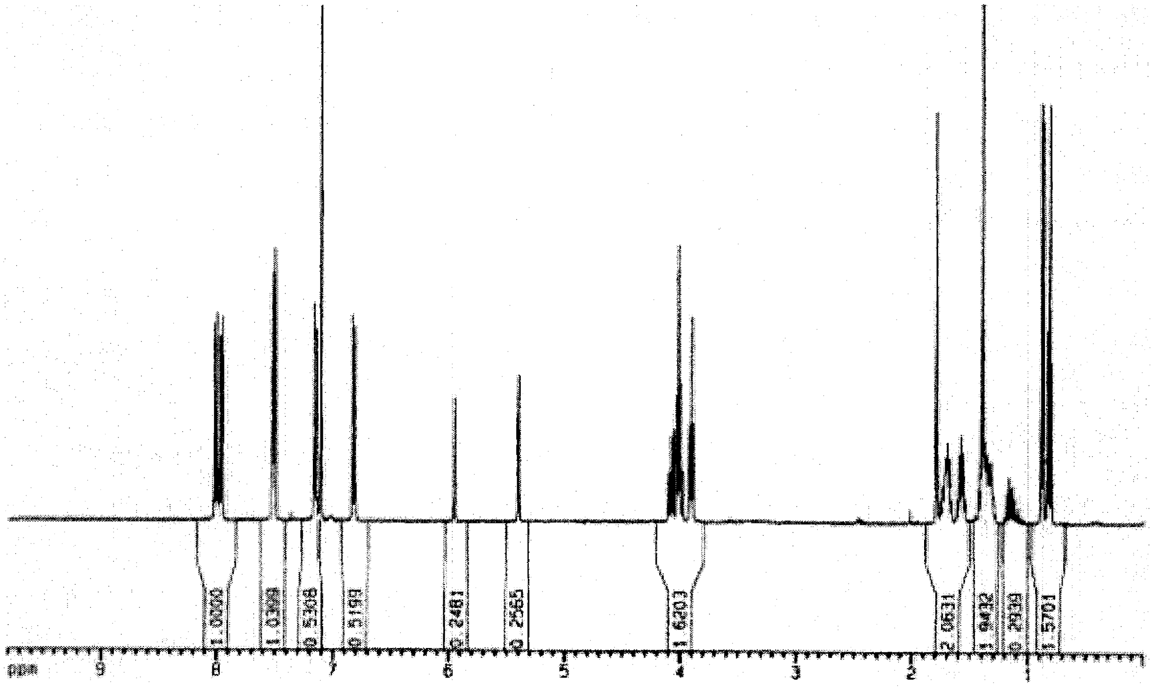

Figure 2.3: ^{1}H NMR spectra for MHBPB methacrylate monomer (5).[20]

2.3.2 Synthesis of PS-b-PLC Diblock Copolymers (7)

The synthesis and characterization was developed in a separate study by Zheng.[6,20] For the ease of reference, details of these procedures are included in this section.

All glassware was dried over two days in a high-temperature oven (120 °C) before anionic polymerization. Magnetic stir bars and syringes were oven-dried. All reagents were purified and dried under high vacuum. The equipment was then moved into a glove box under a nitrogen atmosphere. For the synthesis of diblock copolymers, the amount of initiator to monomer was determined by the desired number of repeat units in the polymer. The initiator, sec-Butyllithium (1.3 M solution in cyclohexane, Aldrich), was dissolved into the THF solvent, followed by addition of the appropriate amount of styrene monomer at room temperature. The accurate amount of the initiator to the monomer was determined by the desired numbers of repeat units in the polymer. Thirty minutes later, a small amount of the solution was isolated to determine the molecular weight distribution of the first block. 1,1-Diphenylethylene (Aldrich) was then added to end-cap the living anions. The reaction temperature was reduced to -78 °C. The mesogenic monomer dissolved in THF was then added. After stirring for three hours, the second-stage polymerization was terminated by pure methanol. All the polymer products were reprecipitated in a large amount of methanol. The yields ranged from 50-80%. The yield was low compared to general anionic polymerization because of the huge LC side chains. The unreacted monomer was isolated and repurified for future use. Figure 2.4 shows typical GPC traces before and after the addition of the mesogenic HBPB monomer.

The PHBPB homopolymer were synthesized at -78 °C by the same procedure without adding the styrene monomer. The yields are usually higher than 90%.

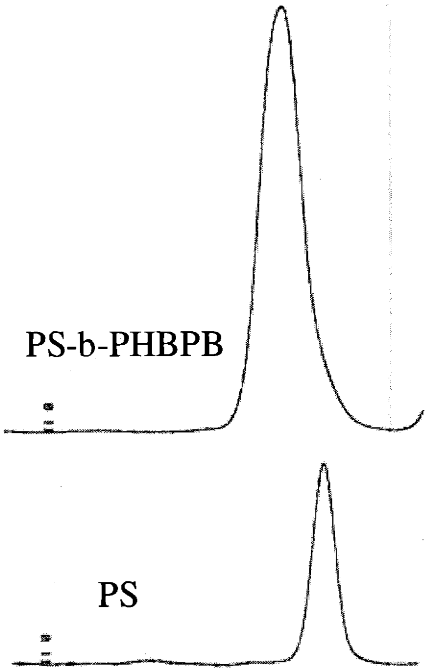

Figure 2.4: Representative gel-permeation chromatogram (GPC) of polystyrene homopolymer and corresponding PS-b-HBPB diblock copolymer.[20]

2.4 SAMPLES LIST AND PHASE DIAGRAM

2.4.1 Material Properties

Several important bulk properties of PS, PHBPB, HBPB, and PS-b-PHBPB diblock copolymers, are reviewed in this section [7-9,11] and listed in Table 2.1 and Table 2.2, such as molecular weight, polydispersity index, block periodicity, morphology, and LC phase transitions. The polystyrene-b-methacrylate-based biphenyl benzoate mesogenic copolymers with hexyl spacer are referred by the following nomenclature PS-b-HBPBx, or in brief, Hx, where x denotes the wt% of the HBPB block. Anthamatten *et al.* [7,9,20] observed strong phase separation ($\chi_{AB}N$ » 10) of this series of diblock copolymers at room temperature from SAXS and TEM data. The bulk morphology and the block periodicity (d-spacing, L_o) were determined by SAXS and confirmed by TEM.[7,9,10,20] The PS block has higher glass transition temperature (Tg) at around 100 °C, and the Tg of the PLC block is approximately 40 °C as determined from measurements using a differential scanning calorimeter (DSC).[6]

Table 2.1: Material properties of polymers used in this research.

	Number averaged molecular weight			Polydispersity index	LC volume ratio	Number of repeat unit		Block periodicity (nm)	
Polymer	PS	PLC	Total			PS	LC	SAXS	TEM
PS	29.3 k	0	-	-	0	293	0	-	-
H41	11.0 k	7.3 k	18.3 k	1.06	0.40	110	13	17.3 (8.5, 5.6, 4.2)	14
H50	8.4 k	11.0 k	19.4 k	1.14	0.57	84	19	14.3, 17.5	-
H79	4.8 k	16.3 k	21.2 k	1.08	0.77	46	28	13 (7.5, 6.5, 4.9)	12
H85	1.7 k	10.4 k	12.1 k	1.09	0.86	16	18	7.2 (3.6)	6.5-7
PHBPB	0	17.3 k	17.3 k	1.05	1.00	0	30	-	-
HPBP	0	572	-	-	1.00	0	1	-	-

Table 2.2: Morphologies and LC transitions of diblock & homopolymers.[a]

Polymer	Room Temp Morphology	LC Phase Transitions (°C)[b]
H41	Lamellae	Heating: (G_{LC}=33) S_C* (G_S=97) S_C* (140) S_A (172) I Cooling: I (159) S_C* (Gs=91)
H50	Perforated Lamellae	Heating: S_C* (161) I Cooling: I (145) S_C*
H79	Hexagonally Packed Cylinder (HPL)	Heating: S_C* (176) S_A (212) I Cooling: I (203) S_A (173) S_C*
H85	Smectic Bilayers	Heating: Sc* (~175) I
PHBPB	-	Heating: (G_{LC}=35)S_C*(120)S_D(137.1)S_A(157)Ch(170) I Cooling: I (150.3) S_A (127.0) S_C* (G_{LC}=33)
HPBP	-	Heating: K (75) S_C* (129) S_A (138) Ch (170) I Cooling: I (153) Ch (133) S_A (125) S_C* (27) K

---

[a] Transitions were determined by optical microscopy, differential scanning calorimetry, and temperature-dependent SAXS.[8,9,20]

[b] G_{LC}: Tg of LC segment; G_S: Tg of polystyrene; S_C*: chiral smectic C phase; S_A: smectic A phase; I: LC isotropization state; K: crystal state

LC domains exhibited a smectic C* phase with a layer spacing of around 3.5 nm (s_o) for all diblock copolymer samples as determined by SAXS.[8,11] Figure 2.1c shows the LC layer versus the block interface. Oriented samples in the bulk state indicated that smectic layers orient perpendicularly to block copolymer interfaces for the hexyl (n=6) alkyl spacers, but it is parallel for the decyl (n=10) spacers. The temperature of the ferroelectric smectic C phase ranged from 40 to 135°C.[7,8,20] Hammond's group[8] also reported previously that the block interface untwisted the helix structure and stabilized the LC domain.

2.4.2 Phase Diagram of PS-PHBPB Series

Figure 2.5 shows the phase diagram of the PS-b-PHBPB series of diblock copolymers with different molecular weights and LC volume fractions. Their molecular weights are tabulated in Table 2.3. The morphologies were determined experimentally by Small Angle X-ray Scattering (SAXS), Differential Scanning Calorimeter (DSC), and polarized optical microscope (POM) in previous studies of Zheng [6,8,11] and Anthamatten.[7,9,20] In this research, we studied different diblock morphologies, including lamellar, cylindrical, and smectic bilayered morphologies[c].

---

[c] The perforated lamellar morphology (PL) in the phase diagram will not be discussed in this thesis. The PL morphology has two sets of peaks in SAXS spectra. SAXS data were acquired as scattered X-ray intensity (I) as a function of the scattering vector, $\mathbf{q} = (4\pi \cdot \sin\theta) / \lambda$, where θ is one-half of the scattering angle and λ is the X-ray wavelength. The lamellar peaks always locate at specific **q** values (1q, 2q, 3q). However, the second set of peaks may show two different **q** ratios. The PL/ML (mixed layer) morphology has the same **q** ratio (1:2:3) but at different locations. The PL/HPC (hexagonal packed cylinder) morphology has the second set of peaks at different **q** ratio ($1:\sqrt{3}: 2$) and positions.

Table 2.3: Molecular weight (Mn) and polydispersity index of this series of PS-b-HBPB diblock copolymers. [20]

Polymer	M_n (kg/mol)			PDI
	PS Block	LC Block	Total	
PS-HBPB12	48.1	4.8	52.9	1.08
PS-HBPB20	21.8	5.3	27.1	1.11
PS-HBPB24	40.3	7.7	48.0	1.12
PS-HBPB32	17.7	7.3	25.0	1.07
PS-HBPB41	11.0	7.3	18.3	1.06
PS-HBPB43	10.3	7.4	18.1	1.08
PS-HBPB50	8.4	11.0	19.4	1.14
PS-HBPB51	6.8	7.7	14.5	1.07
PS-HBPB54	14.9	17.5	32.4	1.19
PS-HBPB56	10.5	11.0	21.5	1.07
PS-HBPB58	8.8	12.0	20.8	1.11
PS-HBPB79	4.8	16.3	21.1	1.08
PS-HBPB80	3.6	14.3	17.9	1.21
PS-HBPB85	1.7	10.4	12.1	1.09
PMHBPB		7.0	7.0	1.10

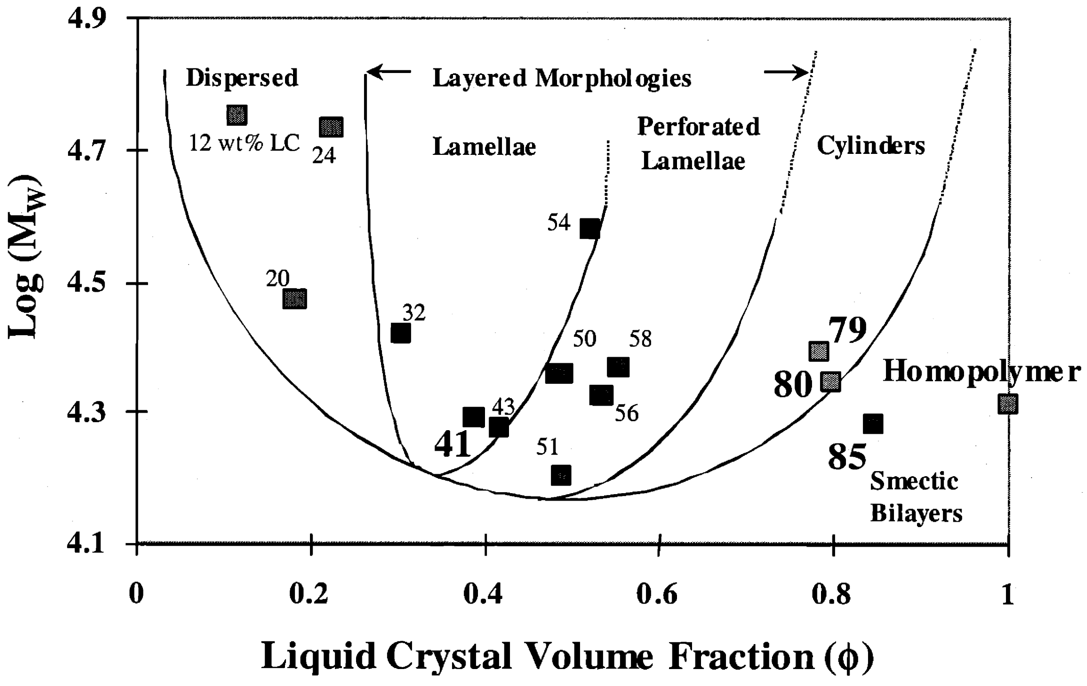

Figure 2.5: Phase diagram of PS-PHBPB series diblock copolymers. The LC volume fraction (Φ) is defined as the ratio of the LC block (including the LC mesogen, the spacer, and the main chain). [20] Bolded numbers were studied in this thesis.

2.5 THIN FILM PREPARATION AND SUBSTRATE SELECTION

2.5.1 Thin Film Preparation by Spin Casting

Samples (polymers and monomer) were dissolved in toluene (Mallinckrodt) at 0.2~2 wt %, and then spin-cast onto pre-cleaned substrates. The spin-casting method was used to make polymer films of 2 to 200 nm in this study. The samples were then kept under vacuum for one day to remove residual solvents, and annealed at an elevated temperature (130 °C, above both Tg) for a week under high vacuum to prevent oxidative degradation of the polymers and dewetting due to hydration of the substrate. Samples of H85 series were annealed at a higher temperature (170 °C) under vacuum for another three days. Average film thicknesses were measured by ellipsometry and AFM.

2.5.2 Thin Film Constraints

Thin film molecular ordering is different from the bulk state due to surface interactions. The ordering is controlled by the geometric constraints caused by the "hard wall", including surface energy minimization, interactions with the substrate, and micro-phase separation.

At the air interface, the polymers tend to self-arrange to arrive at a lower total surface free energy incorporating both enthalpy and entropy contributions. These contributions include: reactions that minimize interfacial area, reductions in surface tension, maximizing chain conformational entropy, and tendencies of components toward preferential surfaces.

2.5.3 Substrate Preparation and Cleaning Procedures

Solid substrate effects are prominent in ultrathin film formation. Different substrates have various surface affinities with polymers. For diblock copolymers, one block will try to cover the surface to decrease the surface tension. For example, the PMMA block of a PS-b-PMMA diblock copolymer prefers to wet the silicon substrate and the PS block covers the air interface. However, the same PMMA block wets gold substrates.

Silicon wafers were used directly after rinsing them with ethanol (200 proof, Pharmco^{TM}, Brookfield, CT). The water contact angles are 57° for advancing and 42° for receding. Silicon wafers were also cleaned by either an acid or base solution to create a hydrophilic surface.[21] Surface properties of silicon were modified to a hydrophobic state by coating the surface with a thin layer of 1,1,1,3,3,3-hexamethyl disilazane. Trichlorosilanes were used to modify the silicon surface chemically. The polymers exhibited better adhesion with hydrophilic substrates than to hydrophobic substrates. Silicon wafers, treated by acid or base solutions, display similar surface properties, which have Si-OH groups at the air interface and are predominantly hydrophilic.

I chose pre-cleaned, prime-grade crystalline silicon wafers to conduct all studies in this thesis. One reason is because of their affinity with our LC copolymer, and the other reason is that they can be prepared using an easy and reliable process. Before treatment, silicon wafers were N-type, phosphorus doped, <100> orientation, low resistivity (1-10 Ω-cm), normal thickness (15 ± 2 mil), and one-side polished. Other common substrates, such as glass, mica, and indium tin oxide (ITO) patterned glass, would be natural candidates to study in the future.

Bare silicon wafers were cleaned and chemically modified to become more hydrophilic by several methods, such as using a "piranha" solution or a base solution. The "piranha" solution is the most widely used method to clean silicon substrates. It is prepared by mixing three parts of hydrogen peroxide (30% H_2O_2, J.T. Baker, Phillipsburg, NJ) to seven parts of sulfuric acid (96% H_2SO_4, Mallinckrodt, Paris, KY). Substrates were immersed into the solution in a petri-dish and stirred with a magnetic bar. The temperature was then slowly raised to 95 °C in half an hour and cooled down. Substrates were then rinsed with DI water and tested for wettability. This cleaning solution is potentially hazardous, which is corrosive and explosive during heating. Keep it away from any organic solvent, such as acetone.

Another commonly used method to clean silicon wafers is the use of base solutions. The base solution was prepared by dissolving 50 g of sodium hydroxide (NaOH, Aldrich) in 150 mL DI water, followed by adding 200 mL ethanol (190 proof, Pharmco). Silicon wafers were immersed in the solution at room temperature for two hours, and flushed by DI water. The water contact angles for the cleaned silicon substrate are 31.1±3° for advancing and 8±2° for receding .

2.6 CHEMICAL CHARACTERIZATION TOOLS

The synthesized polymers were characterized by nuclear magnetic resonance (NMR), gel permeation chromatography (GPC), differential scanning calorimetry (DSC), small angle X-ray scattering (SAXS), and X-ray diffraction.

Nuclear Magnetic Resonance (NMR)

The NMR data for both ^{1}H and ^{13}C were obtained from an Advance DPX-400 NMR Spectrometer, made by Bruker (Billerica, MA). Samples were dissolved in deuterium chloroform-d or dimethyl-d_6 sulfoxide (d-DMSO) (Cambridge Isotope Laboratories, Andover, MA). The NMR was used to verify chemical structures of all materials synthesized and to determine the composition ratio of each block.

Gel Permeation Chromatography (GPC)

A Waters GPC (Milford, MA) set up included a 515 HPLC Pump, a R410 differential refractometer, and a 440 UV absorbance detector. The system was calibrated with PS standards in tetrahydrofuran (HPLC grade, EM Science, Darmstadt, Germany). GPC was used to determine the molecular weight distributions and polydispersities (PDI) of all polymers synthesized.

Differential Scanning Calorimeter (DSC)

For DSC, a Perkin-Elmer DSC7 (Wellesley, MA) was used with a cooling box at temperatures ranging from –40 °C to 250 °C. DSC was used to identify the polymer glass transition temperatures, LC mesophase transition temperatures, and the LC isotropization (T_{iso}) of synthesized monomers, homopolymers, and diblock copolymers.

The data requisition was based on the second heating-cooling cycle. Integration of DSC peaks of both heating and cooling curves provided estimations of various heats of transitions. Thermo-flows were recorded at a scanning rate of 10°/min or 20°/min to identify thermal transitions.

Small Angle X-ray Scattering (SAXS)

Samples were solution cast to form 1 mm films and annealed at 110 °C (below the Tg of the PS block) to encourage phase segregation. SAXS experiments were conducted by a Siemens X-ray system (Erlangen, Germeny). X-rays were generated from a Rigaku RU300 rotating-anode (18 kW), producing Cu Kα radiation, which operated at 40kV and 30mA. The X-ray beam was passed horizontally through an evacuated sample chamber and onto a 2D detector. The reciprocal space data of scattered X-ray intensity (I) was a function of the scattering vector ($q = (4\pi/\lambda)\sin\theta$ (nm^{-1})). Small-angle reflections indicated stacked bilayers, and wide-angle reflections indicated the regular arrangement of side chains within the layers.

X-ray Diffraction

Single crystal X-ray diffraction (X-ray crystallography) is an analytical technique for applications in which X-rays are employed to determine the arrangement of atoms within a crystalline specimen. An automated Bruker Smart/CCD Single Crystal Platform Diffractometer (Billerica, MA) provided X-ray structural analyses of my LC monomer crystals. The instrument was coupled with an automated goniometer with 360-degree ring gears in two-theta and omega angles, plus full 360-degree rotation in phi. The LC monomers were recrystallized several times from dry ethanol before the measurement. This experiment was conducted by Dr. Bill Davis in the MIT Chemistry Department.

Data collections were performed at low temperatures (-50 to -125 °C) with sealed, fine-focus molydenum-target tubes. A microscope-equipped dry box was kept under nitrogen gas for mounting air sensitive crystals. Typical turn-around times under average conditions, from start of data collection to completely refined structure, ranged from under one to three days.

2.7 SURFACE ANALYSIS TOOLS FOR THIN FILMS

2.7.1 Instrumentation and Parameters

Spinner

A photo-spinner from Headway Research Inc. (Garland, TX) was used to spin cast thin films on solid substrates. All substrate-supported polymer films used in this thesis were prepared by spin casting before further analysis. The substrate was held in place by a vacuum. The concentrations of polymer solutions ranged from 0.1% to 2%. The spinning speeds ranged from 2000 to 8000 rpm, depending on the thickness needed. The film thickness was controlled by adjusting the concentration and speed.

Ellipsometry

To measure average film thickness, a model 643-AK Gaertner ellipsometer with a 4mW He-Ne laser was used (Gaertner Scientific Corp., Chicago, IL). The Gaertner Ellipsometer Measurement Program was used to calculate the substrate refraction index (N^s), the extinction coefficient (K^s), and the film thickness using the delta calculation mode. The N^s and the K^s values of substrates were measured before film casting.[22,23]

Goniometer

The goniometer (model NRL C.A. 100-00-115) used was from Rame-Hart Co (Mountain Lakes, NJ) with an Image analysis attachment (model T1-324A, NEC Corp, Japan). The goniometry was used to determine both dynamic and static contact angles of water and hexadecane with the sessile drop method at room temperature. All advancing and receding contact angles were measured on both sides of the drops and averaged over at least five different locations for all samples.

Atomic Force Microscopy (AFM)

The AFM used was a commercially available microscope, Nanoscope IIIa, Dimension 3000 from Digital Instruments (Santa Barbara, CA). It was operated in the tapping mode using a triangular silicon cantilever (length = 127μm, width = 30μm, thickness = 3-5μm) with silicon nitrite tips (Nanoprobe ™ SPM Tips, DI). In the tapping mode, the tip is oscillating near its resonance frequency (304-343 kHz) and only slightly touching the sample surface periodically (sprint constant = 17-64 N/m). This minimizes the lateral destructive forces when scanning through smooth polymeric surfaces. It was used to probe surface topography, film thickness (for scratched samples), and roughness of samples at the air surfaces.

Optical Microscopy (OM)

Optical microscopy studies were performed on a Leitz optical microscope, equipped with crossed polarizers, a CCD camera, a JVC color video camera, and a Mettler FP82HT Hot stage with a FP90 Central Processor. Polarized OM at 0° and 90° was used to identify LC transition temperatures and the types of LC phase of bulk samples by their characteristic birefringent textures.

2.7.2 Transmission Electron Microscopy (TEM) Sample Preparation and Analytical Protocol

For TEM, both JEOL 200CX and 2000FX transmission electron microscopes were used in bright field mode at an acceleration voltage of 120-200 kV. TEM provided direct images of phase-separated morphologies, including type, length scale, and orientation of the morphology (real space data). Some samples were stained for 10 to 30 min with vapor-phase ruthenium tetraoxide (RuO_4, 0.5% stabilized aqueous solution, EM grade, Electron Microscopy Sciences). The heavy metal atoms (ruthenium) imparted selectively to the specific PS block domains in the system.[24-26] This method also protects films against beam thinning in the PMMA area, as staining agents can crosslink ruthenium-attached areas.

Top-view TEM sample Preparation using a Peeling Technology

Fasolka and Mayes *et al.* [27,28] developed a peeling technolique for preparing samples as polymer thin films. Polymer samples were dissolved in the toluene solution and spin-cast onto substrates. Samples were then placed under vacuum to remove residual solvents and annealed at 130 °C for 7 days. AFM was used to probe the topography and ensure that the topography was not changed. A thin layer of carbon (2~5 nm) was coated on the top of the polymer film by the carbon evaporator for protection. The sample was put on the top of the petri-dish cover and covered by a poly(acrylic acid) solution (PAA, MW=90k, 25% aqueous solution, Poly Sciences, Inc.). The PAA layer was then peeled up after it was dried overnight. The polymer and the carbon-protecting layer stayed with the PAA layer and were separated from the substrate. The film was floated on DI water with PAA layer on the bottom to dissolve the PAA. After the PAA layer was dissolved, the polymer films (with a carbon layer on the bottom) were supported by the water surface tension, floated on the water, and picked up by TEM copper grids. Samples were stained on the PS block using RuO_4 vapor for 15 minutes to enhance the contrast between the two blocks. JOEL 200CX was used to get TEM images from 5000 X to 100,000 X for both stained and unstained samples.

Cross-sectional TEM Sample Preparation

The above top-view TEM samples were further processed to obtain the TEM images of the cross-section.[27,28] Another thin layer of carbon (~2 nm) was evaporated on top of the films to protect them. The whole system now includes the carbon layer on top, polymer film, carbon layer on bottom, and the TEM copper grids from top to bottom. The whole system was then embedded into an epoxy mold. The epoxy mold was made by mixing the epoxy resin (Eponate 12 resin, glycerol polyglycidyl ether), DDSA (dodecenyl succinic anhydride), NMA (nadic methyl anhydride), and DMP (2,4,6-tri(dimethyl-aminomethyl) phenol) in a volume ratio of 25:16:14:1.[8,20] The mixtures were well mixed at room temperature for ten minutes, and filled into a mold with films in the center. Samples were heated at room temperature overnight to cure completely. After curing, the mold was filed from the side to the film area and sectioned perpendicular to the film (50 μm thick) using an RMC ultramicrotome (model MT-X) equipped with a diamond knife. The carbon-coating layers were used to locate thin films on the grid, in addition to protecting polymer films from the erosion of epoxy monomers. Only areas evaporated with carbon could be observed under the optical microscope. The microtomed slices (epoxy / carbon / polymer / carbon / grids / epoxy) were floated on the de-ionized water, and collected by other TEM grids. An optical microscope was used to pre-select samples with metal grid dots. A high resolution JOEL FX-2000 TEM operating in bright field with 120-200 kV accelerating voltages was used to get 410,000 X images.

Free-Standing Thick TEM Sample Preparation

Generally, free-standing TEM samples (~ 1 mm thick) were prepared by slowly casting them from a 3% (by wt) toluene solution onto a glass slide coated with a carbon film. They were dried in vacuum for two days, and then annealed at 110 °C for two days. The core of each sample was cut into 50 nm slices with a Reichert-Jung FC4E Ultracut E microtome.[29-32] The slices were floated on de-ionized water, and transferred onto copper grids.

2.7.3 Contact Angles and Hysteresis

The character of the solid-liquid interface is a good indicator for the surface properties. The quality of stable polymer films can be estimated from wetting measurements, and the shape of a liquid drop on the surface is affected by the free energy of the surface.[22,23,33,34] The Young's equation is widely used to describe the equilibrium wetting of an ideal solid surface. An ideal solid surface is rigid, flat, chemically homogeneous, and non-perturbed, where σ_{SV}, σ_{SL}, and σ_{LV} are the solid-vapor, solid-liquid, and liquid-vapor interfacial tensions respectively.

$$\cos \theta_e = (\sigma_{SV} - \sigma_{SL}) / \sigma_{LV} \quad (2.1)$$

However, the wettability does not only depend on the surface energy, but also on the surface roughness. Wenzel [35,36] proposed a theoretical model for the apparent contact angle on a rough and chemically homogeneous surface to modify the Young's equation, where r is the average roughness ratio.

$$\cos \theta_W = r * \cos \theta_e ; \quad r \geq 1 \tag{2.2}$$

The roughness increases the solid-liquid interfacial area by r. The equation indicates that surface roughness enhances the hydrophilicity of a hydrophilic surface and also enhances the hydrophobicity of a hydrophobic surface.

Several liquids with different surface tensions are widely used in the literature [22,23] to measure contact angles. These are liquids, such as water (72.8 dyne/cm at 20 °C), hexadecane (HD), bicyclohexyl (BCH), n-propanol (23 dyne/cm), n-decane (23 dyne/cm), n-octane (21.7 dyne/cm), carbon disulfide (32.3 dyne/cm), methylene iodine (50.76 dyne/cm), glycerol (63.4 dyne/cm), and 1-bromonaphthalene. Water is commonly used for polymer films due to its non-destructive properties to the films. Water is sensitive to the order of hydroxylated groups and the presence of ether linkages on the air interface. The typical contact angle on a methyl ($-CH_3$) surface is ca. 111-115° for water and 45-46° for HD, and the contact angle on a closely packed methylene ($-CH_2-$) surface is ca. 102-103° for water and 0° for HD.[22,23] The experimental errors may result from small differences in the liquid purity as well as from statistical errors in the actual reading of contact angles.

Hysteresis

The hysteresis ($\Delta\theta$) is defined as the maximum difference between the advancing angle (θ_a) and the receding angle (θ_r), as shown in equation 2.3.[37,38] It is a function of the roughness, chemical heterogeneity, the surface polarity, molecular reorientation effects, and polarity of contact liquids.

$$\Delta\theta = \theta_{a,max} - \theta_{r,min} \tag{2.3}$$

The hysteresis increases with the roughness by two effects, the barrier effect, and the capillary effect (by the attraction or depression of grooves).[34,37] Both advancing and receding angles can be fitted by the linear regression of $\Delta\theta$ and θ data in Equation 2.4. The equilibrium angle at room temperature can be extrapolated at $\Delta\theta = 0$.

$$\theta_{(\Delta\theta)} = \theta_e + A * \Delta\theta \tag{2.4}$$

2.7.4 Angle-Resolved X-ray Photoelectron Spectrometry (AR-XPS)

Instrumentation and Parameters

X-ray Photoelectron Spectrometry (XPS), also known as Electron Spectroscopy for Chemical Analysis (ESCA), is a powerful tool for surface analysis and composition determination. This technique can be used to determine the depth profile by combining the ion-etching technique (destructive) or angle-resolved (non-destructive) technique.[39,40] For example, Bongiovanni *et al.* [41] used AR-XPS to measure the fluorine gradient of methacrylic copolymer thin films containing a perfluoropolyether structure by scanning at 45° and 10°. They showed the fluorinated monomers preferentially concentrate at the air interface.

Three different XPS instruments were used in this thesis to determine near surface chemical compositions. High-resolution scans of the C_{1s} region were performed and the carboxylic group ratios were calculated from peak areas.

A Surface Science spectrometer was used to acquire data for films of homopolymer blends and diblock copolymers in Chapters Four and Five. The experiments were supervised by Dr. Yuan Lu at Harvard University (Cambridge, MA). The model was SSL-Fision SSX-100 XPS with a monochromatic AlKα X-ray source. The takeoff angle is 55° to the surface normal.

Angle-resolved (AR) XPS experiments in Chapter Three were done with the help of Dr. E. Libby Shaw at MIT (Cambridge, MA). Data were acquired from the Kratos AXIS-Ultra XPS using mono-chromated Al-Kα (1486.6 eV) X-rays. Six different takeoff angles ($\Phi = 0^\circ, 35^\circ, 40^\circ, 55^\circ, 63^\circ$, and 70°) were used. A pass energy of 10 eV was used with 0.1 eV per step to acquire carbon peaks from 275 to 295 eV. The smallest region for acquisition of an energy spectrum on this XPS is about 20 microns, controlled by the hemispherical analyzer settings. Carbon peaks were smoothed with a 7-point SG smooth and were curve fit with Gaussian peaks.

The XPS experiments of peeled diblock samples in Chapter 4.2.1 were conducted by Dr. N. Carl Miller at Raytheon Co., Reliability Analysis Laboratory (Lexington, MA). Data were acquired on a Physical Electronics 5000LS ESCA with a magnesium X-ray source. The angular-resolved mode was used to scan films with various penetration depths by two different takeoff angles, 15 degrees (near to surface normal, 30 μm^2 spot size) and 75 degrees (glancing angle to the analyzer, 800 μm^2 spot size). The electron flood gun was operated at 20 milliamps and 2.4 volts for charge neutralization. A pass energy of 23 eV was used with 0.1 eV/step to acquire carbon peaks from 275 to 295 eV until reaching a signal/noise ratio of 300. Carbon peaks were smoothed with a 7-point SG smooth and were curve fit with Gaussian peaks.

Table 2.4 shows the standard fitting parameters (peaks, binding energies, and peak ratio) of C_{1s} scans for polystyrene (PS) and poly(methyl methacrylate) (PMMA).[42,43] This provides a reference when fitting our homopolymers and diblock copolymers. Table 2.5 lists the theoretical C_{1S} fitting parameters of PHBPB and polystyrene homopolymers. One example of my curve fitting is demonstrated in Figure 2.6 and Table 2.6.

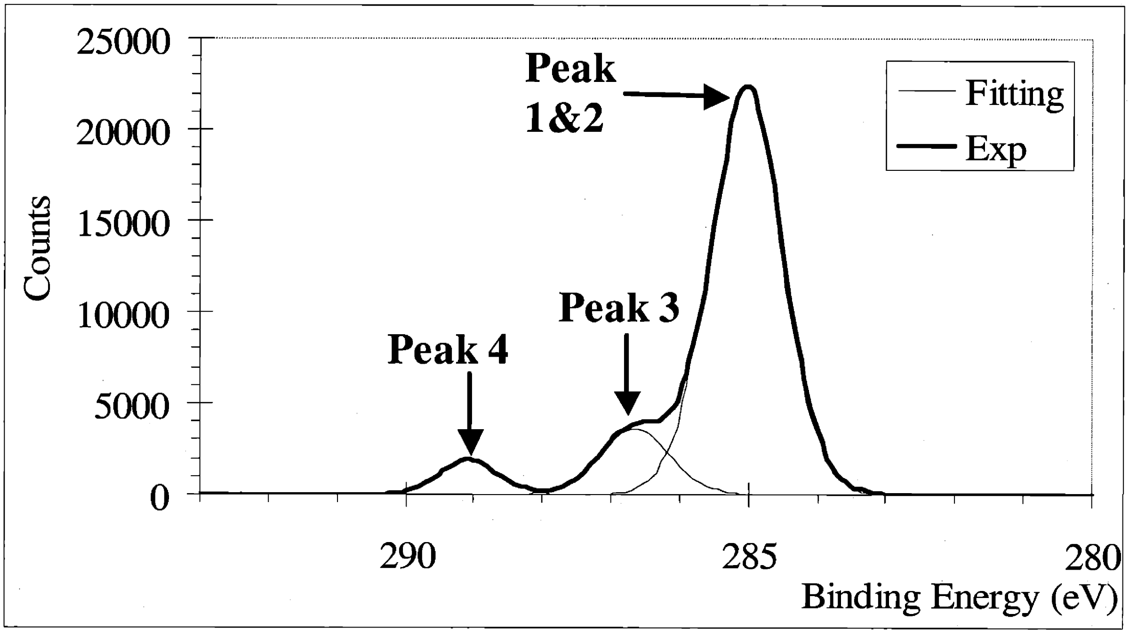

Figure 2.6: Experimental data and fitting curves of high-resolution XPS carbon 1s scan for a PHBPB thin film. Fitting peaks correspond to Table 2.5.

Table 2.4: XPS fitting parameters of C_{1s} scan for poly(methyl methacrylate) (PMMA) and polystyrene (PS) from references.[42]

C_{1s}	PMMA				PS	
Peak #	1	2	3	4	S1	S2
Peak	$-CH_3$ / $-CH_2-$	>C<	$-OCH_3$	-COO-	-CH= (benzene)	$-CH_2-$ / >CH-
Binding Energy (BE, eV)	285.00	285.72	286.79	289.03	284.76	285.00
BE Shift (eV)	-	0.72	1.79	4.03	-	0.24
FWHM (eV)	1.15	1.06	1.28	0.99	0.87	0.96
Area (%)	42	21	21	17	75	25

Table 2.5: Theoretical XPS C_{1s} fitting parameters of PHBPB and PS.

C_{1s}	PHBPB				PS	
Peak #	1	2	3	4	S1	S2
Peak	$-CH_3$ / $-CH_2-$	>C<	$-OCH_3$	-COO-	-CH= (benzene)	$-CH_2-$ / >CH-
# of carbon in a monomer	21	6	5	3	6	2
Area (%)	60	17.1	14.3	**8.6**	75	25

Table 2.6: XPS fitting parameters (before normalization) of LC homopolymer films.

Sample	**Thickness (nm)**	**Peak**	**Binding Energy (BE, eV)**	**FWHM**	**Fitted Peak Area (%)**	**Carbons In a Monomer**	**Theoretical Peak Ratio (%)**
PHBPB Homopolymer	7.34	1 & 2	284.8	1.20	81.8	27	77.1
		3	286.5	1.13	12.6	5	14.3
		4	288.9	0.96	5.6	3	8.6

X-rays can penetrate millimeters into polymer samples. However, conventional X-ray spectroscopy is largely confined to wavelengths of approximately 0.1 Å to 50 Å (1 Å = 0.1 nm) which implies that is will only measure the emission of the photo-emitted electrons from the top layers (~ 5 nm). Only those electrons leaving samples with the same initial energy are detected. Inelastic scattering is a process in which an electron loses energy after collisions with another particle. It leads to the reduction of the energy photoelectrons, or the change of their directions. The photoelectrons from surface atoms have less inelastic scattering potential. The Inelastic Mean Free Path (IMFP, λ_e) of electrons is defined as the average distance of an electron before it is inelastically scattered.

IMFP depends upon the photoelectron kinetic energy and the medium, and can be estimated from the NIST Standard Reference Database 71 (NIST Electron Inelastic-Mean-Free-Path Database, Version 1.1, 1998).[44] The Gries equation is used to estimate the IMFPs of PHPB (3.54 nm, with density = 1.1537 g/cm³ and binding energy = 285 eV) and polystyrene (3.73 nm, with density = 1.05 g/cm³ and binding energy = 285 eV). The IMFP increases with the kinetic energy of the photoelectron, which is what the XPS energy analyzer actually detects. The kinetic energy (KE) can be calculated from the formula below, where hv is the photon energy (1486.6 eV for an aluminum source), BE is the binding energy (about 285 eV for carbon in its electron core level), and WF is the work function of the spectrometer. The work function is normally only about 4 eV.

$$KE = h\nu - BE - WF \tag{2.5}$$

The Beer-Lambert law describes the probability ($P_{(z)}$) of a photoelectron escaping without losing energy, where z is the penetration depth, $\lambda_{e(E)}$ is the IMFP, and Φ is the takeoff angle.

$$P_{(z)} = 1 - \exp\left(-z / (\lambda_{e(E)} * \cos\Phi) \right), \text{ or} \tag{2.6}$$

$$z = \left(-\ln(1-P_{(z)}) \right) * \lambda_e * \cos\Phi \tag{2.7}$$

The majority (63%) of electrons detected come from within one IMFP of the surface, and most (95%) come from within three IMFPs at the zero takeoff angle. The majority (95%) of the signal comes from one IMFP at 70°. Measurements at six different takeoff angles from the surface normal (0°, 35°, 40°, 55°, 63°, 70°) correspond to different penetration depths ($d = 3\ \lambda e * \cos\Phi$, where 95% of the XPS signal intensity from). The calculations of probability and penetration depth at different takeoff angles are listed in Table 2.7 below.

Table 2.7: Calculation of AR-XPS probabilities and estimated penetration depth at different IMFPs and takeoff angles. The penetration depth was calculated at IMFP (λe) = 3.5 nm for my homopolymer system from NIST software.

Takeoff angle	Φ	0°	15°	35°	40°	55°	63°	70°	75°
	cos Φ	1.00	0.97	0.82	0.77	0.57	0.45	0.34	0.26
Probability	P (0-1 IMFP)	0.63	0.64	0.70	0.73	0.83	0.89	0.95	0.98
	P (1-2 IMFP)	0.23	0.23	0.21	0.20	0.14	0.10	0.05	0.02
	P (2-3 IMFP)	0.09	0.08	0.06	0.05	0.03	0.01	0.00	0.00
Penetration depth (nm)	0-3 IMPF	10.5	10.14	8.60	8.04	6.02	4.77	3.59	2.72

Determination of Thickness from AR-XPS Data

The angle-dependent AR-XPS in Chapter Three can be used to estimate film thicknesses based on the relative peak intensities of the film and substrate at different take-off angles.[45] However, this approximation can only be used for thin films (<6 nm), where the photoelectron intensity from the substrate can be measured. The relative intensity (I) of the film (f) and substrate (s) can be expressed by the equation below.[45]

$$\frac{I_f}{I_s} = K\left[\exp\left(\frac{d}{\lambda_s\cos\theta}\right) - \exp\left(\frac{d\lambda_f - d\lambda_s}{\lambda_s\lambda_f\cos\theta}\right)\right] \qquad (2.8)$$

The normalization factor, $K = (I_f^o / I_s^o)(ASF_f / ASF_s)$, can be calculated from the atomic sensitivity factor (ASF). If $\lambda_f \cong \lambda_s = \lambda$, Equation 2.8 can be simplified to Equation 2.9. The photoelectrons of the C_{1s} peak and Si_{2s} peak have similar binding energies (<5%),[45] so the attenuation lengths (λ) are close due to a resultant similar kinetic energy.

$$\ln\left(\frac{I_f}{I_s}\frac{1}{K} + 1\right) = \frac{d}{\lambda}\sec\theta \qquad (2.9)$$

The film thickness (d) can be calculated from the slope by the linear regression of $\ln\{(I_{C1s}/I_{Si2s})(1/K)+1\}$ vs. sec θ to the origin of various angles data. The atomic sensitivity factor (ASF) of C_{1s} (0.25) and Si_{2s} (0.23) are from Kratos Vision software, which are used to calculate K on the silicon surface. The attenuation length (λ) is 3.0 nm for PMMA and 3.1 nm for PS in Al-Kα X-rays.[45]

2.7.5 X-ray Specular Reflectivity (XSR)

Theory

Specular reflectivity scans are sensitive to variations in the electron density perpendicular to the surface and therefore have been used in analyzing the total film thickness, vertical depth profile, electron density and absorptivity of lamellar stacking layers within the film, in addition to determining the roughness between vertical layers, and the air interface roughness of polymer thin films.[46-53] XSR can measure LC films, Langmuir films, Langmuir-Blodgett films, and diblock copolymer films. It can also determine the thickness and the electron density of interfaces, such as the liquid/air interface, the solid/air interface, and interfaces of layers parallel to the substrate. Anastasiadis *et al.* [54] reported the effective width of the symmetric PS-b-PMMA interface is 50 ± 3 Å by neutron reflectivity. The width is independent of the molecular weight. Cai *et al.* [55] examined symmetric PS-b-PMMA thin films using XSR and off-specular scattering at grazing incidence, and found that islands or holes of a uniform height cover the air surface.

The specular reflection of X-rays is accurately described by Fresnel's equation in conjunction with the proper refractive index. Layered model profiles can be obtained by the ratio of reflected to incident intensity, as a function of the perpendicular wave vector (q_z). This technique can measure film thicknesses of several thousand angstroms with a high resolution down to several angstroms. By adjusting the incidence angle or wavelength, layer contrast can be measured by the differences between the electron density and X-ray sources. Because there is very little beam damage to samples, it is also a powerful tool for sequential researches, while the XSR spectra can be taken to check the surface composition variations during surface treatments.

Experimental Setup

X-ray reflectivity experiments were done by Dr. Sushil K Satija at the National Institute of Standards and Technology (NIST, Gaithersburg, MD), using the Cu Kα line (wavelength = 1.54Å and $k = 2\pi / \lambda = 4.07$ Å^{-1}) with a rotating anode generator and a triple axis reflectometer. The perpendicular wave factors (q_z) were detected from 0 to 0.18 Å^{-1} for the homopolymer and from 0 to 0.32 Å^{-1} for the lamellar diblock copolymer. Samples were mounted on the inner stage of a two-stage oven in a dry nitrogen environment. Samples were adjusted to focus along the z-axis (parallel to the surface normal direction). For samples with a thickness of less than 70 nm, the Cu-Kα beam line is mono-chromatized and focused using a bent graphite (002) crystal to give an in-plane resolution of $\Delta q_z = 5.7{*}10^{-3}$ Å^{-1}. The background was subtracted by the software of the instrument. The instrument had applied standard geometrical correction for the beam "footprint". The full width at half maximum (FWHM) of a typical transverse "rocking" scan across the specular reflectivity was around 0.045°. XSR is sensitive to the modulations of the average electron density $\rho(z)$ along the surface normal and collects the reciprocal-space morphological information.

Data Fitting

The reflectivity data could not be directly converted to composition versus depth as the experimental data did not include phase information. I used SERF (Spreadsheet Environment Reflectivity Fitting) software comprised of "add-in" functions in a Microsoft Excel spreadsheet developed by C. Co & K. A. Welp at the University of Delaware.[56] Data fitted to the curve is the iterative matrix solution of the Fresnel equation. Periodic "slab" profiles of electron densities are used separated by interfaces with Gaussian roughness. The fitting reflectivity was calculated by the electron density ($Å^{-2}$) and absorptivity over each wavelength for a series of layers defined by the model. The interface was fitted by tanh and error function gradients. Gaussian smearing functions are taken from Hamley [57] to account for experimental wavelength and angular smearing effects.

I modified the spreadsheet by including the surface roughness (σ) from AFM into calculations ($R_{sr} = R_s * \exp(-q^2*\sigma^2)$). Chi-squared (χ^2) is defined by the sum of the squared differences between SERF and experimental data, divided by a small error allowance. The calculated reflectivity (I_c) and experimental data (I_m) were iteratively minimized as $\Sigma(\log I_m - \log I_c)^2$. I used the excel macro function and visual basic language to write codes for automatic fine tuning of vertical layer thickness, electron density of each layer, total thickness, delta lambda, and delta theta.

2.7.6 Molecular Modeling

CS Chem3D 5.0 of the CambridgeSoft Company was used to perform all model calculations to determine the stable LC mesogen conformations and packing status.

Molecular mechanisms (MM2) simulations were run using the geometry optimization to reach the minimum local energy. Classical physics, based on force fields with embedded empirical parameters, is used for large molecules without transition states. It adds the energies of the bond stretching, angle bending, stretch-bend cross-energy, torsion, van der Waals energy, out-of-plane bending, electrostatics, charge/charge contributions, and dipole/dipole interactions. The convergent criteria for the gradient of the potential energy surface are set to 0.01 of the minimum RMS gradient.

The MOPAC[d] module was applied to calculate dipole moments. MOPAC is a semi-empirical methodology using the restricted closed-shell wave function and the AM1 potential function, which is a self-consistent field method, to solve the Electronic Schrodinger equation. The dipole moment is the first derivative of the energy to an applied electric field. It measures the asymmetry in the molecular charge distribution and is reported as a vector in three dimensions. Dipole moments can be used as an index for affinities between different segments and the substrates.

REFERENCES

(1) Clark, NA; Lagerwall, ST. *Appl. Phys. Lett.* **1980**, *36*, 899-901.

(2) Shibaev, VP; Koslovsky, MV; Beresnev, LA; Blinov, LM; Plate, NA. *Polym. Bull.* **1984**, *12*, 299.

(3) Shibaev, VP; Freidzon, YS; Kostromin, SG. In *Liquid Crystalline and Mesomorphic Polymers*; Lam, V. P. S. a. L., Ed.; Springer-Verlag: New York, 1994; pp 77-120.

(4) Suzuki, T; Okawa, T; Ohnuma, T; Sakon, Y. *Makromol. Chem., Rapid Commun.* **1988**, *9*, 755-760.

(5) Dumon, M; Nguyen, HT; Mauzac, M; Destrade, C; Achard, MF; Gasparoux, H. *Macromolecules* **1990**, *23*, 355.

(6) Zheng, WY; Hammond, PT. *Macromol. Rapid Commun.* **1996**, *17*, 11, 813-824.

(7) Anthamatten, M; Hammond, PT. *Macromolecules* **1999**, *32*, 24, 8066-8076.

(8) Zheng, WY; Hammond, PT. *Macromolecules* **1998**, *31*, 3, 711-721.

---

[d] MOPAC 93 is a semi-empirical computational chemistry programs developed by Fujitsu (Fujitsu America (FAI), 3055 Orchard Drive, San Jose, CA 95134), and J.J.P. Stewart (Dr James J. P. Stewart, Stewart Computational Chemistry, 15210 Paddington Circle, Colorado Springs, CO 80921-2512). MOPAC can be used for the study of the electronic structure and energetics of ground-state and excited-state atoms, molecules, ions, and solids, using the semi-empirical methods MINDO/3, MNDO, AM1, and PM3. Detailed information can be found at the website (http://home.att.net/~mrmopac)

(9) Anthamatten, M; Zheng, WY; Hammond, PT. *Macromolecules* **1999**, *32*, 15, 4838-4848.

(10) Anthamatten, M; Wu, J-S; Hammond, PT. *Macromolecules* **2001**, *34*, 24, 8574-8579.

(11) Zheng, WY; Albalak, R; Hammond, PT. *Macromolecules* **1998**, *31*, 2686-2689.

(12) Anthamatten, M; Hammond, PT. *J. Polym. Sci., Part B: Polym. Phys.* **2001**, *39*, 21, 2671-2691.

(13) Mensinger, H; Stamm, M; Boeffel, C. *J. Chem. Phys.* **1992**, *96*, 4, 3183.

(14) Elben, H; Strobl, G. *Macromolecules* **1993**, *26*, 1013.

(15) Henn, G; Stamm, M; Poths, H; Rucker, M; Rabe, JP. *Physica B* **1996**, *221*, 1-4, 174-184.

(16) van der Wielen, MWJ; Stuart, MAC; Fleer, GJ; deBoer, DKG; Leenaers, AJG; Nieuwhof, RP; Marcelis, ATM; Sudholter, EJR. *Langmuir* **1997**, *13*, 17, 4762-4766.

(17) Wong, GCL; Commandeur, J; Fischer, H; de Jeu, WH. *Phys. Rev. Lett.* **1996**, *77*, 5221.

(18) Sentenac, D; Demirel, AL; Lub, J; de Jeu, WH. *Macromolecules* **1999**, *32*, 3235-3240.

(19) Figueiredo, P; Geppert, S; Brandsch, R; Bar, G; Thomann, R; Spontak, RJ; Gronski, W; Samlenski, R; Mueller-Buschbaum, P. *Macromolecules* **2001**, *34*, 2, 171-180.

(20) Anthamatten, ML. *PhD Thesis: Order in side-chain liquid crystalline diblock copolymers*; MIT: Cambridge, MA, 2001.

(21) Kern, Werner. *Handbook of Semiconductor Wafer Cleaning Technology*; Noyes Publications, 1993; Vol. 10.

(22) Ulman, A. *An Introduction to Ultrathin Organic Films from Langmuir-Blodgett to Self-Assembly*; Academic Press Inc: San Diego, CA, 1991.

(23) Ulman, A. *Characterization of Organic Thin Films*, 1995; Vol. 9.

(24) Andrews, EH. *Proc. Roy. Soc.* **1964**, *A277*, 562.

(25) Kato, K. *Electron Microscopy*, 1965; Vol. 14.

(26) Sawyer, LC; Grubb, DT. *Polymer Microscopy*; Chapman and Hall: London, 1987.

(27) Fasolka, MJ. *PhD Thesis: The Morphology and Lateral Patterning of Diblock Copolymer Thin Films*; MIT: Cambridge, MA, 2000.

(28) Fasolka, MJ; Harris, DJ; Mayes, AM; Yoon, M ; Mochrie, SGJ. *Phys. Rev. Lett.* **1997**, *79*, 3018.

(29) Carvalho, BL; Thomas, EL. *Phys. Rev. Lett.* **1994**, *73*, 24, 3321-3324.

(30) Ruokolainen, J; Saariaho, M; Ikkala, O; ten Brinke, G; Thomas, EL; Torkkeli, M; Serimaa, R. *Macromolecules* **1999**, *32*, 1152-1158.

(31) Osuji, C; Chen, JT; Mao, G; Ober, CK; Thomas, EL. *Polymer* **1999**.

(32) Osuji, C; Zhang, Y; Mao, G; Ober, CK; Thomas, EL. *Macromolecules* **1999**, *Submitted.*

(33) Garbassi, F; Morra, M; Occhiello, E. *Chapter 4: Surface Energetics and Contact Angles*; John Wiley & Sons, 1998.

(34) Schulze, RD; Possart, W; Kamusewitz, H; Bischof, C. *J. Adhes. Sci. Technol.* **1989**, *3*, 39-48.

(35) Wenzel, RN. *Ind. Eng. Chem.* **1936**, *28*, 988-994.

(36) Wolansky, G; Marmur, A. *Colloids Surf., A* **1999**, *156*, 381-388.

(37) Kamusewitz, H; Possart, W; Paul, D. *Colloids Surf., A* **1999**, *156*, 271-279.

(38) Chen, P; Long, J. *Langmuir* **2001**, *17*, 2965-2972.

(39) Nix, Roger. *http://www.chem.qmw.ac.uk/surfaces/scc/scat5_1.htm* **1996**.

(40) Paynter, Royston. *http://goliath.inrs-ener.uquebec.ca/commerce/xps-tech.html*.

(41) Bongiovanni, R ; Malucelli, G ; Lombardi, V ; Priola, A ; Siracusa, V ; Tonelli, C ; Di Meo, A. *Polymer* **2001**, *42*, 2299-2305.

(42) Beamson, G; Briggs, D. *High Resolution XPS of Organic Polymers*; John Wiley & Sons, 1992.

(43) Carlson, TA. *X-ray photoelectron spectroscopy*; Academic Press: New York, 1978.

(44) Powell, CJ; Jablonski, A. *J. Vac. Sci.* **1999**, *A17*, 4.

(45) Ton-That, C; Shard, AG; Bradley, RH. *Langmuir* **2000**, *16*, 2281-2284.

(46) Russell, TP. *Mater. Sci. Rep.* **1990**, *5*, 171.

(47) Russell, TP. *Chimia* **1990**, *44*, 312-315.

(48) Foster, MD. *Crit. Rev. Anal. Chem.* **1993**, *24*, 3, 179-241.

(49) Zhou, X-L; Chen, S-H. *Phys. Rep.* **1995**, *257*, 223-348.

(50) Kago, K; Endo, H; Matsuoka, H; Yamaoka, H; Hamaya, N; Tanaka, M; Mori, T. *J. Synchrotron Rad.* **1998**, *5*, 1304.

(51) Tolan, M; Press, W. *Z. Kristallogr.* **1998**, *213*, 319-336.

(52) Vignaud, G; Gibaud, A; Paris, F; Ausserre, D; Grubel, G. *Thin Solid Films* **1998**, *323*, 1-5.

(53) Als-Nielsen, J; Jacquemain, D; Kjaer, K; Leveiller, F; Lahav, M; Leiserowitz, L. *Phys. Rep.* **1994**, *246*, 251-313.

(54) Anastasiadis, SH; Russell, TP; Satija, SK; Majkrzak, CF. *J. Chem. Phys.* **1990**, *92*, 9, 5677-5691.

(55) Cai, ZH; Huang, K; Montano, PA; Russell, TP; Bai, JM; Zajac, GW. *J. Chem. Phys.* **1993**, *98*, 3, 2376-2386.

(56) Co, C; Welp, KA. *http://www.kalergroup.che.udel.edu/kalerg../NeutronReflectionHelpIndex.htm*.

(57) Hamley, IW. *The physics of block copolymers*; Oxford University Press: New York, 1998.

Chapter 3

LC Alignment of Side-Chain Smectic Homopolymer Thin Films

3.1 INTRODUCTORY REMARKS

The alignment of liquid crystals (LC) is extremely dependent on the nature of surfaces and interfaces. This dependence is even greater for ultrathin films. Effects of LC alignment, the substrate, and the interfaces influence significantly the molecular ordering and thin film properties. The tendency to form an ordered structure and the tunable nature of LC molecules make practical applications, such as the liquid crystal displays (LCD), possible. An understanding of LC ordering in nanoscale ultrathin films is important to the use of these LC properties, especially when the technology trends move towards reduction of the film thickness with requirements to keep surfaces ordered.

The thin film wetting properties of small LC molecules at a solid surface have been studied theoretically by Landau-de Gennes theory,[1,2] and experimentally by variable angle ellipsometry,[3] reflection ellipsometry,[4] deuterium nuclear magnetic resonance (^{2}H-NMR),[5] static light scattering,[6] scanning polarization force microscopy (SPFM),[7] and X-ray reflectivity.[8] Different types of LC anchoring can be preferred at different surfaces.[1,5,7] Crawford *et al.* [5] used surfactants to modify the substrate surface to induce a discontinuous homeotropic-to-planar anchoring transition. Xu *et al.* [7] used SPFM to study 8CB (4'-n-octyl-4-cyanobiphenyl) on silicon wafers. They found that LC molecules in the first monolayer were parallel to the substrate surface, and a layer of nearly vertical molecular dimers form on top of the first monolayer.

The final surface topography of the polymer thin films is determined by the balance between the surface tension and long-range energy contributions. Thin polymer films (< 100 nm) are often unstable, because the intermolecular forces (e.g. van der Waals forces) dominate the chain conformation and cause spontaneously dewetting.[9] In systems with strong long-range correlations, such as LC, the intermolecular structural force usually dominates the stability. More recently, the thin-film wetting properties of LC-containing side-chain liquid crystal polymers (LCP) have been reported.[10-18] LC behaviors in polymer thin films are different than that in small LC molecules due to the polymer backbone constraint.

Van der Wielen *et al.* used AFM and X-ray reflectometry to describe the morphology and structures in thin films of a side-chain LCP with terminal mesogenic methoxybiphenylyloxy groups on silicon wafers.[13,15] The ordered smectic layers were observed parallel to the silicon substrate after annealing above the glass-transition temperature (Tg) for a short period of time. The smectic ordering was independent of film thickness from 8.7 nm up to 40 nm. The molecular ordering in these film thicknesses was only slightly influenced by the substrate and air interfaces. Holes (or islands) with a depth of one bilayer appeared at the air interface. The smectic LC mesogens showed interdigitated homeotropic alignment through out the film thickness except the layer directly at the substrate, where the LC mesogens adopted planar anchoring. They also studied long annealing effects of the same LCP films of 30, 180, and 800 nm thick on silicon substrates.[14] Instead of forming lamellar ordering at short periods, films dewetted into droplets and one residual bilayer (~3.1 nm, independent of the initial film thickness) covered the substrate surface after long annealing. The same LCP was further cast on chemically modified silicon substrates to study the dewetting behaviors at various substrate properties and temperatures.[17] Van der Wielen *et al.* also modified the silicon substrate by adsorbing negatively charged colloidal silica particles to make a rough surface with the same chemical properties as native silicon.[16] The surface modification improved film stability against break-up.

Henn *et al.* [12] studied the order in thin smectic polymer films (6-200 nm thick) on glass substrates by X-ray reflectometry and scanning tunneling microscopy (STM). The LC polymer combined the same mesogenic groups in the main and side chains. The polymer chain showed different types of orientation depending on the film thickness in the S_C* phase. In films thicker than 10 nm, polymer chains were oriented perpendicular to the substrate. Extended terraces were observed at the air interface, which was separated by steps of a single smectic-layer height. However, in films thinner than 10 nm, chains lay predominately flat on the substrate and showed partial dewetting. Holes of the initial film-thickness height were observed. Vix *et al.* [19] studied the dewetting of ultrathin films of a smectic LC main-chain polymer combined with an azoxybenzene by scanning force microscopy, specular X-ray scattering, and off-specular X-ray scattering. No dewetting was detected for films thicker than 10 nm (> three smectic layers). Smectic layers of 3.5 nm thick oriented parallel to the substrate inside the film and the excess material formed smectic islands on top of the film, corresponding to incomplete coverage of the top smectic layer. For films thinner than 10 nm (one or two smectic layers only), films were observed to dewet and form holes or smectic towers. There was no monolayer remaining in the holes and the bare substrate was exposed in some areas.

The majority of studies on supported LC thin film wetting have been only published recently.[10-18] However, clear prediction of processes and observation of the properties of the LC orientation transition region, such as the location and the thickness of the transition, have not been reported. The LC transition could only be estimated by fitting X-ray reflectivity data. Nevertheless, there were only a few studies of LC ordering for films thinner than 5 nm. The aim of this chapter is to describe the LC behavior of side-chain LC homopolymers in ultrathin films.

The LC homopolymer is the best model system to study LC alignment in thin films. The LC mesogens align either in planar position or homeotropically at the interfaces. This phenomenon was illustrated in Chapter 1.3.5 and Figure 1.5. LC molecules can show different LC alignment at the substrate and the air interfaces. It is important to understand LC alignment inside the block domains, since the LC behavior can affect the block morphology and the block copolymer interface can also affect LC alignment. Still, it is challenging to detect and determine LC alignment in complicated diblock copolymer systems. In this chapter, the homopolymer system was used to observe LC orientation, and confirm the existence of two LC anchoring conditions at the substrate surface and the air interface. Most of all, the understanding of the homopolymer system will help further investigation on the more complicated diblock copolymer systems.

Several factors affecting LC alignment are presented in this chapter. One of the primary goals of this chapter is to investigate how LC anchoring is influenced by the substrate and air interfaces in ultrathin films. Instead of using complex diblock copolymers with block boundaries and LC perforations, we studied the LC homopolymer and limited the variables to the substrate effect, the surface free energy, and LC arrangement. For the homopolymer system, films with different thicknesses were cast to determine effects of the substrate, by observing LC orientation as a function of the distance away from the substrate. I expected to observe a transition from the preferred planar orientation at the substrate surface to homeotropic orientation at the air interface as expected.

3.2 METHODOLOGY

Both theoretical and experimental approaches were employed to understand LC alignment and conformations of the side-chain smectic monomer and homopolymer films. Theoretical approaches, including molecular modeling and group contribution theory, have been conducted to calculate the molecular structure and the surface properties. Experimental approaches focus on understanding the thin film structure and LC orientation.

The data for the LC monomer study can help to explain the LC homopolymer behavior, while removing kinetic issues of the polymer backbone mobility, are much less important for the low molar mass system. The molecular structure of this LC homopolymer is shown in Figure 3.1a and the three-dimensional conformation of a dimer from molecular simulation is shown in Figure 3.1b. LC homopolymer films were annealed at 60 °C (S_C* temperature, above the Tg) to enhance smectic ordering. An isotropic polymer normally tends to become smooth during annealing to lower the surface energy. However, a thermotropic LCP can be highly anisotropic and form layered structures. Atomic force microscopy (AFM, 20*20 μm^2 scan), ellipsometry, small angle X-ray scattering (SAXS), transmission electron microscopy (TEM), X-ray diffractometry, and contact angle goniometry (~10 mm²) were used to measure the surface properties. Angle-resolved X-ray photoelectron spectrometry (AR-XPS, ~0.2 mm²) and X-ray specular reflectometry (XSR) were used to directly examine LC orientation inside the film.

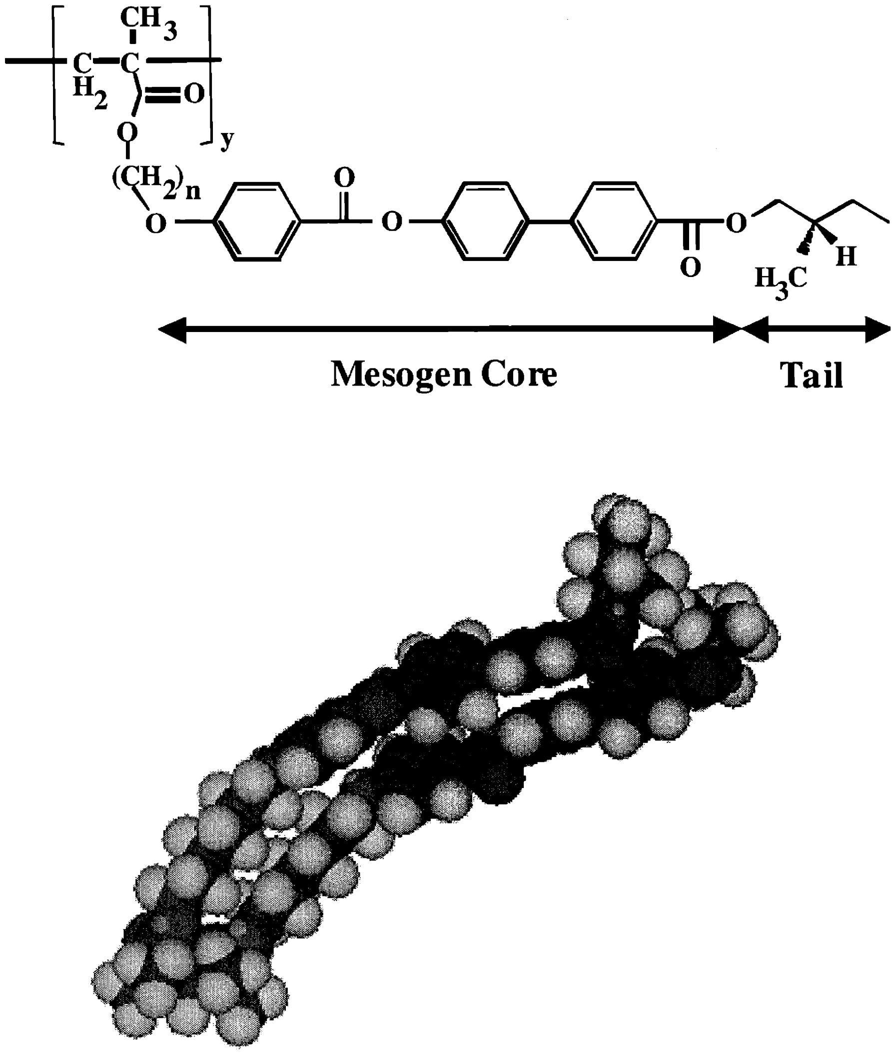

Figure 3.1: (a) Molecular structure of the PHBPB LC homopolymer; (b) 3D structure of a HBPB dimer from a Chem3D simulation.

3.3 RESULTS AND DISCUSSION

3.3.1 Lattice Structure of LC Monomer Crystals: X-ray Diffractometry

X-ray diffractometry was performed on the LC monomer in its crystal form to get a general idea of its crystal structure. Often, the crystal form is similar to the smectic LC form. The unit cell information of the LC monomer crystal from X-ray diffractometry is listed in Table 3.1. The sizes and spatial arrangement were used as a basis for further molecular simulation and analysis. The monomer shows a triclinic crystal system, which has no special relationship between the crystal axis and vibration directions ($a \neq b \neq c$ and $\alpha \neq \beta \neq \gamma \neq 90°$), as defined in Figure 3.2a. There are four molecules per unit cell [20] (Z=4), and the arrangement is shown in Figure 3.2b. When LC molecules adopt planar anchoring, the benzene rings prefer to lie flat to the silicon substrate. Therefore, the average spacing between two planar mesogens is around half of the shortest axis length (axis a = 1.05 nm). The average spacing between mesogens is ca 0.5 nm, which agrees with the simulation results of ca 0.6 nm shown later in Section 3.3.2.

The density was calculated from the volume and molecular weight in Table 3.1. The density of the LC monomer crystal (1.216 g/cm^3) was higher than the density of the LC homopolymer (1.154 ± 0.003 g/cm^3) as observed from other experiments of the same polymer in bulk state [21,22] due to the closer packing of the mesogens without the interference of the polymer chain and the added effect of the polymer's effective volume.

Table 3.1: The unit cell data of the LC monomer crystal collected by X-ray diffraction. Z is the number of formula-entities per unit cell. Alpha (α) is the angle between the two crystal-axes b and c.

Molecular Formula	**Formula Weight (g/mol)**	**Crystal System**	**Z**	**Crystal Axis (nm)**		**Angles**		**Volume (nm^3)**	**Density (g/cm^3)**
$C_{35}H_{40}O_7$	572.67	Triclinic	4	a	1.052	α	89.11°	3.127	1.216
				b	1.444	β	80.18°		
				c	2.091	γ	88.70°		

The closed-packed LC mesogen arrangement, as shown in Figure 3.2b, was rod-like. Its diameter of the mesogen rod (~ 0.58 nm) was calculated based on its length (~ 3 nm) and the volume in Table 3.1.

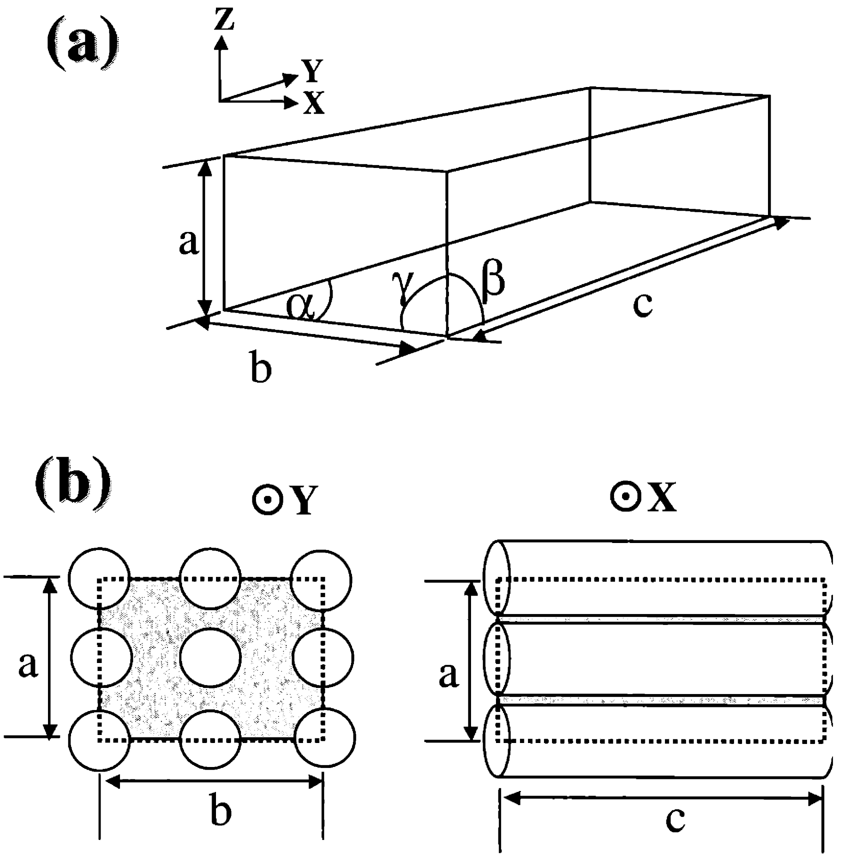

Figure 3.2: (a) Unit cell of the LC monomer crystal. Three crystal axis lengths (a, b, c) and three angles (α, β, γ) are marked. Values are listed in Table 3.1; (b) LC mesogen arrangement inside the unit cell as viewed along two different axes.

3.3.2 Molecular Structure and Packing Energy Calculation: Molecular Modeling

Before analyzing further experimental data, the stable mesogen conformations was checked to see how they packed at a molecular level using a molecular modeling package described in Section 2.7.6. Classic molecular mechanics is used to calculate and minimize the steric energy. The thermal equilibrium structure of an LC dimer (two monomer chains linked together) is shown in Figure 3.1b. The simulation results provide mesogen conformations, relative spacings, and possible carboxylic orientation. Distances between two atoms were calculated from the atom coordination.

The simulation minimized the steric energy of molecules. A single monomer molecule was simulated first, and the steric energy was 38.8 kcal/mol per monomer chain. For a dimer, two different starting conformations, open and packed, were set. The open conformation showed a higher final energy (46.1 kcal/mol per monomer chain) than the two separated monomers (38.8 kcal/mol each), and the packed conformation had the lowest energy (36.7 kcal/mol per monomer chain) due to the preference for of LC packing. For a trimer (oligomer with three repeat units of monomers), three final energy levels with different conformations (37.5, 41.8, and 52.5 kcal/mol per monomer chain) showed different final packing energies, and only one of the values was lower than that of a single monomer, representing the most stable packing.

Table 3.2 lists the relative spacing between specific atoms from X-ray diffractometry experiments and molecular modeling simulations. The LC monomer is separated into three segments for the purpose of analysis, including the mesogen head, the LC mesogen core, and the mesogen tail, as marked in Figure 3.1a. The first segment (head) includes the methyl methacrylate (MMA) part and alkyl spacers. The second segment (LC mesogen core) is the mesogen core, and the last segment (tail) is the alkyl tail in the end of the mesogen. The monomer crystal had two different geometries in X-ray diffractometry. The two side-chains of the dimer in the molecular simulation showed different conformations. Both conditions and their averages were listed in Table 3.2.

All distances were calculated from the atom in coordinates. Distances between carboxylic groups were also calculated to assist in the analysis of AR-XPS data in

Section 3.3.6. End-to-end distances of the LC side-chain were calculated. The distances of the LC monomer crystal agreed with the longest crystal axis (axis c = 2.09 nm) in Table 3.1. The distances from simulation were larger than those of the LC crystal, and was closer to the smectic spacing in bulk state (3.1 - 3.5 nm).[23,24] These simulation data correspond well to SAXS data from bulk polymer analysis and X-ray diffractometry data from crystals.

Table 3.2: Relative segmental spacings (nm) from the X-ray diffraction and the MM2 simulation.

		Head	LC Core	Tail	COO^1 - COO^2	COO^2 - COO^3	COO^3 - End	End-to-end Distance of Side-chain
X-ray Diffractometry Experiment	Crystal 1	0.71	1.14	0.4	1.023	0.694	0.528	2.121
	Crystal 2	0.75	1.11	0.28	0.991	0.730	0.395	2.018
	Average	0.7	1.1	0.3	1.0	0.7	0.5	2.1
Simulation	Monomer	1.11	1.69	0.50	1.523	1.075	0.618	3.139
Simulation	Dimer 1	1.10	1.75	0.50	1.491	1.085	0.585	2.804
	Dimer 2	1.08	1.73	0.50	1.496	1.082	0.619	3.138
	Average	1.1	1.7	0.5	1.5	1.1	0.6	3.0

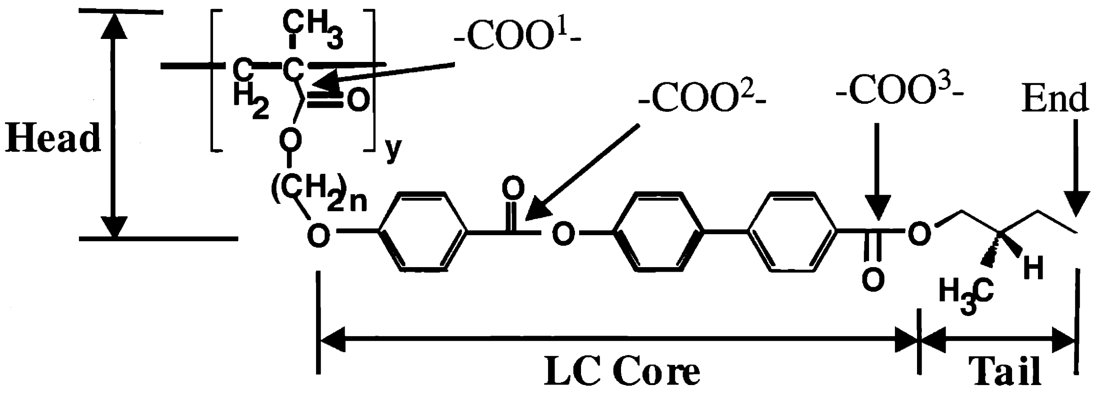

Anthamatten *et al.* [21,22] reported the bulk properties of this series of the LC homopolymer and diblock copolymers using small-angle X-ray scattering (SAXS). SAXS diffractograms of oriented samples indicated different LC orientation in roll-cast films with different spacers. For the diblock copolymer with a hexyl spacer, smectic layers were oriented perpendicular to the lamellar morphology. However, the longer decyl spacer system resulted in orientation of the smectic layers parallel to the lamellae. These results implied that the degree of decoupling of the mesogen from the polymer backbone would be critical to LC orientation within the block copolymer domains. They also reported that the isotropization of the LC domain could trigger the order-disorder-transition (ODT) of the diblock copolymer.

In this methacrylate-based LC homopolymer, the glass-transition temperature (Tg) was ca 35-40 °C, as determined by DSC. LC thermal transitions were identified using polarized optical microscopy combined with calorimetry. From Table 2.2, the LC homopolymer (PHBPB) shows various smectic phases, such as S_C*, S_D, and S_A at different temperature ranges. The smectic periodicity from SAXS changes from 3.00 nm to 3.15 nm while heating to ca 160 °C, which is consistent with the second-order S_C* to S_A transition observed at 163 °C from DSC. The increase in periodicity is caused by a lowered tilt angle in of the S_C* phase, which was estimated to be ~30° for aligned samples. Upon entering the S_A phase, the mesogens orient orthogonal to the layer plane and create larger layer spacing, although part of the layer spacing is due to the flexible methacrylate main-chain backbone at higher temperatures. The S_A phase has a lower density.

Generally, the LC polymer backbone assumes a more oblate configuration in the LC state, and is sandwiched in an extended state between smectic layers. Upon heating into the less ordered S_A phase, the entropic driving force is stronger for the LC backbone to assume a more random conformation and to cross over into neighboring smectic layers.

3.3.3 Surface Tension Estimation: Group Contribution Theory

The group contribution process is a simple method to roughly estimate surface tensions by summing up the contributions from different segments of the same molecule.[25,26] This method assumes the same contributions for different functional groups to the thermodynamic properties. The solubility parameter (δ) of each segment was first estimated by group contribution theory.[25,26] The surface tension (σ) was then calculated from the solubility parameter (δ_i) by the equation below.[27]

$$\sigma = \frac{\Delta E_i^v \bullet V_i^{-2/3}}{A} = \frac{\delta_i^2 \bullet V_i^{1/3}}{A} \tag{3.1}$$

In Equation 3.1, the surface tension of the component i (σ_i) is calculated by solubility parameter ($\delta_i \equiv \sqrt{Cohesive\_Energy\_Density} = \sqrt{\frac{\Delta E_i^v}{V_i}}$), the energy of vaporization (E_i), and the molar volume (V_i). A is an empirical constant.[27]

From Table 3.3, the mesogen core has the highest surface tension; hence, mesogens will prefer to expose their tail groups and pack in an upright manner with respect to the air interface to minimize the surface energy and bury the high-energy LC regions. The calculated surface tension of polystyrene at 20°C agreed with the literature data, such as 29.1 mN/m,[28] and 30.15 mN/m.[29] The estimated surface tensions may not be accurate because of the inaccuracies of using the group contribution method; however, these data clearly distinguish surface-tension differences among segments.

The contact angle (θ) of a solid polymer can also be calculated using the combination of Young's equation [30] and Neumann's equations [28,31] given by

$$\cos\theta = -1 + 2\sqrt{\frac{\sigma_{SV}}{\sigma_{LV}}}\exp\left[-\beta(\sigma_{LV} - \sigma_{SV})^2\right] \tag{3.2}$$

where σ_{LV} is the liquid surface tension (72.8 mJ/m² for water at 20 °C), σ_{SV} is the polymer surface tension from group-contribution calculations, and $\beta = 0.000115$ (m²/mJ)². The experimental contact angles will be discussed later in Section 3.3.5.

In addition, dipole moments were calculated from MOPAC, as described in Section 2.7.6. In Table 3.3, the data show that the LC core has the highest dipole moment, which is more favorable in interacting with the polar, hydrophilic Si-OH surface, whereas the tail section has a lower dipole moment, more appropriate for the air interface.

Table 3.3: Surface tensions and contact angles estimated by group contribution methods [25,26] and dipole moments from MOPAC simulations.

Segments		MW	Density	σ^a	σ^b	σ^c	σ^d
		g/mol	g/cm^3	mN/m	mN /m	mN /m	mN/m
Styrene	C_8H_8	100	1.045 ± 0.01[22]	26.7	30.0	27.2	27.3
Monomer	$C_{35}H_{40}O_7$	572	1.154 ± 0.003[22]	53.7	54.7	53.9	51.7
Head	$C_{10}H_{19}O_2$	169	1.05	26.2	28.3	29.2	25.5
LC Core	$C_{20}H_{12}O_5$	332	1.26	51.3	50.0	51.6	49.2
Tail	C_5H_{11}	71	0.92	26.9	29.3	21.5	25.7

Segments	Average σ	Calculated contact angles (θ) from surface tensions	Dipole moments
	(mN/m)	(°)	(Debye)
Styrene	27.8	91.2	0.01
Monomer	53.3	50.4	7.30
Head	27.3	92.0	1.86
LC Core	50.5	55.0	26.92
Tail	25.8	94.4	0.32

[a] calculated from Small: heat of evaporation measurements

[b] calculated from van Krevelen: cohesive energy density data

[c] calculated from Hoy: vapor pressure measurements

[d] calculated from van Krevelen and Hoftyzer: cohesive energy data of polymer

3.3.4 Roughness Analysis: Atomic Force Microscopy (AFM)

Surface roughness can be represented in terms of statistical deviations from an average height. Two types of surface roughness can be calculated from AFM images as defined by the AFM software (Digital Instruments). The root-mean-square roughness (RMS, R_q) is the standard deviation of Z values (perpendicular to the surface plan) within a given area, where Z_i is the height of the ith point and N is the total number of points.

$$R_q = \{ \Sigma(Z_i - Z_{ave})^2 / N \}^{0.5} \tag{3.3}$$

The mean roughness (R_a) is defined as the mean value of the surface related to the center plane, where f(x,y) is the surface relative to the center plane and L_x and L_y are the dimensions of the surface of the given area.

$$R_a = \frac{\int\int |f_{(x,y)}| dxdy}{L_x \times L_y} \tag{3.4}$$

Thin films of both monomers and homopolymers were scanned by AFM (a 20 μm * 20 μm area) to measure the surface roughness. The roughness data were averaged over several scans at different regions of each film. All error bars in this chapter indicate one standard deviation. In Figure 3.3a and 3.3b, both the RMS roughness (R_q, square symbol) and the mean roughness (R_a, triangular symbol) decrease significantly with increasing film thickness.

The proposed models in Figure 3.4 present ordering of mesogens at the silicon and the air interface. Four zones are defined here based on the film thickness for discussion, corresponding to the zones labeled in Figure 3.3. The property difference between Zone I and Zone II mainly comes from the surface coverage of the hydrophobic polymer (monomer) layer. The incomplete coverage of Zone I exposes the hydrophilic silicon and creates the chemical heterogeneity on the surface. The difference between Zone II and Zone IV is based on different LC orientation, planar or homeotropic. The substrate tends to hold the mesogens planar; however, the mesogen can use the non-polar tail to reduce the air surface energy at higher thicknesses. Possible explanations can be drawn from analyzing the AFM roughness results in Figure 3.3.

LC Homopolymers

The AFM roughness of the homopolymer system in Figure 3.3a is discussed in this section. The same analysis can be applied to the monomer system in Figure 3.3b.

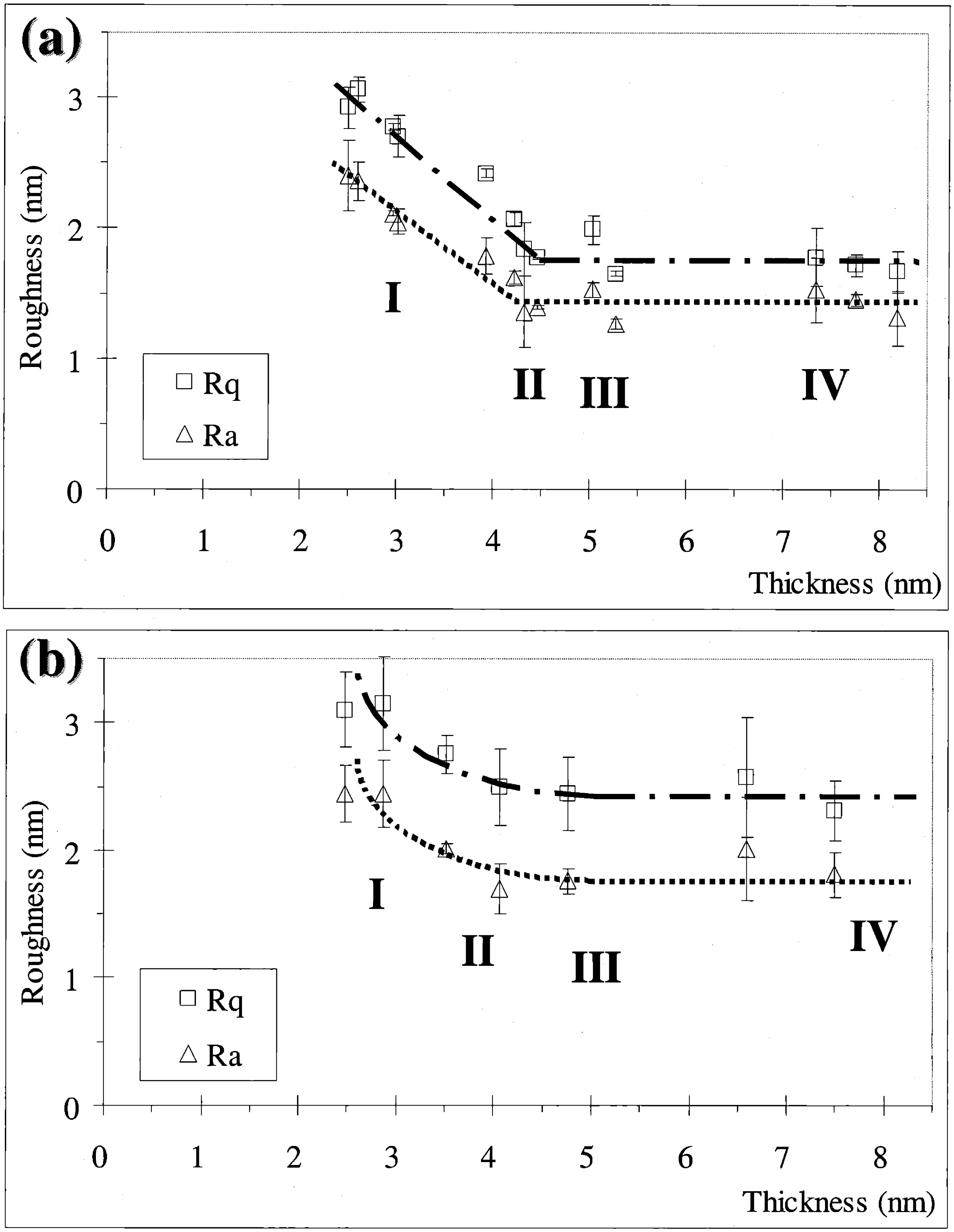

Figure 3.3: AFM Roughness data for the LC homopolymer (a) and monomer (b) of different film thicknesses. Square symbols (■) represent the vertical roughness (R_q). Triangular symbols (▲) indicate the in-plane roughness (R_a). Lines are guides to the eye.

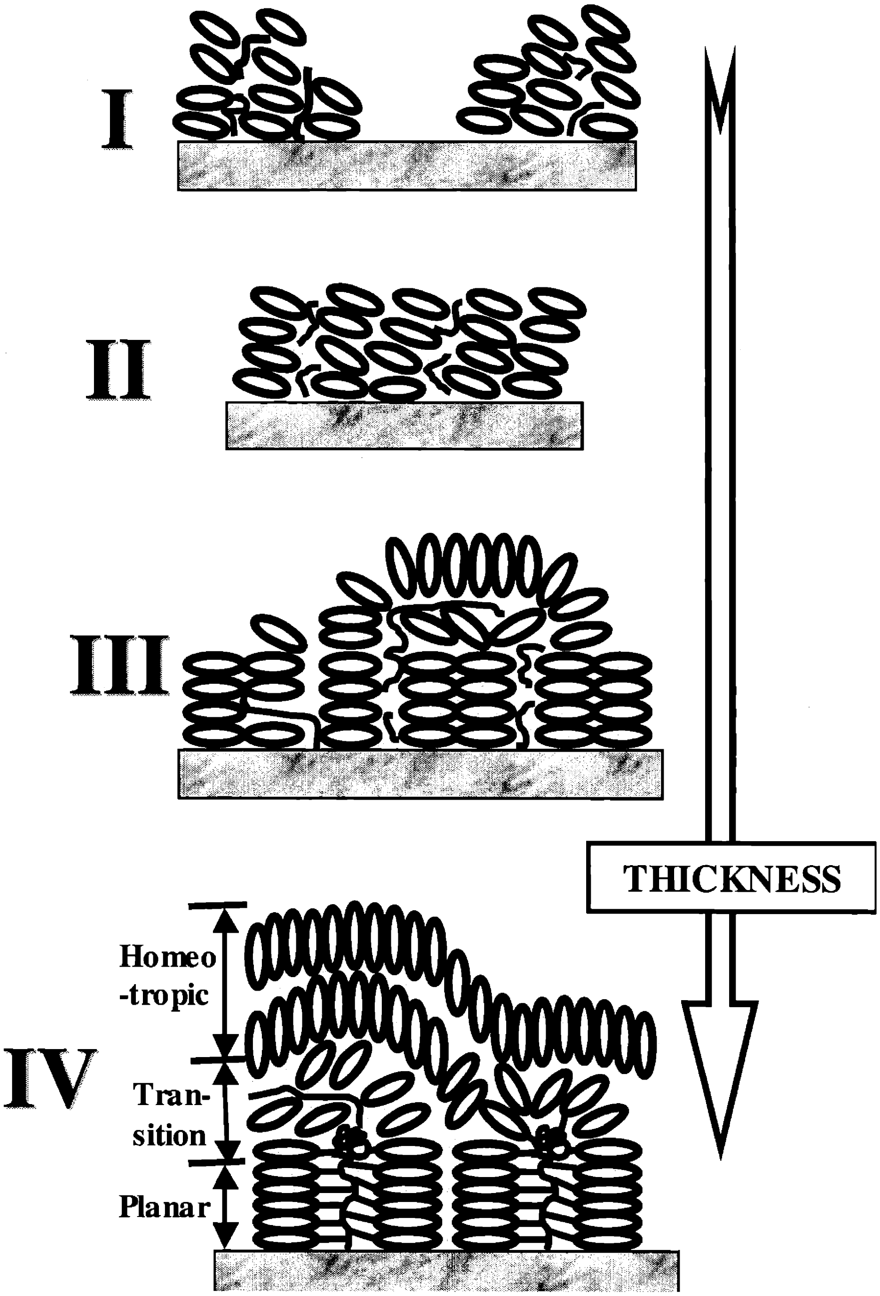

Figure 3.4: Proposed models of LC stacking as film thickness increases.

The first cartoon in Figure 3.4 (Zone I) shows LC mesogens stacking together to form valleys and hills. Due to the strong LC mesogen-mesogen interactions, mesogens stack together atop the high energy Si-OH surface in a non-uniform manner. The silicon surface in the valley is exposed to air, because the LC mesogens have the tendency to form smectic layers instead of spreading out. The non-uniform coverage contributes to the roughness in Zone I of Figure 3.3. The roughness drops as the film averaged thickness increases from 2.5 nm until ca. 4.5 nm, as the mesogens fill the valleys gradually.

The LC mesogen in Zone I adopts a planar LC orientation with the aromatic portions of the mesogens oriented along the silicon surface. This alignment is a compromised arrangement because the high-energy LC mesogen core is forced to expose to air.

The roughness drops to a minimum at around 4~5 nm then remains constant (Zone II). This happens when the mesogens completely fill all valleys and form a stable, smooth planar LC anchored film, and a presumably complete film as shown in the model II in Figure 3.4. The number of planar mesogens to compose this specific thickness is calculated. The average spacing between two planar mesogens is ca 0.5 nm from the analysis of the monomer crystal structure (Section 3.3.1) and molecular simulation results (Section 3.3.2). Therefore, the thickness of Zone II (~4.5 nm) corresponds to approximately nine planar mesogenic layers. Theoretically, the steric energy per chain becomes lower after packing more mesogens together, and then reaches a plateau. The total free energy affecting LC orientation in supported thin films is due to the balance among the interactions between air and the polymer, the interactions between the polymer and the substrate, and the LC packing. If the film is sufficiently thin (<100 nm), the long-range dispersive van der Waals contribution toward the free energy of the film is inversely proportional to the square of the distance away from the substrate ($\propto d^{-2}$).[32] In this system, the substrate tends to induce planar mesogen alignment, while homeotropic alignment is more favorable at the air interface. At Zone II, the strong substrate attraction causes the LC molecules to adopt a planar conformation, although it is unfavorable at the air interface.

Freedericksz first studied the LC transition of deformation in a field in the 1930s, when applying an external field (electric field or magnetic field) to a thin LC layer confined by two glass substrates.[33] Treatment of the glass surface orients the LC parallel to the substrate, while the field tends to align the director perpendicular to the substrate. The LC molecules near the substrate are not easily affected by the field, but the molecules in the middle are relatively free to orient. The deformation does not occur gradually as the strength of the field is gradually increased. For the field strength below a specific value, no change would occur. However, above the threshold value, the deformation increases with the field strength. This transition is not an LC phase transition (e.g. nematic to smectic), because the LC ordering remains the same. This transition from an undeformed to deformed texture at a certain value of the field is called the Freedericksz transition.

In my case, the LC molecules are confined by heterogeneous boundary conditions. The substrate orients them planarly, but the air interface exerts an external force to deform them into homeotropic orientation. At Zone I and II in Figure 3.4, the deforming force is still below the threshold value, so the LC molecules keep planar. The thickness of Zone II (~4.5 nm) corresponds to the 'threshold' value. Above this thickness, homeotropic alignment starts to form at the air interface as thickness increases. A computer simulation with heterogeneous boundary conditions is necessary for deeper understanding about the specific maximum numbers of mesogens needed to keep planar anchoring conditions stable.

A homeotropic LC alignment starts to form at the air interface (Zone III) at the thickness beyond that of nine planar-stacked mesogens. This transition is observed in experimental data, such as angle-resolved XPS (Section 3.3.6), and X-ray specular reflectivity (Section 3.3.7). Above 4.5 nm, as the substrate interaction diminishes, the mesogens try to stack together to build islands with homeotropic packing (Zone III) at the air interface. As the film thickness increases, the density of islands increases gradually, and fewer areas with planar orientation remain at the air interface. The thickness of Zone III is estimated to be around 3 nm (one smectic height) higher than the Zone II.

After approximately 7.5 to 8 nm, the entire surface is covered by homeotropic LCs (Zone IV), achieving a stable equilibrium roughness and a hydrophobic surface. The same roughness can be observed in films up to 20 nm thick. The equilibrium roughness corresponds to the roughness of the homeotropic-stacked layers. Note that the thickness at Zone IV is approximately 3 to 3.5 nm higher than at the fully planar films at 4.5 nm. It represents the height of one full homeotropic smectic layer.

A schematic model of different types of LC orientation inside the same film is shown in Figure 3.4 (IV). The transition region between close-packed homeotropic and planar regions is expected to have a lower packing density. Film thickness constraints make the mesogens switch from a planar to a homeotropic alignment, which is caused by a complex balance of interfacial energies, smectic layer ordering, and conformational contributions from chain folding.

The equilibrium roughness of the thin films is around 1.6 nm for R_q and 1.2 nm for R_a. It can be used to estimate the number of LC layers stacking at the air interface. Equation 3.5 and Equation 3.6 show the relationship of the surface roughness and surface smectic steps. To simplify, we made the assumption that the thin film is only composed of regions with two different heights (t_a and t_b; $t_a < t_b$). The region of thickness t_a covers x % of the entire surface while t_b covers (1-x)% of the surface. Based on the assumption and the definition of RMS roughness (R_q), we get the following two equations, where t_{av} is the average film thickness.

$$x * t_a + (1-x) * t_b = t_{av} \tag{3.5}$$

$$R_q^2 = x * (t_a - t_{av})^2 + (1-x) * (t_b - t_{av})^2 \tag{3.6}$$

These two equations can be used to derive the following expressions.

$$t_a = t_{av} - R_q * \sqrt{\frac{(1-x)}{x}} \tag{3.7}$$

$$t_b = t_{av} + R_q * \sqrt{\frac{x}{(1-x)}} \tag{3.8}$$

$$t_b - t_a = R_q * \left[\sqrt{\frac{x}{(1-x)}} + \sqrt{\frac{(1-x)}{x}} \right] \tag{3.9}$$

$$x = \frac{t_b - t_{av}}{t_b - t_a} = \frac{1}{2} - \frac{1}{2}\sqrt{1 - 4 \times \left(\frac{R_q}{t_b - t_a}\right)^2} \qquad (3.10)$$

The smectic layer thickness (s_o) is around 3 to 3.5 nm in this series of PS-b-PHBPB diblock copolymers, and the RMS roughness (R_q) is around 1.6 nm (around ½ s_o).

From AFM images of the LC homopolymer film, such as in Figure 3.9a, the top first layer covers round 50% of the air interface. From Equation 3.9, the height difference at the air interface is around one smectic layer (t_b-t_a = s_o). This calculation support the concept that the fully annealed homopolymer thin films at Zone IV have a top surface layer with homeotropic alignment at the air interface, and the height difference between surface regions is around one smectic layer. The same phenomenon is also observed in block copolymers with the same LC mesogen, which will be discussed in the following chapters.

Equation 3.9 simply estimates the relationship between the surface height difference and the surface coverage. For example, the surface coverage (x) is 6.6% (93.3%) if the height difference is two smectic layers (t_b-t_a = 2 s_o).

LC Monomers

The roughness of films prepared from the LC monomer in Figure 3.3b has a similar trend as that for films of the LC homopolymer. The polymer has more mechanical strength compared to the monomer, but the main-chain backbone also constrains the LC mobility. At Zone I (before the Zone II arrangement), the roughnesses of the polymer and monomer samples were similar. But at Zone IV, the roughness of films from the monomer was larger than that of the homopolymer. This finding implies that surface roughness is reduced due to the constraint of the polymer backbone.

Roughness analysis of the LC monomer and the LC homopolymer provides the direct evidence of the transition from Zone I (partially coverage) to Zone II (fully coverage). However, more experimental data is necessary to determine that whether the bottom of holes at Zone I is just the bare silicon substrate or is covered by a thin wetting polymer layer. The roughness analysis does not show clear evidence of the LC alignment transition from Zone II (planar) to Zone IV (homeotropic), which will be further analyzed in Section 3.3.6.

3.3.5 Surface Wettability: Contact Angle Measurement

Contact angle measurement is a simple and straightforward way to determine the surface wettability. Here, the water contact angles for LC monomers and LC homopolymers were measured as a function of the film thickness. It is expected that, based on the differences in the surface energy of the mesogen core versus the mesogen tail (see, e.g. Table 3.3 and Figure 3.1a), the surface energy should also vary with the type of LC anchoring at the surface or interfaces. Homeotropic anchoring should create a lower surface tension than planar anchoring for this mesogen. Another factor for contact angle differences is the exposure of the silicon substrate to air, which is more hydrophilic than the polymer surface.

Contact angles for films of the LC monomer and the homopolymer are shown in Figure 3.5 for both advancing and receding angles. The water contact angles for the cleaned silicon substrate are 31±3° for advancing and 8±2° for receding from my experimental measurement, as plotted at zero thickness in Figure 3.5a. The Si-OH surface is more hydrophilic than a natural oxide surface (SiO_2), which has contact angles of 56.6° for advancing and 42.1° for receding as reported in the literatures.[34,35] The silicon substrate was treated by a strong base solution as detailed in Section 2.5.4. The higher water contact angles on the films imply lower surface tensions, when the surface is covered by polymer or monomer films.

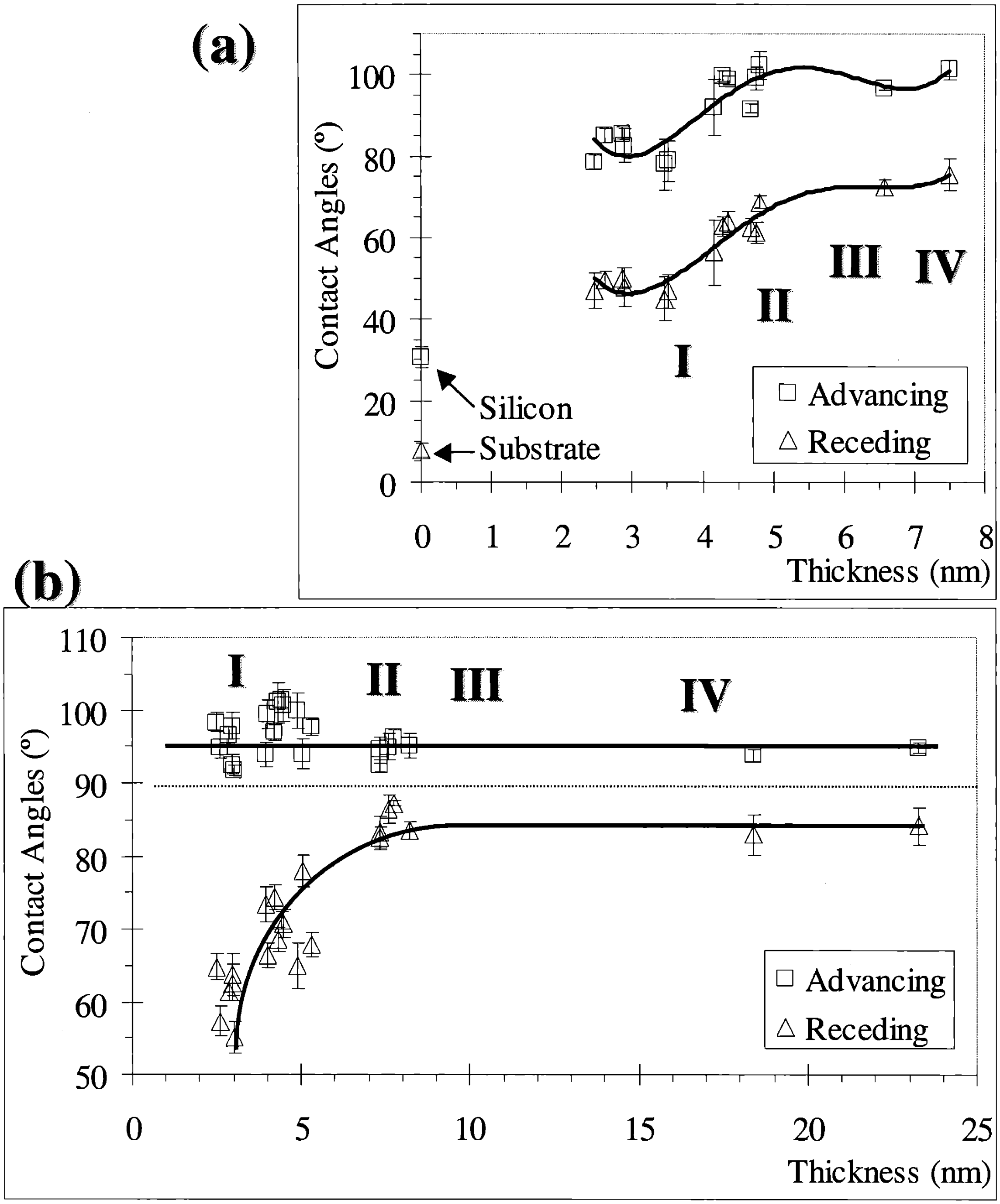

Figure 3.5: Water contact angle measurements on cast films of the LC monomer (a) and homopolymer (b). Square symbols (■) indicate advancing angles, and triangular symbols (▲) indicate receding angles. Error bars indicate one standard deviation. When no error bar is shown, the error falls within the symbol. Lines are guides to the eye.

LC Monomer

The LC monomer, which is easier to reorient than the LC homopolymer, shows increasing advancing and receding angles as the thickness increases in Figure 3.5a. In thinner films (Zone I, $t < 3.5$ nm), the film is rough at the air surface and only partially covered by monomers. The substrate tends to induce the LC mesogens to adopt a planar alignment because of favorable interactions between the Si-OH group and the mesogen core. Because the LC mesogen coverage on the highly energetic Si-OH surface, the surface energy of the LC layer is lower than that of the bare silicon surface. However, planar anchoring still has a higher energy surface (more hydrophilic) than homeotropic alignment, due to the exposure of the much more polar mesogen cores to air. When the thickness increases to around 5 nm (Zone II), we presume the complete surface coverage of a planar LC layer as explained in the previous section on roughness analysis (Section 3.3.4). The contact angles in Zone II are higher because of no silicon exposure. Mesogens form a full coverage layer with planar LC anchoring. Finally the contact angle values reach a stable value as the entire surface is covered with a complete monomer (or polymer) layer. The contact angle differences between planar and homeotropic LC anchoring are not observed in data of the LC monomer films.

LC Polymer

In Figure 3.5b, the receding angle behavior of the homopolymer films is similar to the monomer films in Figure 3.5a. The receding angles increase as the film thicknesses increase at thinner films (Zone I), change dramatically to show a clear transition at around 4-7 nm, and reach a stable value. However, the advancing angles remain about the same at all film thicknesses by exposing the hydrophobic moieties to the air interface. This implies that the mesogens in homopolymers do not adopt a fully planar alignment as in the monomers, even in very thin films (Zone I). The highly hydrophobic surface (high contact advancing angles) at Zone I may be caused by the PMMA backbone covering the air interface to hide the mesogen core in order to minimize the surface tension. In the LC monomer system, the vinyl group of MMA is more polar than the

PMMA backbone of the LC homopolymer. That is why the homopolymer and the monomer show different advancing wettability at Zone I.

The roughness and chemical heterogeneity of the surface affect the contact angle measurement of a thin film. The roughness effect, described by Wenzel's law in Section 2.7.3,[36] cannot explain the change in hysteresis with thicknesses, because it has the same effect on the measured advancing and receding angles. The chemically heterogeneous surface enhances the hysteresis. In these homopolymer thin films, the surface components depend on the film thickness. At Zone I, the hydrophobic LC polymer and the hydrophilic silicon coexist at the air interface. As the average film thickness increases, the exposure area of silicon decreases, and the hysteresis decreases. The large surface energy difference between the silicon and the polymer cause the large hysteresis in contact angle measurement. However, the difference of LC alignment between Zone II (planar) and Zone IV (homeotropic) is not observed in the contact angle experiments.

Equilibrium Contact Angle

In my PS-b-PHBPB diblock copolymer systems, the equilibrium contact angle (θ_e) was calculated from Equation 2.4 and shown in Figure 3.6 in a contact angle (θ) versus hysteresis ($\Delta\theta$) plot.[37,38] The linear least-square regression results of the homopolymer system (■, ▲) are listed below in Equation 3.11 and 3.12.

$$\theta_{(\Delta\theta)} = \theta_e + A * \Delta\theta \qquad (2.4)$$

$$\theta = 0.23\ \Delta\theta + 91.88;\ R^2 = 0.71 \text{ for advancing} \qquad (3.11)$$

$$\theta = -0.77\ \Delta\theta + 91.88;\ R^2 = 0.97 \text{ for receding} \qquad (3.12)$$

The monomer data in Figure 3.6 (□, △) could not be fitted by the linear regression model. The equation of the general linear model cannot fully explain the behavior of the LC systems. The theoretically fitted equilibrium contact angle was 91.9° for the homopolymer, which is slightly larger than 90 degrees. As the advancing angle (θ_a) shows little change and the receding angle (θ_r) shows most of the changes, this implies a heterogeneous surface of the polymer and the bare silicon.

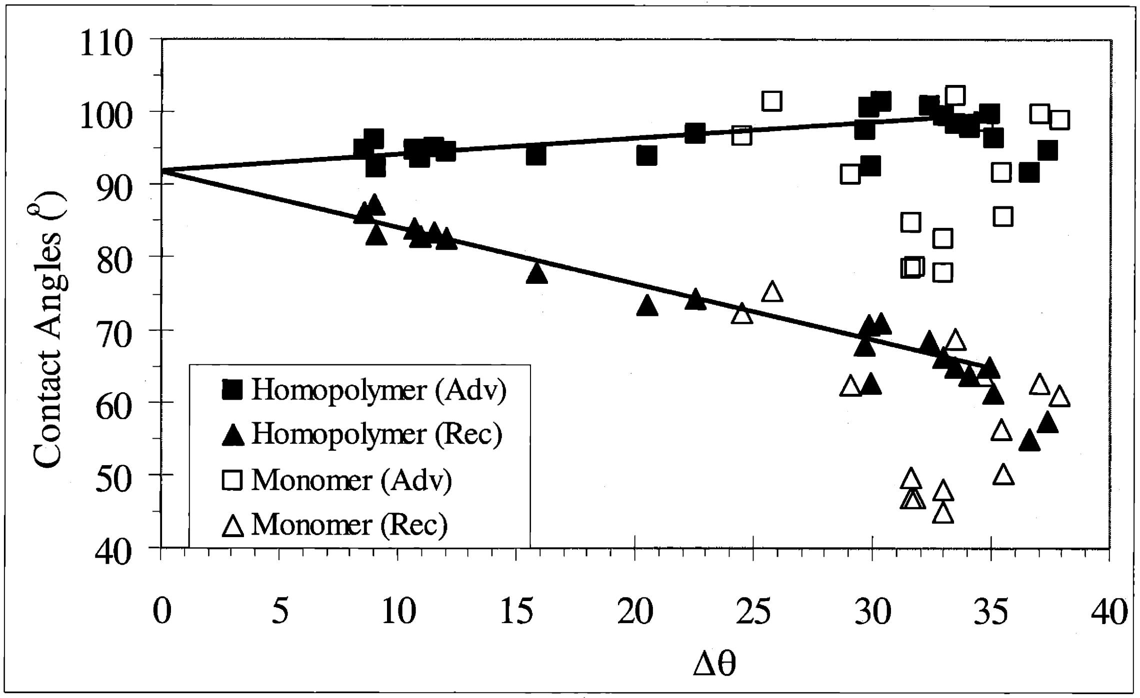

Figure 3.6: Contact angles (θ) versus hysteresis (Δθ) of thin films of the HBPB LC monomer and the PHBPB LC homopolymer.

Contact angle experiment provides the direct evidence of the heterogeneous surface at Zone I and the transition from Zone I (partially coverage) to Zone II (fully coverage). However, it does not show clear evidence of the LC alignment transition from Zone II (planar) to Zone IV (homeotropic).

3.3.6 Depth Profiles: Angle-Resolved X-ray Photoelectron Spectrometry

Angle-Resolved X-ray Photoelectron Spectrometry (AR-XPS) was used to calculate the film thickness. From the survey scans (binding energy = 0-1100 eV) of films with different thicknesses at a 0° takeoff angle ($\Phi = 0^o$), I observed the ratio of the Si_{2P} (or Si_{2S}) peak to the C_{1S} peak becomes smaller as the average film thickness (from ellipsometry) increased. The decay of Si_{2P}/ C_{1S} ratio implies the steady growth of films.

Thickness calculated from Si / C signal ratios

The AR-XPS data from survey scans can also be used to determine the film thickness.[39] The thicknesses of several homopolymer films were calculated using the least-square regression of Equation 2.9 in Chapter Two.

$$\ln\left(\frac{I_f}{I_s}\frac{1}{K}+1\right)=\frac{d}{\lambda}\sec\theta \qquad (2.9)$$

For three different films, the calculated thicknesses from AR-XPS (2.16, 1.47, and 1.31 nm) were around 20% smaller than that found from previous ellipsometry measurements (2.8, 1.9, and 1.6 nm). The error may come from the low resolution of the survey scan.

Carboxylic Percentage vs. Film Thickness

Because there are three carboxylic groups (-COO-) throughout the length of the LC side chain, whether the LC mesogen is aligned or randomly distributed can be determined using the profile of carboxylic concentrations with film thickness. AR-XPS was used to detect the top layer of the thin film surface, then the data curve was fitted using different functional groups corresponding to various carbon status, such as C, CH, CO, and COO.[40,41] The percentage of carbons in the carboxylic group (~ 4 eV shift) to all carbon 1s peaks was calculated. A detailed fitting procedure was described in Chapter Two.

The theoretical overall carboxylic carbon percentage of the homopolymer (or monomer) is 8.6% (3 carboxylic carbons over a total of 35 carbons in a monomer unit). Due to the exponential signal decay of photoelectrons escaping from different penetration depths, I can expect to find different carboxylic percentages detected between the entire planar LC film and vertically layer-ordered structures. Because the XPS detector is only sensitive to its normal direction, the films with entirely planar LC anchoring at the 0° takeoff angle do not have vertical carboxylic concentration variation. The carboxylic concentration (8.6%) for planar anchoring should be independent of the film thickness; thus the carboxylic group is equal to the bulk composition.

Simple calculations are done for seven mesogens in a square density box in two different types of alignment (homeotropic or planar). The results are presented below in Table 3.4 and Figure 3.7. The mesogen is simply treated as a rod (volume=3.127 nm^3, area=0.893 nm^2, and length L=3.5 nm from Table 3.1). The calculation focuses on the photoelectron collection region, which are three IMFPs (Inelastic Mean Free Path) from the air interface for this polymer as calculated in Chapter Two. The perfect homeotropic alignment is assumed to have every carboxylic group located inside a ΔL ($\equiv Z_2 - Z_1$) thick region (e.g. 0.1 nm) at three different depths (0.6, 1.7, and 3.2 nm from the air interface) for each IMFP, based on the molecular simulation data in Table 3.2. The thickness is calculated from the

The photoelectron-escape probability of each carboxylic region was calculated from the Beer-Lambert law below in Equation 3.13 and summarized in the table. The carboxylic probability of homeotropic-aligned mesogens in first three IMFPs could be estimated as shown in Table 3.4.

$$P(Z) = 1 - \exp (-Z / (\lambda_{e(E)} * \cos \Phi) \tag{2.6}$$

$$P(Z_2-Z_1) = \exp (-Z_1 / (\lambda_{e(E)} * \cos \Phi)) - \exp (-Z_2 / (\lambda_{e(E)} * \cos \Phi)) \tag{3.13}$$

Table 3.4: Calculation of homeotropic/planar carboxylic group ratio.

IMFP		Depth (nm)	Homeotropic (H) Probability (%)	Planar (P) Probability (%)
1	COO^1	0.6	2.41	
	COO^2	1.7	1.76	
	COO^3	3.2	1.15	
2	COO^1	4.1	0.89	
	COO^2	5.2	0.65	
	COO^3	6.7	0.42	
3	COO^1	7.6	0.33	
	COO^2	8.7	0.24	
	COO^3	10.2	0.16	
SUM			**7.98**	**8.57**
H/P Ratio			**0.9313**	

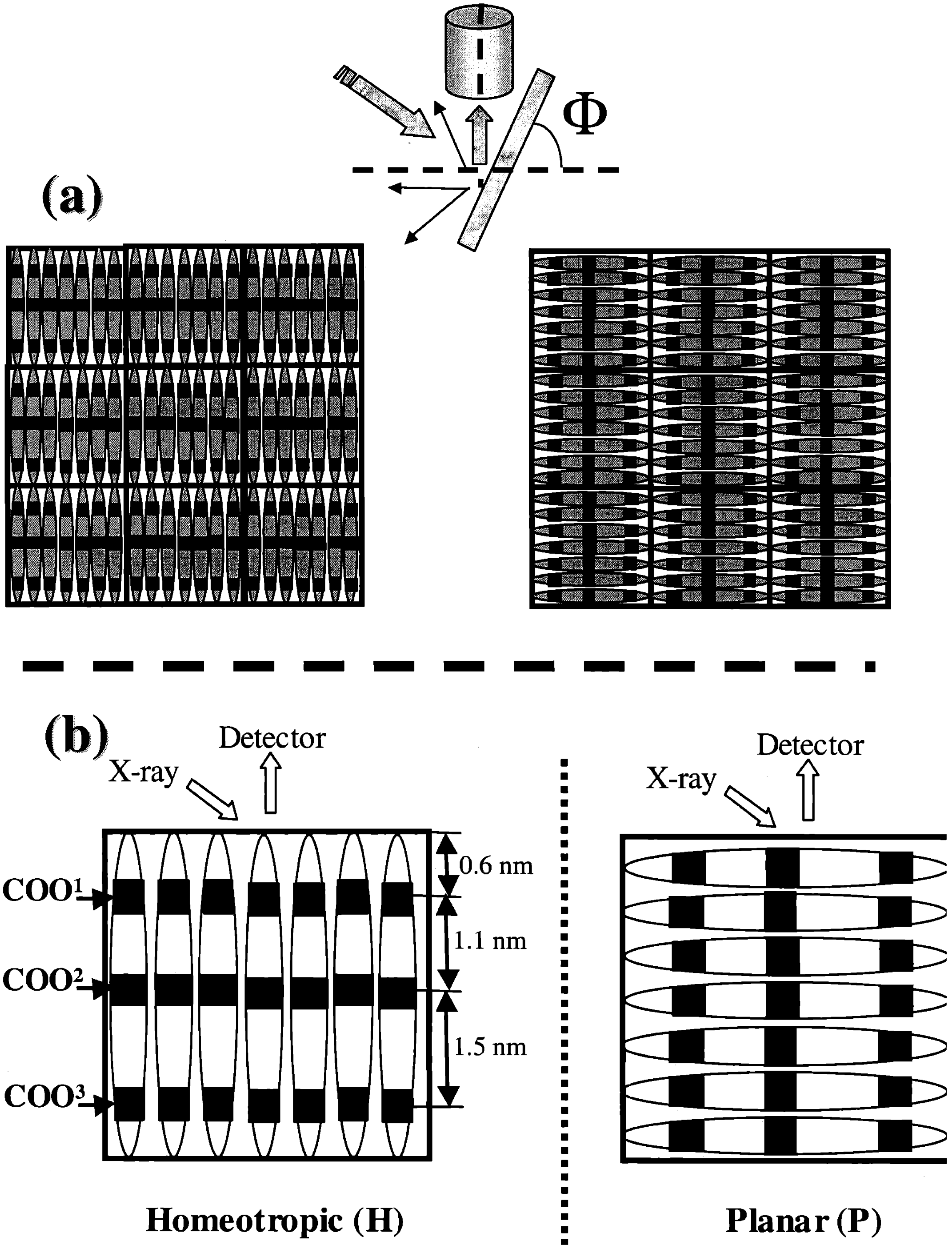

Figure 3.7: Calculating carboxylic percentages of the mesogens by XPS at homeotropic (H) and planar (P) alignment. (a) top three IMFPs; (b) one IMFP. Results are listed in Table 3.4.

For a planar anchoring film, the carboxylic concentration is thickness-independent in planar anchoring. The overall probability is equal to the bulk concentration, three carboxylic groups in total 35 carbons (8.57%).

The result of this calculation shows that the intensity of homeotropic alignment is around 93% of planar alignment within the first three IMFPs at a 0° takeoff detection angle. Homeotropic alignment shows lower carboxylic percentages to planar anchoring. Since the carboxylic groups are located in specific regions along the mesogen, various penetration depths by various angles of AR-XPS can demonstrate different carboxylic percentages in films with homeotropic LC alignment.

Experimental Data

Figure 3.8 presents the carboxylic percentage ($\frac{COO}{C+CO+COO}*100$) versus thickness data as determined from AR-XPS. Four zones are labeled corresponding to the model in Figure 3.3. From Figure 3.8a, the monomer shows a sharp peak at 4.5 - 5 nm for all three take-off angles (0°, 35°, and 70°). As shown in the above model in Figure 3.4, the film provides uniform planar coverage with the highest carboxylic percentage observed at a specific thickness corresponding to Zone II (thickness ~ 4.5 nm). Then homeotropic alignment starts to form (Zone III), while the carboxylic percentage decreases. The carboxylic percentage should be the same in Zone I and Zone II, but a lower percentage was observed in Zone I. A possible reason is incomplete or uneven film coverage at very thin film thicknesses. Since the number of carboxylic groups is very small, a little carbon contamination can lower the percentage significantly. This peak location corresponds to a change in LC orientation supported by other experimental data including AFM roughness and contact angle measurement.

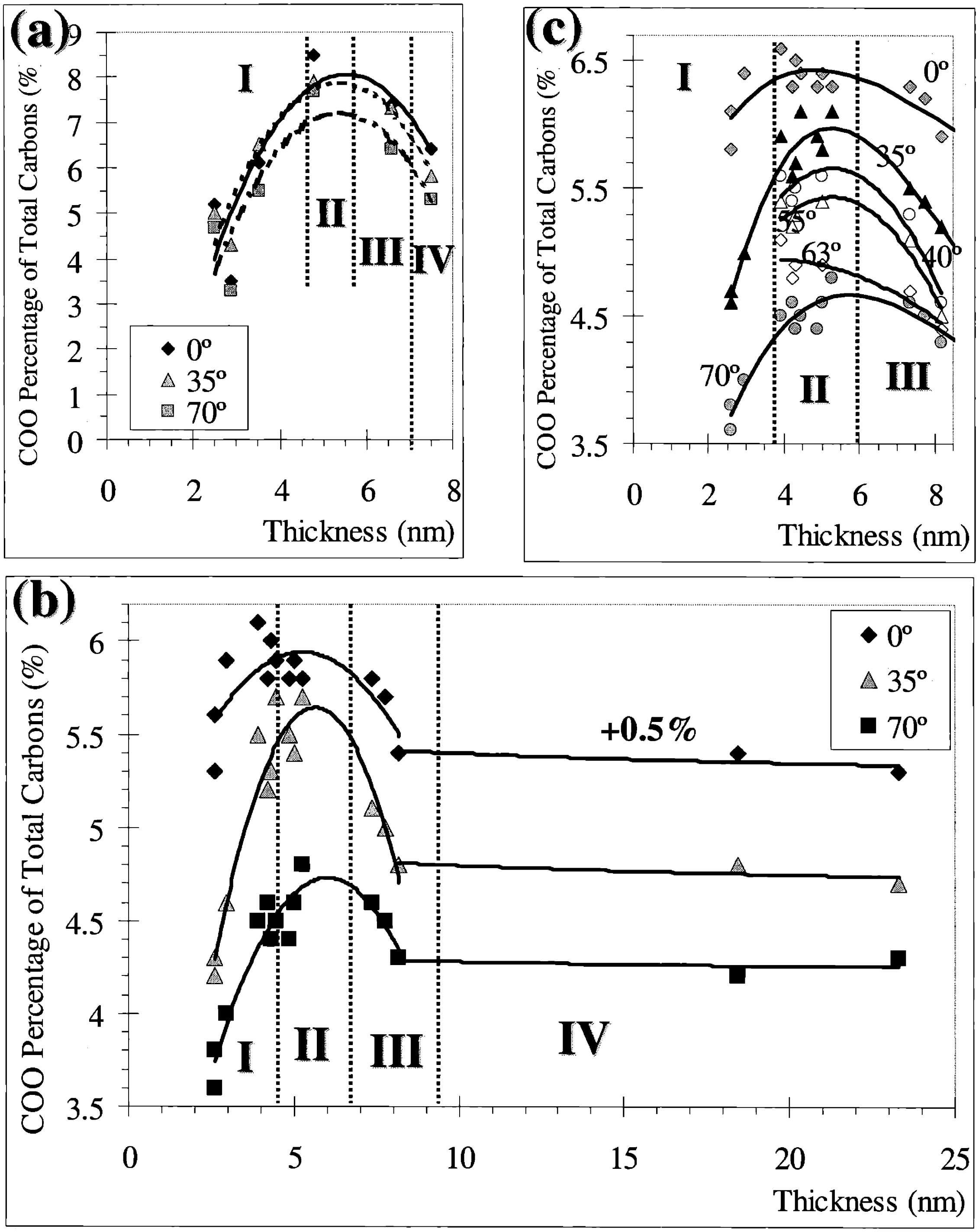

Figure 3.8: Angle-resolved XPS analysis of carboxylic carbon percentage vs. different film thickness at various takeoff angles (a) LC monomer films at 0°, 35°, and 70°; (b) LC homopolymer films. Data of 0° were shifted up 0.5%. (c) LC homopolymer films in transition zones (Zone I to III) at six different takeoff angles (0°, 35°, 40°, 55°, 63°, and 70°). Curves are shifted up by 0% (0º), 0.1% (35º), 0.2% (40º), 0.3% (55º), 0.4% (63º), and 1% (70º).

Figure 3.8b shows the carboxylic percentages of LC homopolymer thin films at three takeoff angles (0°, 35°, 70°) to demonstrate the carboxylic percentage differences among the different penetration depths. The curve of the 0° takeoff angle is shifted absolute 0.5% vertically on Y-axis. The carboxylic percentages for all angles reach a maximum at around 5 nm (Zone II), which exhibits uniform planar LC anchoring. The planar LC is expected to have higher carboxylic percentages as shown in previous calculations. The experimental data are lower than the theoretical value (8.6%) due to organic contaminations. The organic contaminations increase the contents of C and CH peaks, especially at Zone I. The carboxylic percentage decreases at higher thickness (Zone III). Then the value remains the same at Zone IV, indicating the formation of a stable surface. In Figure 3.8b, the ratios of the carboxylic percentages between Zone IV (homeotropic) and Zone II (planar) are around 0.91 (at $\Phi = 0^{\circ}$), 0.88 (at $\Phi = 35^{\circ}$), and 0.94 (at $\Phi = 70^{\circ}$). These values agree with the previously calculated homeotropic-to-planar ratio (0.93) at a 0° takeoff angle. We conclude that homeotropic alignment forms at the air interface for thicker films (Zone IV), as stated for our previous results.

Figure 3.8c shows the expansion region of Figure 3.8b. Homopolymer thin films with different thicknesses at the transition area (Zone I and III) were plotted at six different takeoff angles (0°, 35°, 40°, 55°, 63°, and 70°) for different penetration depths. All curves demonstrate the clear transition.

The highest takeoff angle scan ($\Phi = 70^{\circ}$) retrieves 95% signals from the top most IMFP (~ 3.5 nm) as described in Chapter Two. The depth is around the height of the top homeotropic mesogen layer in thick films. Scans at this angle can be used to directly observe the LC orientation at the air interface. In the spectra obtained at the 70° takeoff angle, the carboxylic percentage is at its highest in Zone II, giving strong evidence that a thick planar layer of LC is found at this thickness of 4.5 nm, in support of the model described here in thinner films.

As the takeoff angle decreases, the analyzed depth increases to probe the subsequent layers gradually as shown in the previous chapter. Ninety-five percent of XPS signals come from the first three IMFPs (~10.5 nm) at the zero takeoff-angle ($\Phi = 0^{\circ}$), while 91% of XPS signals come from first two IMFPs at the 35° takeoff angle. The intensity at 0° is slightly higher than 35°, but is around a full percentage of 1~2% higher than at 70°. The signal at 0° focuses on the complete film, including more of the bottom planar anchoring layers, so the overall signal is higher. The lower carboxylic percentage at high angles represents the fact that the alkyl tail next to the air interface is more emphasized.

In conclusion, the results show two types of orientation at different thicknesses for both LC monomers and polymers.

3.3.7 X-ray Specular Reflectivity (XSR)

X-Ray Specular Reflectivity (XSR) was used to determine the appropriateness of the model of LC alignment at the substrate surface and the air interface as a function of thickness. A uniform film is necessary for XSR analysis. Homopolymer films with different thicknesses show different fittings. In this section, two films of different thicknesses were compared.

Figure 3.9a shows the AFM image of the sample. The average air surface roughness (1.14 nm) from AFM and the film thickness (6.45 nm) from ellipsometry were included in the fitting. Figure 3.9c shows the XSR experimental data points and fitting curve of a thin film (6.45 nm, ~bilayer). The fitting parameter is listed in Table 3.5 and Appendix III. The density of this LC homopolymer was measured experimentally by Anthamatten and Hammond.[21,22] The estimated electron scattering length density values (SLD, $Å^{-2}$) and the absorptivity were calculated from the 'Scattering Length Density Calculator' at the NIST website[e] based on the molecular formula ($C_{35}H_{40}O_7$) and the LC homopolymer density. A detailed fitting procedure has been described in Chapter Two. The thin film does not show a Bragg peak, indicating the smectic layers are not ordered parallel to the interfaces. The fitted thicknesses and SLD agreed with the estimated values in Table 3.5, although roughness (0.32 nm) at the air interface was lower than roughness from ellipsometry (1.14 nm).

---

[e] http://www.ncnr.nist.gov/resources/sldcalc.html

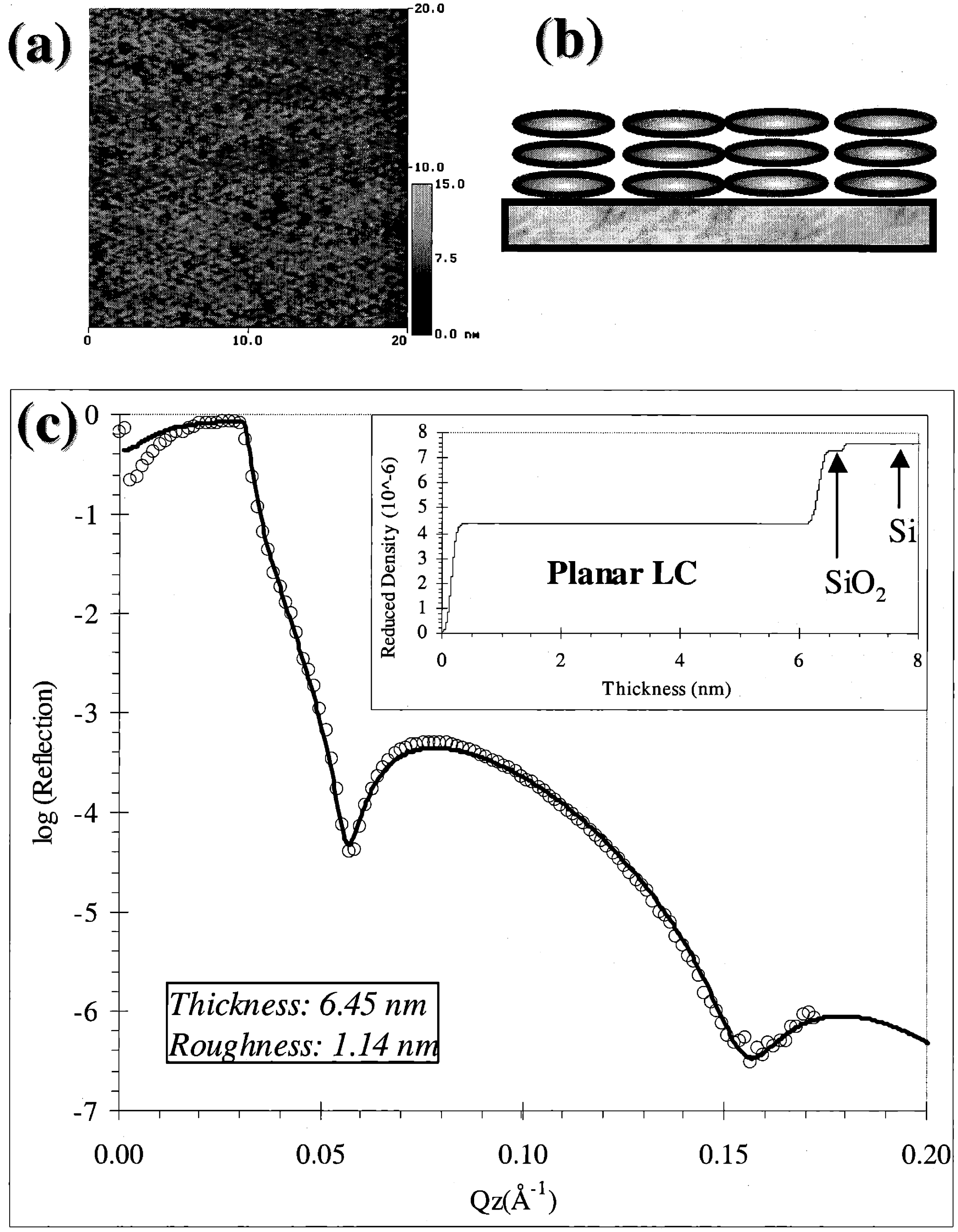

Figure 3.9: XSR of a thin PHPBP homopolymer film (6.45 nm) at Zone III. (a) The AFM image of the sample (20*20 μm²); (b) Cartoon of planar LC anchoring at the substrate; (c) XSR experimental data (O) and the fitting curve (solid line). The inset is the vertical electron density profile.[f]

---

[f] Reduced density = SLD * ($\lambda^2 r_e / 2\pi$). λ is 1.54 Å for X-ray and r_e is the classic radius of electron. It is dimensionless.

Table 3.5: The estimated and fitted models for XSR experimental data of a 6.45 nm thick film of PHBPB homopolymer.

Layer	**Density (g/cm^3)**	**Calculated**		**XSR Fitted**	
		Thickness (nm)	**SLD (ρ, $Å^{-2}$)**	**Thickness (nm)**	**SLD (ρ, $Å^{-2}$)**
Air	-	-	1.00E-08	-	1.00E-08
Interface	-	-	-	**0.32**	-
Film	1.154	**6.45**	1.05E-05	**5.84**	1.16E-05
Substrate interface	-	-	-	**0.32**	-
Total film	-	**6.45**	-	**6.48**	-
SiO_2	2.32	-	1.94E-05	0.24	1.94E-05
Silicon	2.328	-	2.00E-05	-	2.00E-05

From the electron density profile in the inset of Figure 3.9c, the best fit was simply achieved by a one-layer model (a homogeneous LC planar layer). The fitting was calculated assuming a constant electron density perpendicular to the film. The planar schematic anchoring model at the substrate is shown in Figure 3.9b. The fitting is programmed on the Microsoft Excel platform using Excel macro language. Although the film is located in Zone III based on the average thickness, LC orientation is basically planar, and the model of uniform planar anchoring (Zone II) can still fit the data well.

A thicker film (12.7 nm) at Zone IV was also examined using XSR. Figure 3.10a and Figure 3.10b show the model used to fit the data. Figure 3.10c indicates that the experimental data curves have a completely different shape when compared to thinner films, and the one-layer model was not able to fit the data. Several more complex models were employed to find the best fit. The air surface roughness (1.17 nm) was included in the fitting routine. Based on the model of Zone IV in Figure 3.4, we divided the film into four ordered layers as in Figure 3.10b, and calculated the electron density for each layer. The estimated and fitted parameters for each layer are listed in Table 3.6 and Appendix III. Then the electron density profile was applied to fit the data. Figure 3.10a shows the final fitting and the explanation for each layer as marked. It shows a planar LC layer with a high electron density near the substrate, two homeotropic mesogenic layers at the air interface, and a lower density transition zone between them. The polymer density and SLD of the top homeotropic layer (Layer 1) are lower because of incomplete surface coverage. The surface coverage of Layer 1 was ca. 64%, which was estimated by the SLD ratio of Layer 1 (5.54E-6 Å^{-2}) and Layer 2 (8.68E-6 Å^{-2}). The transition layer (Layer 3) has a lower packing density as described in Figure 3.4 and Figure 3.10b due to poor packing in the transition region. The bottom planar anchoring layer (4) has the highest fit SLD due to better packing induced by the substrate.

The thickness and SLD of each layer, before and after fitting, are listed in Table 3.6. The fitted thicknesses agreed with our expectation values. The LC mesogens prefer to anchor in a planar fashion at the silicon substrate, but adopt a homeotropic alignment at the air interface to minimize the surface energy by the aliphatic non-polar ends. We also tried to remove the top homeotropic layer, and the model could not fit the data as shown in Figure 3.10d.

Table 3.6: The estimated and fitted models for XSR experimental data of a 12.7 nm thick PHBPB film. The film is divided to four regions as shown in Figure 3.10.

Layers	Layer #	**Estimated**		**XSR fitted**		
		Thickness (nm)	**SLD (ρ, Å^{-2})**	**Thickness (nm)**		**SLD (ρ, Å^{-2})**
Air Interface		-	-	1.66	-	-
Incomplete Homeotropic	1	3.5	1.05E-05	0.93	2.98	5.54E-06
Interface		-	-	0.77	-	-
Homeotropic	2	2.0	1.09E-05	1.66	2.14	8.68E-06
Interface		-	-	0.19	-	-
Transition	3	**2.7**	9.39E-06	2.92	**3.33**	4.84E-06
Interface		-	-	0.63	-	-
Planar	4	**4.5**	1.05E-05	2.85	**3.90**	1.20E-05
Substrate Interface		-	-	0.73	-	-
Total		**12.7**[g]	-	12.34	**12.34**	-

---

[g] The thickness obtained from the ellipsometry measurement

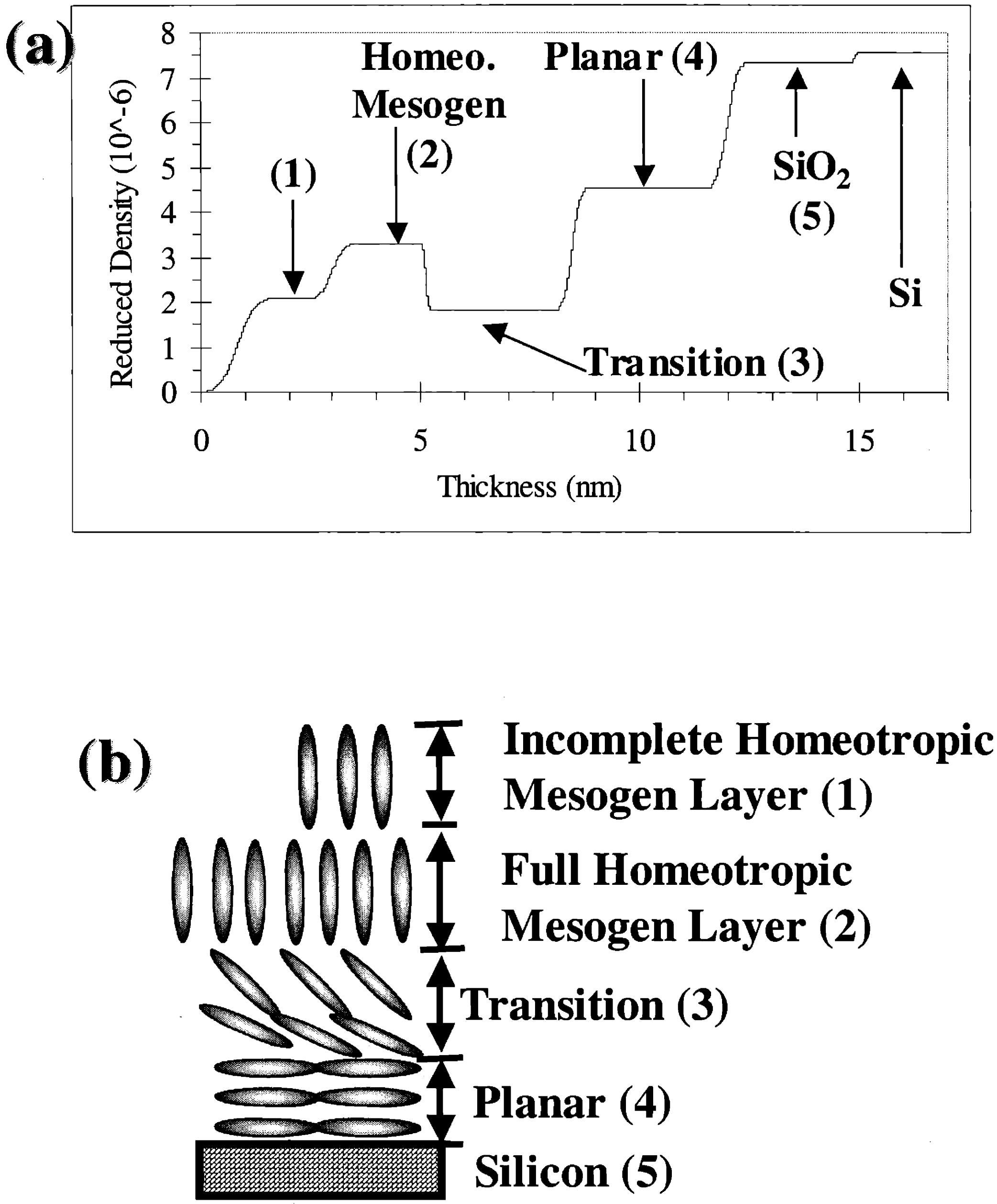

Figure 3.10: XSR of a thick homopolymer film (12.7 nm) in Zone IV (a) the electron density profile used to fit the data (b) model of LC orientation in Zone IV (c) experimental data and fitting curve (d) fitting without the top homeotropic layer

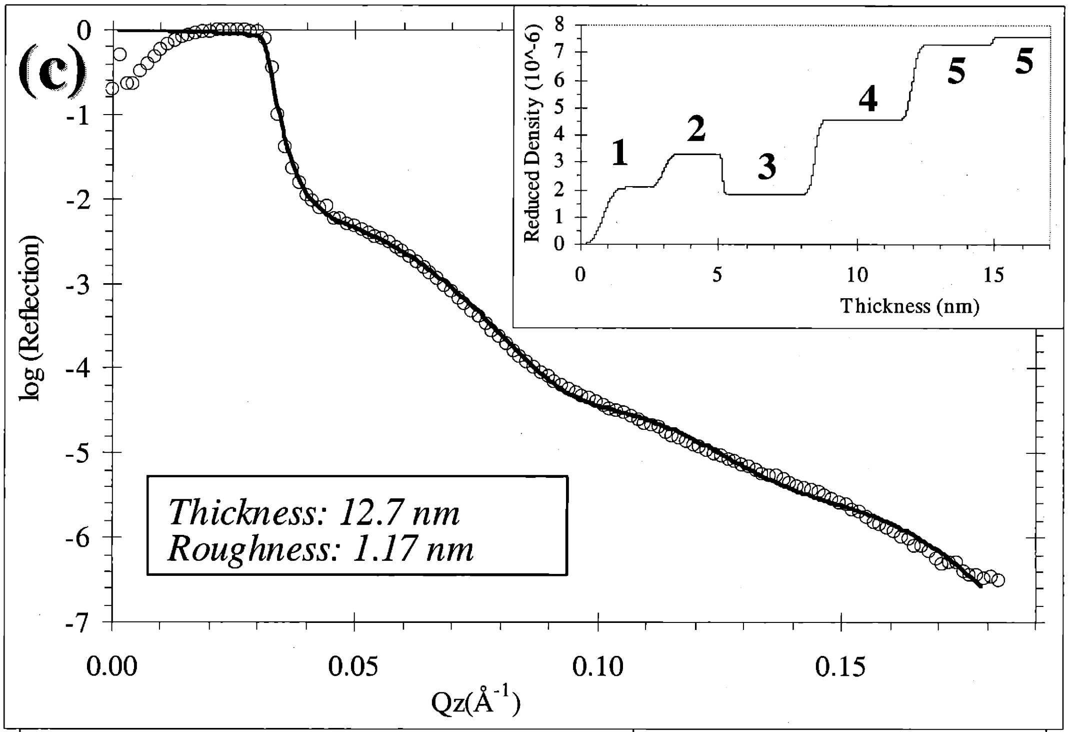
(c)
log (Reflection)
0
-1
-2
-3
-4
-5
-6
-7
0.00
0.05
0.10
0.15
Qz(Å^{-1})
Thickness: 12.7 nm
Roughness: 1.17 nm
Reduced Density (10^-6)
0
1
2
3
4
5
6
7
8
0
5
10
15
Thickness (nm)
1
2
3
4
5
5

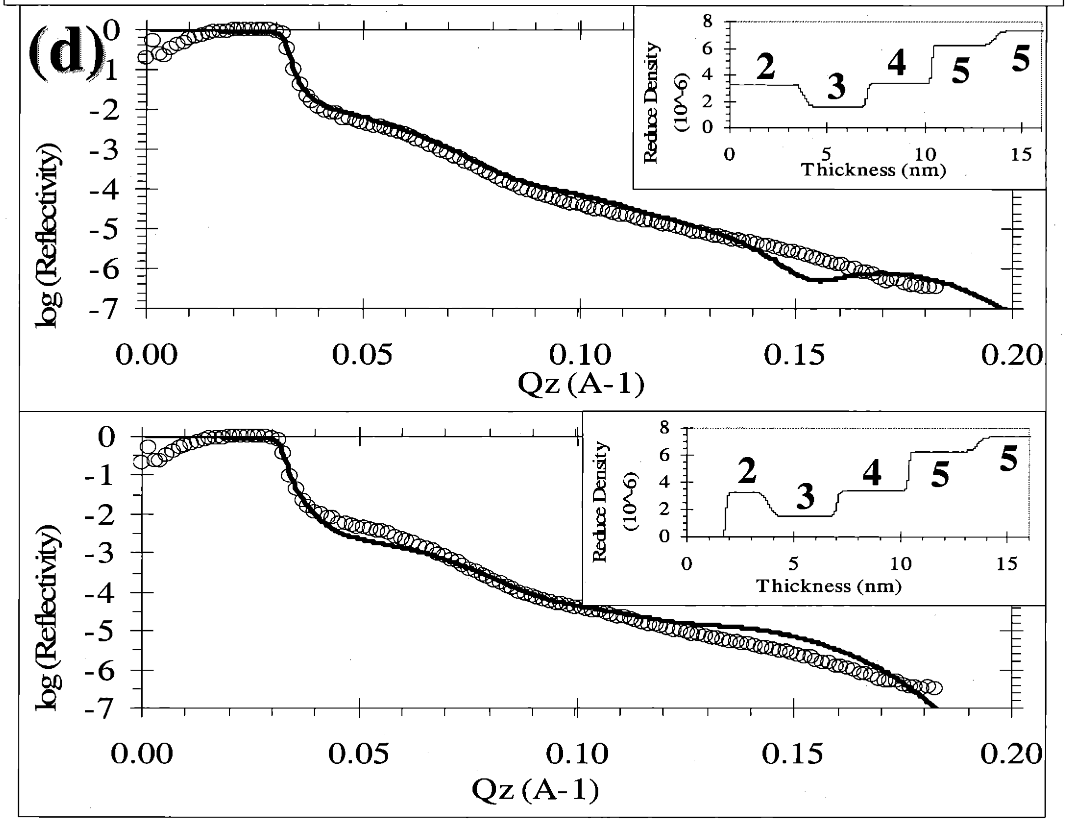
(d)
log (Reflectivity)
0
-1
-2
-3
-4
-5
-6
-7
0.00
0.05
0.10
0.15
0.20
Qz (A-1)
Reduce Density (10^-6)
0
2
4
6
8
0
5
10
15
Thickness (nm)
2
3
4
5
5
log (Reflectivity)
0
-1
-2
-3
-4
-5
-6
-7
0.00
0.05
0.10
0.15
0.20
Qz (A-1)
Reduce Density (10^-6)
0
2
4
6
8
0
5
10
15
Thickness (nm)
2
3
4
5
5

3.3.8 Effect of High Annealing Temperature

All samples I discussed above in this chapter were annealed at a temperature below the T_{iso} (LC clearing point, LC isotropization temperature) and then cooled slowly to room temperature. The surface healing and LC reordering processes slowly but smoothly approached the lowest energy state. The average water contact angles for these films at Zone IV were 94.5°±1.2° for advancing and 84.2°±1.8° for receding (film thickness = 7-24 nm) as discussed in Section 3.3.5.

Annealing temperatures affect the surface roughness. I can achieve uniform films for all samples with roughness less than 3 nm at temperatures below the T_{iso}. Especially when the LC mesogens can orient to homeotropic alignment at the air interface (Zone IV), the roughness is lower than 2 nm. However, when films are annealed (thickness = 7 – 27 nm, Zone IV) at higher temperatures ($T > T_{iso}$), the LC phase loses its ordering, and mesogens are free to rearrange. Upon cooling back down, LC mesogens can form larger and more stable domains. The whole structure can reform to the more favorable state. I expect that in this case, the homeotropic phase become more ordered. The average water contact angles for thin films annealed high temperatures are 98.5°±2.4° for advancing and 88.3°±0.8° for receding. The contact angle measurement shows a more hydrophobic surface after annealing at higher temperatures. The roughness I measured from AFM was always larger than 5 nm at high annealing temperatures. From the same calculation above, there should be at least four smectic layers (t_b-t_a = $4s_o$) at the air surface if the surface roughness is twice of the smectic height ($2s_o \sim 6$ nm). The high annealing temperature provides the entropic energy to create extra boundaries to form a rougher surface.

3.4 CHAPTER SUMMARY

From the experimental data and the theoretical calculations, I deduced that the LC mesogens could exhibit different types of alignment within the same film based on different wetting or anchoring conditions from the analysis of angle-resolved XPS and X-ray specular reflectivity. LC orientation is homeotropic at the air interface via the non-polar end group, yet planar near the substrate via the polar mesogen core. The LC polymer (or LC monomer) partially covers the air interface when the film is thinner than ca. 5 nm to form a heterogeneous surface, with the exposure of the bare silicon substrate. This homopolymer study is fundamental for understanding the further complex diblock copolymer systems. I will investigate the morphologies and LC alignment of diblock copolymer thin films with lamellae, cylinders, and smectic bilayers in Chapter Four and Chapter Five.

Likewise, this study can be continued on more detailed characterization of LC alignment. LC alignment can be further measured by several other instruments, such as second harmonic generation (SHG), infrared (IR) / sum frequency generation (SFG), grazing-angle Fourier transform infrared (FTIR), attenuated total reflection (ATR), near-edge x-ray absorption fine structure (NEXAFS), and angle-resolved ellipsometry.

REFERENCES

(1) Braun, FN; Sluckin, TJ; Velasco, E. *J. Phys. Condens. Matter.* **1996**, *8*, 2741-2754.

(2) Jacobs, AE; Mukamel, D; Allender, DW. *Phys. Rev. E: Stat. Phys., Plasmas, Fluids* **2001**, *63*, 021704.

(3) Immerschitt, S; Elben, H; Holthoff, H; Strobl, G. *J. Phys. Chem.* **1994**, *98*, 3, 376-382.

(4) Kasten, H; Strobl, G. *J. Chem. Phys.* **1995**, *103*, 15, 6768.

(5) Crawford, GP; Ondris-Crawford, RJ; Doane, JW; Zumer, S. *Phys. Rev. E: Stat. Phys., Plasmas, Fluids* **1996**, *53*, 4, 3647.

(6) Sigel, R; Strobl, G. *J. Chem. Phys.* **2000**, *112*, 2, 1029.

(7) Xu, L; Salmeron, M; Bardon, S. *Phys. Rev. Lett.* **2000**, *84*, 7, 1519.

(8) Lucht, R; Marczuk, P; Bahr, Ch; Findenegg, GH. *Phys. Rev. E: Stat. Phys., Plasmas, Fluids* **2001**, *63*, 041704.

(9) Brochard, F; Redon, C; Rondelez, FCR. *Acad. Sci., Ser. II* **1988**, *306*, 1143.

(10) Mensinger, H; Stamm, M; Boeffel, C. *J. Chem. Phys.* **1992**, *96*, 4, 3183.

(11) Elben, H; Strobl, G. *Macromolecules* **1993**, *26*, 1013.

(12) Henn, G; Stamm, M; Poths, H; Rucker, M; Rabe, JP. *Physica B* **1996**, *221*, 1-4, 174-184.

(13) van der Wielen, MWJ; Stuart, MAC; Fleer, GJ; deBoer, DKG; Leenaers, AJG; Nieuwhof, RP; Marcelis, ATM; Sudholter, EJR. *Langmuir* **1997**, *13*, 17, 4762-4766.

(14) van der Wielen, MWJ; Stuart, MAC; Fleer, GJ. *Langmuir* **1998**, *14*, 24, 7065-7071.

(15) van der Wielen, MWJ; Stuart, MAC; Fleer, GJ; Schlatmann, AR; de Boer, DKG. *Phys. Rev. E: Stat. Phys., Plasmas, Fluids* **1999**, *60*, 4, 4252-4256.

(16) van der Wielen, MWJ; Stuart, MAC; Fleer, GJ. *Adv. Mater.* **1999**, *11*, 11, 918.

(17) van der Wielen, MWJ; Baars, EPI; Giesbers, M; Stuart, MAC; Fleer, GJ. *Langmuir* **2000**, *16*, 26, 10137-10143.

(18) Figueiredo, P; Geppert, S; Brandsch, R; Bar, G; Thomann, R; Spontak, RJ; Gronski, W; Samlenski, R; Mueller-Buschbaum, P. *Macromolecules* **2001**, *34*, 2, 171-180.

(19) Vix, ABE; Muller-Buschbaum, P; Stocker, W; Stamm, M; Rabe, JP. *Langmuir* **2000**, *16*, 26, 10456-10462.

(20) Ladd, MFC. *Structure Determination by X-ray Crystallography*; New York : Plenum Press, 1993.

(21) Anthamatten, M; Hammond, PT. *Macromolecules* **1999**, *32*, 24, 8066-8076.

(22) Anthamatten, M; Zheng, WY; Hammond, PT. *Macromolecules* **1999**, *32*, 15, 4838-4848.

(23) Zheng, WY; Hammond, PT. *Macromolecules* **1998**, *31*, 3, 711-721.

(24) Zheng, WY; Albalak, R; Hammond, PT. *Macromolecules* **1998**, *31*, 2686-2689.

(25) Brandrup, J; Immergut, EH. *Polymer Handbook*, 4th ed.; Wiley: New York, 1999.

(26) Van Krevelen, DW. *Properties of Polymers*, 3rd ed.; Elsevier, 1992.

(27) Michaels, AS. *ASTM Tech. Publ.* **1963**, *340*, 3.

(28) Shimizu, RN; Demarquette, NR. *J. Appl. Polym. Sci.* **2000**, *76*, 1831-1845.

(29) Kwok, DY; Lam, CNC; Li, A; Zhu, K; Wu, R; Neumann, AW. *Polym. Eng. Sci.* **1998**, *38*, 1675.

(30) Glasstone, S. *Textbook of Physical Chemistry*, 2nd ed.; D. Van Nostrand: Toronto, Canada, 1946.

(31) Matuana, LM; Balatinecz, J; Park, CB. *Polym. Eng. Sci.* **1998**, *38*, 765.

(32) Limary, R; Green, PF. *Macromolecules* **1999**, *32*, 24, 8167-8172.

(33) Collings, PJ. *Liquid Crystals - Nature's Delicate Phase of Matter*; Princeton University Press: Princeton, NJ, 1990.

(34) Extrand, CW; Kumagai, Y. *J. Colloid Interface Sci.* **1995**, *170*, 2, 515-521.

(35) Extrand, CW; Kumagai, Y. *J. Colloid Interface Sci.* **1997**, *191*, 2, 378-383.

(36) Wenzel, RN. *Ind. Eng. Chem.* **1936**, *28*, 988-994.

(37) Schulze, RD; Possart, W; Kamusewitz, H; Bischof, C. *J. Adhes. Sci. Technol.* **1989**, *3*, 39-48.

(38) Kamusewitz, H; Possart, W; Paul, D. *Colloids Surf., A* **1999**, *156*, 271-279.

(39) Ton-That, C; Shard, AG; Bradley, RH. *Langmuir* **2000**, *16*, 2281-2284.

(40) Briggs, D. *Handbook of x-ray and ultraviolet photoelectron spectroscopy*; Heyden: London, 1977.

(41) Hunt, BJ; James, MI. *Polymer Characterization*; Blackie Academic & Professional, 1993.

Chapter 4

Morphology of Substrate Supported Lamellar Diblock Copolymer Thin Films

4.1 INTRODUCTORY REMARKS

In Chapter Three, I carefully examined the morphology and orientation of the side-chain LC homopolymer thin films at both air and substrate interfaces. I concluded that LC anchoring of the mesogen was planar at the silicon substrate, but homeotropic at the air surface for the LC homopolymer. This observation was consistent with the observations of similar block copolymer systems.[1,2] Homeotropic anchoring of the LC mesogen was also observed in the free-standing films.[3] All above information provided a basic understanding of LC behaviors and enabled further exploration of the morphology of diblock copolymer thin films. I will first study the diblock copolymers with the lamellar morphology in this chapter, then those with cylindrical and smectic-bilayered morphologies in the following chapter. From previous bulk SAXS studies of lamellar diblock copolymers,[4] the LC domains exhibited a smectic C* phase with a layer spacing (s_o) of 3.5 nm and the smectic layer oriented perpendicular to the block interfaces (lamellar period, L_o = 17.3 nm). The smectic ordering plays an important role in the diblock ultrathin film morphologies.

In this chapter, I address the lamellar thin film morphology at different film thicknesses, from one-half to ten times the block copolymer periodicity (L_o). The thin film wetting structure of lamellar diblock copolymers was first studied. X-ray Photoelectron Spectrometry (XPS) and microdroplet experiments were used to detect the wetting block for each surface and to confirm the correct wetting situation. Furthermore, AFM and TEM were used to study the complex thin film morphology and LC orientation. In the end of this chapter, I also studied sub-micron thick films (4-8 L_o) and verified the possible factors which contributed to the stability of thin films.

4.2 DETERMINATION OF THE LAMELLAR DIBLOCK THIN FILM STRUCTURE

Before analyzing the lamellar thin film morphology, I must determine which of the blocks wets the silicon and air interfaces. Two wetting models were proposed, including symmetrical wetting and anti-symmetrical wetting. The film wetting characteristics were determined by the microdroplet method described below in Section 4.2.1. Contact angle measurements of both homopolymer films (PS and PLC) were first used to determine the surface hydrophobicity. These measurements illustrated a similar surface free energy for these two blocks; thus, XPS was used to determine the surface compositions. The background and fitting parameters of XPS have been stated in Chapter Two and tabulated in Appendix II. This technique enabled us to identify the wetting of blocks at different interfaces. For the substrate-wetting block, I knew from the literature data and studies of the LC homopolymer in Section 3.3.3 that the LC block had a higher affinity to the polar silicon substrate than the PS block, because the LC side-chain mesogen had a higher dipole moment than the benzene ring of polystyrene. Experimental XPS data will be discussed in Section 4.2.2. In Section 4.2.3, it will be shown that the block with lower surface energy covered the air interface, which is directly determined by XPS. Section 4.2.4 describes the XPS data of lamellar diblock copolymer thin films and discusses the wetting structure.

4.2.1 Symmetric or Anti-symmetric Wetting - Microdroplet Experiment

Diblock copolymer thin films can wet the substrate in either a symmetrical or anti-symmetrical manner. The microdroplet experiment developed by Fasolka *et al.* [5] was used to determine the natural wetting situation, as shown in Figure 4.1a. A dilute polymer solution in toluene was prepared for this experiment. Tiny drops were made on the pre-cleaned substrate with a 5 μL micropipette. Drops were slowly air-dried, placed under vacuum to remove the residual solvents, and annealed at 130 °C under vacuum for one week. Microdroplets were formed on the edge of the drops, and checked simply by reflection-mode optical microscopy. The heights of the edges of the micro-droplets were then measured by AFM. The heights exhibited along the terraced droplets were 0.5 L_o and 1.5 L_o (L_o = 17.3 nm) as shown in the AFM image in Figure 4.1b. The black area is the bare silicon substrate, the gray area represents a film thickness of 0.5 L_o thick, and the white area represents a thickness of 1.5 L_o. The height differences were also observed directly from the cross-sectional profile analysis of Figure 4.1c.

The bulk morphology of this diblock composition (41%) was determined to be lamellar from previous SAXS and TEM studies.[4,6] The result of $\frac{1}{2}L_o$ and $1\frac{1}{2}L_o$ height experiments suggested that this lamellar diblock copolymer naturally forms anti-symmetric films on the silicon substrate.[7,8] Thin films of polystyrene-b-poly(methyl methacrylate) (PS-b-PMMA) diblock copolymers on silicon exhibited similar anti-symmetric morphologies with PMMA at the substrate, and PS at the free surface; in this case, the PS block had comparatively lower surface tension and the PMMA block had a stronger interaction with the silicon surface.[9-11] In my PS-LC methacrylate diblock copolymer system as well, one block covers the air interface and the other block covers the substrate to form anti-symmetric wetting.

4.2.2 Composition at the Substrate- XPS of Peeled Films

While further characterizing the supported film structure, the next step is to understand which block has higher affinity to wet the substrate. In order to determine the silicon wetting block nature, the lamellar diblock copolymer thin films were peeled off from the silicon substrate by the same method I used to prepare TEM samples, as described in Section 2.7.2. The process is presented in Figure 4.2. A thin layer of carbon (~ 10 nm) was first evaporated on top of the substrate-supported thin films for protection. A layer of poly(acrylic acid) (PAA, ~1 mm) was then used to cover the film, and dried at room temperature for one day. The whole film was peeled off the silicon substrate and the diblock copolymer thin film stayed with the PAA layer. The substrate-wetting layer was exposed to the air interface, and the chemical compositions at the interface could be directly analyzed by XPS.

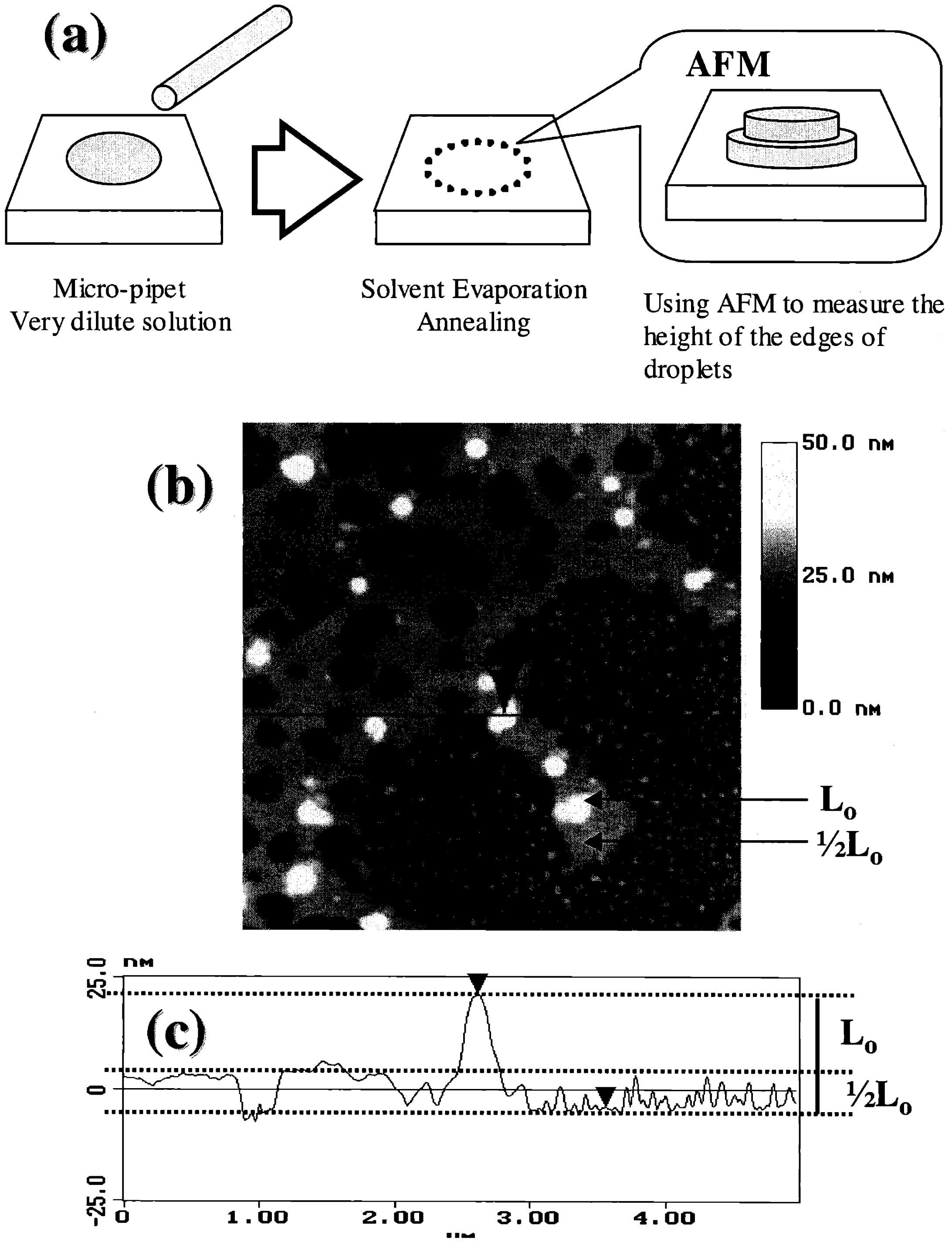

Figure 4.1: Microdroplet experiment to determine thin film wetting of diblock copolymers (a) experimental procedure; (b) AFM top-view image (5*5 μm^2) of a H41 diblock copolymer thin film; (c) AFM image of cross-sectional view.

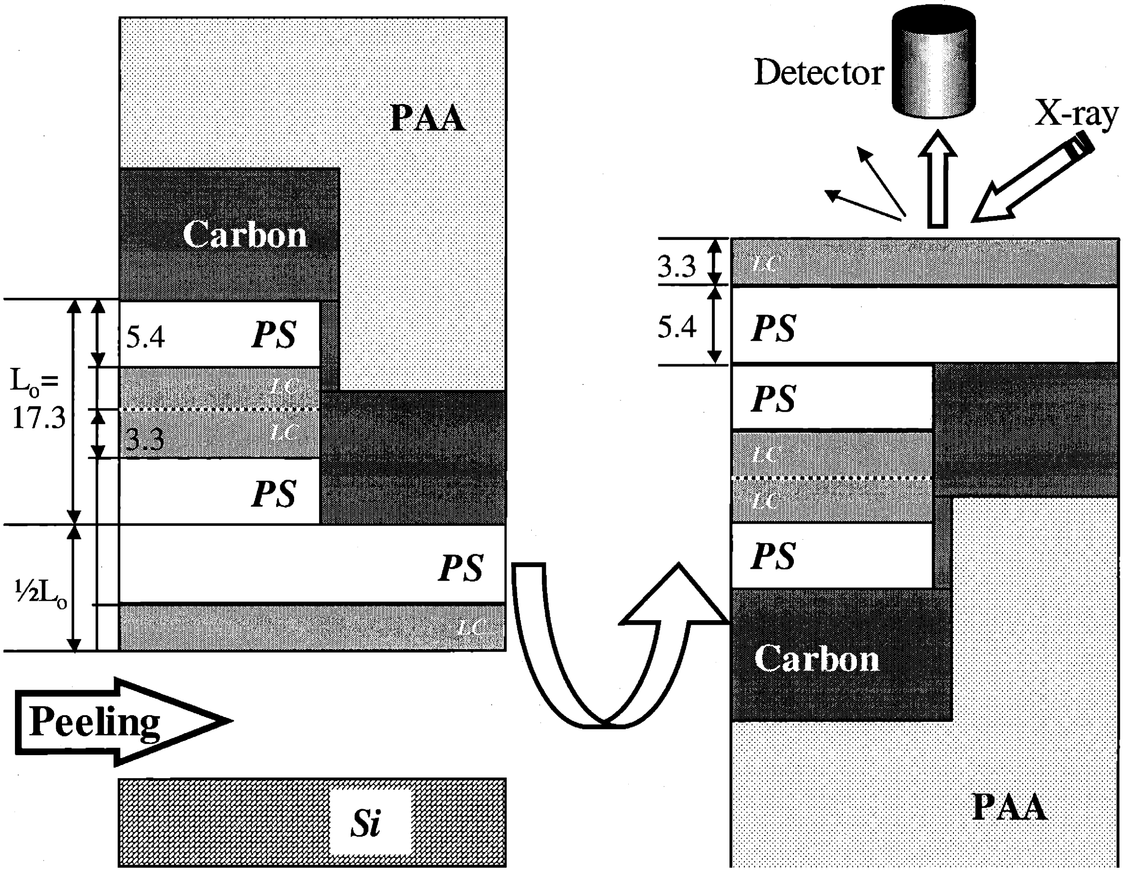

Figure 4.2: Using XPS to determine the substrate-wetting layer. The anti-symmetric diblock copolymer thin film was peeled up from the substrate and examined by XPS. The unit for length used in this figure is nm.

X-ray photoelectron spectroscopy can detect the chemical compositions of polymer films to around top five nanometers. Thus, it was chosen to determine the chemical components at the air interface. The high-resolution mode was used to scan the carbon region (binding energy = 275-295 eV) and monitor the presence of the +4 eV shift (~289 eV) of the carboxylic groups from the main carbon peak in the LC mesogen.

Angle-resolved XPS experiments at two different takeoff angles (15° and 75° to the surface normal) were conducted on the peeled diblock copolymer surface of the diblock-carbon-PAA films, as shown in Figure 4.3a (15°, close to surface normal direction) and Figure 4.3b (75°, glancing angle) after normalizing the largest carbon peak (C-CH) to 285 eV. Results are tabulated in Table 4.1 and detailed fitting parameters are listed in Appendix II. All samples with different thicknesses and tilt angles (different penetration depths) show the carboxylic group peak in the XPS analysis. This suggests the LC block covers the substrate interface, as explained below.

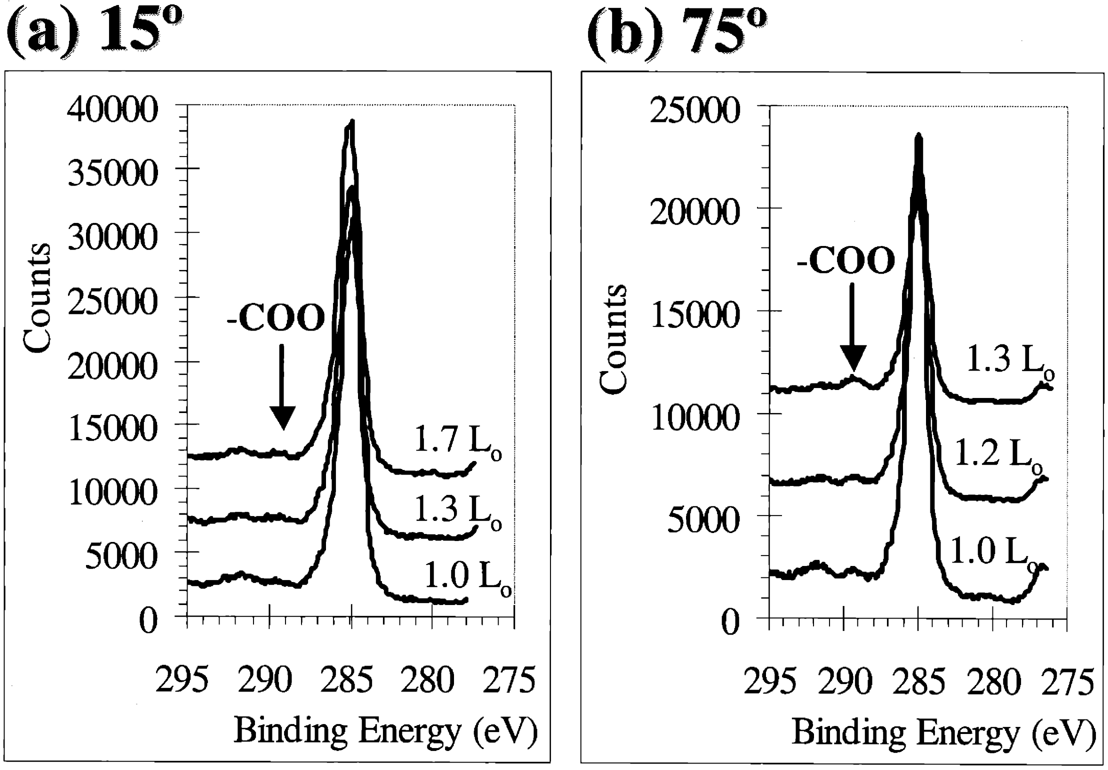

Figure 4.3: XPS analysis of peeled H41 lamellar diblock copolymer films at two different takeoff angles (a) 15° (b) 75°. Thickness (n L_0) is marked for curves although the -COO- value should be thickness independent after films are thicker than ½L_0.

Table 4.1: XPS fitting ratios of peeled lamellar diblock copolymer (H41) films at two different angles.

Takeoff Angle	**Peak**	**Peak Area (%)**	**Peak Area (%)** **(average of only 1.3 L_0 and 1.0 L_0)[h]**
15°	CH / C	86.6 ± 3.0	-
	CO	12.2 ± 3.1	-
	COO	**1.3 ± 0.1**	-
75°	CH / C	88.4 ± 4.8	91.1 ± 1.5
	CO	8.4 ± 3.0	6.7 ± 0.9
	COO	**3.3 ± 1.8**	**2.3** ± 0.6

---

[h] The fitting was done by Dr. Miller in Raytheon Co. One data point shows a very high COO ratio, and is not averaged in this column. Please check Appendix II for detail.

In Figure 4.2, the PS-layer thickness (5.4 nm) and LC-layer thickness (3.25 nm) of a half lamellar layer (½L_o = 8.65 nm) were calculated by the block periodicity (L_o = 17.3 nm) and the volume ratio of blocks. The volume ratio was calculated by the volumes of the PS block (MW = 11 kg/mol, density = 1.045 g/cm³ [i]) and the LC block (MW = 7.3 kg/mol, density = 1.154 g/cm³ [12]). The XPS penetration depths were ca. 10.1 nm at 15° (63% signals from top 3.5 nm), and 2.7 nm at 75° takeoff angles for our samples, as calculated and listed in Table 2.5. If the LC block wets the substrate as shown in Figure 4.2, the carboxylic group should be detected by XPS. If the PS block is the substrate-wetting layer, its thickness (5.0 nm) should be enough to prevent detection of the underlying LC layer. From Figure 4.3, all samples show carboxylic peaks, although the CO/COO peak ratios are not consistent. The theoretical carboxylic ratio for this LC monomer from the chemical structure should be 8.6% (three carboxylic groups over total 35 carbons), however, the experimental carboxylic ratios of LC homopolymer films were usually lower as explained in Chapter Three. When these two tilt angles were compared, the measurement at a glancing angle (75°) detected shorter penetration depths from the surface. From Table 4.1, the carboxylic ratio is higher at 75° than 15°, indicating that a greater LC block concentration is present at the substrate-LC surface. This agrees with what I proposed. The carboxylic ratio here was lower than the homopolymer value because the LC thickness (3.7 nm) was thinner than the XPS penetration depth at 0° takeoff angle, so that the PS layer underneath was also detected. The peeling process might also leave a thin layer of LC at the substrate, and cause the LC wetting layer to be even thinner. From the above results, I concluded that the LC block wetted the silicon substrate.

These results confirm that the LC block is the one that preferentially wets the substrate surface, as opposed to the PS block in Figure 4.2, and is consistent with other studies of PS – lauryl methacrylate diblock copolymer systems.[13]

---

[i] The density of polystyrene is 1.04-1.065 g/cm³ at amorphous state and 1.11-1.12 g/cm³ at crystalline state from Polymer Handbook.

4.2.3 Composition at the Air Interface - XPS of Homopolymer Blends

The next step is to understand which block has a lower surface tension and thus is able to cover the air interface. We chose homopolymer blends of these two blocks for this study because the diblock copolymers might form a mixed surface morphology with both blocks coexistent at the air interface. Since these two homopolymers (PS/PLC) were chemically dissimilar, the blends would tend to show full phase separation after they were annealed. The homopolymer with the lower air surface tension should cover the air interface.

Blends of polystyrene homopolymer (GPC standard, MW = 29.3 kg/mol) and LC homopolymer (MW = 17.3 kg/mol) were prepared using two solutions with a 1:1 weight ratio and 1:1 molar ratio, respectively, because the size of the LC repeat unit (MW = 572 g/mol) is far larger than the PS repeat unit (MW = 104 g/mol). The volume ratios of the LC homopolymer to the PS homopolymer were ca. 5:1 for the 1:1 mole ratio blends, and ca 0.9:1 for 1:1 weight ratio blends. In order to make films of different thicknesses on pre-cleaned silicon wafers, both solutions were spun cast at different concentrations and spinning speeds. Homopolymer blend films were prepared with thicknesses ranging from 20 to 60 nm.

The XPS results of the two blends are shown in Figure 4.4a (1:1 wt ratio) and Figure 4.4b (1:1 mol ratio). Table 4.2 shows carbon peak ratios for the PS homopolymer, LC homopolymer, PS/PLC homopolymer blends, and H41 diblock copolymers. Detailed fitting parameters are listed in Appendix II. Both weight and molar ratios at different thicknesses show the clear presence of carboxylic groups at the top surface.

Table 4.2: XPS fitting ratios of homopolymers, homopolymer blends, and H41 lamellar diblock copolymer thin films at a 55º takeoff angle.

Sample	**Thickness (nm)**	**Peak**	**Theoretical peak ratio (%)**	**Peak Area (%)**
PS	17.4 - 20.5	CH / C	100	100
PLC Homopolymer	26.1 - 32.0	CH / C	77.1	87.6 ± 4.1
		CO	14.3	9.4 ± 3.2
		COO	**8.6**	**3.0 ± 0.9**
1/1 wt Blend	30.2 - 57.5	CH / C	81.6	93.5 ± 0.6
		CO	12.1	5.2 ± 0.4
		COO	**7.3**	**1.4 ± 0.2**
1/1 mol Blend	22.2 - 23.6	CH / C	88.5	89.9 ± 3.2
		CO	7.2	7.9 ± 2.8
		COO	**4.3**	**2.2 ± 0.4**
H41	16.1 - 30.8	CH / C	91.4	92.2 ± 0.8
		CO	5.4	7.8 ± 0.8
		COO	**3.2**	**0**

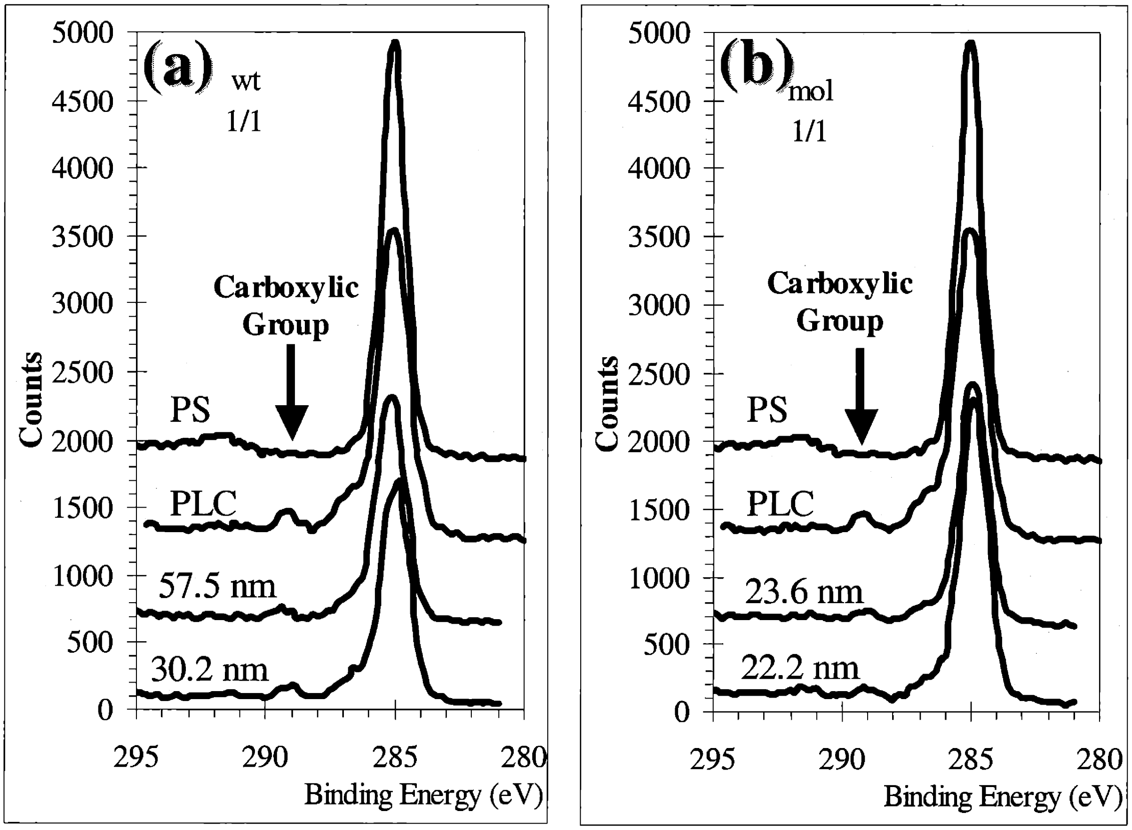

Figure 4.4: XPS analysis of films of homopolymer blends of PS and PHBPB homopolymers. (a) 1:1 wt ratio; (b) 1:1 mol ratio. PS and PHBPB homopolymers are plotted as reference.

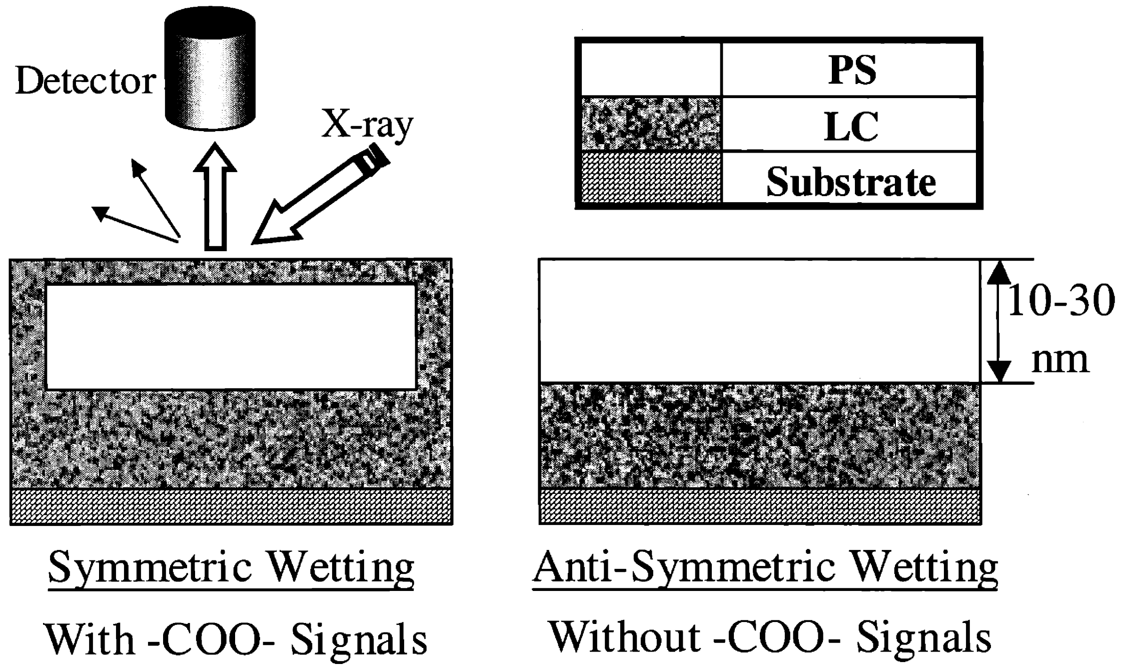

Figure 4.5: Two possible arrangements of PS/PLC homopolymer blends.

In symmetrical wetting, the LC homopolymer wraps around the PS block. In anti-symmetrical wetting, the two homopolymers arrange parallel to the substrate. The XPS detection depth at a 0° takeoff angle is usually around 10 nm. If the PS homopolymer has a lower surface tension (and is therefore, anti-symmetrical), the PS layer at the air interface is at least 10 nm thick, based on the total film thickness and the PS/PLC ratio. This thickness would be sufficient to avoid the photoelectrons excited from the LC layer to be detected. The carboxylic peak indicates that the LC homopolymer resides at the top surface of phase-separated films, as there is no carboxylic group in the PS homopolymer. From Figure 4.4 and Table 4.2, the data suggest the presence of a thin LC layer wetting the air interface, although the carboxylic ratios of blends are lower than the value of the LC homopolymer. There may still be a few PS miscible components in the LC-rich layers. The carboxylic ratio of 1:1 mol blends is higher than the carboxylic ratio of 1:1 wt blends due to the larger quantity of LC in the samples.

Different types of LC alignment at the air interface create different surface tensions. As discussed in Chapter Three, a homeotropic alignment of LC mesogens at the air interfaces creates a thin hydrophobic layer (~0.6 nm) due to the alkyl mesogen tail. Therefore, the surface tension of planar LC alignment is far larger than that of homeotropic LC alignment. The polar silicon surface is thought to induce planar anchoring, but the non-polar air interface can act to induce homeotropic anchoring. These two different surface interactions show that an LC film undergoes a transition in its orientation from surface to air. I have shown that the LC orientation of the LC homopolymer is planar near the silicon substrate and homeotropic at the air interface if the film is thicker than ca 5 nm. The results of different LC anchoring at different surfaces were consistent with the observations in various smectic LC systems, such as small molecular LC,[14-16] and LC homopolymers.[17,18] For supported diblock copolymer thin films, other researchers [1,19-21] have reported different LC alignment at different thicknesses; however, different alignment in the same film was only observed in diblock copolymers.[21]

In our polymer blend system, the surface tension of PS should be close, but larger than that of homeotropic LC alignment based on the chemical structure. The mesogens of the LC homopolymer can orient their side group homeotropic alley to the air interface, exposing only the more hydrophobic alkyl tail region to air to effectively reduce the surface energy. Therefore, we conclude that the LC block has lower surface energy at the air interface for these blended thin films.

4.2.4 Composition at the Air Interface- XPS of Lamellar Diblock Films

From Section 4.2.2 and Section 4.2.3, I determined that the LC block prefers to wet both interfaces. Based on these data, one might anticipate that the diblock copolymer would form symmetrical wetting thin films with the LC layer at both surfaces; however, this is not what we observed from the microdroplet experiment in Section 4.2.1, for which the lamellar diblock demonstrated anti-symmetrical wetting. This is due to the constraints of ordering within the confined block copolymer domains and the air interface, which play a role in these differences.

X-ray photoelectron spectroscopy was used to examine H41 PS-LC methacrylate lamellar diblock copolymer thin films with different thicknesses, as shown in Figure 4.6

and Table 4.2. Detailed fitting parameters are listed in Appendix II. No significant carboxylic peaks for any of these thicknesses are observed. This evidence suggests that a significant fraction of the PS block covers much of the air interface, even though the LC block has the tendency to be exhibited at both surfaces as, described in the previous two sections, in situations when a homeotropic alignment is preferred at the air interface. Combined with the evidence of LC wetting the substrate, the lamellar thin film should exhibit anti-symmetrical wetting as determined by the microdroplet method in Section 4.2.1.

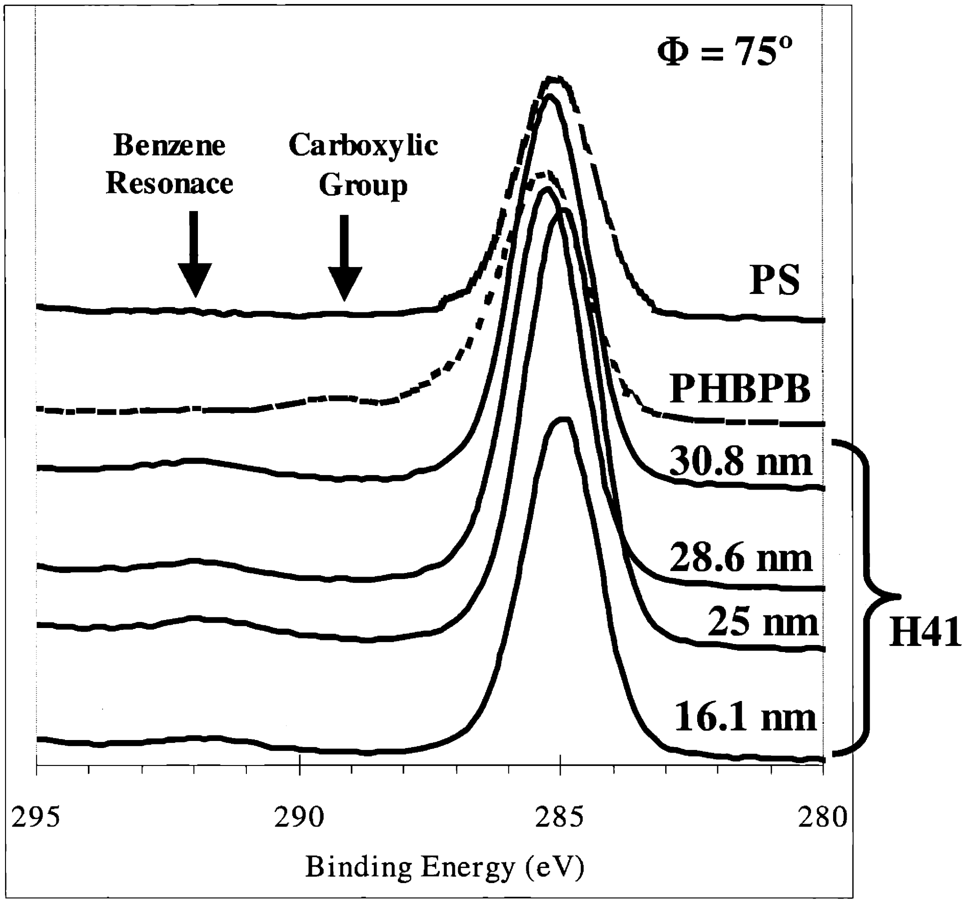

Figure 4.6: XPS analysis of films of H41 lamellar diblock copolymers at a 55° takeoff angle. PS and PHBPB homopolymers are plotted as reference.

The results seem to contradict each other: the LC block has a lower surface tension, but the PS block covers the air interface more completely. This can be attributed to the fact that different surface tensions come from different LC ordering ($\sigma_{\text{planar LC}} > \sigma_{\text{PS}} > \sigma_{\text{homeotropic LC}}$). The LC layer with homeotropic alignment has a lower surface tension than the PS layer. However, it adopts a planar anchoring and lets the PS block cover the air interface. This is because the LC block has different interactions at the two surfaces. The LC/substrate interaction induces a planar arrangement in the first layer of the film. However, planar arrangement does not present a surface tension as low as polystyrene to air. When the lamellar film is sufficiently thin, the PS block predominately wets the air interface, and a mixed surface morphology is formed. The LC layer perforates through the top PS layer due to homeotropic LC alignment at the perforation areas. The direct evidence of this mixed morphology will be shown later in TEM images.

I have also observed symmetrical wetting, in which the LC block covers both surfaces, for the same series of diblock copolymer films at higher LC ratios, including PS cylinders in the LC matrix and a smectic bilayered morphology in Chapter Five. This further demonstrates that the LC block has affinities for both interfaces compared to the PS block, although the affinity to the air interface is based on a specific homeotropic orientation. In thin films, the LC block is planar at the silicon surface and inside the film on arrangement, which does not give the lowest surface tension. Moreover, it is notable to mention that the LC mesogens adopt planar anchoring inside the film in the bulk study.[4,22] The preferred orientation of the LC mesogen with respect to the block copolymer is perpendicular, which reinforces planar arrangement. Only as we get further from the surface can we see evidence of homeotropic arrangement present in smectic terraces. When the morphology is more readily supporting homeotropic anchoring at the air interface at higher LC/PS ratios, the symmetrical wetting behavior dominates the morphology, although H41 films do not show symmetrical wetting in thicker films.

I conclude that the LC block wets the substrate and the PS block predominately wets the air interface of the LC diblock films at thicknesses of $\frac{1}{2}L_o$ to ~ $2L_o$. A detailed morphology will be further discussed by microscopic studies in the next section.

4.3 MICROSCOPIC OBSERVATION OF LAMELLAR THIN FILMS

4.3.1 Topographic Information from AFM Images

Atomic Force Microscopy (AFM) was used to directly observe the thin film surface topography. Surface topologies with holes or islands (depending on the overall film thickness) were observed, as shown in Figure 4.7. Based on the block copolymer concepts mentioned in Chapter One, film thicknesses with exact (n+½) L_o formed a flat hole-free top surface for anti-symmetrical wetting films. Hole defects of L_o depth were exhibited when the average film thickness fell between n L_o and (n+½) L_o. In Figure 4.1a, the average film thickness of 21.2 nm (~1.2 L_o), measured by ellipsometry, fell between L_o and 1.5L_o, and holes were observed as expected. The theoretical area ratio of holes at 1.2 L_o is 30%, which agrees with the experimental observation. Similar observations of isolated islands of L_o height were formed at thicknesses from (n-½) L_o and n L_o. In Figure 4.1b, islands appeared for the overall film thickness of 16.1 nm (~0.9 L_o, between ½L_o and L_o). The theoretical area ratio of islands at 0.9 L_o is 40%, which also agrees with the experimental observation. Hole (or island) structures have been reported in Section 1.3.2 for general diblock copolymer thin films.[7,8] On the top of this plateau, the surface contains irregularly shaped ribbons of material on the surface (Region III), which are consistently 2.7-3.5 nm thick. All of these films with thicknesses larger than ½L_o exhibit these submicron-scale terraces of exactly one LC smectic layer (s_o = 3.5 nm) in height, suggesting the presence of a single smectic layer atop the polymer-air interface. The smectic layer thickness at the air interface may be lower than that in the bulk because of mesogen tilting.

From AFM images in Figure 4.7, films are divided into three regions in heights as labeled in the figure, including the bottom of holes (Region I, thickness = ½L_o), the top plateau (Region II, thickness = 1½L_o), and the smectic terraces on the top of the plateau (Region III, thickness = 1½L_o + s_o). The underlying bottom layer has a height of ½L_o thickness (Region I), as measured by AFM on a scratched sample. The top plateau of the film (Region II) displays holes with a depth equal to approximately 17.8 nm, which is close to the block copolymer lamellar periodicity (L_o = 17.3 nm).

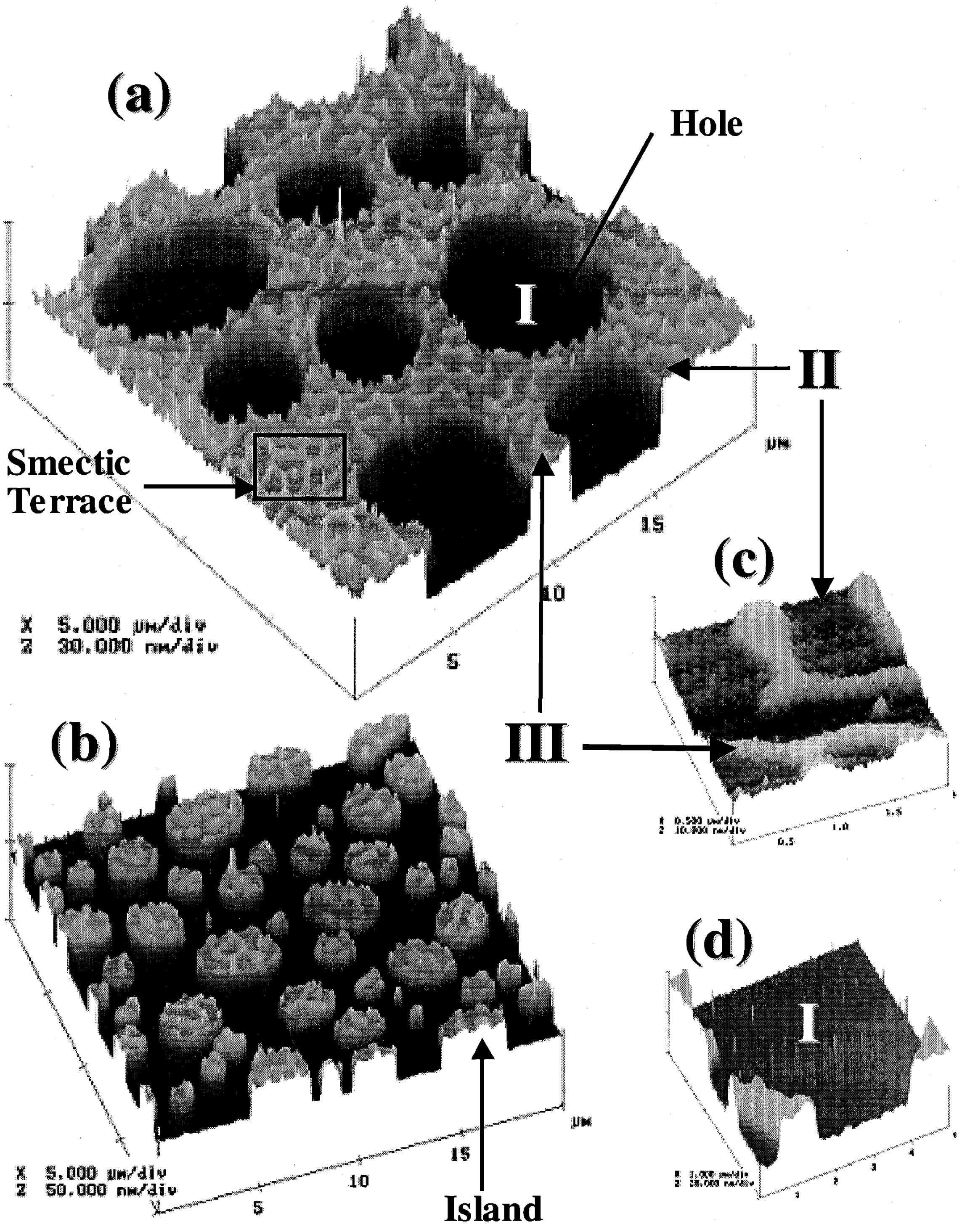

Figure 4.7: AFM images of H41 lamellar diblock copolymer thin films with (a) hole defects; (b) island defects; (c) scanning of the highest surface in (a); (d) scanning of the lowest surface in (a).

The terrace structure of Region III appears to be a single homeotropic LC layer on the top film surface. It is uniformly distributed and has self-oriented ordering at the air interface with micron scale width (~ 0.25 μm), which is notably larger than the block copolymer periodicity (~20 nm) and the smectic LC layer thickness (~3 nm). While scanning smaller regions (5*5 μm^2) in different areas of the film, it was determined that the smectic terraces only appeared on top of the plateau (Region II) in Figure 4.7c, but not on the bottom of holes (Region I) in Figure 4.7d. We first reported this smectic LC terrace at the air interface,[21] when the films were annealed at 130 °C above both Tgs ($Tg_{,PS}$ ~ 100 °C and $Tg_{,LC}$ ~ 40 °C) for a week. These terraces only exist above a specific film thickness of ½L_o. If the films are thinner than half L_o (0.3-0.5 L_o), they simply dewet and are not able to form smooth films, since the LC molecules have a tendency to pack together in clusters or aggregates. If the films are too thick (larger than 4 L_o), the film thickness damps out the influence of the surface. The topography is not as well defined due to the substantial distance between the substrate and the air interface, and the loss of the influence of the silicon surface on the LC and block copolymer ordering. The development of surface-directed spinodal composition waves for thicker films may also affect the topography. These two cases will be further discussed in detail later in this chapter.

Calculation of Surface Coverage from AFM Images

AFM analysis can be used to get information about the depth profile and the surface coverage. The AFM topography and the cross-sectional view are shown in Figure 4.8a. This film contains all three regions. The depth profile is shown in Fig 4.8b with three clear peaks. The height difference between top and middle peaks is around 2.8 to 3.1 nm, corresponding to the top smectic terrace height (s_o). The height difference between middle and bottom peaks is around 17.2 to 18.7 nm, and it represents the depth of holes (L_o). The area of each peak was calculated. The top first peak (smectic terraces) covered around 13% of the whole film surface including holes in this sample. I also evaluated the ratio of the smectic terraces on a hole-free area from the small box in Figure 4.8a, which yielded around 24 to 29% surface coverage of the top plateau surface. Specifics on the depth profile are valuable to the surface analysis and constructing a model for complex thin film morphologies.

The surface coverage measured from AFM agrees with that calculated from the average film thickness (ellipsometry). For example, the surface coverage of holes of a 1.2 L_o thick film (Figure 4.7a) is around 30% from both AFM and ellipsometry. The surface coverage of islands of a 0.9 L_o thick film (Figure 4.7b) is around 40%.

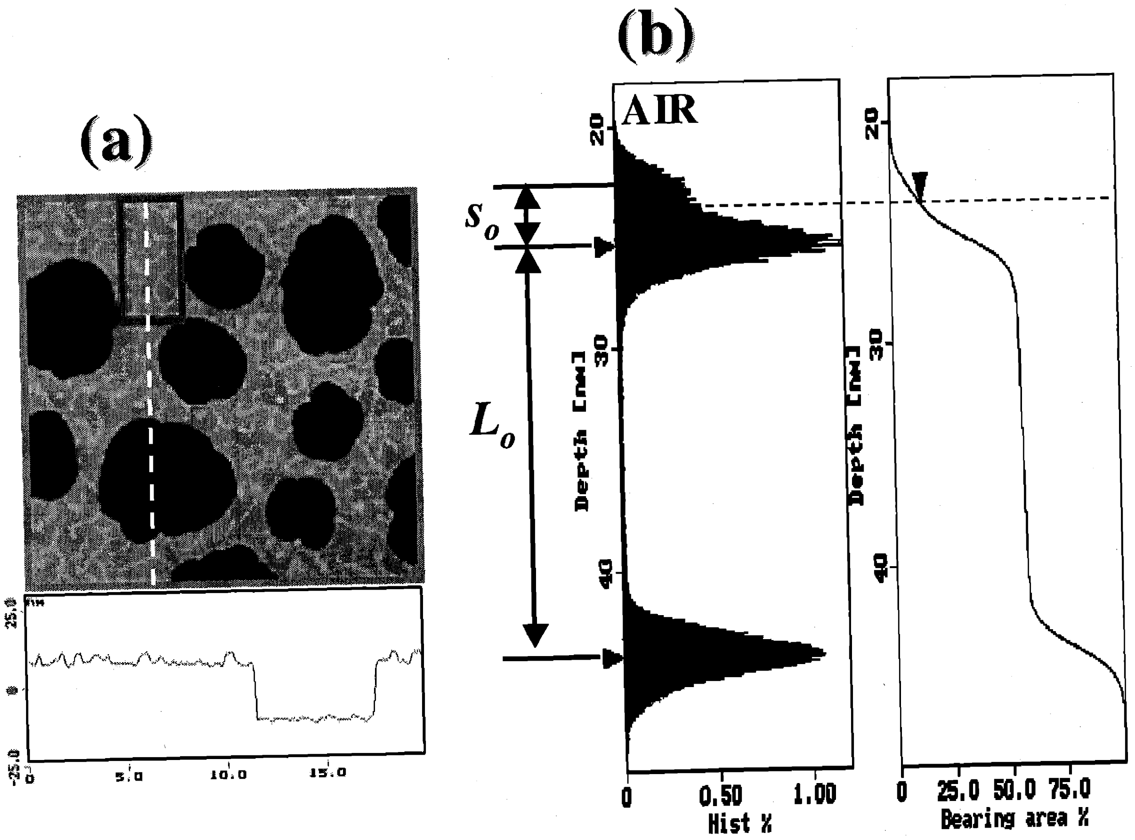

Figure 4.8: Calculation of surface coverage from AFM images of a H41 diblock copolymer thin film.

4.3.2 Compositional Variation from Top-view TEM Micrographs

Transmission Electron Microscopy (TEM) was used to directly observe the compositional variations of the film. The image contrast came from the thickness difference and the compositional variations. Thicker parts were darker because fewer electrons could penetrate through the film. The more electron-dense materials deflected more electrons, making the image appear darker. Heavy metals were used in some cases to selectively stain one block to increase the contrast. In this series of PS-b-PLC diblock copolymers, RuO_4 was used to stain the PS block in this experiment as described in Section 2.7.2. Studies of the bulk block copolymer films at various block ratios have shown that the PS block stained preferentially over the LC block,[6] although both blocks would undergo staining after exposure to RuO_4 for a long time.

Top-view TEM images of thin films here reveal a complex morphology, in which the PS and LC blocks coexist in Region I and II. Figure 4.9a and Figure 4.9b are complementary TEM images of stained films (21.2 nm and 16.1 nm), corresponding to AFM images in Figure 4.7a and 4.7b. The analogous regions (I, II, and III) are labeled. Dark regions indicate PS domains in these two images. Thickness variations in different regions are directly observed, including holes, islands, and top smectic terraces. We can also see that the block domains in Region II are larger than the domains in Region I.

Figure 4.9c shows an unstained TEM image with an island structure. The LC block has a higher density (1.154 g/cm³)[4] than the PS block (~1.045 g/cm³),[4,23] yielding a higher contrast (darker) in unstained thin films. The high electron density of the three packed aromatic rings in each LC side-chain is greater than that in the amorphous PS phase, in which there is only one benzene ring per styrene. The selective staining on the PS block has been studied in bulk state for the same series of diblock copolymers.[4,6,22,24,25] These independent studies included comparative staining experiments of each homopolymer, and staining of a series of diblocks at different volume fractions. From AFM studies, Region I is a half lamellar layer (½ L_o, ~ 8.6 nm) in anti-symmetrical wetting films. At the bottom level (Region I), the figure clearly illustrates isolated regions of LC blocks (darker regions) immersed in a continuous PS matrix (lightest regions), suggesting that the LC block perforates the top PS layer. The perforated dots (~ 8.6 nm diameter and ~ 6.8 nm² area) are really small compared to the surface, so the XPS cannot detect the COO signal. Other researchers [26,27] have shown that sub-monolayer films can exhibit laterally ordered polymer micro-domains. More recently, perforations or columnar structures were observed to occur in lamellar PS-poly(n-alkyl methacrylate) copolymer systems [13,28] and in PS-b-poly(methyl methacrylate) films.[9,10] In Figure 4.9c, these tiny circular regions are approximately ½L_o in diameter and are randomly dispersed. These ½L_o perforations were previously predicted by simulations,[5,28,29] and reviewed in Chapter One. The top plateau of the film (Region II) consists of larger dark LC domains, which are larger than the black dots (LC perforation) in Region I. The heterogeneous PS dense areas provide information on horizontal compositional variations. In Region III, large, sub-micron-sized terraces form puddle-like areas of height s_o on the film surface as shown in the AFM images. The height suggests that the terraces are composed of one homeotropic smectic layer at the air interface. The width of these strips is around 2.5 μm. There is no LC perforation in Region III, as is evident from the TEM images, which are flat and untextured in this region. In addition, on the top surface, the LC block is able to form a separate homeotropic layer to minimize the surface free energy, as the homeotropic LC block has lower surface energy than the PS block. However, the surface-terracing phenomenon does not happen in the bottom area (Region I), which directly contacts the silicon surface. The plan-view TEM micrographs offer us information of compositional variations through the film and the LC perforation density in different regions.

In order to make sure I did selective staining on the PS block, further evidence can be seen in these samples. The H41 diblock copolymer contains 37.5 vol % of LC and 64.5 vol % of PS. Therefore, the PS block should occupy more area than the LC block in plan-view TEM images. Both Figure 4.9b (stained) and Figure 4.9c (unstained) show the island structure. In stained samples, the PS block was selective stained by RuO_4. When both island areas were compared (Region II), the stained sample (Figure 4.9b) had dominant black areas, whereas the unstained sample (Figure 4.9c) had dominant white areas. These two images are thus reversed. Therefore, the darker region is the stained PS block.

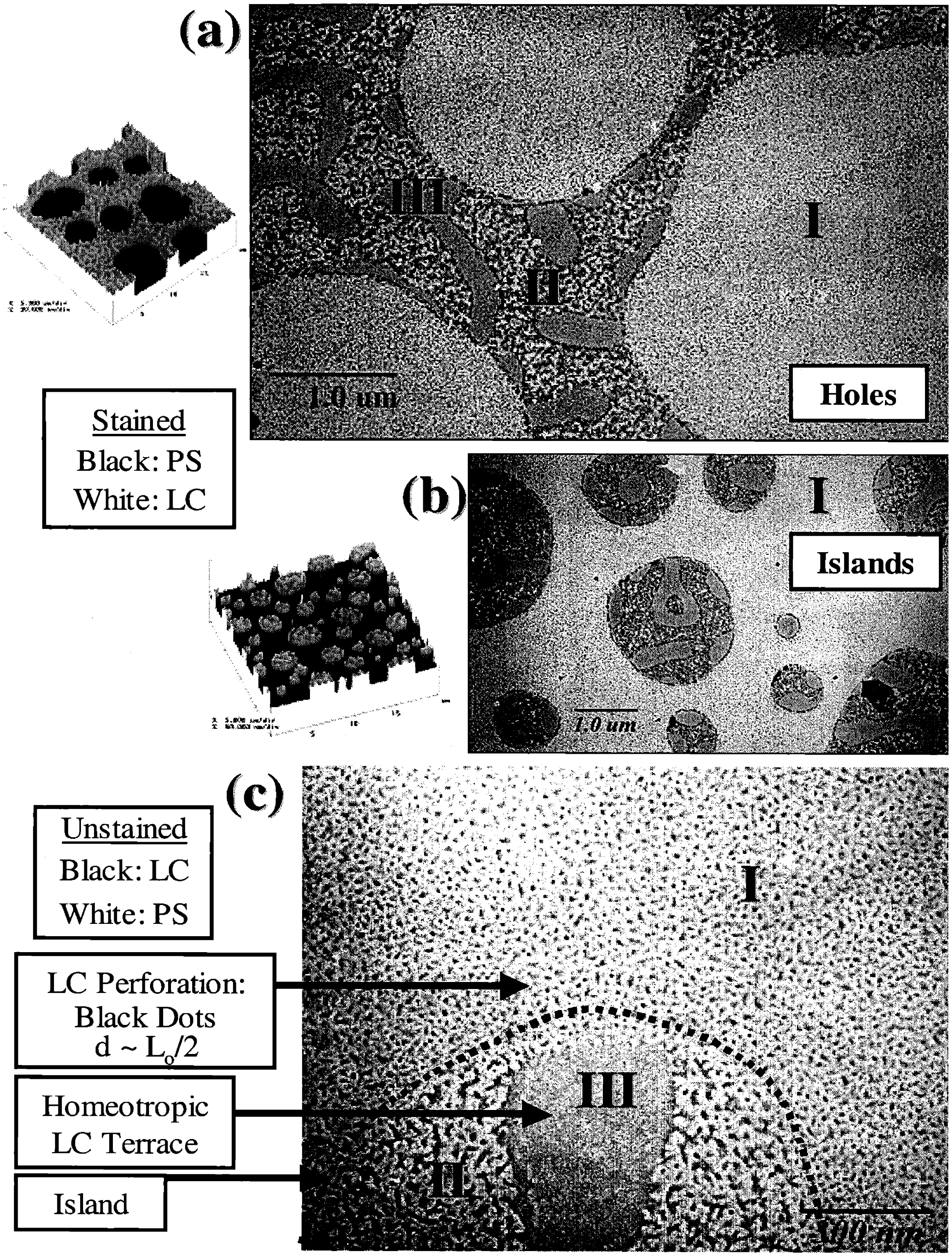

Figure 4.9: TEM micrographs of H41 lamellar diblock copolymer thin films with (a) stained hole defects; (b) stained island defects; (c) unstained island defects.

4.3.3 Vertical Profiles from Cross-sectional TEM Micrographs

Cross-sectional TEM micrographs can offer direct evidence of the vertical film profile. The TEM samples examined in plan-view were further processed to obtain a cross-section [5,28] as described in Section 2.7.2. A multi-layered model for the cross-sectional TEM samples is shown in Figure 4.10a. The whole system included the polymer film, carbon layers on top and bottom, the TEM copper grid, a possible tiny residual poly(acrylic acid) (PAA), and the epoxy matrix. Samples were observed using high-resolution TEM.

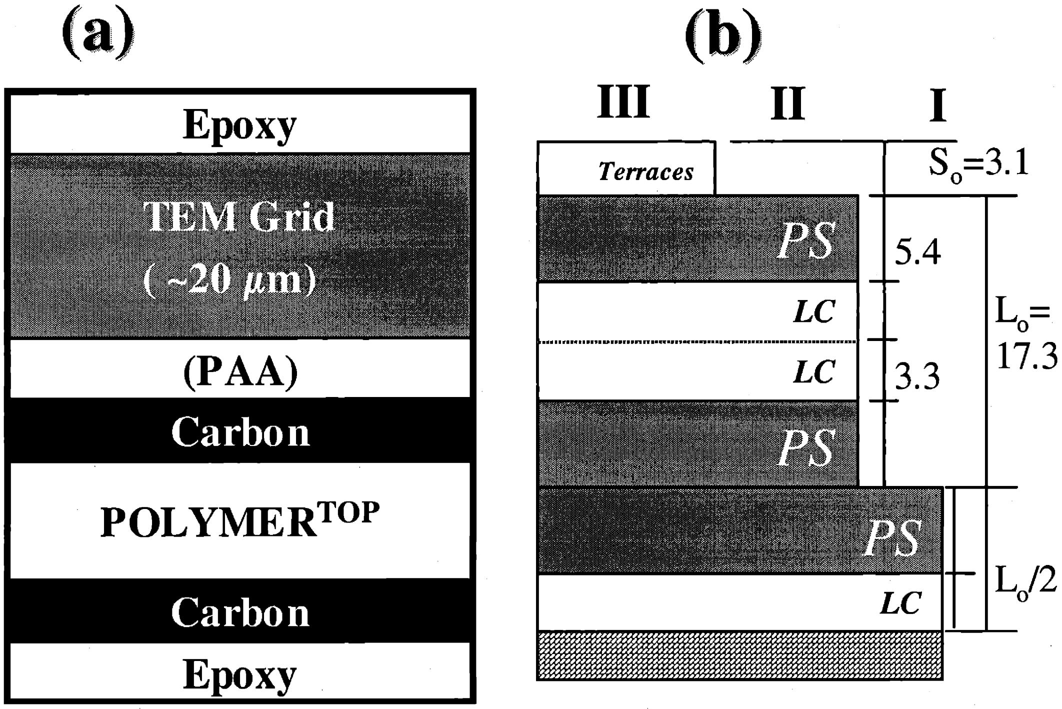

Figure 4.10: (a) A multi-layered structure of cross-sectional TEM samples; (b) Model marked with theoretical thickness of each layer in the cross-sectional view. The unit for length used in this figure is nm.

A simple schematic thin film model of anti-symmetric wetting was drawn in Figure 4.10b to provide perspective regarding the layer sequence and the thickness of each layer. The layer thicknesses were calculated based on the volume ratio of two blocks. A full lamellar layer ($L_o = 17.3$ nm) consisted of two LC layers (3.26 nm each) and two PS layers (5.4 nm each). The perforation structure of the film was not shown here for simplicity. The three regions defined previously were also labeled.

The cross-sectional TEM images in Figure 4.11a and Figure 4.11b demonstrate the morphological vertical profiles of Region II (1½ L_o). These images indicate that an interconnected morphology is present within the layers. The PS block with RuO_4 staining appears gray and the LC block appears white in contrast. The black layer was the carbon-protecting layer. Figure 4.11a is the image taken from the non-perforation area. The LC layers and PS layers arrange alternately to each other and parallel to the substrate. Figure 4.11b shows that the central LC layer is sandwiched by two gray PS layers. A thin PS layer covers the air surface. This is similar to Figure 4.11a, but the central white LC layer is not continuous. The gray PS block penetrates through the parallel LC layer, connecting two PS layers. This observation is important, as this incident cannot be observed in other experiments, and it indicates a displacement of the LC block by the PS block. The cross-sectional TEM data give direct evidence of the morphology inside the film and helps to construct the model in the next section.

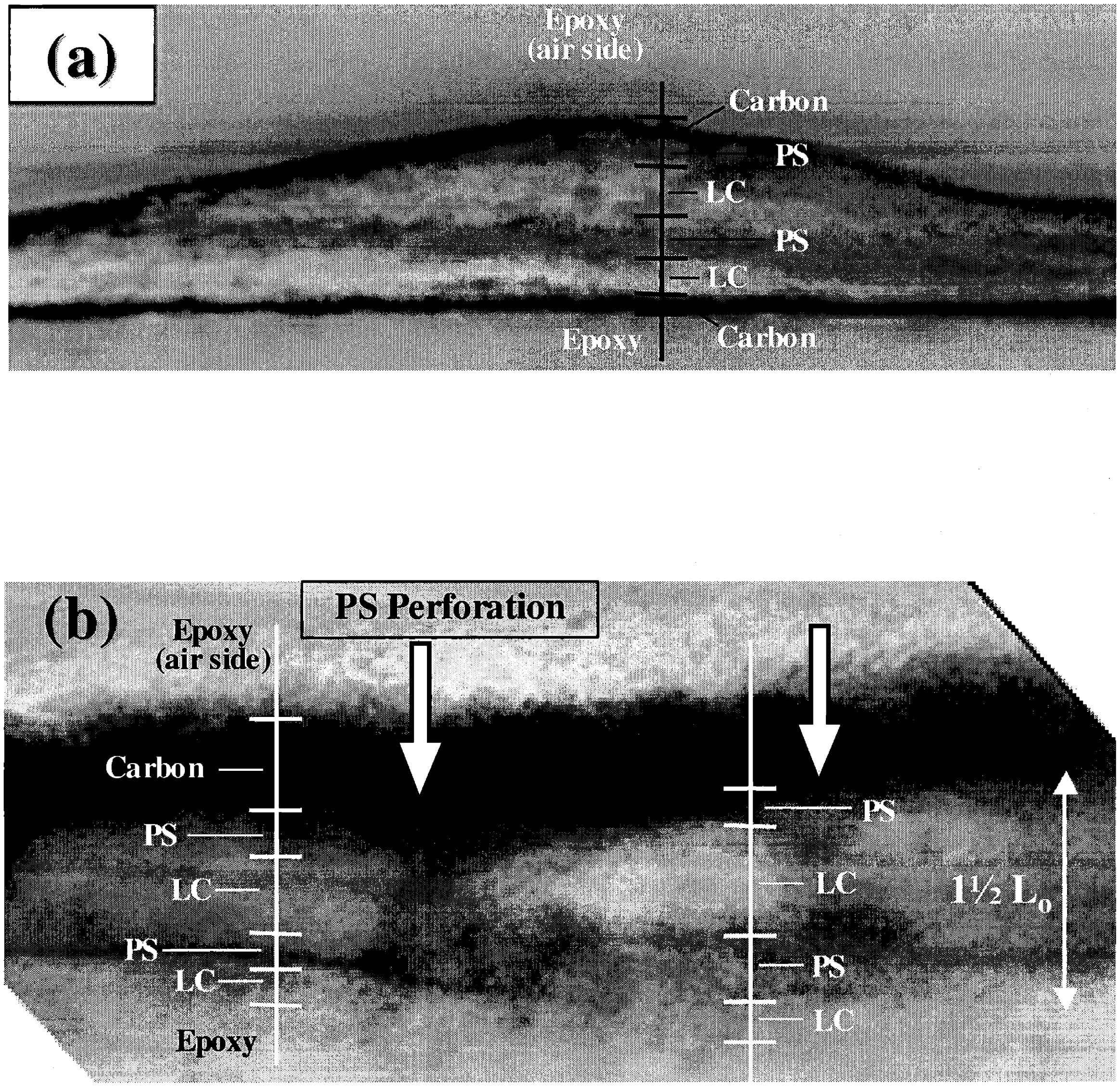

Figure 4.11: Cross-sectional TEM micrographs of H41 lamellar diblock copolymer thin films at Region II. Images of (a) and (b) are taken at different films of the same material.

4.4 PROPOSED MODEL OF LAMELLAR DIBLOCK COPOLYMER THIN FILMS

4.4.1 Proposed Model of Lamellar Diblock Thin Films

A proposed model of this complex lamellar thin film is shown in Figure 4.12. This model combines all of the above observations. It can be divided into three regions. Region I is a single monolayer of ½L_0 height. Region II has the height of 1½L_0. Both regions show anti-symmetrical wetting. Region III shows two full lamellae with symmetrical wetting.

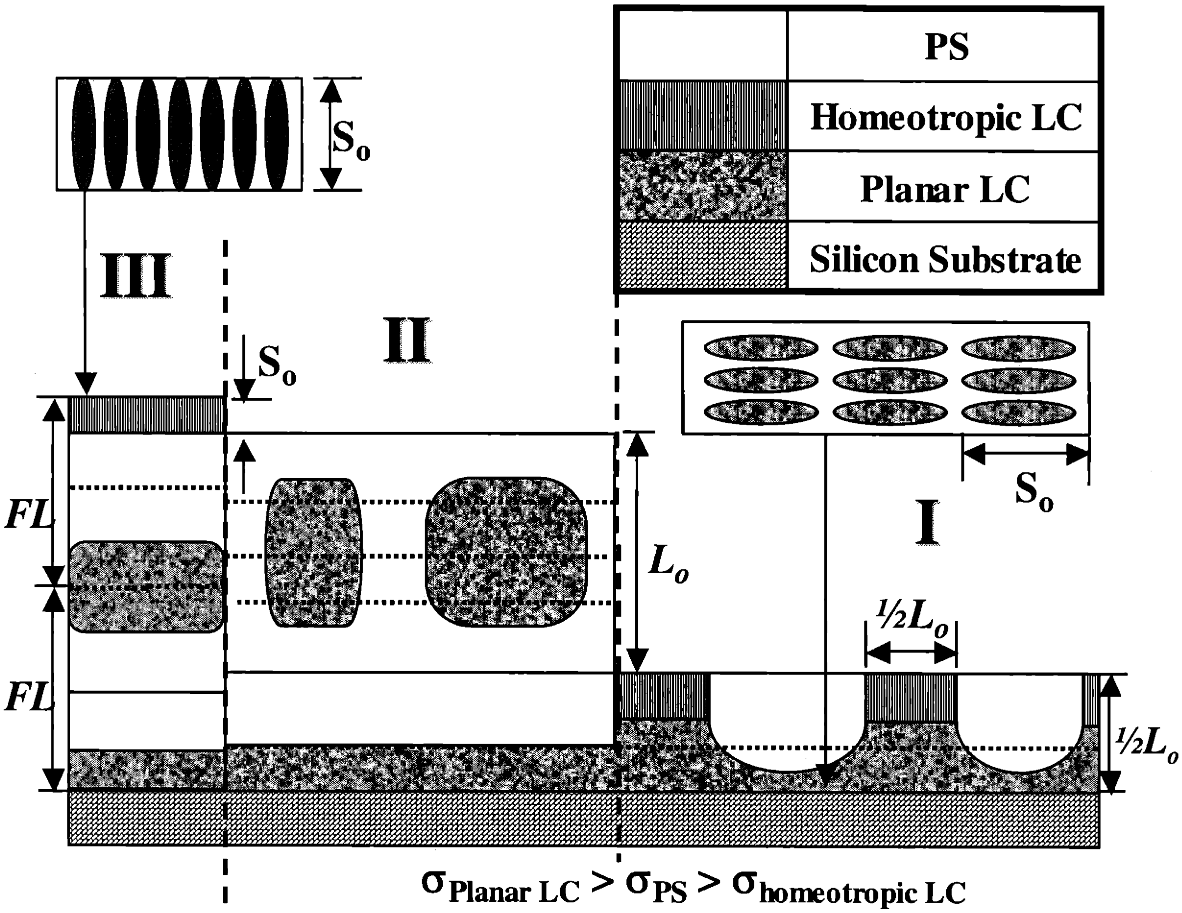

Figure 4.12: Model of lamellar LC diblock copolymer thin films.

In Region I (0.5 L_0 thick), the LC block wets the silicon surface, and the PS block predominately wets the air interface, with random perforations of the LC layer. The ½

L_o perforation structure of general amorphous-amorphous diblock copolymer thin films (ex. PS-PMMA [28]) has been reported theoretically [29] and experimentally [13] as a hybrid structure. It has also been reviewed in the background section of Section 1.3.2 and Figure 1.3. This work includes the first report of this structure in a complex side-chain LC-containing diblock copolymer system.[21] It is believed that the LC phase actually stabilized this structure due to its dual wetting characteristics. The lamellar morphology of this diblock copolymer prefers this planar arrangement to the interface in the bulk state, as shown in Figure 2.1c. Planar LC anchoring was favored at the silicon substrate based on its chemical structure and dipole moment calculation in Chapter Three, but was not favored at the air interface. The PS block wets the air interface if LC mesogen anchoring can stay planar. However, if homeotropic arrangement is possible, wetting of the air interface with the LC phase is favorable.

Figure 4.13 illustrates a schematic model of the perforation for the LC containing diblock copolymers at Region I. The LC mesogens are anchored planar to the substrate and block copolymer interfaces. The perforation here allows homeotropic LC alignment when it is exposed to the air interface. This perforation is stabilized when the LC mesogen has a non-polar end and prefers homeotropic anchoring to the air interface as displayed in the structure we have presented. The perforation lowers the overall energy by exposing the mesogen tail, which has lower surface tension (σ) than the PS.

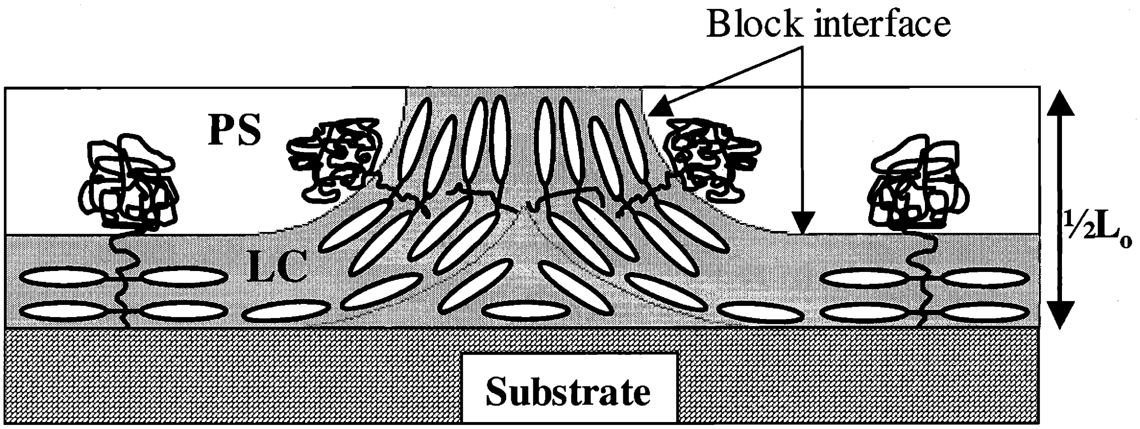

Figure 4.13: A model of the bottom LC layer perforates through the PS layer in Region I. Orientation of LC mesogens switches from planar near the substrate to homeotropic at the air interface.

The plateau regions (Region II) in Figure 4.2 of the film were 1½ L_o thick and islands (or holes) with L_o depth were observed by AFM. Coarser LC domains were observed from top-view TEM images in Figure 4.9, while the substrate effect was damped out, according to previous cross-sectional TEM analysis. The LC layer inside the film was not continuous and was interrupted by perforations of the PS layer. The upper LC layer was no longer anchored to a silicon surface, and was more able to rearrange due to the lowering of the surface constraints. However, the diblock lamellar period was still perpendicular to the substrate surface due to the surface effects. For this reason, there were larger regions over which the LC block maintained a planar arrangement with the diblock lamellae, as preferred in bulk state, and the PS block, having lower surface tension, covered the air interface.

In Region III, large LC regions appear at the top of the plateau, where the LC mesogens are able to switch their orientation to create a homeotropic smectic top layer. This top layer with homeotropic LC arrangement has the lowest surface tension with air, due to the low surface energy provided by the alkyl tails at the ends of the mesogens. The top homeotropic terraces consist of one parallel smectic layer in which the mesogens are perpendicular to both air and block copolymer interfaces, as shown in Figure 4.12. It is noted that this layer might consist of a more tilted smectic C phase than that observed in the bulk, as the values of the terrace spacings are lower than s_o by 0.5-0.7 nm. This structure is favorable despite the energetics involved in the relative orientation with the diblock lamellae (less favored homeotropic arrangement).

From Figure 4.12, the film in this region forms two 'suppressed' symmetrical-wetting full lamellae (FL), to maintain the block periodicity. There is no perforation in this thickest region. The volume fraction of the LC block of this sample is ca. 38-vol % and the lamellar periodicity (L_o) is 17.3 nm. The anticipated size of the LC domains is ca 6.8 nm, which are approximately two smectic layers ($2\ s_o = 7$ nm). Because the LC block can exhibit lower surface tensions at both surfaces, the film forms symmetrical wetting while homeotropic orientation predominates at the air interface in the absence of a strong substrate effect. This suppressed full lamellar structure in Region III still roughly keeps the bulk period dimension. The thickness of films in Region III is 1½ L_o plus 1 s_o (= 29.45 nm), which is ca 85% of two full lamellar layers ($2\ L_o = 34.6$ nm). A substrate-supported diblock copolymer thin film can keep the FL structure at this thickness. The simulation results in Figure 1.3c show that a full lamellar structure exists from 0.7-1 t/L_o at R=0 and from 0.3-1 t/L_o at R=1, where R is defined as the affinity ratio of the B block to the air interface and the substrate ($R = S^B{}_{air} / S^B{}_{substrate}$).[13] Hence, 85% of two FL thicknesses are sufficient to remain a FL thin-film morphology based on similar explanations. The flat block interface of the FL structure also reduces the energy required to create new surfaces for a perforated structure as shown in Region I. While a homeotropic layer has formed at the air interface, there is no driving force for perforations.

4.4.2 Confirmation of Model by X-ray Specular Reflectivity (XSR)

X-ray specular reflectivity (XSR) has been used to confirm the model. The XSR is only sensitive to the electron density variation in the surface normal direction. This is useful to probe the vertical profiles of thin polymer films. The theory and experimental parameters of XSR experiments have been described in both Chapter Two and Chapter Three.

A lamellar diblock thin film without holes or islands (only Region II and III) was selected to conduct this XSR experiment. The thickness was 26.8 nm (~1.55 L_o) as determined with an ellipsometer, and the roughness was ca 1.33 nm as measured by AFM. Figure 4.14 shows XSR data, fitting curves, and three different models. Fitted layer thickness and scattering length density (SLD) are listed in Table 4.3.

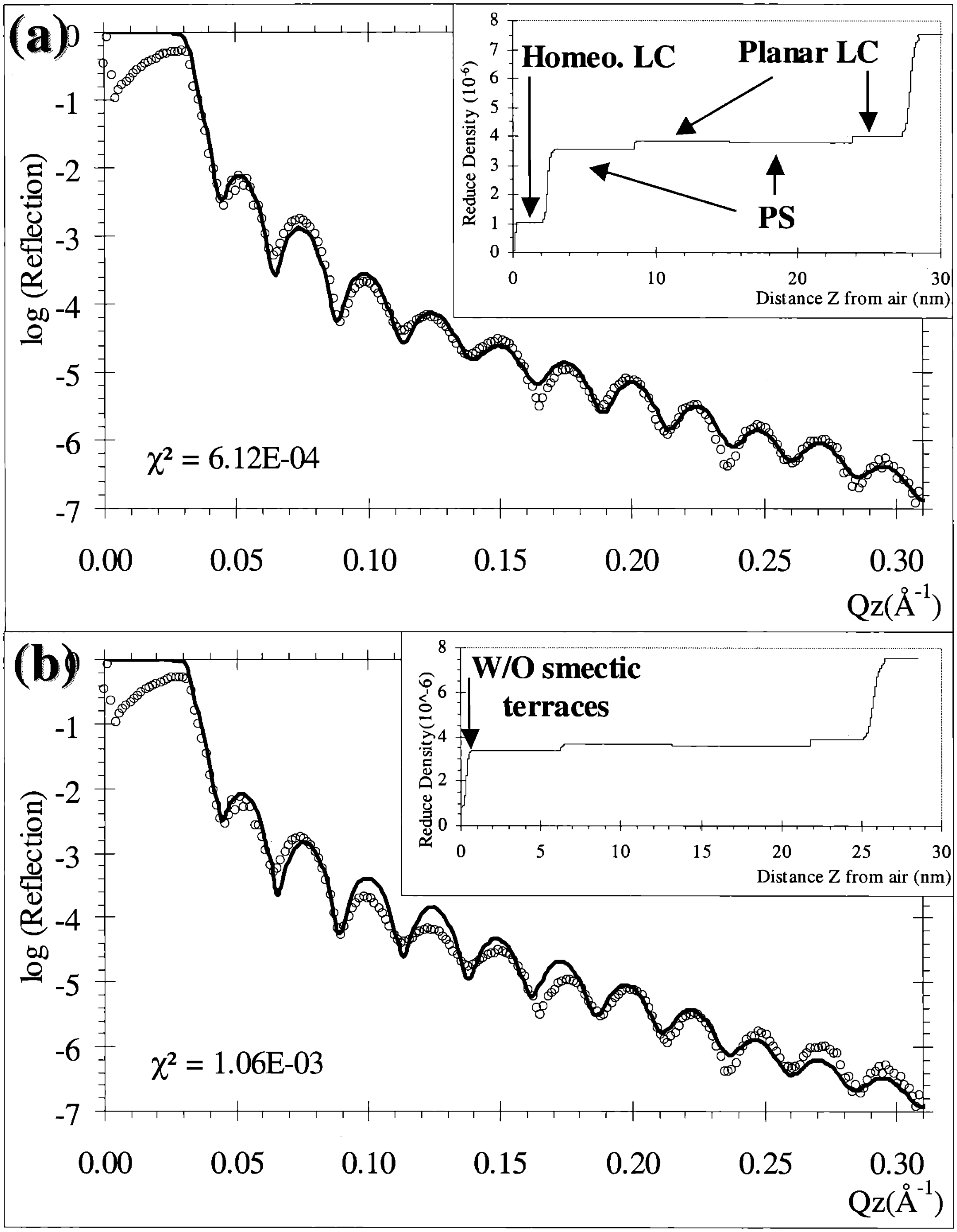

Figure 4.14: X-ray specular reflectivity data {○} and the fitting curve of a H41 lamellar diblock copolymer thin film. The insert is the electron density model used to fit the curve (a) model with layer structure; (b) model with only incomplete surface smectic terraces.

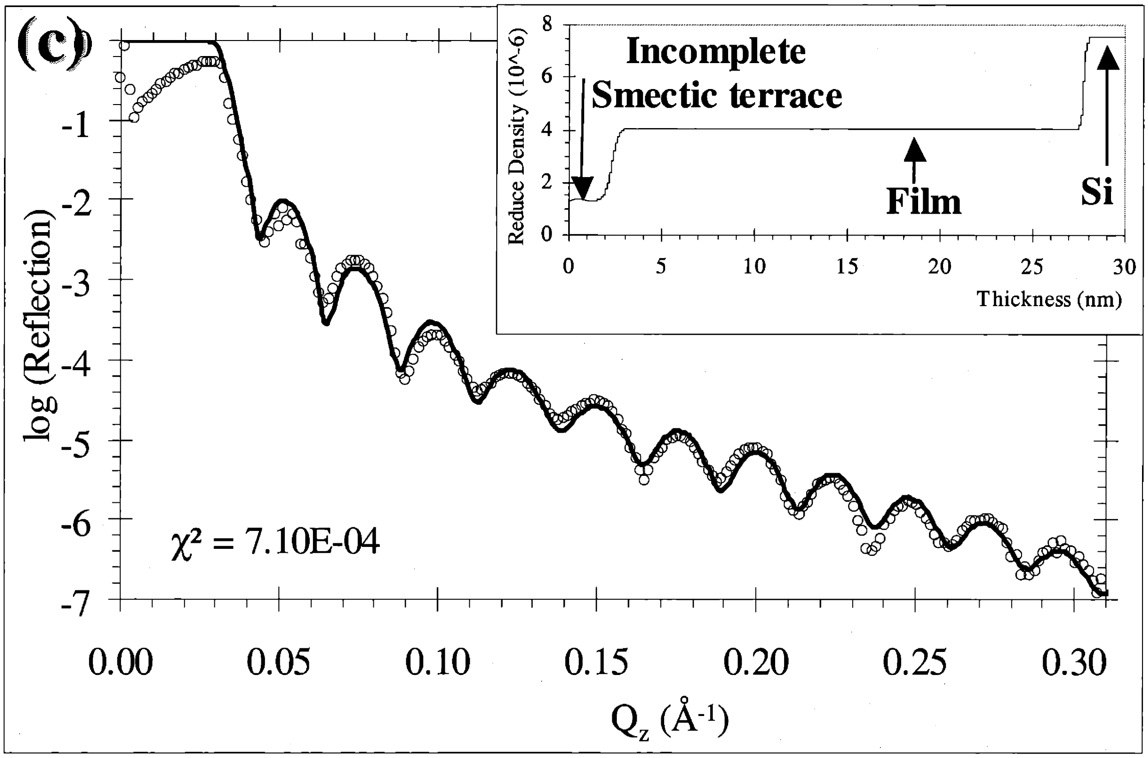

Table 4.3: Estimated and fitted layer thicknesses of a H41 lamellar diblock copolymer thin film from XSR data.

	Layer #	**1**	**2**	**3**	**4**	**5**	
	Layers	**Homeo-tropic LC**	**PS**	**Parallel LC**	**PS**	**Parallel LC**	**Overall**
Calculated	**Thickness (nm) (1.5 L_o + s_o)**	~ 3	5.28	6.75	10.55	3.37	28.95
	SLD (Å^{-2})	1.05E-5	9.82E-6	1.05E-5	9.82E-6	1.05E-5	-
XSR Fitted	**Thickness (nm) in Figure 4.14a**	2.44	6.11	6.61	8.71	4.62	28.47
	SLD (Å^{-2})	2.70E-6	9.34E-6	1.02E-5	9.99E-6	1.06E-5	-
	Thickness (nm) in Figure 4.14c	2.44	26.01				28.45
	SLD (Å^{-2})	3.39E-6	1.05E-5				-

Figure 4.14a shows the XSR data, the fitting curve, and the model. The model was assigned with different electron densities for each layer inside the film, including a homeotropic LC layer, PS layers, and planar LC layers. Detailed fitting parameters are tabulated in Appendix III. The mesogen layer has a higher electron density than the PS layer. Higher electron density at the center of the smectic layer is attributed to the packing of the LC side chains and the increased electron density of the three aromatic rings in the mesogen. According to the fitting results, the electron density of the middle planar LC layer (Layer 3) is lower than the bottom planar LC layer (Layer 5) due to the perforation of the PS block in this non-continuous LC layer, as shown previously in the model and cross-sectional TEM images. The electron density becomes lower after averaging with PS perforations, which has a lower electron density. The low density of the top smectic terraces (Layer 1) is due to the incomplete surface coverage. The electron density ratio of a full LC layer (Layer 5) to the smectic terraces (Layer 1) in this fitting was around 3.8, which represented the smectic terraces covering 21% of the air interface. This result agrees with the AFM analysis.

Figure 4.14b shows the fitting curves of the model without the top smectic terraces. The fitting result is poor, and this confirms the importance of the smectic terraces to the model. Figure 4.14c shows the fit using the model without electron density variations within the film. The fit looks similar to the multi-layer model in Figure 4.14a; however, we have shown from other experimental evidence that paralleled lamellar stacking existed inside the film, with PS perforations. It is not surprising that the XSR results do not change much with the introduction of the PS/LC layers; the high degree of perforation lowers the electron density differences among layers. In Figure 4.14c, the electron density ratio of the film to the smectic terraces in this fitting was around 3.1, which shows that the smectic terraces covered 24% of the air interface.

The theoretical calculated and data fitted layer thicknesses for these two models are listed in Table 4.3. The fitting thicknesses are close to theoretical estimated values, except for the bottom PS layer (layer 5). The overall film thicknesses are 26.8 nm from ellipsometry, 28.95 nm from calculation (1.5 L_o + s_o), and 28.47 nm (~1.65 L_o) from XSR data fitting. The fitting model agrees with the vertical profile of our proposed model. The homeotropic LC terraces (Layer 1) were thinner than calculated because of mesogen tilt. The PS layer (Layer 4) is thinner in order to compensate for the perforation in the LC layer on top of it (Layer 3).

4.4.3 XPS Analysis of Different Regions

In this section, we focus on specific topologies (regions) using XPS. Figure 4.15 shows the AFM images (20 * 20 μm^2) of H41 lamellar diblock copolymer thin films with three different topologies, including a film with islands (Figure 4.15a, with Regions I, II, III), a film without islands or holes (Figure 4.15b, with Regions II, III only), and a ½L_o thick film (Figure 4.15c, with Region I only). Figure 4.16 shows the XPS results for these three types of films. The results are listed in Table 4.4 and Appendix II. Figure 4.16a is the XPS data collected at the 15°-takeoff angle. The detector was set 15° to the film surface normal. Figure 4.16b was measured at the 75°-takeoff angle (glancing angle).

XPS data in Figure 4.16a for both 15° and 75° takeoff angles, were measured from a thin film with islands and smectic terraces on top of the plateau, as shown in the AFM image of Figure 4.15a (Regions I, II, and III). There was no significant COO or CO peak at both angles, as discussed in Section 4.2.4 (Figure 4.6 and Table 4.2). The PS block predominately covered the air interface, while the LC mesogen adopted planar anchoring. The PS surface layer was thicker than 5 nm. XPS data in Figure 4.16b were measured on a thin film without islands or holes, as in the AFM image of Figure 4.15b. Smectic terraces were uniformly distributed at the top surface and covered around 25% of the areas. There was still no significant COO or CO peak in both 15° and 75° measurements. The PS block covered most of the air interface for Regions II and III.

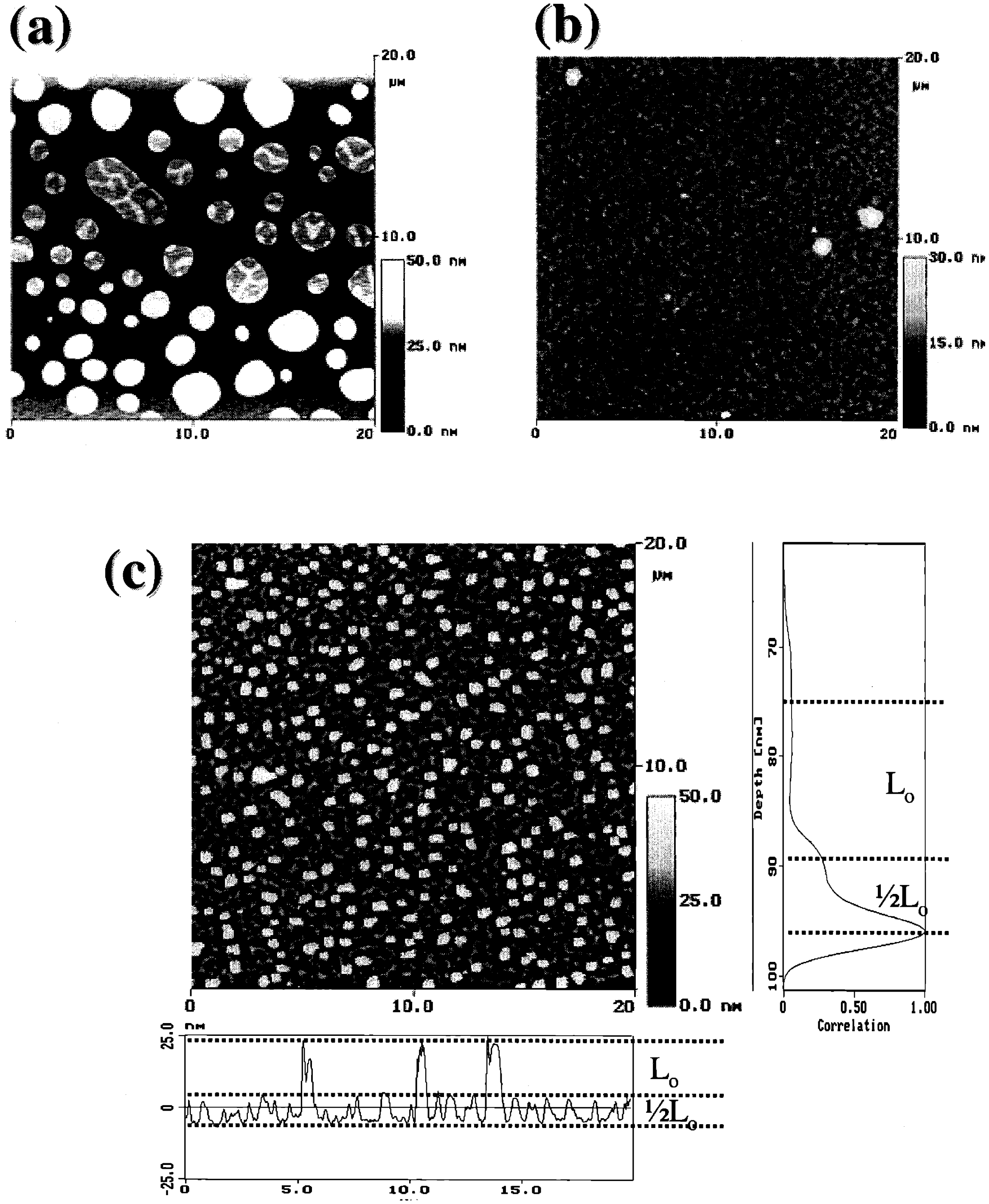

Figure 4.15: AFM images (20*20 μm^2) of H41 lamellar diblock copolymer thin films with different topologies and thicknesses (a) a 30.8 nm (1.78 L_o) film with islands and top smectic terraces; (b) a 28.6 nm (1.65 L_o) film with only smectic terraces (without holes or islands); (c) a 8.5 nm (0.49 L_o) dewetted film with ½ L_o and 3/2 L_o layers.

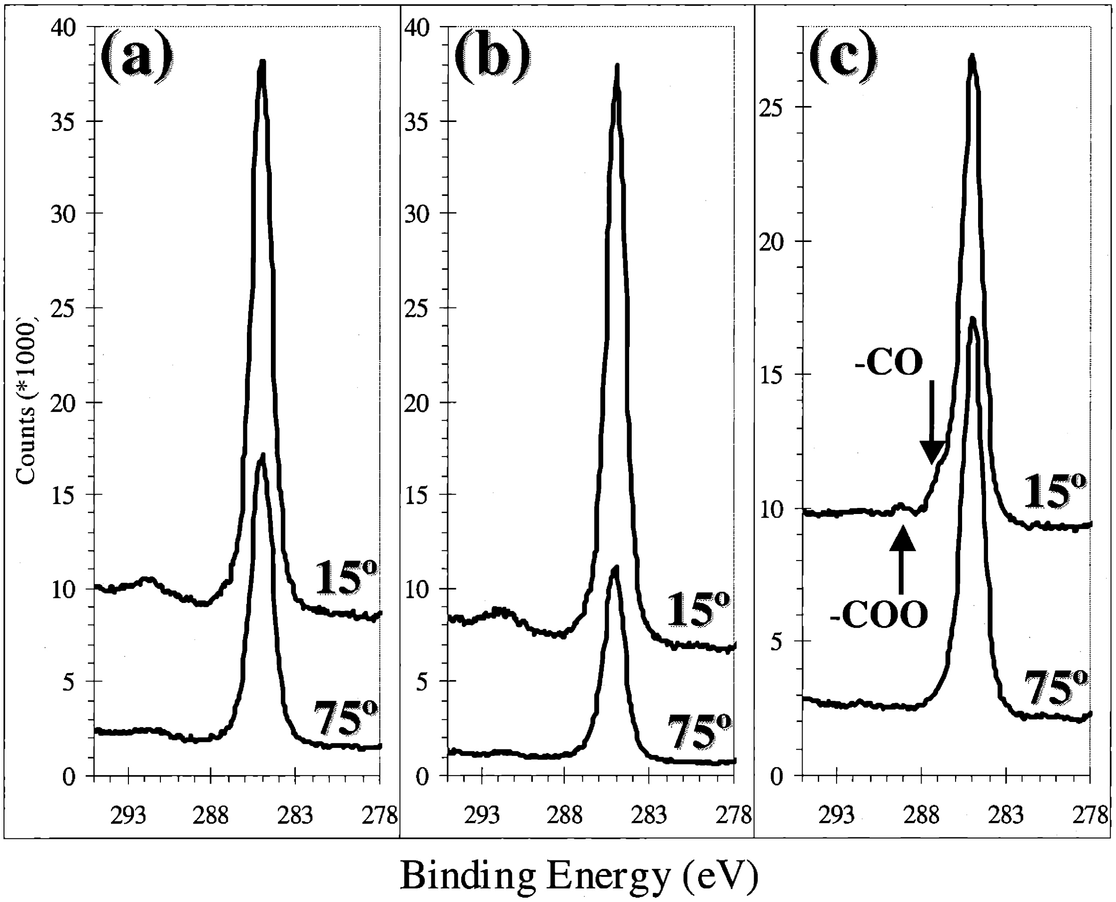

Figure 4.16: XPS spectra of H41 lamellar diblock copolymer films at 15° (close to the surface normal) and 75° (glancing angle scan) takeoff angles, with different topologies corresponding to the AFM images of (a) Figure 4.15a with Regions I, II, and III; (b) Figure 4.15b with Regions II and III; (c) Figure 4.15c with Region I only.

Table 4.4: XPS fitting ratios at two takeoff angles (15° and 75°) of H41 diblock copolymer thin films with three different topologies.

Sample	Thickness	Peak	15° Peak Area (%)	75° Peak Area (%)
Figure 4.15a, 4.16a (Regions I / II / III)	30.8 nm 1.78 L_o	CH / C	97.1	97.7
		CO	**2.9**	**2.4**
Figure 4.15b, 4.16b (Regions II / III) No hole or islands	28.6 nm 1.65 L_o	CH / C	96.3	96.6
		CO	**3.7**	**3.5**
Figure 4.15c, 4.16c (Region I)	8.5 nm 0.49 L_o	CH / C	89.8	94.6
		CO	**10.2**	**5.4**

We have studied the H41 diblock copolymer thin films with thicknesses from 0.9 L_o to 1.8 L_o. Here we extended the study to even thinner films and tried to cast a single monolayer film (½ L_o thick, Region I only). The results are shown in Figure 4.15c (AFM) and Figure 4.16c (XPS). The film is slightly scratched by a razor blade, and the AFM image shows that it is a clear dewetted film. Moreover, the average film thickness is only 0.5 L_o, so the black area should be the bare silicon substrate to include both ½L_o and L_o heights. As discussed in Chapter Three, the thin LC homopolymer film (< 5 nm) has the tendency to dewet, which is similar to what we observed here for the LC diblock copolymers.

The gray area is ½ L_o height, and the white area is 1½ L_o height. The height differences are observed clearly in the depth profile on the right of the AFM image, and cross-sectional view on the bottom. Vix *et al.* [30] reported a similar instability of LCP thin films with film thickness less than 3 smectic layers (10 nm, $3s_o$). In this H41 LC diblock copolymer, we cast several different films with thicknesses ranging from 5.1 nm (0.29 L_o) to 9.3 nm (0.54 L_o), and all of them showed a similar dewetted structure, as in Figure 4.15c. This dewetted structure appears the same as the result of microdroplet experiments in Figure 4.1. I could not make a monolayer film at the silicon substrate using these preparation conditions. A clear CO shoulder of XPS data at both detection angles is marked in Figure 4.16c. The CO peak decreases at 75° (shallow detecting depth). The peak area drops from ca. 10% to 5%. This indicates the LC layer is covered by a thinner layer of PS at the air interface in dewetted structures. This agrees with what we propose that the PS layer covers the air interface in very thin films, while the LC mesogens maintain a planar orientation.

Further Explanation of XPS Data in Region III

I did not observe the carboxylic signal on the carbon scan for film thicknesses from 16 to 31 nm in Figure 4.6. However, the top smectic LC terraces were observed at the air interface in Figure 4.7 (AFM) and Figure 4.9 (TEM). This can be explained if some simple calculations are provided. The theoretical carboxylic ratio for the LC monomer is 8.6% (three carboxylic carbons in total thirty-five carbons in one monomer unit). For the H41 diblock copolymer, the theoretical carboxylic value becomes 2.9% in the bulk state if one accounts for 59% PS into the calculation.

From the model proposed in Figure 4.12, the smectic terraces are the major LC component directly exposed to the air interface. The LC perforations in Region I do expose LC dots at the air interface, but the area ratio is really low because the perforated diameter is only around ½L_o (~ 8.7 nm). From the data of surface coverage analysis in Figure 4.8, the homeotropic smectic terraces covers around 25% of the air interface in the box area without holes or islands. The carboxylic group is 8.6% inside the smectic terraces, so the theoretical carboxylic ratio at the air interface is ca 2.2% for the whole film (one quarter of 8.6%). For a film with a hole structure, there is only ca. 13% of smectic terraces covering the whole air interface from AFM analysis in Figure 4.8. The ratio depends on the hole sizes and the density. There are no smectic terraces inside the hole areas and the PS block covers the air interface. The theoretical carboxylic ratio thus becomes ca. 1.1% (13% of 8.6%). For the island structure, the smectic terraces cover less than 10% of the whole film at the air interface, so the carboxylic ratio might be less than 0.8%. These ratios are really low, and may not be accurately detected by XPS for this particular system.

Moreover, the experimental data of LC homopolymer films show only around 3% of the carboxylic ratio for films with different thicknesses in Table 4.2. These LC homopolymer data were collected by the same instrument that we used to conduct all non-angle resolved XPS measurements. The value of the LC homopolymer showed only around 35% of theoretical value. So the experimental data of diblock copolymers would be expected to be even lower. Thus, it is hard to observe the carboxylic signal even though other experiments indicate the LC terraces exist at the air surface in the H41 lamellar diblock copolymer thin films.

4.5 LC ORIENTATION IN DIBLOCK COPOLYMER THIN FILMS

The presence of one smectic-layer height at the air interface indicated a homeotropic arrangement of the LC mesogens at the air interface. The chemical structure of the mesogen also indicates that a homeotropic alignment provides lower surface tension at the air interface. Other researchers have also observed homeotropic LC anchoring of LC-containing polymers with an alkyl tail at the air interface.[1,17,19,20]

Earlier works by Wong *et al.* [19] showed perpendicular wetting of the hybrid lamellae in a symmetric diblock film (Φ_{PS}=0.49), and parallel wetting in an asymmetric diblock film (Φ_{PS}=0.64). For both types of lamellar alignment, LC was planarly anchoring to the block interface. Sentenac *et al.* [1] reported different LC anchoring in different environments. In bulk perpendicular lamellar morphology, the LC mesogens anchored planar to the block interface. In films with parallel lamellar morphology, the LC mesogens anchored homeotropic to the substrate and the block interface.

In our system, the existence of holes (or islands) of L_o periodicity indicates that the block copolymer lamellae are parallel to the substrate throughout the film. When the film thickness approaches a half-integral multiple of L_o greater than one, the holes disappear; however the top smectic terraces remain. The top smectic-terrace layer is parallel to the substrate and the block interface. The opposite of this coplanar arrangement was found in the bulk state in oriented films from SAXS, for which the smectic and copolymer domains were perpendicular.[4] We find that the surface layers are more tilted than the interior layers due to surface interactions and finite size effects.[31]

These observations suggested that, despite the preferred perpendicular "bookshelf" block morphology observed in the bulk state for these materials and several others,[32-35] a parallel arrangement relative to the lamellae was induced by surface effects. It was relevant to note here that in the case of the block copolymers with a decyl (n = 10 rather than 6) spacer group, the LC smectic layers exhibited parallel arrangement even in the bulk equilibrium state due to the effective decoupling of the mesogen from the main chain, and favorable anchoring interactions at the interface.[24] At the air interface of Region III, the block copolymer with a hexyl spacer described here took on this configuration, minimizing the interfacial free energy. Notably, the bottom regions of holes (Region I, ½L_o thick films) showed no topographical features at the top surfaces. This observation suggested that orientation of the smectic layers in the bottom monolayer (Region I) was not in a homeotropic arrangement, as found in the top regions of the film (Region III). In the case of cholesteryl LC block copolymers investigated by de Jeu and co-workers,[19,36] the smectic layers were consistently perpendicular rather than parallel to the domain morphology. These differences were probably due to the non-polar nature of the cholesteryl tail group on the mesogen. In more recent reports from this group, a biphenyl mesogen with an ethyl ester tail group [1] was involved. Sentenac *et al.* [1] reported similar stable homeotropic smectic terraces at the air interface. The lamellae and smectic layers aligned parallel to the substrate through the whole film. Henn *et al.* [20] also reported homeotropic LC anchoring through the whole film in a combined LCP with the same mesogenic groups in the main and side chains. However, two different types of LC alignment at the air and substrate interfaces were only observed by van der Wielen *et al.* [17] and in our LCP system.[21]

4.6 MORPHOLOGY OF SUB-MICRON THICK LAMELLAR FILMS

From results of previous sections, the lamellae of block copolymers arranged parallel to the substrate in ultrathin films, because the substrate effect was important. However, if films were sufficiently thick to damp out the substrate effect, what would be the lamellar direction and LC orientation? In this section, we studied the morphology of the thicker films (thickness = 3 - 8 L_o).

A stained TEM micrograph of a thicker film (136.5 nm, 7.9L_o) is shown in Figure 4.17a, which is a direct negative scan without inversion. The LC block here is black and the PS block is white in the negative films after staining with RuO_4. The big white areas around 100 nm wide are caused by the inhomogeneous surface, due to the development of surface-directed spinodal decomposition waves.[37,38] If we examine the image carefully, lamellar fingerprints show up clearly all over the film, even though we can only see them in the white areas. Two small figures on top indicate the curves of the lamellar fingerprints. This tells us the lamellar layer is perpendicular to the air interface inside the film. It appears that once the film is thick enough to damp out the strong preferential interactions of the silicon substrate, the block copolymer rearranges to form perpendicular layers at the air interface.

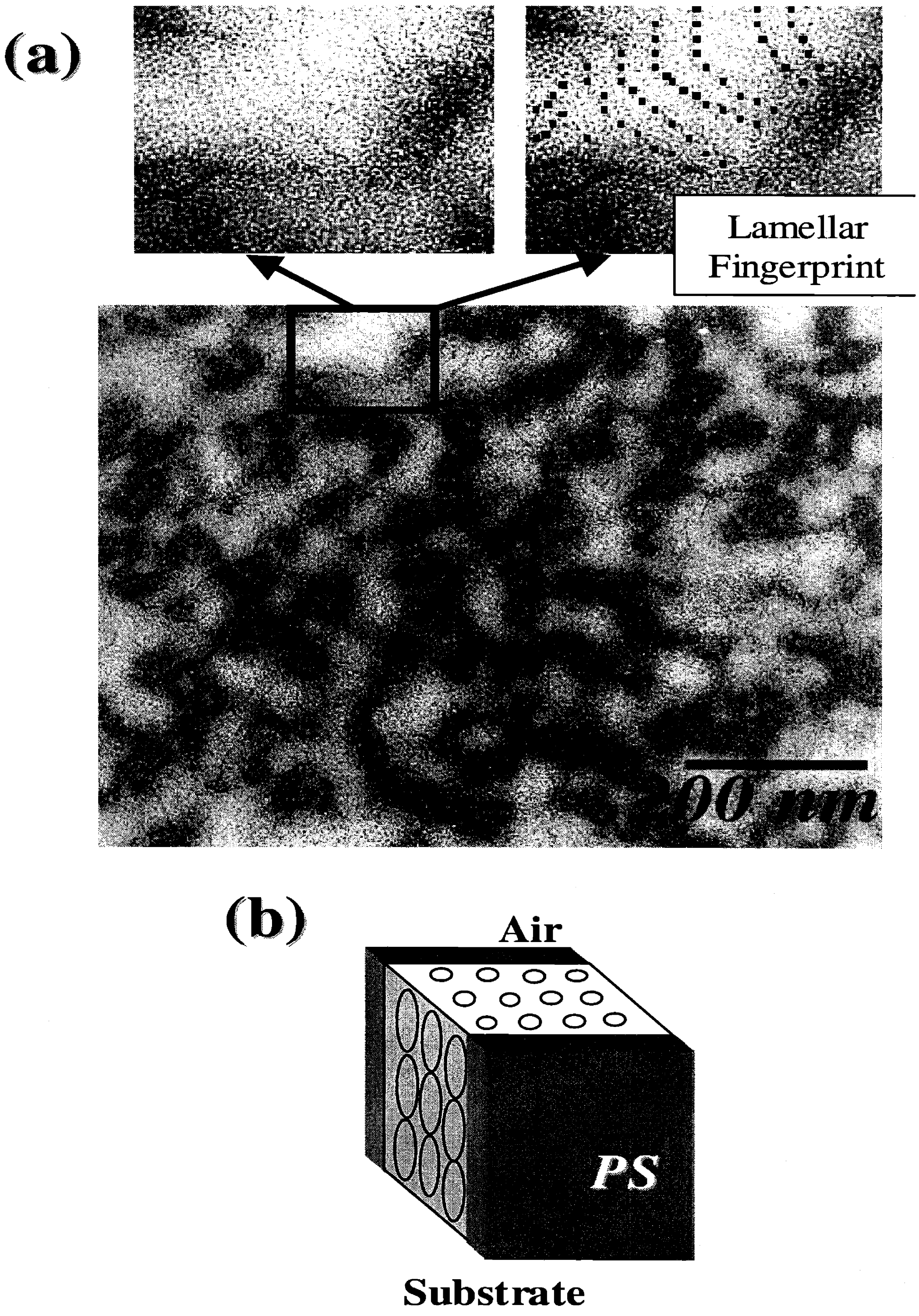

Figure 4.17: Morphological study of a sub-micron thick H41 lamellar diblock copolymer film (136.5 nm, 7.9 L_o) (a) TEM micrograph. Two small graphs demonstrate the black lamellar fingerprint all over the whole film; (b) Model of LC alignment shows that mesogens are planar anchoring to the block interfaces.

Thicker films of the same H41 diblock copolymer (thickness > 2 L_o) indicate that the terraced topography (Region III) is eventually damped out and disappears as the influence of the substrate and the confinement effects of the film subside. For these films, both blocks can coexist at the air interface in a perpendicular arrangement. A model is shown in Figure 4.17b. In this arrangement, the LC smectic layers can arrange in the more desirable homeotropic manner at the air interface, while maintaining the desired planar anchoring at the block interface. The mesogens inside the LC layer prefer homeotropic alignment so as to expose the alkyl tail. Since this is the most desirable structure for both LC alignment and the LC/PS block conformation, there are no smectic terrace structures or perforations at the air interface.

Figure 4.18 shows water contact angle experiments of this lamellar diblock copolymer (H41) at different thicknesses (0.7 – 8 L_o). These data can be divided into two groups by the thickness. Thinner films (< 30 nm) have high contact angles (~101° for advancing and ~86° for receding), while thicker films have lower contact angles (~93° for advancing and ~78° for receding). Thinner films are more hydrophobic. These data indicate the transition from parallel lamellae to perpendicular lamellae with respect to the substrate as thicknesses increased. The contact angle experimental data will be further discussed with respect to other sample compositions (H79, H80, H85, PHBPB, HPBP, PS, and blends) in the next chapter. This contact angle differences at two thickness zones are caused by the surface heterogeneity. It may be also due to a decrease in surface roughness because of loss of holes and smectic terraces.

Typically, the perpendicular lamellar structure of regular diblock copolymers was experimentally observed [5,13,28] and theoretically calculated [29,39-42] only for very thin films, especially when the thickness was less than ½ L_o. However, in the LC-containing diblock copolymer system, the perpendicular lamellae might be favorable for thicker films, because the LC mesogens prefer to anchor planarly to the block interface and homeotropically to the air interface by exposing the low surface-tension alkyl tails to the air, as shown in Figure 4.17.

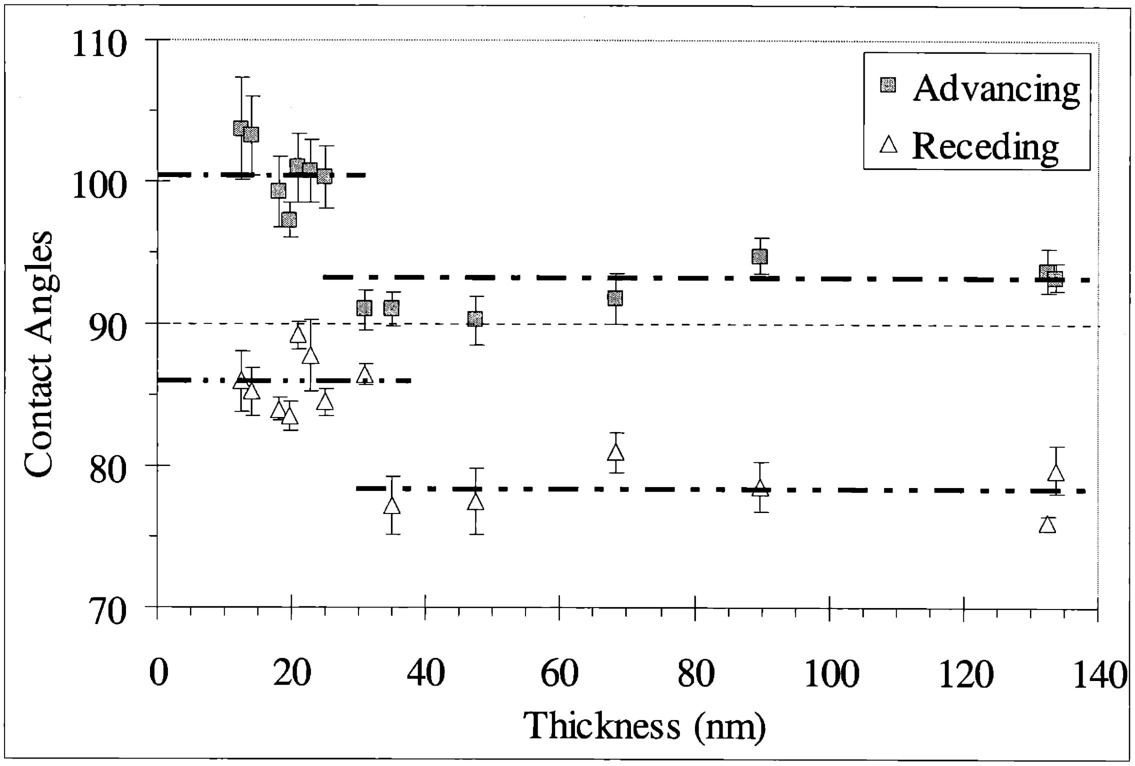

Figure 4.18: Contact angle measurements of water on H41 lamellar diblock copolymer films of different thicknesses.

In Section 4.6 here, the block copolymer adopts a perpendicular lamellar alignment for thicker films. LC molecules align planar to the block interface, which is similar to the alignment in the bulk state. In thin films (< 2 L_o), LCP shows parallel lamellar arrangement as in the model of Figure 4.12. The terraced and perforated morphologies observed in mono- and bilayer ultrathin films were due to the strongly preferential wetting of the substrate by the mesogens in the LC block.

4.7 FACTORS AFFECTING THIN FILM MORPHOLOGY

It is important to study the stability of the film morphology. Several factors were considered which might contribute to the stability, including the solvent vapor exposure, annealing effects, and aging effects. In the following sections, I studied each factor in detail with different techniques.

4.7.1 Solvent Vapor Exposure and Sample Preparation Methods

An LC diblock thin film was kept in a sealed glass container to test the effect of solvent vapors, which changed the nature of the free surface. The free surface of the film changes from non-polar air to polar solvent vapors. Toluene was selected in this experiment since it is a good solvent for both blocks in this diblock copolymer. It was also the solvent we used to cast the film. The film was kept in an environment with saturated toluene vapor at room temperature for three days, as shown in Figure 4.19. After taking the film out of the solvent vapor environment, the residue solvents inside the film were removed slowly under vacuum at room temperature for another three days.

Optical microscope (OM) and AFM were used to observe the topography and to calculate the surface roughness before and after the whole process. Before the exposure of solvent vapors, the film was thoroughly flat under OM, and the surface showed well-defined topologies under AFM with islands and smectic terraces on top of islands as in Figure 4.7b. The RMS roughness (R_q) was ca 2.64 nm. The islands and homeotropic LC terraces have been discussed in the previous sections. The cross-sectional view of the AFM image clearly showed two heights. After exposure to the toluene vapor, the surface became very rough under OM. AFM was then used to scan a flat area. Lowered RMS roughness (1.26 nm) in the box area indicated the loss of the island topography. The previous morphology could not be reconstructed under typical annealing conditions (130 °C for 3 days).

Ribbe and Hashimoto [43] found similar effects in a poly (2-vinylpyridine)-b-polyisoprene cylindrical copolymer thin films (~ 20 nm) after spin casting from a chloroform solution on piranha-cleaned silicon surface (Si(111)). After exposing the film to the chloroform vapor for a couple minutes, the film thickness decreased dramatically and the original texture of the surface disappeared.

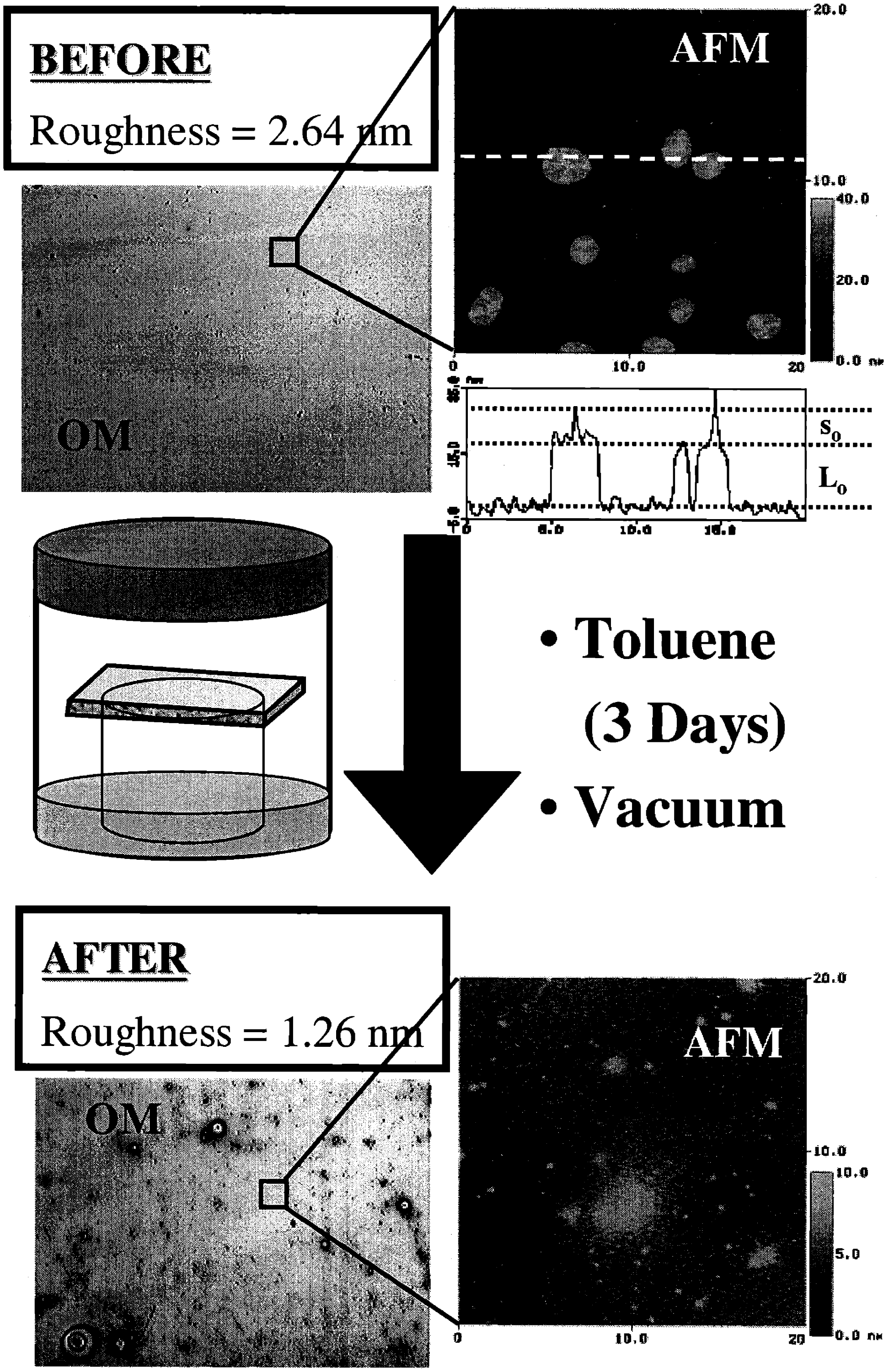

Figure 4.19: Solvent vapor exposure of a lamellar LC diblock copolymer thin film (thickness = 30.8 nm, 1.5 L_o). On the left side are the images from optical microscope (OM) and on the right side are the images from AFM. The cartoon in the center illustrates the experimental setup for keeping the film in the saturated solvent vapor environment.

While the film is exposed to the environment of saturated solvent vapors, the air interface switches from non-polar air to polar solvent vapor. The topography of the film can change in response to different environments. The homeotropic smectic terraces, which are favorable in the non-polar environment, are not expected to exist. That is why the topography was erased after removing solvents under vacuum. Moreover, the solvent can diffuse into the film and dissolve both blocks. The diblock copolymer becomes miscible by the aid of solvent and causes the loss of phase separation. The solvent-silicon interaction may also form a thin toluene-wetting layer on top of the substrate, lift the thin film off the substrate (delamination), and create both polar symmetric boundaries.

If the film is annealed at adequately high temperatures, polymer chains can flow to heal defects. Upon cooling down and reannealing at 130 °C for enough time, the original morphology and topography will be restored. The annealing effect will be further discussed in the next two sections. The boundary effect plays an important role in the thin film morphology. It is also the key parameter to using the LC diblock copolymer in real applications.

4.7.2 Annealing Studies

Annealing was the second factor we studied that might contribute to the stability. We tested the morphology at higher temperatures and confirmed the study with the aid of AFM. There are two critical temperatures for the LC diblock copolymers: LC clearing point (LC isotropization temperature, T_{iso}) and order-disorder-transition temperature (T_{ODT}). LC clearing point is the temperature at which the liquid crystals lose their ordering. In H41 lamellar LC diblock system, the T_{iso} is around 185 °C, and the T_{ODT} is around 210 °C.[6] The glass-transition temperature (Tg) of the PS block is around 97 °C and the Tg of the LC block is around 33 °C. Previous samples in this chapter were annealed at 130 °C. This annealing temperature was below the T_{iso} and T_{ODT}, but higher than the Tgs of both blocks to allow the chain movement of both blocks. Because ultrathin supported films are easy to dewet, they cannot be annealed at high temperatures for a long period of time, although higher temperatures are advantageous to allow polymer chains to flow quickly to a more favorable state. In this section, we tried to observe the morphology at higher temperature zones.

The lamellar diblock sample studied here was annealed at 170 °C for three days after annealing at 130 °C for a week. Figure 4.20a shows the topography by AFM. It shows holes and smectic terraces on the top surface. The topography did not change after second annealing. Figure 4.20b shows the topography after annealing at 180 °C (close to T_{iso}) for another two days. The holes merged to form bigger holes. The smectic terraces also merged, yet still kept the same height (one s_o). We did not observe the merging of smectic terraces when the annealing temperature is far below the T_{iso} (~ 175 °C). This implied that the smectic terraces had the tendency to merge to bigger terraces if they had adequate energy and mobility. Moreover, homeotropic LC alignment at the air interface remained after the smectic terraces merged.

Afterwards, we annealed the LC samples at a temperature between T_{iso} and T_{ODT}. At this temperature range, the LCs lost their ordering but the two blocks were still phase-separated. In our experiment, the same film was put back into the vacuum oven and annealed at 180 °C for another day. The annealing temperature was slowly raised up to 195 °C and kept for three more days to completely remove the LC ordering. Figure 4.20c shows the AFM images. Islands with L_o height formed at the air interface, but the smectic terraces have disappeared. The topography now appears like a general amorphous-amorphous diblock copolymer thin film. This observation agrees with our hypothesis for the LC diblock copolymer thin films.

After lowering the annealing temperature from 195 °C ($T > T_{iso}$) to 130 °C for another week, the smectic terraces formed again as in Figure 4.20d. After heating above the T_{iso}, the smectic terraces disappear and the hole/island structure remains while losing the LC ordering. The low annealing temperature (130 °C) is not adequate for polymer chains to flow efficiently enough to heal those holes, but it is high enough to allow the smectic ordering to pack and align at the air interface. This experiment showed us that the smectic terrace structure was a stable morphology, and that the whole process was reversible when annealing below the block copolymer T_{ODT}.

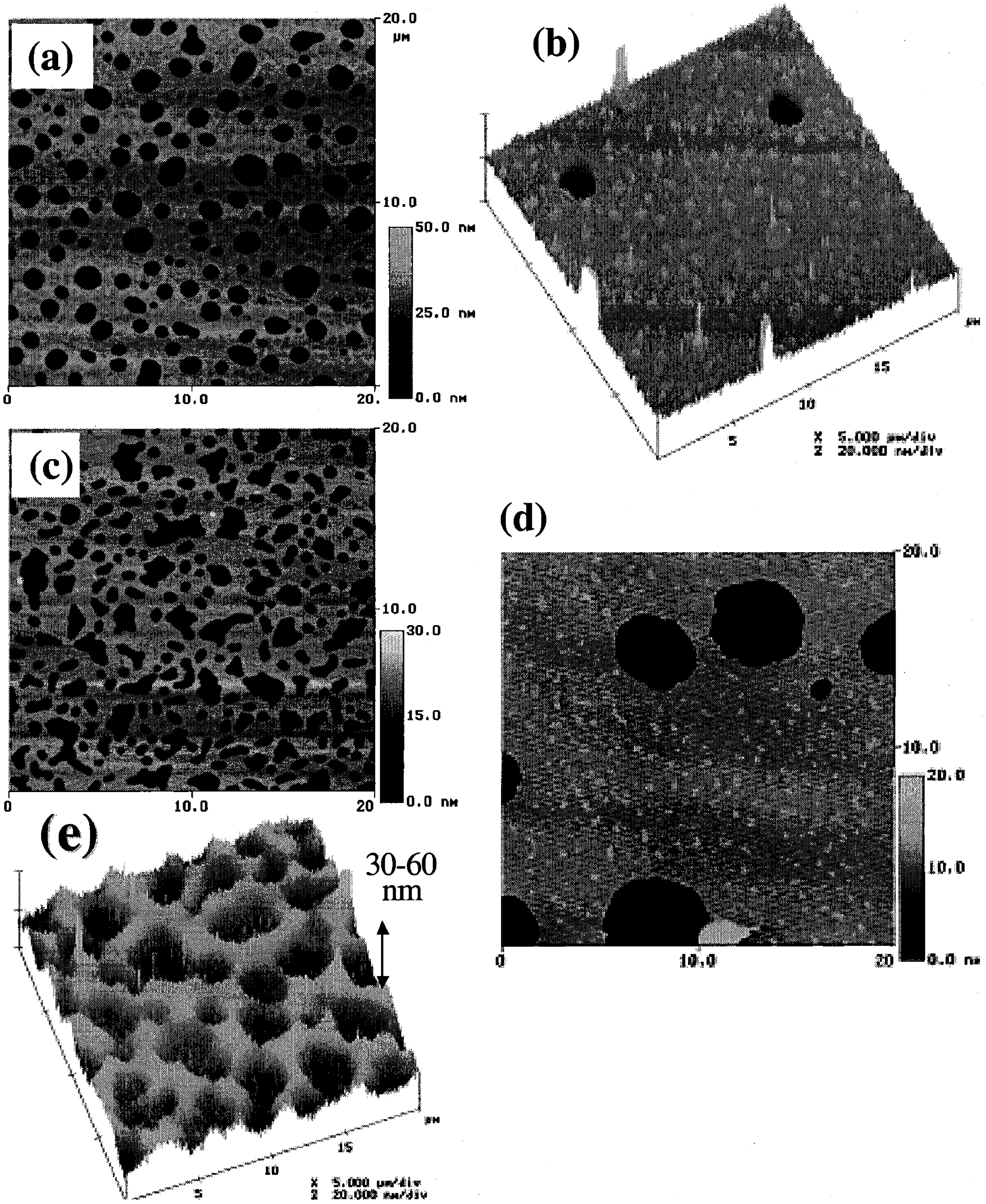

Figure 4.20: AFM images (20*20 μm^2) of a lamellar LC diblock copolymer thin film through various annealing at different temperature steps (a) 170 °C for another three days after annealing at 130 °C for one week; (b) 180 °C for another two days; (c) 195 °C for another 3 days; (d) reannealing at 130 °C for three days after annealed at 195 °C; (e) 250 °C for one day.

The same film was further heated to 250 °C for another day and quenched. The AFM image of Figure 4.20e shows a dewetted film; and it can be observed that the topography became very rough. The height differences are larger than several L_o and there is no specific height to describe it. At temperatures above T_{ODT}, two blocks become miscible as energy builds up which can overcome the barrier to merge together. This process became irreversible. After the film dewets, polymer droplets or the continuous structure formed at the air interface, therefore, the smectic terrace structure or the hole structure are not present.

We have shown that various LC diblock morphologies can be controlled by annealing at different temperature zones. This information is valuable to design specifics and when seeking a desirable topography. The annealing study is also presented in the next chapter for different high LC-ratio diblock morphologies.

4.7.3 Aging

From the theory of time-temperature superposition, the heating effect can also be duplicated within certain timeframes at lower temperatures. Thus, time is also an important factor to be considered for the stability study for the topography. This is critical in our samples because the Tg of the LC block is just about room temperature. The Tg of the PS block is ca. 97 °C, and the Tg of the LC block is 33 °C for the H41 lamellar diblock copolymer. Since the Tg of the LC block is close to room temperature, the morphology is not fully frozen. The morphology can change in a long period of storage or at elevated temperatures.

The film studied here was a lamellar diblock copolymer around 1.8 L_o thick (31.5 nm). The smectic terraces were uniformly distributed on the whole air interface (without holes and islands), and can be observed by AFM as in Figure 4.21a. The same film was kept in air at room temperature for one and an half years, and scanned by AFM again. Figure 4.21b shows the smectic terraces merged to bigger terraces, but the height stayed at one smectic layer (s_o). This phenomenon was the same as the annealing temperature effect in the previous section. This confirmed the homeotropic LC terraces were stable, even after one year.

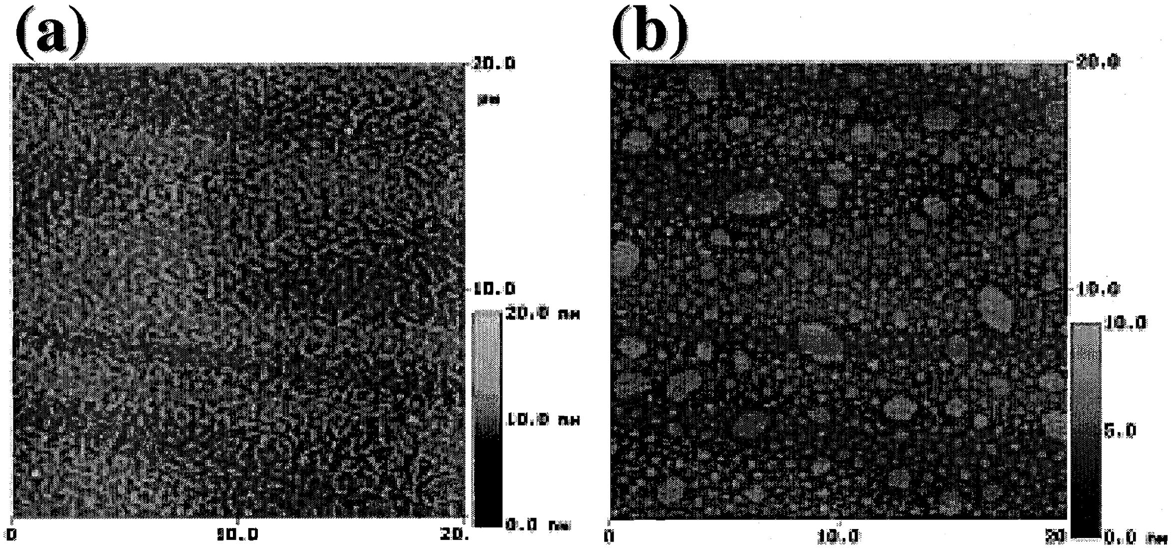

Figure 4.21: Aging effect of a lamellar LC diblock copolymer thin film. All images are all 20*20 μm^2 AFM scans. (a) Original; (b) after 1.5 years.

4.8 CHAPTER SUMMARY

In this chapter, I have extended my studies to thin films of lamellar LC diblock copolymers, after learning about LC alignment characteristics in Chapter Three. Due to the wetting properties of the LC diblock copolymers, LC terraces were observed on the top surfaces corresponding to a single smectic layer spacing. Holes and islands equal in depth to the block copolymer period were also observed from AFM. Perforation structure was shown by TEM for the film, except in the smectic terrace region.

LC anchoring is planar at the substrate, but homeotropically aligns at the air surface. This was observed in both homo- and block copolymers. I believe that the anchoring of the LC block to the silicon substrate, air, and the block interface caused the terraced surface morphology. For thicker films, the lamellar orientation showed a transition from parallel stacking near the substrate to perpendicular standing at the air surface. The fundamental understanding of this self-oriented LC diblock copolymer thin film behavior is important for future nano-patterning or electro-optical applications.

REFERENCES

(1) Sentenac, D; Demirel, AL; Lub, J; de Jeu, WH. *Macromolecules* **1999**, *32*, 3235-3240.

(2) Sentenac, D; Ostrovskii, BI; de Jeu, WH. *Adv. Mater.* **2001**, *13*, 14, 1079.

(3) Mach, P; Huang, CC; Stoebe, T; Wedell, ED; Nguyen, T; de Jeu, WH; Guittard, F; Naciri, J; Shashidhar, R; Clark, N; Jiang, IM; Kao, FJ; Liu, H; Nohira, H. *Langmuir* **1998**, *14*, 15, 4330-4341.

(4) Anthamatten, M; Hammond, PT. *Macromolecules* **1999**, *32*, 24, 8066-8076.

(5) Fasolka, MJ. *PhD Thesis: The Morphology and Lateral Patterning of Diblock Copolymer Thin Films*; MIT: Cambridge, MA, 2000.

(6) Zheng, WY; Hammond, PT. *Macromolecules* **1998**, *31*, 3, 711-721.

(7) Coulon, G; Collin, B; Ausserre, D; Chatenay, D; Russell, TP. *J. Phys.* **1990**, *51*, 24, 2801-2811.

(8) Maaloum, M; Ausserre, D; Chatenay, D; Coulon, G; Gallot, Y. *Phys. Rev. Lett.* **1992**, *68*, 1575.

(9) Russell, TP; Menelle, A ; Anastasiadis, SH ; Satija, SK. *Macromolecules* **1991**, *24*, 6263-6269.

(10) Morkved, TL ; Jaeger, HM. *Europhys. Lett.* **1997**, *40*, 643.

(11) Morkved, TL; Lopes, WA; Hahm, J; Sibener, SJ; Jaeger, HM. *Polymer* **1998**, *39*, 16, 3871.

(12) Anthamatten, M; Zheng, WY; Hammond, PT. *Macromolecules* **1999**, *32*, 15, 4838-4848.

(13) Fasolka, MJ; Banerjee, P; Mayes, AM; Pickett, G; Balazs, AC. *Macromolecules* **2000**, *33*, 5702-5712.

(14) Braun, FN; Sluckin, TJ; Velasco, E. *J. Phys. Condens. Matter.* **1996**, *8*, 2741-2754.

(15) Crawford, GP; Ondris-Crawford, RJ; Doane, JW; Zumer, S. *Phys. Rev. E: Stat. Phys., Plasmas, Fluids* **1996**, *53*, 4, 3647.

(16) Xu, L; Salmeron, M; Bardon, S. *Phys. Rev. Lett.* **2000**, *84*, 7, 1519.

(17) van der Wielen, MWJ; Stuart, MAC; Fleer, GJ; deBoer, DKG; Leenaers, AJG; Nieuwhof, RP; Marcelis, ATM; Sudholter, EJR. *Langmuir* **1997**, *13*, 17, 4762-4766.

(18) van der Wielen, MWJ; Stuart, MAC; Fleer, GJ. *Langmuir* **1998**, *14*, 24, 7065-7071.

(19) Wong, GCL; Commandeur, J; Fischer, H; de Jeu, WH. *Phys. Rev. Lett.* **1996**, *77*, 5221.

(20) Henn, G; Stamm, M; Poths, H; Rucker, M; Rabe, JP. *Physica B* **1996**, *221*, 1-4, 174-184.

(21) Wu, J-S; Fasolka, MJ; Hammond, PT. *Macromolecules* **2000**, *33*, 1108-1110.

(22) Anthamatten, M; Wu, J-S; Hammond, PT. *Polym. Prepr.* **1999**, *40*, 1, 427-428.

(23) Brandrup, J; Immergut, EH. *Polymer Handbook*, 4th ed.; Wiley: New York, 1999.

(24) Zheng, WY; Albalak, R; Hammond, PT. *Macromolecules* **1998**, *31*, 2686-2689.

(25) Anthamatten, M; Wu, J-S; Hammond, PT. *Macromolecules* **2001**, *34*, 24, 8574-8579.

(26) Koneripalli, N; Levicky, R; Bates, FS; Ankewer, J; Kaiser, H; Satija, SK. *Langmuir* **1996**, *12*, 6681-6690.

(27) Kellogg, GJ; Walton, DG; Mayes, AM; Lambooy, P; Russell, TP; Gallagher, PD; Satija, SK. *Phys. Rev. Lett.* **1996**, *76*, 14, 2503-2506.

(28) Fasolka, MJ; Harris, DJ; Mayes, AM; Yoon, M ; Mochrie, SGJ. *Phys. Rev. Lett.* **1997**, *79*, 3018.

(29) Pickett, GT; Balazs, AC. *Macromolecules* **1997**, *30*, 10, 3097-3103.

(30) Vix, ABE; Muller-Buschbaum, P; Stocker, W; Stamm, M; Rabe, JP. *Langmuir* **2000**, *16*, 26, 10456-10462.

(31) Fera, A; Opitz, R; de Jeu, WH; Ostrovskii, BI; Schlauf, D; Bahr, C. *Phys. Rev. E: Stat. Phys., Plasmas, Fluids* **2001**, *64*, 2, 21702.

(32) Mao, G; Wang, J; Clingman, SR; Ober, CK; Chen, JT; Thomas, EL. *Macromolecules* **1997**, *30*, 2556-2567.

(33) Fischer, H; Poser, S; Arnold, M. *Liq. Cryst.* **1995**, *18*, 503-509.

(34) Adams, J; Gronski, W. *Makromol. Chem., Rapid Commun.* **1989**, *10*, 553-557.

(35) Yamada, M; Iguchi, T; Hirao, A; Nakahama, S; Watanabe, J. *Macromolecules* **1995**, *28*, 50-58.

(36) Jerome, B; Commandeur, J; De Jeu, WH. *Liq. Cryst.* **1997**, *22*, 6, 685-692.

(37) Krausch, G; Dai, CA ; Kramer, EJ; Marko, JF; Bates, FS. *Macromolecules* **1993**, *26*, 5566.

(38) Sung, L; Karim, A; Douglas, JF; Han, CC. *Phys. Rev. Lett.* **1996**, *76*, 4368.

(39) Walton, DG; Kellogg, GJ; Mayes, AM; Lambooy, P; Russell, TP. *Macromolecules* **1994**, *27*, 6225.

(40) Matsen, MW. *J. Chem. Phys.* **1997**, *106*, 18, 7781.

(41) Kikuchi, M; Binder, K. *J. Chem. Phys.* **1994**, *101*, 4, 3367-3377.

(42) Tang, WH; Witten, TA. *Macromolecules* **1998**, *31*, 3130-3135.

(43) Ribbe, AE; Hashimoto, T. *Kyoto University, Kyoto, Japan* **Not published**.

Chapter 5

Morphologies of High LC Ratio Thin Films
- Cylinder and Smectic Bilayers

5.1 INTRODUCTORY REMARKS

Diblock copolymers demonstrate different morphologies as a function of block ratio, such as spheres (<21%), cylinders (21-33%), double gyroids (Ia3d, 33-37%), double diamonds (Pn3m, 33-37%), and lamellae (37-50%). The minority block of a diblock copolymer usually forms uniformly distributed cylinders or spheres in the majority matrix for highly asymmetrical amorphous-amorphous diblock copolymers.[1] However, we have found that the presence of a side-chain LC phase affects the general phase diagram, shifting known morphologies to different known volume ratios [2-4] or inducing the formation of new morphologies.[3,5] In this chapter, the surface morphologies of asymmetrical LC diblock copolymers at high LC ratios, exhibiting cylindrical and recently observed smectic-bilayered morphologies in the bulk state, will be discussed in detail.

5.2 MATERIALS

Diblock copolymers were synthesized and characterized as described in Chapter Two. Polymers were first purified by the solvent / non-solvent system and were further fractionated using a preparative gel permeation chromatography (GPC) column to remove any excess monomer or homopolymer, using tetrahydrofuran as the mobile phase. These diblock polymers exhibited a smectic phase (S_C* or S_A*). Properties of diblock copolymers mentioned in this chapter are listed below in Table 5.1.[3-5]

Table 5.1: Sample properties of high LC-ratio diblock copolymers. N is the number of repeating units. D is the domain size determined by both SAXS and TEM. LC phase transitions were assigned by a combination of DSC and OM.

Polymer	Mn_{PS}	Mn_{PLC}	Mn_{Total}	M_w/M_n	LC ratio	N_S	N_{LC}	d_{SAXS} (nm)	d_{TEM} (nm)
H79	4.8 k	16.3 k	21.1 k	1.08	0.77	46	28	13 (7.5, 6.5, 4.9)	12
H85	1.7 k	10.4 k	12.1 k	1.09	0.86	16	18	7.2 (3.6)	6.5-7

Polymer	Room Temp Morphology	Bulk LC Phase Transitions (°C)
H79	Hexagonally Packed Cylinder	Heating: S_C* (176) S_A* (212) I Cooling: I (203) S_A (173) S_C*
H85	Smectic Bilayers	Heating: Sc* (~175) I

5.3 THIN FILM MORPHOLOGY OF CYLINDRICAL LC DIBLOCK COPOLYMERS (H79 SERIES)

5.3.1 Orientation of PS Cylinders and LC Mesogens

A cylindrical morphology was observed for the 79% LC sample in bulk films, as verified in a previous study using TEM and SAXS, discussed in Chapter Two and shown in the phase diagram in Figure 2.3. TEM and SAXS also confirmed that the PS cylinders are packed hexagonally in a continuous LC matrix at high LC ratios. The bulk information is the basis for further exploring the thin film morphology.

The thin film of LC-containing cylindrical diblock copolymers has the block properties of general cylindrical diblocks. The cylindrical axis aligns parallel to the substrate for most cylindrical diblock copolymer thin films due to the lower energy state achieved by this orientation. Parallel alignment can be directly observed from TEM.[6,7] Cylinders perpendicular to the substrate occur only when special conditions or parameters are applied, such as specific thicknesses,[8,9] the use of patterned substrates,[6,7,10,11] specifically adjusted surface interfacial energies,[12-16] or in the presence of external fields.[17-23] In our system, PS cylinders are parallel to the substrate.

The possible orientation of LC mesogens inside the LC matrix has been determined in bulk LC samples. There are two types of possible orientation with respect to the PS cylinders. The LC mesogenic axis can be parallel (Figure 5.1a) or perpendicular (Figure 5.1b) to the cylindrical axis (block copolymer interface).[3,24,25] According to the SAXS data of melt fiber-drawn samples, LC mesogens are parallel to the cylindrical axis in the bulk of the material, as shown in Figure 5.1a, when there is an external force to enhance alignment in the bulk state.[3] In thin films, the substrate surface can induce an orientational force. The smectic-layer orientation in Figure 5.1a is more stable than that shown in 5.1b, because orientation in Figure 5.1b leads to an extra chain of the PS block stretching along the block interface at an excess entropic cost. For the H79 sample, the smectic spacing is 2.85 nm for smectic C* phase and 3.2 nm for smectic A* phase from temperature-dependent SAXS experiments.[3] The morphology remains ordered above the LC isotropization temperature (T_{iso} = 212 °C), indicating that the block copolymer order-disorder-transition temperature (T_{ODT}) is higher than T_{iso}.

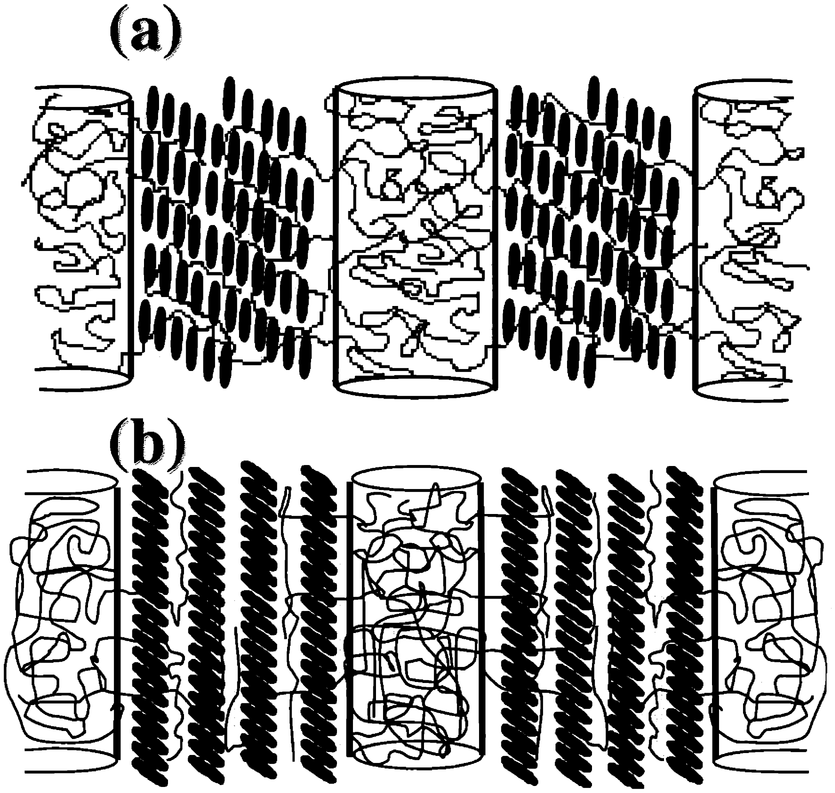

Figure 5.1: Various LC alignment vs. block interfaces in cylindrical diblock copolymers (a) LC mesogen axis parallel; (b) perpendicular to the cylindrical axis.

5.3.2 Wetting Structure Determination of LC Cylindrical Thin Films

The thin film structure of the cylindrical diblock copolymers (PS-b-PLC) was determined by XPS, AFM, and micro-droplet experiments as previously described in Chapter Four. In order to determine which block covered the air interface, XPS was used to determine the surface compositions. Three carboxylic groups (-COO-), which were unique to the mesogen and the methacrylate backbone, were chosen to identify the LC block. We prepared a series of films with different thicknesses and performed high-resolution XPS scans at the carbon 1s region. The detector was set parallel to the surface normal direction at the 0° takeoff angle and the penetration depth was around five nanometers (~ 63% from top 3.5 nm). The chemical shift of the carboxylic group (~4 eV) in the LC block was used to identify the block at the air interface directly. For the diblock copolymer films with PS cylinders in the LC matrix, we observed a clear carboxylic peak on the top film surface for samples at different thicknesses, as shown in Figure 5.2 and Table 5.2. These results suggest that the LC block has a lower surface tension and covers the air interface.

Table 5.2: XPS analysis of H79 cylindrical LC diblock copolymer thin films.

Sample	**Thickness (nm)**	**Peak**	**Peak Area (%)**
PS	17.4 - 20.5	CH / C	100
PLC Homopolymer	26.1 - 32.0	CH / C	87.64 ± 4.07
		CO	9.36 ± 3.17
		COO	**3.02 ± 0.90**
H79 Cylindrical Diblock Copolymer	54.3	CH / C	82.59
		CO	14.15
		COO	**3.26**

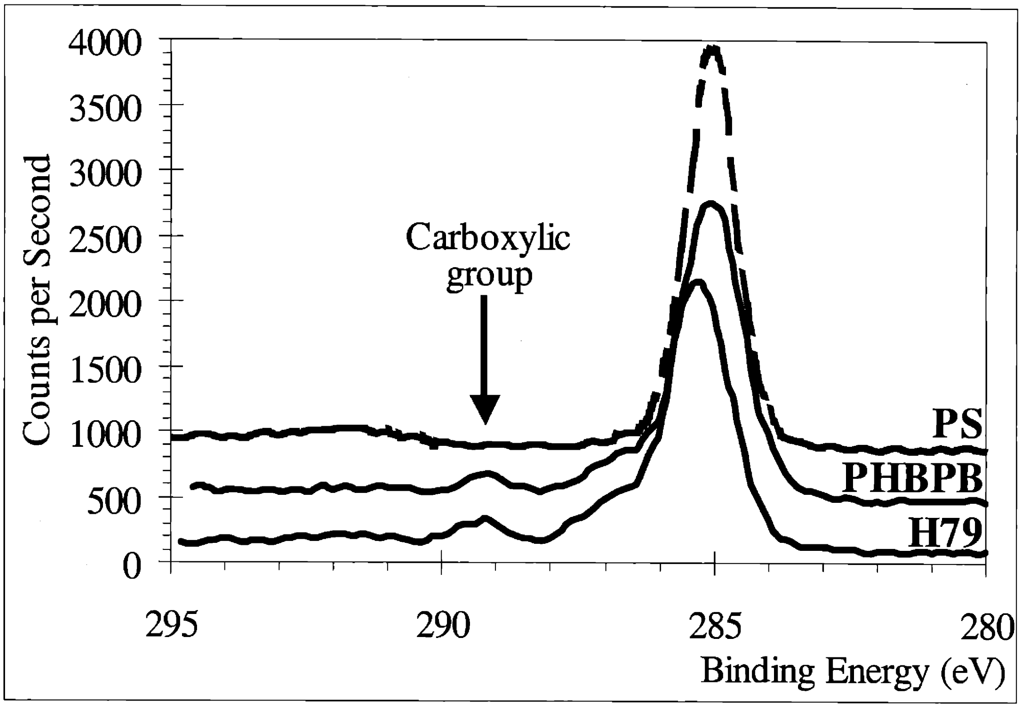

Figure 5.2: XPS analysis of PS homopolymer, PHBPB homopolymer, and H79 cylindrical diblock copolymer (54.3 nm) thin films. The carboxylic group (COO) is clearly shown for PHBPB and H79 in this figure.

In order to determine whether the block copolymer film exhibited symmetrical (thickness = n L_o) or anti-symmetrical (thickness = (n+½) L_o) wetting, AFM was used to measure the heights of micro-droplet edges, according to the same method reported in Section 4.2.1. The terrace heights of multiple L_o (n*L_o) indicates symmetrical wetting, based on diblock copolymer thin film concepts discussed earlier in Chapter One. Since the LC block can exhibit a lower surface tension than the PS block and effectively wet the air, based on the polymer blend experiments in Section 4.2.3, the LC block appears to wet both the air and silicon oxide interfaces.

5.3.3 Topography at Different Annealing Temperatures

The cylindrical LC diblock copolymer (H79) shows different topologies at different film thicknesses and annealing temperatures. The ultrathin film morphology is controlled by the following factors: the block periodicity, LC ordering, and substrate effects. The surface topography of thin films was measured by Atomic Force Microscopy (AFM, 20*20 μm^2 scan) in tapping mode as shown in Figure 5.3. The depth profile is displayed at the right of the plane-view AFM image. The top of the depth profile is the air interface, and each peak corresponds to a specific height. The bottom peak corresponds to the thinnest region of the film. The cross-sectional view (line scan) is also shown underneath the AFM image. The characteristic length scales are approximately 2.8-3.5 nm (smectic layer thickness, s_o), 8 nm (cylinder diameter, d), and 13 nm (inter-cylinder center-to-center spacing, L_o), respectively. Due to the wetting properties of this series of LC block copolymers, terraces were observed at the top air surface, corresponding to smectic layer spacings (s_o). One single smectic terrace structure has been discussed in a previous chapter (Chapter Four), as well as by other researchers.[26-30] In Figure 5.3a, multiple steps of the smectic layer thickness (s_o) at the air interface were observed at the free surface for a partially annealed sample (130 °C for 3 days). Four peaks with similar spacings (2.7, 3.1, and 3.5 nm) are clearly observed in the depth profile and the cross-sectional view, indicating different smectic levels. Only homeotropic LC alignment at the air interface can cause the formation of regular smectic steps. This observation confirmed homeotropic LC ordering at the air surface. Homeotropic alignment can be induced by energy reductions at the interface using the non-polar end of the LC mesogen, which has been explained in Chapter Three and Four. Several groups have also reported similar observations of multi-smectic steps.[31-33]

If annealed for a long period of time at the same temperature (130 °C for 2 weeks) below $T_{SC\rightarrow SA}$, the multi-smectic layers slowly coalesced, and finally only one terraced level of thickness s_o remained, as shown in Figure 5.3b. The bulk LC clearing temperature (T_{iso}) is ca. 212 °C and the transition temperature from smectic C* phase to smectic A* phase ($T_{SC\rightarrow SA}$) is ca. 176 °C, as listed in Table 5.1. The reduction of smectic layers minimizes the surface area and curvature, making a single smectic terrace as the most stable conformation for cylindrical diblock copolymer thin films upon annealing below T_{iso}.

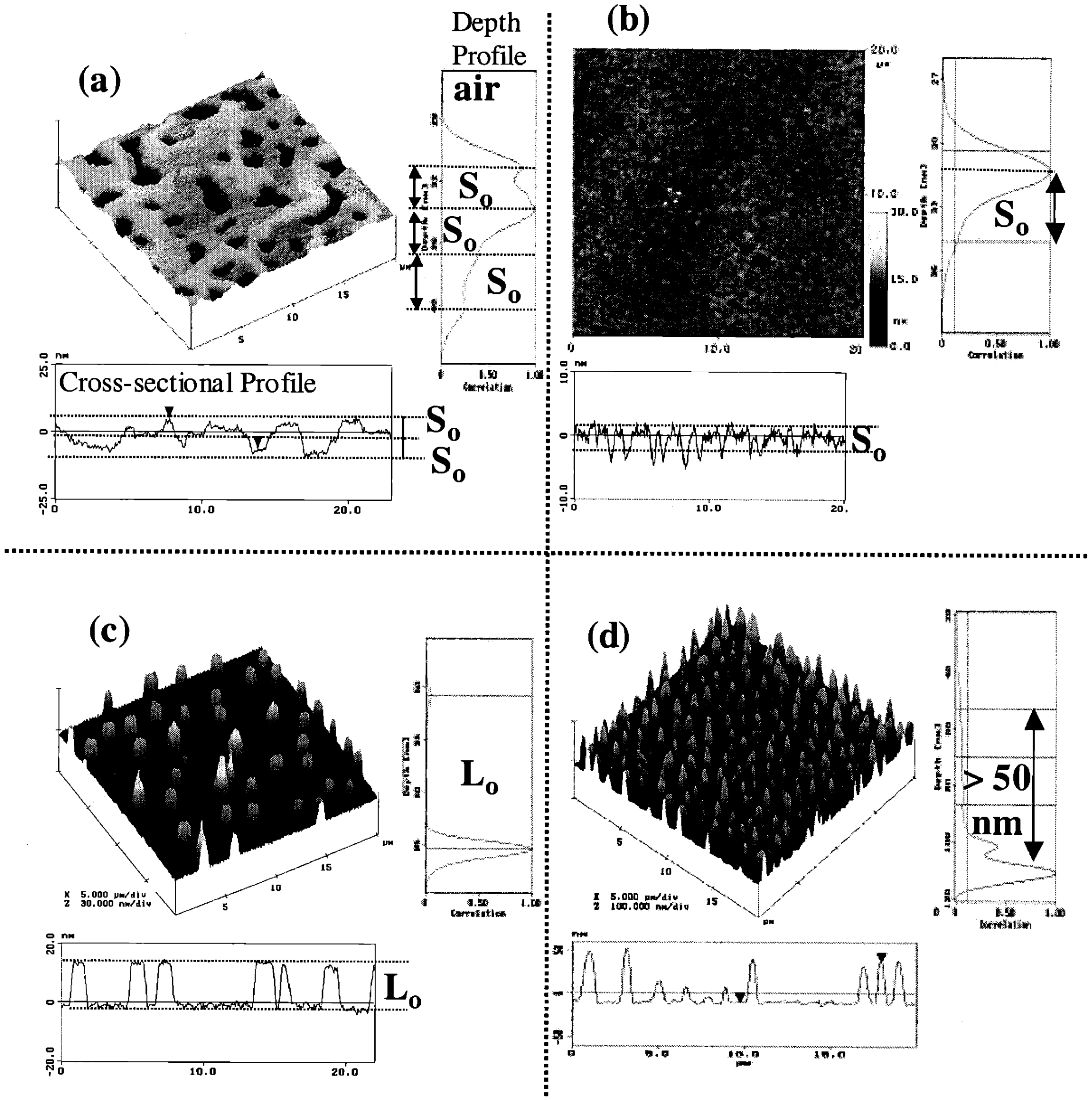

Figure 5.3: AFM images of cylindrical diblock copolymer thin films (H79). The depth profile is plotted at the right of each image, while the cross-sectional profile is at the bottom. (a) A partially annealed film (thickness = 35.7 nm, ~ 2.75 L_o) annealing at 130 ºC for 3 days, with multiple smectic steps at the air surface; (b) A film (thickness = 24.5 nm, ~ 1.88 L_o) after long annealing times at 130 ºC for 2 weeks, shows only one single smectic terrace remaining; (c) A film (t = 15.6 nm, ~ 1.2 L_o) with Islands of 16.5 nm height while annealing at 130 ºC for a week; (d) A dewetted film (t = 17.7 nm, ~ 1.36 L_o) after annealing at 170 ºC for three days

Regular islands with heights approximately equal to a typical, L_o height (L_o = 13 nm) were also observed when the film was thinner than 1½ L_o and annealed at 130 °C for two weeks as in Figure 5.3c. The film was 15.6 nm thick (~ 1.2 L_o) and islands were around 16.5 nm. In ultrathin films, the islands may be a discrete layer of parallel cylinders at the air interface. Lammertink and Vancso *et al.* [34] reported an island (or hole) structure for film thicknesses that are incommensurate with the domain spacing (26 nm), in a 27000 / 12000 g/mol cylindrical polystyrene-b-polyferrocenylsilane diblock copolymer. From Chapter Three, the LC mesogens prefer planar anchoring at the polymer-substrate interface and the PS/PLC block interface. Therefore, the PS cylinders prefer to adopt a parallel stacking orientation to the substrate. Parallel cylinders are usually a more stable conformation than perpendicular ordering for classic amorphous-amorphous cylindrical diblock copolymers. The island/hole structure may form due to the existence of an incomplete top cylinder layer. This structure can be further shown by TEM experiments. Green *et al.* [35] did a serious of annealing experiments at different temperatures for thicker films of the same diblock copolymer (H79). They found the similar island (hole) structure with L_o height (13.5 nm, lamellar structure) for film thicknesses from 50 to 300 nm, while annealing at 165 °C (< $T_{SC \to SA}$, ~ 176 °C). However, the topography becomes rough and loses the specific features after annealing at 185 °C. The study of Green's group focused on thicker films, which are 2 to 20 times thicker than films in our study. The island/hole structure was observed in two different thickness ranges.

Furthermore, if samples (film thickness < 30 nm) were annealed closer to the LC transition temperature ($T_{SC \to SA}$, ~ 170 °C) for another three days, the ultrathin film would dewet to form large mounds or drops that were higher than 50 nm for all thicknesses we studied (thickness < 35 nm), as shown in Figure 5.3d. The height of the mounds has no relation with block copolymer (L_o, 13 nm) or LC periodicities (s_o, ~ 3 nm). The excess free energy for long-range dispersive van der Waals interactions is inversely proportional to the square of thickness ($\Delta G = \dfrac{-A}{12\pi t^2}$) for thin films (thickness < 100 nm), where t is the film thickness and A is the Hamaker constant. It shows that thinner films are easy to dewet. Limary and Green *et al.* [36] reported that thin PS-b-PMMA symmetric diblock copolymer films dewetted silicon substrates at temperatures higher than the bulk T_{ODT}, and form different topographical features depending on the initial film thickness (3 - 45 nm). The topographical features showed bicontinuous spinodal-like patterns for thickness $t < 3.5$ nm, discrete holes for thickness between 3.5 and 7 nm, and autophobic behavior for thicknesses between 7 and 35 nm. In our system, the topography of dewetted films is thickness independent. The film does not revert back to the previous morphology even after long annealing times (2 weeks) at the previous temperature (130 °C). The dewetting temperature for nm-scale ultrathin films is usually a lot lower than the μm thick films, due to the interaction with the substrate. Moreover, the LC molecules have the tendency of packing, which allows the film to dewet more easily. In the bulk state, this diblock copolymer (H79) can become phase-separated after cooling from temperatures above T_{ODT}. In ultrathin films, the polymer chains cannot spread out again on the substrate by themselves without introduction of a spinning process, after they have the enough entropy to pull themselves together at high temperatures.

5.3.4 Proposed Model of PS Cylinders in the LC matrix

A model of PS cylinders inside the LC matrix is proposed in Figure 5.4a based on the information we presented above. Homeotropic LC alignment forms steps with the smectic height (s_o) near the air interface from the observation of AFM images. A height profile is inserted in Figure 5.4b at the left of the model to show those three smectic steps. We believe the PS cylinders are perpendicular to the air interface on the top surface, while the LC mesogens still anchor planar to the block interface. On the bottom part of the Figure 5.4a, the LC mesogens prefer planar anchoring at the silicon substrate and inside the film, as mentioned in Chapter Two and Chapter Three. Inside the film, LC mesogens align with respect to the direction of the parallel PS cylindrical axis. Planar LC orientation is the same as in the bulk state. There is a transition area near the free surface where LC orientation switches from planar to homeotropic.

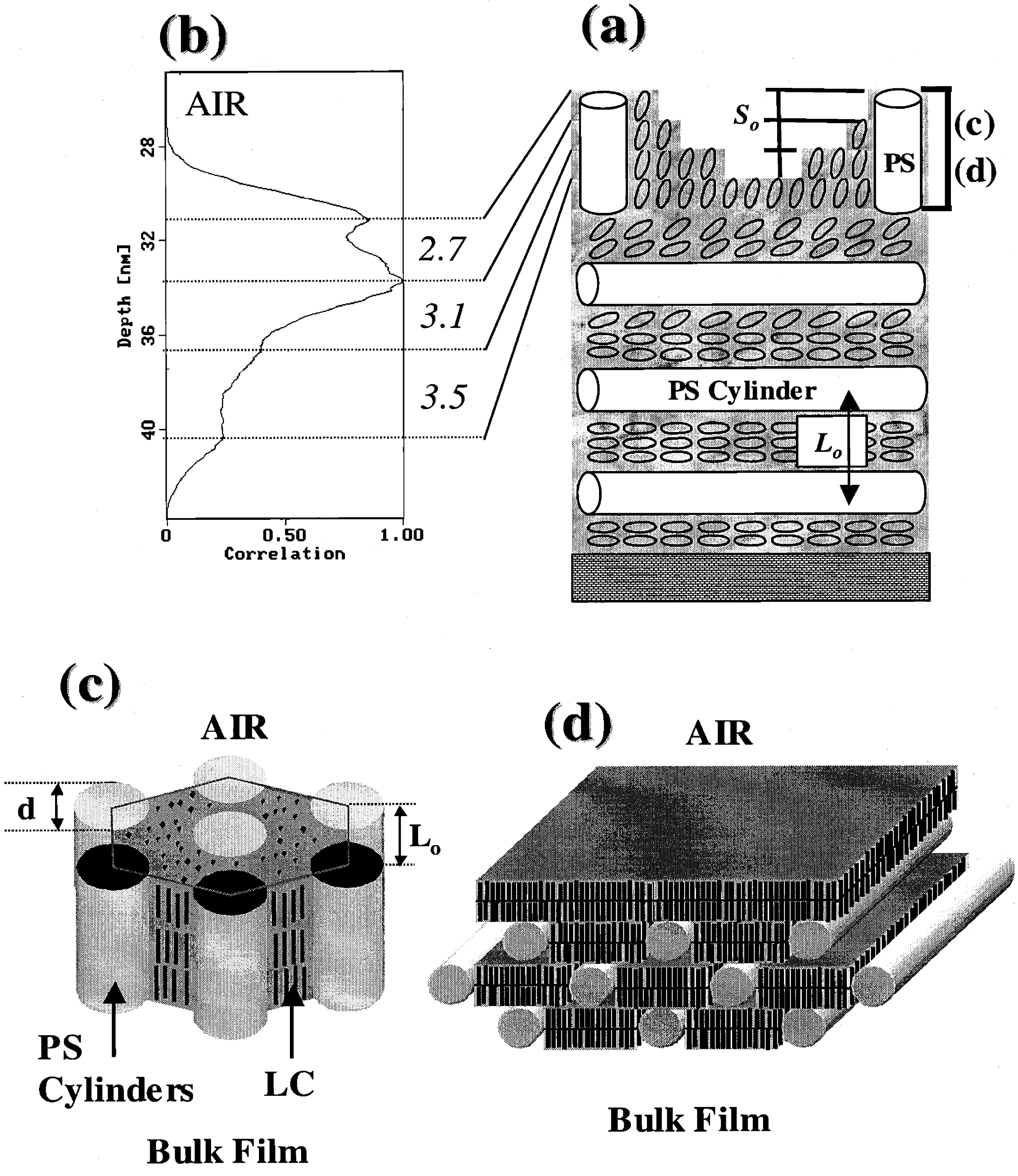

Figure 5.4: (a) A proposed model of cylindrical LC diblock copolymer thin films; (b) a depth profile of the top smectic terraces; (c) a schematic plot of perpendicular PS cylinders and planar LC anchoring at the air interface for top smectic terraces; (d) a schematic plot of hexagonal packed parallel PS cylinders at the air interface for top smectic terraces.

Figure 5.4c and Figure 5.4d show two different types of morphological alignment for the top smectic terraces. The PS cylinders are perpendicular to the air interface in Figure 5.4c, and parallel to the air interface in Figure 5.4d. LC molecules anchor planarly to the interfaces for both cases. The structure in Figure 5.4d is expected to have more distortions and defects, such as variation of the mesogen tilt angle near the IMDS (inter-material dividing surface), and curvature of smectic layers. The morphology in Figure 5.4c is believed to be more stable, as discussed by Osuji and Thomas *et al.* [37,38]

The volume fraction of the PS block of the H79 cylindrical diblock copolymer was 24.5%, based on the molecular weights and densities of each block. Since the PS cylinders packed hexagonally, the diameters of cylinders could be calculated. Figure 5.4c shows a schematic plot of hexagonally packed cylinders inside the film. The PS diameter (d) calculated was 6.75 nm, corresponding to ca. two smectic layer height ($s_o \sim$ 3.2 nm). Similar cylinder alignment models of LC diblock copolymers in the bulk state (~ 10 μm thick film) were discussed by Mao, Ober, and Thomas *et al.*[39]

The multiple terraces are not the most stable configuration, and collapse to one incomplete layer after long annealing, as discussed previously. However, homeotropic LC alignment is observed to be the most stable conformation at the air interface.

5.4 THIN FILM MORPHOLOGY OF SMECTIC-BILAYERED DIBLOCK COPOLYMERS (H85)

In 85% LC samples with low MWs, the LC phase formed a smectic bilayer morphology (S_{C2}) in the bulk phase, which was also observed in ultrathin films.[5] The LC bilayer morphology is caused by the tendency of LC mesogens to pack into well defined layers, forcing the short PS chains into an intermediate layer as oblate, pancake shaped disks. The same smectic bilayered structure remained in supported ultrathin films. A bulk spherical morphology was observed when samples were quenched from temperatures between T_{iso} and T_{ODT}. These LC order-induced morphologies should have interesting but different thin film topologies.

5.4.1 Bulk Morphologies

The bulk morphology of the smectic LC bilayer structure was reported by our group [5] and is summarized here. At 85%-wt of the LC block, which should lead to a spherical PS morphology, the PS domains are deformed into highly oblate ellipsoids, and arranged hexagonally between smectic bilayers. The smectic bilayer model in Figure 5.5a was determined from bulk SAXS and TEM data to describe this morphology. Figure 5.5b shows peaks of the SAXS data at room temperature. The two strong peaks at 7.2 nm and 3.6 nm represent the first and second order reflections of lamellar-layered periodicity of the smectic layer. The two weaker Bragg peaks at 18 nm and 14 nm indicate a larger secondary structure. This periodicity is around twice the smectic layer height (~3.5 nm).[5]

TEM micrographs provide direct evidence of the described morphologies. The left half of the TEM image in Figure 5.5c represents the view from the X or Y direction, while the right portion represents a graph boundary viewed from the Z direction, with respect to the model for room temperature. The regular black dots at the right part are the top view of the stained PS disks. The diameter of the PS disks is around 8 nm from TEM images. Each PS disk consists of about 75 PS chains according to calculations given in an earlier paper.[5]

The same sample can exhibit another morphology at temperatures above the LC clearing point (T_{iso}). Figure 5.5d shows a TEM micrograph taken after rapidly quenching the sample from 180°C. The quenching temperature is above T_{iso}, but below the block copolymer order-disorder transition temperature (T_{ODT}). The diameters of the spheres range from 2 to 10 nm (around 6-7 nm average), and are consistent with the expected 7.5 nm diameter from the random-coil calculation. Hence, a disordered spherical morphology exists at temperatures below T_{ODT} and above the T_{iso}. The diblock copolymer exists as the general diblock when there is no LC ordering. However, when the annealing temperature is below T_{iso}, LC mesogens stay packed to maintain the smectic mesogenic ordering, which presses the LC spheres to oblates. This sample can be re-annealed at the previous conditions and will regain the smectic bilayered morphology. This is a great example for the order-order transition due to LC ordering.

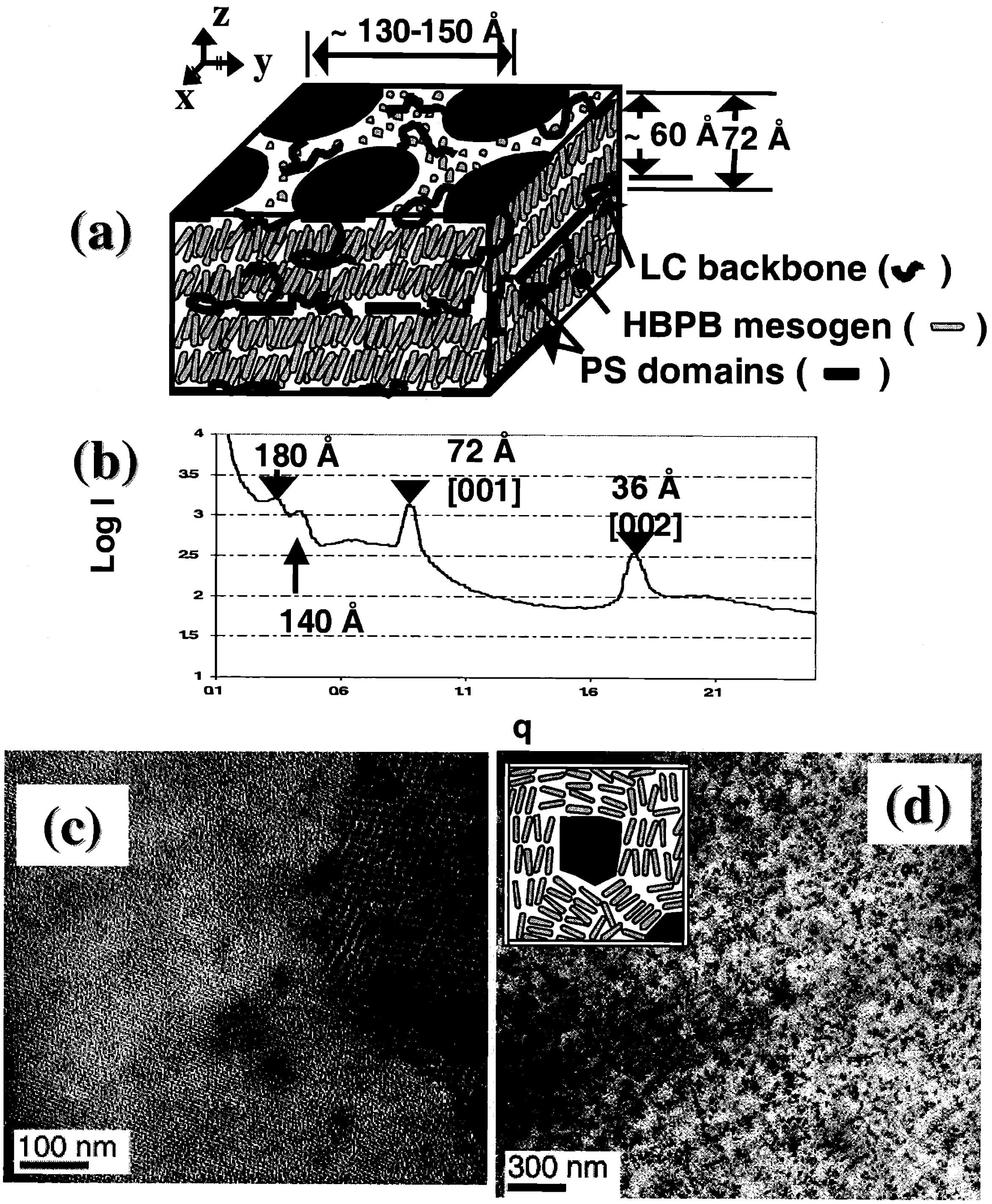

Figure 5.5: Bulk morphology of the smectic bilayers diblock copolymer (H85) (a) model; (b) SAXS data; (c) TEM micrograph of sample annealed below T_{iso}; (d) TEM micrograph of high temperature quenched sample.

5.4.2 Structure Determination of Smectic Bilayered Thin Films

The same approaches have been used to determine the film structure for samples with smectic bilayered structure in the bulk state (H85). The microdroplet experiment indicates that symmetrical wetting occurs. The XPS data at a 0° takeoff angle (surface normal direction) indicates that the LC block covers the air interface, as shown in Figure 5.6 and Table 5.3, although the carboxylic ratio is lower than the theoretical value (8.6%). Thus the LC block prefers to cover both interfaces, but the PS block may coexist at the surface with the LC block.

Table 5.3: XPS analysis of H85 smectic bilayered thin films.

Sample	**Thicknesses (nm)**	**Peak**	**Average Peak Area (%)**
H85	6.2 - 22.7	CH / C	84.67 ± 2.65
		CO	13.38 ± 2.69
		COO	**1.96 ± 0.43**

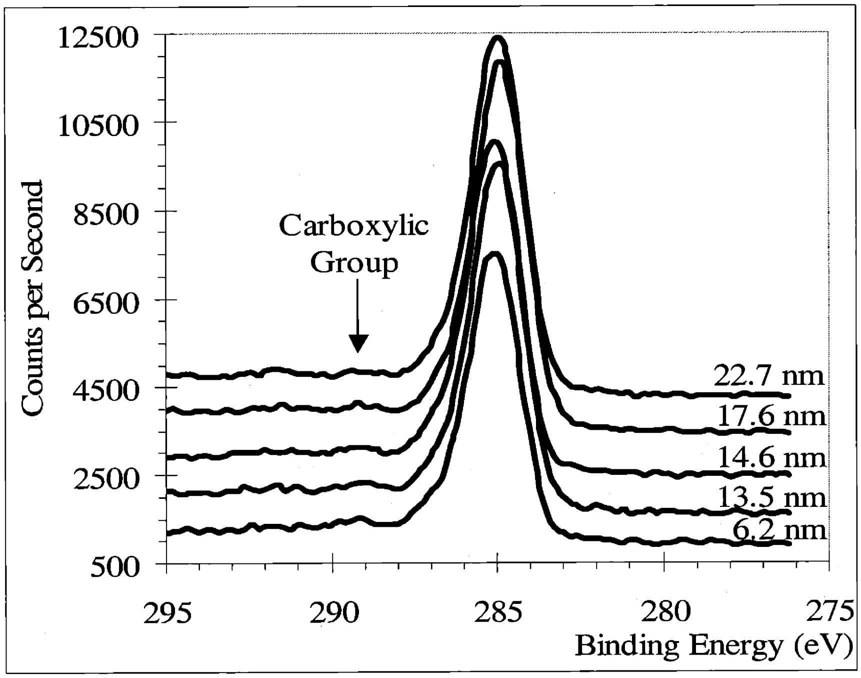

Figure 5.6: XPS analysis of films of smectic bilayered diblock copolymers with different thicknesses.

5.4.3 Microscopic Observations of Smectic Bilayered Thin Films

The thin film topography of the smectic bilayered structure is studied in this section. It is expected to have similar morphological behaviors as the lamellar thin films presented in Chapter Four. AFM was used to examine films with different thicknesses. Surface topographical scans (20*20 μm^2) using AFM provided information about roughness, depths between peaks, and relative peak areas (bearing ratio), as listed in Table 5.4. Bearing analysis from the DI software provided a method of plotting and analyzing the distribution of surface heights over the film.

Table 5.4: Thin film surface information of LC diblock copolymers with smectic bilayer structure. Film thicknesses were measured by ellipsometry. Roughness (Rq), depths, peak areas were determined using AFM.

Sample	**Film Thickness (nm)**	**Rq (nm)**	**Depths between peaks (nm)**	**Relative peak area (% / %)**	**Annealing Temp (°C)**
H85-8	5.8 (~0.81 L_o)	2.0	-	-	170
H85-2	17.6 (~2.44 L_o)	3.5	5.6	64.2 / 35.8	170
H85-1	18.4 (~2.55 L_o)	3.2	6.4	71.0 / 29.0	170
H85-5	22.7 (~3.16 L_o)	2.8	3.2 / 6.1	15.7 / 77.6 / 6.7	170
H85-5	22.7 (~3.16 L_o)	1.7	-	-	190

The bearing ratio, or what percentage of surface lied above or below any arbitrarily chosen height, was calculated. The same analytical procedures have been applied in Section 4.3.1 and Figure 4.8. The bearing ratio curve represented the integral of the surface height histogram and plotted the total percentage above a reference plane as a function of depth. Every peak indicated a specific height. The depths between peaks showed the height difference directly observed from AFM topography, such as s_o (smectic layer height) and L_o (block periodicity). For example, the sample of H85-5 shows three peaks with the area ratio of 15.7%, 77.6%, and 6.7% in Table 5.4. The height difference between the top two peaks is 3.2 nm (s_o) and the difference between the second and third peaks is 6.1 nm (L_o). Four samples will be discussed in this chapter.

Thin film topography was determined using AFM and TEM as in Chapter Four. The AFM images of sample H85-1 (18.4 nm, ~2.55 L_o) in Figure 5.7 appeared similar to lamellar LC diblock copolymer thin films, such as sample H41. Figure 5.7a shows the AFM image. Three heights were observed clearly. The black regions represent the bottom layer (Region I), the gray regions represent the top plateau (Region II), and the white regions represent the top smectic terraces (Region III). Figure 5.4b is the same image scanned by the phase mode. Figure 5.7d shows the cross-sectional view of two height differences (s_o and L_o). Figure 5.7e shows the depth profile. Two major peaks demonstrate the islands and the bottom structures. The depth between these two peaks corresponds to the block periodicity (L_o).

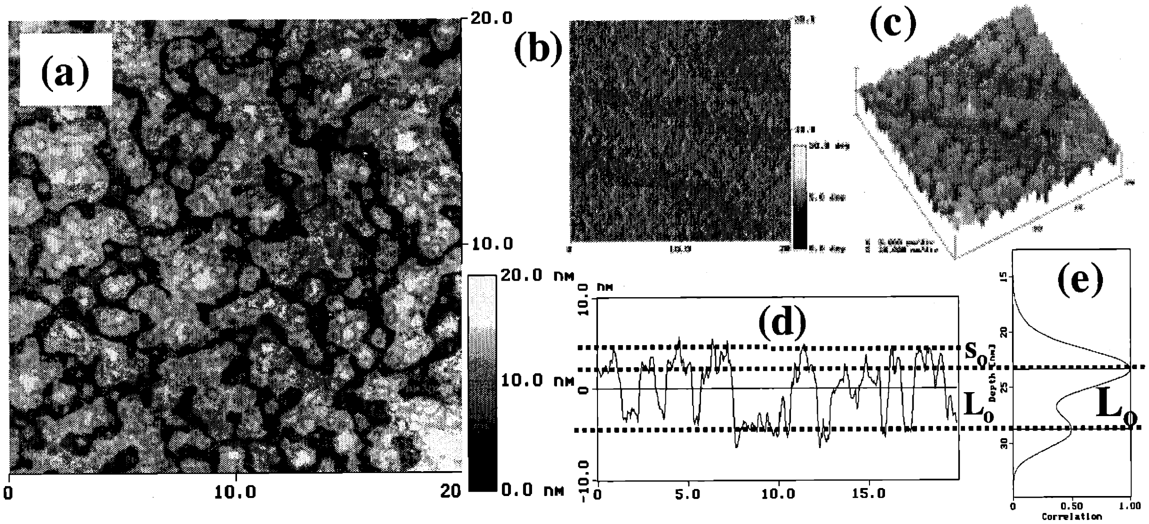

Figure 5.7: A 20*20 μm^2 scan AFM image of smectic bilayered thin film (H85-1) (a) plane-view; (b) phase mode; (c) 3D view; (d) cross-sectional view; (e) depth profile.

Islands with L_o heights covered around 71% of the surface area in Table 5.4. The island structure (or the hole structure for films with different thicknesses) was observed in general lamellar diblock copolymer systems with thicknesses incommensurate to the lamellar thickness with heights corresponding to the block copolymer period (L_o) at the air interface. Nevertheless, the lamellar (layered) structure was not predicted at the very asymmetrical compositions in the diblock copolymer thin films, where spherical morphologies were common. As mentioned earlier, the lamellar structure was observed in the bulk as smectic bilayers. This thin film study provides us with further direct evidence of the smectic bilayered morphology in the high LC volume fraction area. The height of the islands is usually a bit lower than the bulk bilayer periodicity ($2\ s_o = 7.2$ nm), presumably because the LC tilt angle at the air interface is often larger than in the bulk. The phase shift in Figure 5.7b provides contrast based on the mechanical property differences on the surface. A single smectic layer (s_o) can be observed on the top of islands (L_o) from the cross-sectional profiles in Figure 5.7d. Another thinner film (H85-2, 17.6 nm, ~2.44 L_o) showed similar AFM topography as H85-1, but the islands covered 10% less surface area.

Figure 5.8a and Figure 5.8b are plane-view TEM images with low magnification (10 KX). The contrast of TEM images comes from both the thickness difference and compositional variations. The PS block of all samples discussed in this chapter was selectively stained by RuO_4 to be darker. In Figure 5.8a and Figure 5.8b, the different contrasts in TEM images correspond well with different heights observed in the AFM images in Figure 5.7a, although there exist some white surface strips caused by peeling the film from the substrate. The TEM image of Figure 5.8a shows three contrasts. The lighter (white) part is the valley (bottom layer), the gray part is the island, and the darkest part is the top single smectic terrace. This agrees with the AFM image. The other TEM image in Figure 5.8b shows white ribbons around islands. Since these ribbons do not show up in the AFM images, they must reflect compositional fluctuations. When the PS block is selectively stained by the heavy metal oxide, the areas with more PS are darker in TEM images. The ribbon (white ring) has the same height as the bottom (light gray area), but it has fewer PS disks. This indicates that the PS disks are not uniformly distributed in the film. More PS disks may be located underneath the homeotropic LC layers to support the exposed top smectic terraces, and the white ribbon shows no PS disks at the outside circular regions.

When the film is annealed on the substrate, the lamellar layers prefer to be parallel to the substrate. The plane-view TEM images in Figure 5.8 were taken only from the Z direction, as shown in the bulk model of Figure 5.5a. We expect that the PS disks are similar to those seen in the right part of Figure 5.5c. From higher magnification images of Figure 5.8c (100 KX) and Figure 5.8d (200 KX), black dots are clearly observed.

These black PS disks have diameters of approximate 10 nm. This confirms the model and shows that the highly oblate ellipsoidal PS micro-domains are hexagonally packed among LC bilayers. It also shows the presence of PS and LC wetting the air interface. The smectic bilayered structure is preferred in high LC-ratio thin films.

These films were kept at room temperature for at least three months and then scanned by AFM again; no obvious change could be found. Thus, the morphology appears to be reasonably stable at room temperature.

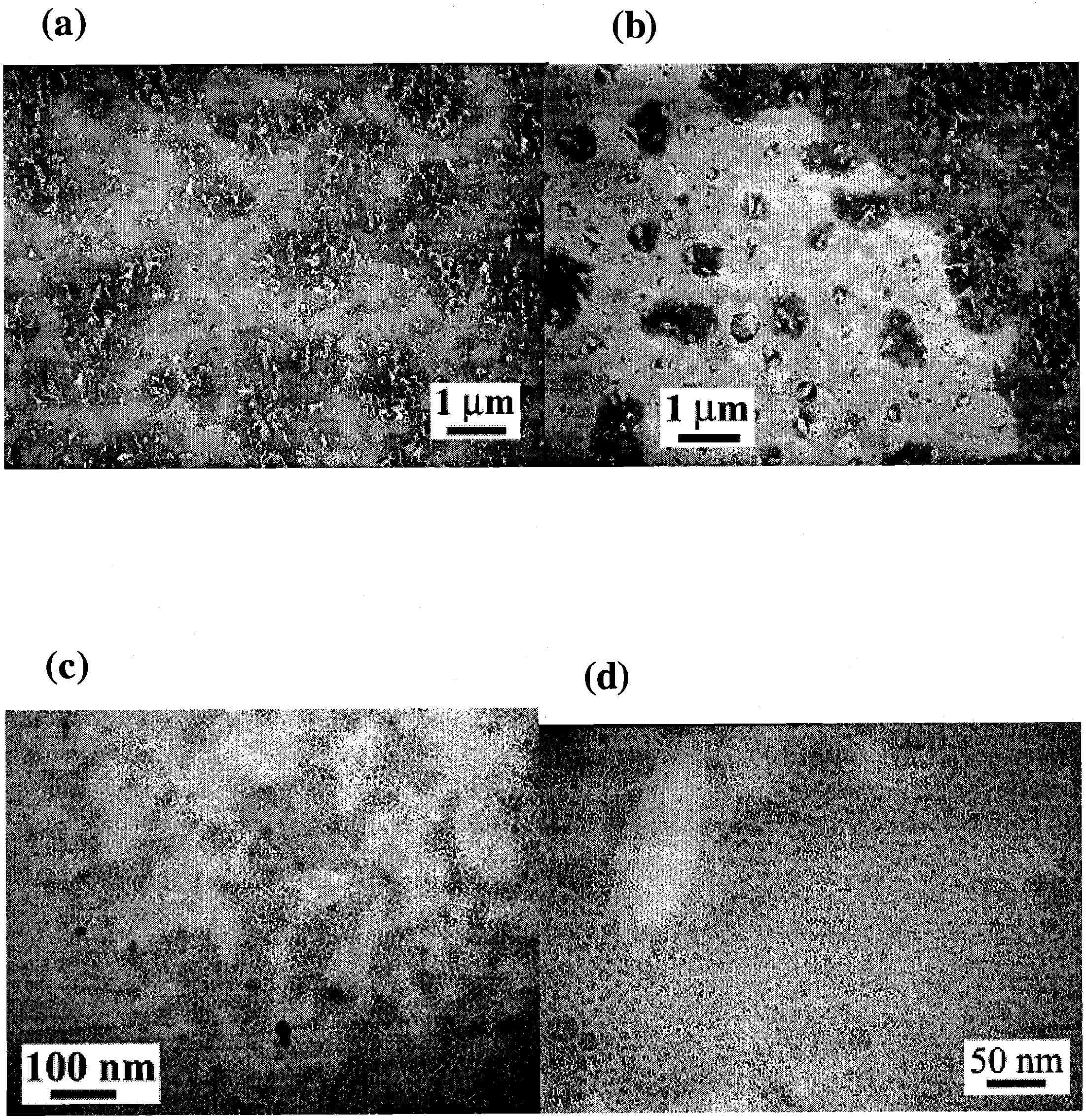

Figure 5.8: TEM micrographs of smectic bilayered thin films. (a) 10 KX of H85-2; (b) 10 KX of H85-2; (c) 100 KX of H85-1; (d) 200 KX of H85-2.

5.4.4 Homeotropic LC Terraces in Smectic Bilayed Thin Films

The homeotropic, smectic LC terrace structure existing in the smectic bilayered morphology is interesting. We would like to examine whether it is a stable conformation and whether it is the same as that in the lamellar diblock copolymer.

The smectic terraces are more pronounced at some specific film thicknesses. There are three clear height levels in the AFM images of the sample H85-5 in Figure 5.9. The vertical depth profile in Figure 5.9e shows three peaks corresponding to those three heights (smectic terraces, top plateau, and bottom) in the cross-sectional view. The data are listed in Table 5.4. The height of the top white plateau is around 3.2 nm from the height difference of the top first and second peaks. It is equal to one smectic layer height (s_o). The depth of the holes is around 6.1 nm approximately equal to L_o (one smectic bilayer), from the height difference between second and third peaks. The topography is similar to what we have reported in the same series of side-chain LC diblock copolymer lamellar morphologies (H41) [27] in the previous chapter, although the top smectic terrace structure of H85 does not form continuous ribbon structures like H41. A primary difference is the preferred anchoring of the smectic phase with respect to the block interface.

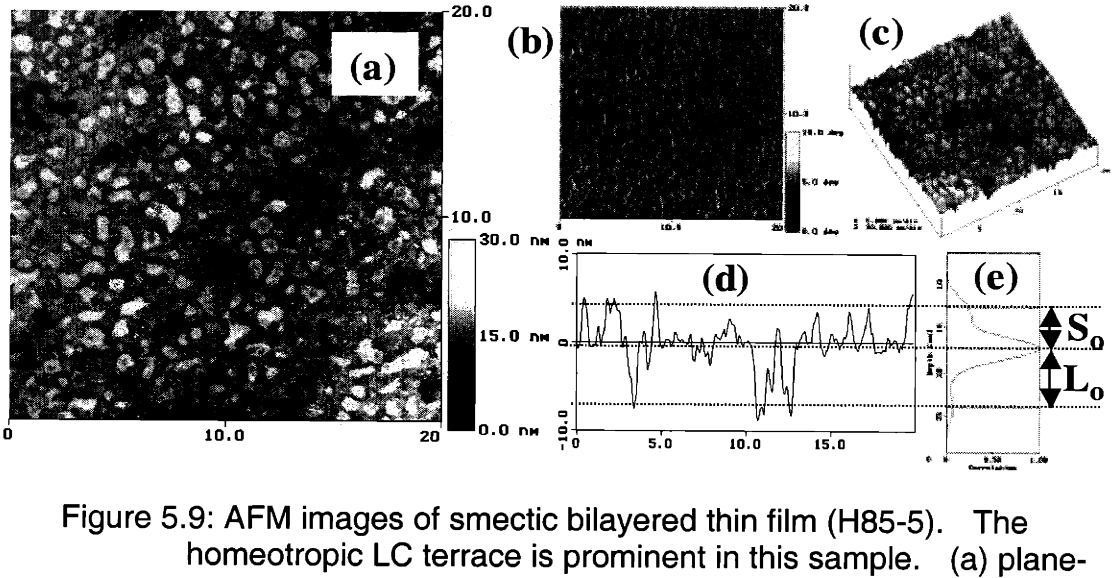

Figure 5.9: AFM images of smectic bilayered thin film (H85-5). The homeotropic LC terrace is prominent in this sample. (a) plane-view; (b) phase mode; (c) 3D view; (d) cross-sectional view; (e) depth profile.

5.4.5 Proposed Model of Smectic Bilayered Thin Films

The proposed model for the smectic bilayered thin film morphology is shown in Figure 5.10. It is based on the bulk smectic-bilayer model in Figure 5.5a and H41 lamellar thin film model in Figure 4.12. The LC block wets the substrate, and LC molecules anchor planar in the layer next to the substrate. Small PS disks (white color in the figure, diameter ~ 8 nm) arrange between smectic bilayers. There are fewer PS disks near the edges of islands, as we saw in TEM images of Figure 5.8b. At the air interface, PS disks cover part of the air interface in Region I and II, but a part of the surface is also covered by homeotropic LC mesogens (Region III). A mixed surface with homeotropic LC alternating with PS disks as in the bulk morphology is formed in Region I and II. Homeotropic LC alignment is still preferred by both the block copolymer and the air interface to cover part of the air interface. Smectic terraces with a s_o height stand on part of the island in the upper part in Region III. The height of islands (L_o) is around twice the smectic layer height (s_o). The overall thickness of Region III is ca. 2 L_o.

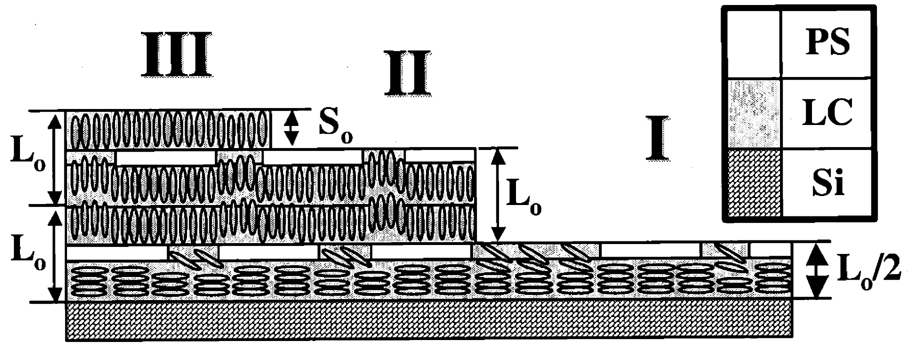

Figure 5.10: Proposed thin film model of smectic bilayer morphology.

5.4.6 Spherical Morphology at Temperature above T_{iso}

The bulk morphology undergoes an order-order transition (OOT) from smectic bilayers to spheres when the annealing temperature is above the LC clearing point (T_{iso}) but below the block copolymer T_{ODT}.[5] PS spheres, instead of smectic bilayers, formed at this temperature range in the bulk quenching studies. We want to verify whether the OOT occurs in the ultrathin films.

The same film (H85-5, 23 nm) as in Figure 5.9 was annealed at a higher temperature (190 °C) and allowed to quench down quickly. The LC should lose the smectic order while two blocks still remained phase-separated at this temperature. The AFM roughness (Rq) in Table 5.4 was much lower at high annealing temperatures, and the layered topography disappeared, as shown in Figure 5.11. All the surface layer structures were erased. As seen in the plane-view in Figure 5.11a, several holes are around one smectic-layer height (~ 3 nm). It shows that a few smectic layers are still formed when the quenching is not fast enough. The LC block forms the matrix and is homeotropic at the air interface. PS spheres are buried inside and there are no island or hole structures.

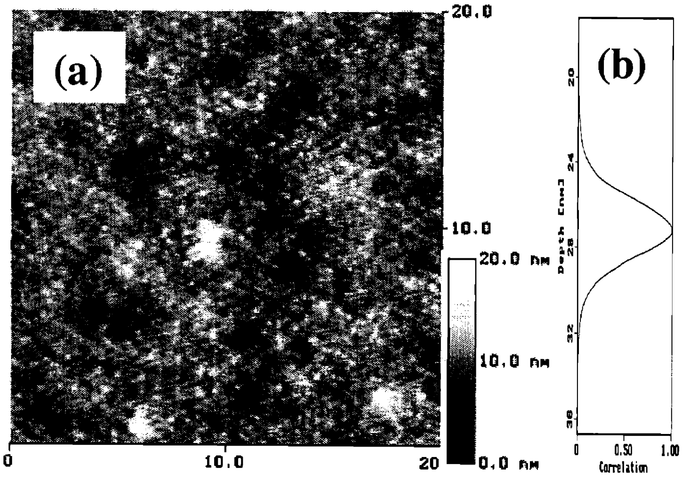

Figure 5.11: AFM images of H85-5 after quenching from a higher temperature (190 °C) (a) plane-view; (b) depth profile.

If the smectic bilayers and top LC terraces are equilibrium structures, they should be thermally reversible. The sample was first annealed at 170 °C for a couple days. We then heated the sample to 190 °C, cooled it down slowly, and held the temperature at 170 °C for three days. The topography returned to the structure it had before heating up to 190 °C, indicating that the smectic bilayer structure is stable.

5.5 ANNEALING EFFECT OF THE SMECTIC BILAYERED THIN FILMS

Annealing temperature and time are two critical factors in reaching the equilibrium morphology. All films in this study were spun cast from toluene solutions. Spin casting is an easy and reliable way to make thin polymer films. Annealing is a necessary process for molecules to reorganize and return to the more energetically favorable state of random coils. This healing process goes faster at high annealing temperatures. However, transitional morphologies are easier to observe and record while annealing at lower temperatures. The effects of annealing time and temperature will be discussed in this section.

Another sample (H80) we studied in this section also shows the smectic bilayered structure as H85. The block copolymer, denoted by H80, is a 3600 g/mol polystyrene - b- 14300 g/mol PHBPB diblock. The polydispersity is 1.21. The molecular weight and block ratio of H80 are close to that of H85. Moreover, the topography from AFM shows two characteristic lengths, L_o (13 nm) and s_o (3.1 nm), which is the same as the topography of H85 in Figure 5.9. The island structure only exists in the morphology of lamellae or smectic bilayer. The block ratio is too high for lamellae, so we believe it has smectic bilayered structure.

5.5.1 Time Dependence at Low Annealing Temperature

The island formation was observed at the air interface while annealing at a low temperature (130 °C) for different annealing times. Figure 5.12 demonstrates the kinetic approach of the surface topography. The AFM image in Figure 5.12a shows the early stage of annealing after three days. The surface is still rough and there are no specific features. After another six days of annealing at the same temperature, small islands with L_o height form at the air interface in Figure 5.12b. The entropy gain from the LC smectic bilayer packing and block copolymer periodicity can overcome the surface tension to create more air interface by forming the island topography. The same sample is put back into the vacuum oven and annealed for another ten days. The result shows some bigger islands as shown in Figure 5.12c. Islands merge together to reach a lower energy state by reducing the surface area and curvature. The size of the islands remains constant for another week of annealing at the same temperature. This concludes that the island (or hole) defect is the most stable surface morphology of the smectic bilayered structure at this annealing temperature. Annealing time plays a critical role in approaching the equilibrium morphologies, although the final morphology may be kinetically trapped instead of thermodynamic equilibrium.

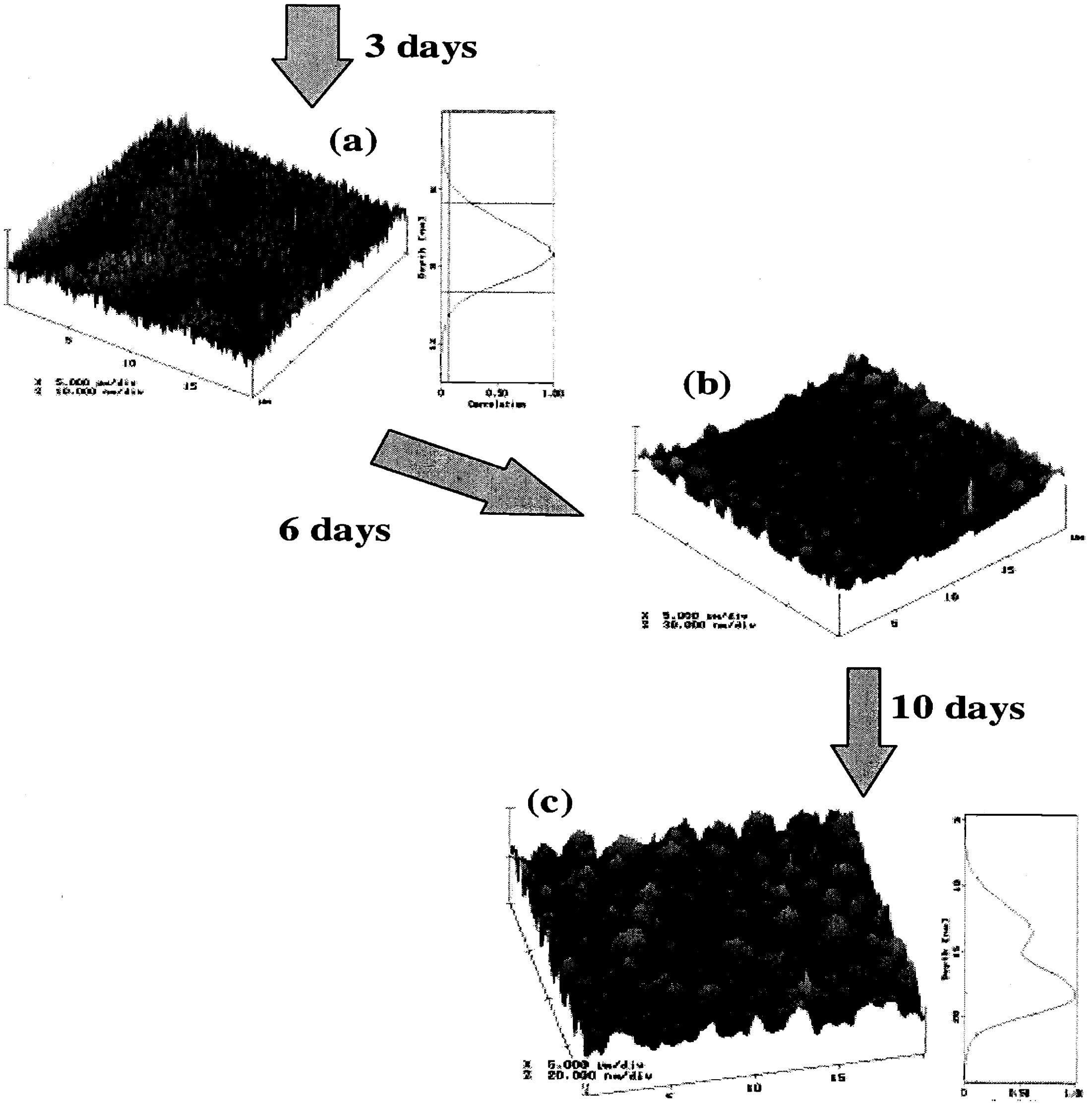

Figure 5.12: Islands merge while annealing for longer times at 130 °C. The film has 80% of LC and is 32 nm thick. (a) Flat surface when annealed for only three days; (b) Small islands at the air interface when annealed for another six days; (c) Islands merge to bigger ones when annealed for another ten days. The depth profile shows two clear separate peaks.

5.5.2 Temperature Dependence of Annealing

Annealing temperature is another key factor to overcome the energy barriers and reach the equilibrium state. Figure 5.13a shows the topography after annealing at 130 °C for only two days. The surface is flat and there is no obvious structure. The depth profile shows only one broad peak. However, after annealing at the same temperature for another week, the typical topography with holes (L_o) and smectic terraces (s_o) appears on the free surface as in Figure 5.13b. This is clearly the smectic bilayered structure we have discussed previously in this chapter. Black holes represent the thinnest part of the film and the white area represents the smectic terraces. From the depth profile at the right of the AFM image, there are three peaks corresponding to three heights. The distances of peaks are equal to one smectic height (s_o) and the block periodicity (L_o).

After raising the annealing temperature to 170 °C, fewer holes are on the surface. In Figure 5.13c, the depth profile showing the lowest peak (corresponding to the bottom of holes) diminishes, and the middle peak (corresponding to the top plateau) increases. The hole defects are gradually healed at higher temperatures. The area covered by top smectic terraces is around the same as covered by the plateaus. This is similar to what we observed in the cylindrical morphologies in Figure 5.3a and 5.3b. The most stable situation is the existence of only one single smectic terrace at the air interface. This gives the least surface area and also keeps the LC characteristics. The multi-smectic terraces at the air interface only happen when the film is mainly composed of the LC block.

The topography shows only the island structure when quenching from the annealing temperature of above T_{iso} in Figure 5.11d. At this temperature, LC molecules lose their ordering, and there are no prominent top smectic terraces. However, the polymer still tries to keep the diblock periodicity as a smectic bilayered structure. Figure 5.13d demonstrates this phenomenon. The depth profile clearly shows only two peaks with L_o heights.

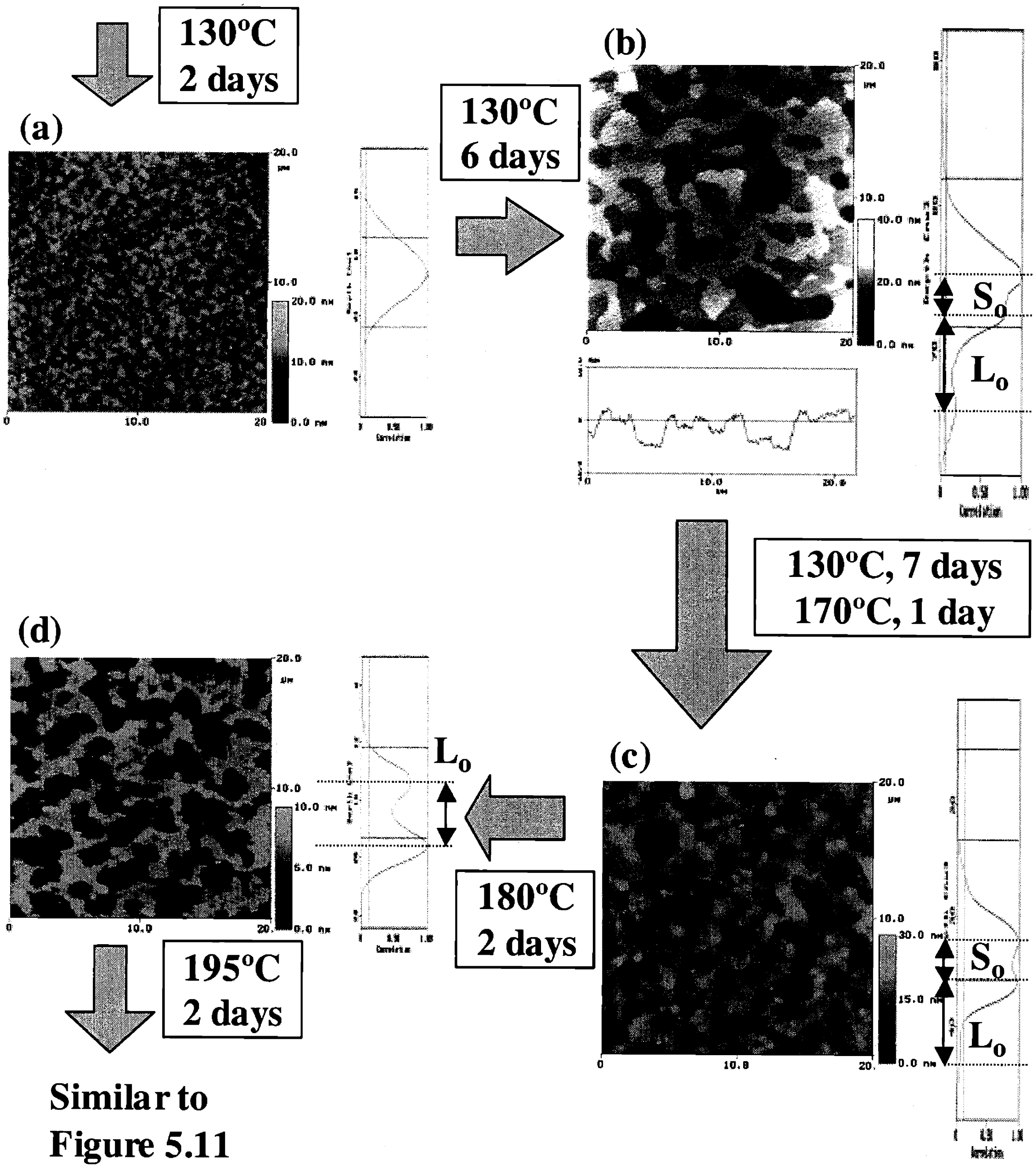

Figure 5.13: Surface morphologies of the smectic bilayered structure at different annealing temperatures (thickness = 41 nm). (a) Flat surface when annealed at 130 °C for only two days; (b) Typical three layer structure with s_o and L_o heights when annealed at 130 °C for another 6 days; (c) Fewer holes on the surface when annealed at 130 °C for another week and 170 °C for one day; (d) Islands with only L_o spacing when annealed at 180 °C for another two days.

When raising the annealing temperature well above the T_{iso} (195 °C), the topography was erased as in Figure 5.11. The sample lost LC ordering sequentially and acts as the general diblock copolymers at temperatures above T_{iso}. Without LC packing, the film shows a spherical morphology as the basic diblock copolymer conformation, instead of smectic bilayers.

Different annealing temperatures overcome different energy barriers to create various morphologies. Examination of these effects shows the possible kinetic approaches that molecules use to reorient and reach stability. Therefore, different morphologies are formed in different processing conditions.

5.6 CONTACT ANGLE MEASUREMENT OF DIFFERENT LC RATIO DIBLOCK COPOLYMERS

We would like to present measurements of average contact angles (both advancing and receding) for the whole series of samples mentioned in this thesis. The samples were divided into two groups by the film thickness.

Several factors of the air surface wettability will be discussed first. The wetting of LC-containing thin films is determined by the surface components (PHBPB or PS coverage) and LC alignment (homeotropic or planar). Different components at the air interface provide different surface tensions, for example, PS and PHBPB homopolymers have dissimilar contact angle values. Secondly, the surface tensions of LC-containing materials also depend on the film thickness. In this series of LC diblock copolymers, LC mesogens prefer planar anchoring at the substrate and homeotropic alignment at the air interface. If films are very thin, the substrate holds the LC molecules planar. If films are sufficiently thick, LC mesogens can pack well by their own nature and neglect the substrate effects. The homeotropic anchoring at the air interface is the preferential alignment created to lower the surface tension. This substrate phenomenon is most pronounced in films thinner than ca. 25 nm in this series of LC diblock copolymers.

Table 5.5 shows contact angles of films with thickness below 25 nm. The contact angles of PHBPB homopolymer and HBPB monomer have been discussed in Chapter

Three and summarized here. The surface properties of PHBPB and HBPB depend on LC alignment at thicknesses below 7 nm. LC alignment at the air interface transits from planar for very thin films (thickness < 4.5 nm) to homeotropic (thickness > 7 nm). After 7 nm, the LC mesogens form homeotropic alignment covering the air interface. However, when the film thickness is below 25 nm, the LC molecules are still affected enough by the substrate to show larger tilt angles. That is why we usually observe thinner smectic layer thicknesses (s_o) in ultrathin films (2.8 – 3.2 nm) compared to the bulk samples (3.1 - 3.5 nm). Therefore, the free surface of a thin film (7-25 nm) is less hydrophobic than that of very thick films. The standard deviations of HBPB monomers are large because HBPB includes two different types of alignment. For PS homopolymer ultrathin films (thickness ~ 4 Rg), the contact angles are higher than thick PS homopolymer films. This may be caused by the stronger interaction of benzene rings and the silicon. So the PS backbone covers the air interface to make a more hydrophobic air interface. More experiment evidences are needed to explain the detailed relationship between contact angles and film thickness.

Table 5.5: Contact angle data for thin samples (< 25 nm).

Sample	**PS**[j]	**H41**	**H50**	**H79**	**H85**	**PHBPB**	**HBPB**
Morphology[k]	-	LAM	P-LAM	HPC	S_{C2}	-	-
Thickness range (nm)	18.2-22.3	12.6-25.0	12.0-21.5	13.2-20.8	5.8-22.7	2.5-25.1	2.4-7.5
Average thickness (nm)	20.3	19.0	16.5	16.2	13.3	8.2	4.6
Advancing (°)	102±2.3	100.8±3.1	93.5±6.5	97.7±4.0	95.5±3.3	90.5±2.8	86.6±12.8
Receding (°)	88.5±2.2	85.8±2.4	78.8±6.3	71.5±4.6	76.7±2.8	68.3±5.4	67.0±11.6
Hysteresis (°)	13.5	15.0	14.8	26.2	18.8	22.2	19.6

---

[j] A GPC-standard mono-dispersed polystyrene homopolymer with 29.3 kg/mol MW was selected here. The radius of gyration (Rg) of a random coil is ca. 4.8 nm.

[k] LAM: lamellae, P-LAM: perforated lamellae, HPC: hexagonally packed cylinders, S_{C2}: smectic C* bilayers

The contact angles of diblock copolymers are usually between the values of PS and PHBPB homopolymers. The lamellar films (H41) have very high contact angles. This implies that the surface is hydrophobic for all three Regions (I, II or III). Those angles are even higher than the PHBPB homopolymer angles. The mesogens inside block domains pack more ordered and straight to cause a more hydrophobic air interface. The H79 and H85, with higher LC contents, have contact angles lower than H41.

For films thicker than 30 nm, the surface LC layer forms a well-packed homeotropic alignment. Table 5.6 shows the contact angle results. The advancing contact angle of the PS homopolymer film (μm-scale thick) is around 90, which has also been reported by another group.[40-42] The random coil conformation of PS has lower contact angles than that in nm-scale ultrathin films. Thick films of PS/PLC homopolymer blends are phase-separated and PLC homopolymers cover the air interface as determined by XPS in Chapter Four. The contact angle data show this blend forms a very hydrophobic air surface (advancing contact angle larger than 100°). The LC packing is more uniformly homeotropic when there is less substrate effect. The alkyl group at the end of the mesogen is exposed to minimize the surface energy. The advancing contact angle is close to the typical value of water on closely packed methylene (-CH_2-) surface (102-103°). Thick films of H80 diblock copolymer have similar contact angles as homopolymer blends. Homeotropic alignment dominates thick smectic bilayered morphology, and the LC block covers the air interface instead of the anti-symmetrical mixed surface noticed in thick films. The lamellar structure adopts a perpendicular alignment with the coexistence of both blocks at the air interface, as shown in Section 4.6. The air interface is a surface mixed with the PS block and the homeotropic PLC block. The contact angles of H41 thick films are therefore lower than in thin films.

Table 5.6: Contact angle data of thicker films (> 30 nm).

Sample	**PS**	**H41**	**H80**	**Blend**
Morphology	-	LAM	S_{C2}	-
Thickness range (nm)	-	30.8-133.7	31.2-50.6	22.2-57.5
Average thickness (nm)	3~4 μm	76.7	37.7	35.4
Advancing (°)	92.5	92.3 ± 2.0	103.3 ± 3.4	101.5 ± 2.1
Receding (°)	87.5	79.3 ± 3.4	83.3 ± 2.6	82.3 ± 1.8
Hysteresis (°)	5.0	13.0	20.0	19.2

Contact angle measurements of the whole series of LC diblock copolymer films at different thicknesses provide an overview of the interactions among the substrate, the air interface, the block interfaces, and LC ordering.

5.7 CHAPTER SUMMARY

Thin film morphologies of high LC ratio diblock copolymers have been discussed, including the cylindrical and smectic bilayer morphologies. When we compared the high LC ratio diblock copolymers with PHBPB homopolymers, we found that just a short PS block changed the whole thin-film morphology. Fifteen percent of PS switched the morphology from the pure smectic LC layers to the smectic bilayers with holes or islands (block periodicity). Twenty percent of PS moved the LC homopolymer to the cylindrical morphology. This opens another door for material designs. The thin film study in this chapter is beneficial in understanding and characterizing other LC defects and superstructures.

The future work should include synthesizing more diblock samples with different molecular weights and block ratios in the high LC-ratio region. More data points are helpful to clarify the smectic bilayered regions in the phase diagram. Cross-sectional TEM is useful in providing direct measurements of vertical profiles.

REFERENCES

(1) Leibler, L. *Macromolecules* **1980**, *13*, 1602-1617.
(2) Anthamatten, M; Zheng, WY; Hammond, PT. *Macromolecules* **1999**, *32*, 15, 4838-4848.
(3) Anthamatten, M; Hammond, PT. *Macromolecules* **1999**, *32*, 24, 8066-8076.
(4) Zheng, WY; Hammond, PT. *Macromolecules* **1998**, *31*, 3, 711-721.
(5) Anthamatten, M; Wu, J-S; Hammond, PT. *Macromolecules* **2001**, *34*, 24, 8574-8579.
(6) Rockford, L; Liu, Y; Mansky, P; Russell, TP; Yoon, M; Mochrie, SGJ. *Phys. Rev. Lett.* **1999**, *82*, 12, 2602-2605.
(7) Rockford, L; Mochrie, SGJ; Russell, TP. *Macromolecules* **2001**, *34*, 5, 1487-1492.
(8) Fasolka, MJ; Harris, DJ; Mayes, AM; Yoon, M ; Mochrie, SGJ. *Phys. Rev. Lett.* **1997**, *79*, 3018.
(9) Fasolka, MJ; Banerjee, P; Mayes, AM; Pickett, G; Balazs, AC. *Macromolecules* **2000**, *33*, 5702-5712.
(10) Harrison, C; Adamson, DH; Cheng, ZD; Sebastian, JM; Sethuraman, S; Huse, DA; Register, RA; Chaikin, PM. *Science* **2000**, *290*, 5496, 1558-1560.
(11) Wang, Q; Nealey, PF; de Pablo, JJ. *Macromolecules* **2001**, *34*, 10, 3458-3470.
(12) Huang, E; Pruzinsky, S; Russell, TP; Mays, J; Hawker, CJ. *Macromolecules* **1999**, *32*, 16, 5299-5303.
(13) Mansky, P; Liu, Y; Huang, E; Russell, TP; Hawker, C. *Science* **1997**, *275*, 5305, 1458-1460.
(14) Huang, E; Mansky, P; Russell, TP; Harrison, C; Chaikin, PM; Register, RA; Hawker, CJ; Mays, J. *Macromolecules* **2000**, *33*, 1, 80-88.
(15) Huang, E; Russell, TP; Harrison, C; Chaikin, PM; Register, RA; Hawker, CJ; Mays, J. *Macromolecules* **1998**, *31*, 22, 7641-7650.
(16) Mansky, P; Russell, TP; Hawker, CJ; Pitsikalis, M; Mays, J. *Macromolecules* **1997**, *30*, 22, 6810-6813.
(17) Thurn-Albrecht, T; DeRouchey, J; Russell, TP; Jaeger, HM. *Macromolecules* **2000**, *33*, 9, 3250-3253.
(18) Thurn-Albrecht, T; Steiner, R; DeRouchey, J; Stafford, CM; Huang, E; Bal, M; Tuominen, M; Hawker, CJ; Russell, TP. *Adv. Mater.* **2000**, *12*, 15, 1138-1138.
(19) Schaffer, E; Thurn-Albrecht, T; Russell, TP; Steiner, U. *Nature* **2000**, *403*, 6772, 874-877.
(20) Mansky, P; DeRouchey, J; Russell, TP; Mays, J; Pitsikalis, M; Morkved, T; Jaeger, H. *Macromolecules* **1998**, *31*, 13, 4399-4401.
(21) Morkved, TL; Lu, M; Urbas, AM; Ehrichs, EE; Jaeger, HM; Mansky, P; Russell, TP. *Science* **1996**, *273*, 931-933.
(22) Russell, TP; Thurn-Albrecht, T; Tuominen, M; Huang, E; Hawker, CJ. *Macromol. Symp.* **2000**, *159*, 77-88.
(23) Ashok, B; Muthukumar, M; Russell, TP. *J. Chem. Phys.* **2001**, *115*, 3, 1559-1564.
(24) Zheng, WY; Albalak, R; Hammond, PT. *Macromolecules* **1998**, *31*, 2686-2689.

(25) Anthamatten, M; Wu, J-S; Hammond, PT. *Polym. Prepr.* **1999**, *40*, 1, 427-428.

(26) Figueiredo, P; Geppert, S; Brandsch, R; Bar, G; Thomann, R; Spontak, RJ; Gronski, W; Samlenski, R; Mueller-Buschbaum, P. *Macromolecules* **2001**, *34*, 2, 171-180.

(27) Wu, J-S; Fasolka, MJ; Hammond, PT. *Macromolecules* **2000**, *33*, 1108-1110.

(28) Sentenac, D; Demirel, AL; Lub, J; de Jeu, WH. *Macromolecules* **1999**, *32*, 3235-3240.

(29) van der Wielen, MWJ; Stuart, MAC; Fleer, GJ; deBoer, DKG; Leenaers, AJG; Nieuwhof, RP; Marcelis, ATM; Sudholter, EJR. *Langmuir* **1997**, *13*, 17, 4762-4766.

(30) Wong, GCL; Commandeur, J; Fischer, H; de Jeu, WH. *Phys. Rev. Lett.* **1996**, *77*, 5221.

(31) van der Wielen, MWJ; Stuart, MAC; Fleer, GJ; Schlatmann, AR; de Boer, DKG. *Phys. Rev. E: Stat. Phys., Plasmas, Fluids* **1999**, *60*, 4, 4252-4256.

(32) Sentenac, D; Ostrovskii, BI; de Jeu, WH. *Adv. Mater.* **2001**, *13*, 14, 1079.

(33) Vix, ABE; Muller-Buschbaum, P; Stocker, W; Stamm, M; Rabe, JP. *Langmuir* **2000**, *16*, 26, 10456-10462.

(34) Lammertink, RGH; Hempenius, MA; Vancso, GJ; Shin, K; Rafailovich, MH; Sokolov, J. In *Macromolecules*, 2001; Vol. 34, pp 942-950.

(35) Green, PF. *The University of Texas at Austin* **2001**, Not Published.

(36) Limary, R; Green, PF. *Macromolecules* **1999**, *32*, 24, 8167-8172.

(37) Osuji, CO; Chen, JT; Mao, G; Ober, CK; Thomas, EL. *Polymer* **2000**, *41*, 25, 8897-8907.

(38) Osuji, C; Zhang, Y; Mao, G; Ober, CK; Thomas, EL. *Macromolecules* **1999**, *Submitted.*

(39) Mao, G; Wang, J; Ober, CK; Brehmer, M; O'Rourke, MJ; Thomas, EL. *Chem. Mater.* **1998**, *10*, 6, 1538-1545.

(40) Shimizu, RN; Demarquette, NR. *J. Appl. Polym. Sci.* **2000**, *76*, 1831-1845.

(41) Kwok, DY; Lam, CNC; Li, A; Zhu, K; Wu, R; Neumann, AW. *Polym. Eng. Sci.* **1998**, *38*, 1675.

(42) Wu, S. *J. Polym. Sci., Part C* **1971**, *34*, 19.

Chapter 6

Conclusions and Future Directions

This chapter includes the summaries from the previous chapters of this thesis research and outlines ideas of future work.

6.1 CONCLUSIONS

This thesis presented a study on the surface morphology and LC ordering of side-chain LC homopolymer and diblock copolymer ultrathin films. LC alignment in ultrathin films was first determined in the LC homopolymer system. Morphologies of lamellae, cylinder, and smectic bilayers were chosen to study the influence of LC alignment on the ultrathin film morphology. The spherical morphology was not discussed for two reasons: the morphology of PS spheres inside the LC matrix does not typically occur in this series of diblock copolymers, and the morphology of LC spheres inside the PS matrix contains an insufficient number of LC molecules trapped separately in spheres to affect the morphology.

A series of polystyrene-b-(LC side-chain methacrylate) diblock copolymers with chiral smectic C* mesogens was designed and synthesized by sequential anionic polymerization. These two blocks were phase-separated at room temperature and had similar surface tension propensities to form mixed surfaces. A chiral non-polar end was attached at the end of the mesogen to induce homeotropic LC alignment at the air interface. Ultrathin films were spun cast from a toluene solution and annealed at various temperatures for different studies. The switchable LC side chains have the potential for future electro-optical applications.

In Chapter Three, I established a systematic method to study the complex LC alignment in ultrathin films. In order to have a better understanding of the LC behavior at the substrates, we synthesized the LC homopolymer and spun cast thin films with different thicknesses. The fundamental understanding of the structure and behavior of the LC molecules was studied first. X-ray diffractometry was used to acquire data on the lattice structure and the unit cell structure of LC monomer crystals. Molecular mechanics (MM2) simulation was used to understand the stable conformations and molecule dimensions, and to calculate the packing steric energy of mesogens. Moreover, I have theoretically shown the estimation of LC orientation at different interfaces. The mesogen was divided into several segments. The dipole moment of each segment was calculated from the MOPAC simulation. This enabled us to determine the LC anchoring situation at the substrate. The surface tension of each segment was calculated to estimate which segment prefers to wet the air interface by the group contribution method. Thirdly, experimental approaches were conducted by atomic force microscopy (AFM), contact angles measurements, angle-resolved x-ray photoelectron spectrometry (AR-XPS), and x-ray specular reflectivity (XSR). The AFM roughness analysis demonstrated LC stacking and alignment as a function of distance away from the substrate at different film thicknesses. The transition from planar to homeotropic alignment can be observed directly. Contact angle measurements illustrated the different hydrophobicity of planar and homeotropic alignments and illuminated the transition thickness. AR-XPS data of a series of films with various thicknesses demonstrated different carboxylic group ratios for two types of LC alignment. XSR measurements on both thin and thick films showed that two diverse electron density profile models were necessary to fit the data of these two films. The model showed different kinds of LC alignment and determined the thickness of each layer inside the film. A model of LC alignment at various thicknesses can be proposed by combination of the above information.

In our LC homopolymer system, I identified the preferred LC alignment at different thicknesses and the influences of the substrate. LC alignment was balanced by effects from two heterogeneous interfaces. The polar silicon surface prefers planar LC anchoring due to the high dipole moment mesogen core, and the non-polar air interface prefers homeotropic alignment to minimize the surface free energy. These four experimental methods clearly illustrated planar LC anchoring was preferred in films thinner than 4.5 nm, and homeotropic alignment was preferred at the air interface in films thicker than 7 nm, where the substrate effect was not sufficient to hold mesogens planar. The transition thickness and transition range were directly observed. The same methodology can also be applied to other LC homopolymer systems.

In Chapter Four, I developed a systematic way to analyze the ultrathin film morphology of LC diblock copolymers. The first step was to determine the thin film wetting structure. A microdroplet experiment and AFM were used to confirm the thin film wetting behaviors. The block covering the substrate was theoretically identified by the surface hydrophobicity and dipole moments from the MOPAC simulation. Experimentally, thin films were peeled off from the substrate, and XPS was used to examine the compositions of the polymer-substrate interface. In order to determine the block that was wetting the air interface, homopolymers of each block were synthesized and blended. X-ray Photoelectron Spectrometry was used to examine the surface compositions of fully annealed homopolymer-blend films and to determine which block had a lower surface tension. XPS was also used to scan the diblock copolymer thin films. Secondly, AFM was used to probe the surface topography and roughness. Plane-view TEM was used to detect the compositional variations, and cross-sectional TEM was used to directly observe the vertical layer profile. The proposed model was built from the above information and confirmed by XSR. The precise layer thicknesses were decided from XSR fitting. Sub-micron thick films were also examined by previous methods in order to compare different properties between the bulk and ultrathin films.

I analyzed the morphology of lamellar LC diblock thin films in Chapter Four. First I determined the thin film exhibited anti-symmetrical wetting by the microdroplet experiment. The block covering the polymer-substrate interface was the LC block, as determined by the films peeled from the substrate using XPS. The LC block was also shown to have a lower surface tension by the homopolymer blend experiments using XPS. However, XPS data of diblock copolymer thin films showed that the air interface was predominately covered by the PS block. From Chapter Three, the LC mesogens had two types of ordering depending on the interface and the film thickness. The surface properties are determined by LC orientation. The surface tension of the PS block is lower than that observed in planar LC alignment, but higher than that in homeotropic LC alignment ($\sigma_{\text{planar LC}} > \sigma_{\text{PS}} > \sigma_{\text{homeotropic LC}}$). Therefore, for very thin films, the substrate holds the LC mesogens planar, and the PS block covers the air interface, instead of the LC block symmetrically wetting both interfaces. If the film is thick enough and there are enough LC mesogens to form the surface layer, a homeotropic LC layer dominates the air interface. The complicated thin film morphologies were derived by several experimental techniques, such as AFM, TEM, XPS, and XSR. The film can be divided into three regions for three specific thicknesses. Region I was ½ L_o height and region II was 1½ L_o height. These two regions had anti-symmetrical wetting. The LC block wetted the substrate and the PS block predominately wetted the air interface. The LC block perforated to the air interface to form a mixed surface in Region I. Region III displayed symmetrical wetting. A film thickness of ca. 1.7 L_o (1.5 L_o + 1 s_o) formed two suppressed full lamellae (2 L_o), while the LC block adopted their preference of homeotropic alignment at the air interface and planar anchoring at substrate interface. The plane-view TEM images of sub-micron films showed lamellae fingerprints at the air interface. The lamellae switched from parallel alignment near the substrate to perpendicular alignment at the air interface. The LC mesogens can expose their low-energy tail and align planar to the block interface as in the bulk. This demonstrated the most stable morphology without substrate effects.

In Chapter Five, I studied two morphologies of LC diblock copolymers at high LC ratios, including cylinder and smectic bilayers. The same experiment methodology in Chapter Four was applied to analyze the thin film morphology and LC alignment. From XPS and the microdroplet experiments, I determined both films had symmetrical wetting properties. The LC block wetted both substrate and air interfaces. Compared to H41 (lamellae) thin films, H79 (cylinder) and H85 (smectic bilayer) have higher LC contents, which can cover both interfaces. Symmetrical wetting with homeotropic LC alignment at the air interface was the most preferred state even though there were influences from the substrate.

In cylindrical diblock copolymer thin films (H79), the topology showed multiple smectic steps for partially annealed films. This indicated homeotropic LC alignment at the air interface. The multiple smectic steps merged to one after long annealing. For films thinner than 20 nm, the topology showed islands with ca. one L_o height. In smectic-bilayered thin films (H85 and H80), the topology from AFM was similar to what I observed in lamellar diblock copolymers. Both s_o (single homeotropic smectic LC layer height) and L_o (the height of holes or islands) coexisted at the air interface. The PS domains deformed into highly oblate ellipsoids and arranged hexagonally between smectic layers in both bulk and thin films. I modified the lamellar model in Chapter Four to the smectic-bilayered morphology, where LC mesogens aligned homeotropically at the air interface and inside the film except for the substrate-contacting layer. Both cylindrical and smectic bilayered morphologies showed the single smectic terrace at the air interface. This also confirmed the proposal of homeotropic smectic LC alignment.

Lastly, in order to explore the stability of thin films, samples with different morphologies were subjected to various factors, such as annealing temperature, annealing time, and solvent exposure. In this thesis, I have added to the scientific literature precise morphological studies and information on LC alignment in side-chain LC diblock copolymer ultrathin films.

6.2 FUTURE DIRECTIONS

Here several possible future studies and directions will be discussed.

6.2.1 Different MW/LC Ratio of the same series of diblock copolymers

One possible direction for future work on LC morphology would follow the path of investigating the effects that different molecular weights and LC ratios in the same series of diblock copolymers would have on film properties. For example, the LC spheres in the PS matrix and perforated lamellae. In addition, an in-depth study of the same series of LC diblock copolymer represents a natural extension of this work.

6.2.2 Different Substrates

Another interesting and potentially critical for future applications study should look at the behavior of LCs on different substrates.. Many common bare substrates are important, such as gold, glass, or silicon nitride (Si_3N_4). There are several simple modifications that allow us to tune the surface properties. Self-assembled monolayers (SAM) built on gold or silicon substrates are one way to change the surface properties. In the semiconductor industry, a thin layer of 1,1,1,3,3,3-hexamethyl disilazane ((CH_3)-NH-Si-$(CH_3)_3$) is spun cast on silicon wafers to create a hydrophobic surface. Pre-aligned substrates can also help the LC orientation.[1,2]

6.2.3 Electric Field Alignment

Electric fields (EF) can be used to align ultrathin LC diblock thin films to achieve larger and more uniform domains. It is well known that an electric field can align LC molecules. Recently, it was found that electric fields could align the block copolymer morphology at high temperature and hold it at temperature below the glass transition temperature (Tg).[3] The investigation of the influence of electric fields on LC alignment, block copolymer morphological alignment, and block copolymer order-disorder transition is a fascinating and involved subject. Cases in which diblock copolymer thin films were aligned by electric fields were reported in detail in Section 1.3.3. Moreover, LC containing thin films may be used as a 'commanding layer' for bulk LC layers.[4-9] It is possible to adjust block copolymer morphology using EF and control their properties. However, this requires a very large electric field to align block boundaries. When we incorporate LC ordering inside the block domains, the LC molecules will help the morphological alignments under electric fields. This reduces the required field strength and makes the whole process more applicable. In addition, it can be used as a reference for designing new block copolymers.

I made a mask with inter-digitated circuits for photolithography following the method proposed by Russell *et al.*[10-12] The electrolyte intervals ranged from 4 to 20 μm. A thin silicon nitride coating is applied on top of double-sided polished silicon wafers. The aluminum circuits were printed on top of the silicon nitride. Small wells on the backside of silicon wafers were etched to create small silicon nitride windows. The polymer films were cast on the silicon nitride substrate between electrolytes. Since it is transparent under TEM, the morphologies before and after electric fields could be observed directly without peeling films from the substrate. The same film can be applied under different field strengths to determine the critical value of alignments.

However, before studying the electric field effect, it is important to understand the LC behaviors of ultrathin films at the silicon nitride substrate. This part can be deduced directly from the methods developed in the previous chapters. LC diblock copolymer thin films aligned by electric field can be used as a possible model to approach real thin film applications.

6.2.4 Amphiphilic LC Diblock Copolymer

Amphiphilic diblock copolymers consist of both hydrophobic and hydrophilic blocks chemically linked together. The hydrophobic effect results in a strong segregation between blocks. The occurrence of spontaneous self-assembly of macromolecules creates the opportunity of observing nanoscale patterning. For amphiphilic diblock copolymers, phase separation can even occur at temperatures higher than the bulk order-disorder-transition temperature (T_{ODT}) for general diblock copolymers. For example, thick symmetrical amphiphilic diblock copolymer films (100-1000 nm) can still possess a layered structure without distinguishable disordering transition at high temperatures. The strong phase separation is important to consider in several applications.

The surface is usually more specific to one of the blocks. When annealed as thin films, if blocks went preferentially toward different surfaces, they would segregate into an ordered layer morphology (ex. lamellae arranged). For instance, one block uniformly covers the substrate surface as the other one is localized at the air/polymer interface. For example, a PS-b-PVP diblock thin film shows layer structures at the silicon oxide substrate. The PVP block is preferentially adsorbed to the substrate, while the PS layer covers the air interface with lower surface tension.

If the film is composed of only one monolayer, amphiphilic diblock copolymers form brush structures (anchored by one block onto a solid surface). Tirrell *et al.* did theoretical [13] and experimental [14-17] work to examine both PS/P2VP and PI/P2VP polymer brush systems in toluene on oxidized silicon and mica substrates. They also made the measurements of forces of interaction between pairs of layers of diblock copolymers in a "surface force apparatus". They also showed that the surface adsorption prefers small PS block length (fixed PVP) or large PVP block length (fixed PS). Eisenberg *et al.* [18-21] did research on several amphiphilic diblock copolymer aggregates in solution, like PS-b-poly(ethylene oxide), PS-b-poly(acrylic acid), PS-b-PAN, PEO-b-poly(butyl methacrylate). Bates and Gruner *et al.* [22,23] reported the phase behavior of PS-P2VP diblock copolymer. They used dynamic mechanical spectroscopy, SAXS, SAN and TEM to estimate χ and determined the preferred ordered morphologies, including hexagonally perforated layers and bicontinuous cubic/gyroid.

The special properties of diblock copolymer brushes point to the importance of exploring the field of LC diblock copolymer brushes. Simply coating an LC-brush monolayer can modify the surface wettability, permeation, and surface rigidity. I can also create an orientable (adjustable) LC layer at the free surface. Furthermore, the thin alignable commanding surface can be used as template to align other small liquid crystals on top of it.

I plan to change our PS-b-PHBPB LC diblock copolymer to an amphiphilic diblock copolymer by replacing the PS block with a more hydrophilic block, such as poly 4-vinylpyridine (P4VP) or poly ethylene-oxide (PEO). The new LC diblock brush can be used to adjust surface properties or used in a multiple layer-by-layer assembly process due to its water solubility. The nature of LC ordering will make the diblock brush more powerful. There are several other potential applications, such as nano-reactors, porous materials for separation, hybrids with inorganic materials (ex. clay), and electro-optical active devices.

I have successfully synthesized the PMMA-b-P4VP diblock copolymer in THF solution at low temperature. However, the same experimental condition cannot be directly applied to PHBPB-b-P4VP. The synthesis is more difficult than common PS-b-P4VP because the anionic strength is similar for PMMA and P4VP. After the first group of monomers (HBPB) is fully polymerized, it is hard to initiate the second monomer at the same solvent. Moreover, the huge LC side-chain will form a big shell around the active reaction center. Monomers need to diffuse into the shell to react. Although 4-vinyl pyridine (4VP) is soluble in THF, P4VP is not. After several 4VP monomers were added to the chain, the whole diblock polymer became a suspension with soluble PLC arms and an insoluble P4VP core. Due to substantial differences between the solubility of P4VP and PMMA, no solvent is equally effective for both constituent blocks. A solvent mixture of THF/pyridine is recommended to continue this polymerization.

Finally, I also worked on another synthetic strategy. The same LS mesogen was synthesized separately with an alkene functional end group. It would be interesting to try to attach the mesogens to the PMMA-P4VP backbond after protecting the P4VP layer and hydrolyzing PMMA to PMAc. The LC amphiphlic diblock copolymer could have many remarkable applications.

REFERENCES

(1) Stohr, J; Samant, MG; Cossy-Favre, A; Diaz, J; Momoi, Y; Odahara, S; Nagata, T. *Macromolecules* **1998**, *31*, 1942-1946.

(2) Chen, XL; Bao, Z; Sapjeta, BJ; Lovinger, AJ; Crone, B. *Adv. Mater.* **2000**, *12*, 5, 344-347.

(3) Mansky, P; Liu, Y; Huang, E; Russell, TP; Hawker, C. *Science* **1997**, *275*, 5305, 1458-1460.

(4) Doron, A; Katz, E; Portnoy, M; Willner, I. *Angew. Chem. Int. Engl.* **1996**, *35*, 1535.

(5) Lahav, M; Ranjit, KT; Katz, E; Willner, I. *Chem. Commun.* **1997**, 259.

(6) Seki, T; Fukuda, R; Tamaki, T; Ichimura, K. *Thin Solid Films* **1994**, *243*, 675.

(7) Seki, T; Sakuragi, M; Kawanishi, Y; Suzuki, Y; Tamaki, T; Fukuda, R; Ichimura, K. *Langmuir* **1993**, *9*, 211.

(8) Ichimura, K; Suzuki, Y; Seki, T; Hosoki, A; Aoki, K. *Langmuir* **1988**, *4*, 1214.

(9) Buchel, M; Minx, C; Menzel, H; Johannsmann, D. *Thin Solid Films* **1996**, 257.

(10) Mansky, P; DeRouchey, J; Russell, TP; Mays, J; Pitsikalis, M; Morkved, T; Jaeger, H. *Macromolecules* **1998**, *31*, 13, 4399-4401.

(11) Morkved, TL; Lopes, WA; Hahm, J; Sibener, SJ; Jaeger, HM. *Polymer* **1998**, *39*, 16, 3871.

(12) Morkved, TL; Lu, M; Urbas, AM; Ehrichs, EE; Jaeger, HM; Mansky, P; Russell, TP. *Science* **1996**, *273*, 931-933.

(13) Misra, S; Tirrell, M; Mattice, W. *Macromolecules* **1990**, *29*, 6056.

(14) Hadziioannou, G; Patel, S; Granick, S; Tirrell, M. *J. Am. Chem. Soc.* **1986**, *108*, 2869.

(15) Parsonage, E; Tirrell, M; Watanabe, H; Nuzzo, RG. *Macromolecules* **1991**, *24*, 1987.

(16) Watanabe, H; Tirrell, M. *Macromolecules* **1993**, *26*, 6455.

(17) Dhoot, S; Tirrell, M. *Macromolecules* **1995**, *28*, 3692.

(18) Zhang, L; Eisenberg, A. *Science* **1995**, *268*, 1728.

(19) Yu, K; Eisenberg, A. *Macromolecules* **1996**, *29*, 6359.

(20) Astafieva, I; Khougaz, K; Eisenberg, A. *Macromolecules* **1995**, *28*, 7127.

(21) Kabanov, AV; Bronich, TK; Kabanov, VA; Yu, K; Eisenberg, A. *Macromolecules* **1996**, *29*, 6797.

(22) Schulz, MF; Khandpur, AK; Bates, FS; Almdal, K; Mortensen, K; Hajduk, DA; Gruner, SM. *Macromolecules* **1996**, *29*, 2857.

(23) Bates, FS; Schulz, MF; Khandpur, AK; Forster, S; Rosedale, JH; Almdal, K; Mortensen, K. *J. Chem. Soc. Faraday Trans.* **1994**, *98*, 7.

Appendix I: Nomenclature and Acronyms

English Symbols

I	X-ray relative scattered intensity
k	Boltzman's constant
L_o	Block copolymer periodicity
M_n	Number-averaged molecular weight
M_w	Weight-averaged molecular weight
$\mathbf{q}$	X-ray scattering vector
R	Roughness
R_g	Radius of gyration
S	Smectic
s_o	Smectic layer thickness
T	Temperature
T_g	Glass transition temperature
T_{iso}	Isotropization temperature
T_{ODT}	Order-disorder transition temperature
T_{OOT}	Order-order transition temperature

Greek Symbols

χ	Flory-Huggins interaction parameter
ϕ_{LC}	Liquid crystal volume fraction
λ	X-ray wavelength
σ	Surface tension
δ	Solubility parameter
θ	Contact angle (a: advancing, r: receding)
Φ	Takeoff angle

Acronyms

AFM	Atomic Force Microscopy
BPB	Biphenyl Benzoate
AR-XPS	Angle-Resolved X-ray Photoelectron Spectroscopy
DSC	Differential Scanning Calorimeter
IMDS	InterMaterial Dividing Surface
GPC	Gel Permeation Chromatography
LC	Liquid Crystal or Liquid Crystalline
LCP	Liquid Crystal Polymer
IMFP	Inelastic Mean Free Path
NMR	Nuclear Magnetic Resonance
ODT	Order-Disorder Transition
OM	Optical Microscopy
OOT	Order-Order Transition
SAXS	Small Angle X-ray Scattering
PLC	Liquid Crystal Polymer
PMMA	Poly Methyl Methacrylate
PS	Polystyrene
SCLCP	Side-Chain Liquid Crystalline Polymer
SCLCBC	Side-Chain Liquid Crystalline Block Copolymer
SLD	Scattering Length Density
TEM	Transmission Electron Microscopy
XPS	X-ray Photoelectron Spectroscopy
XSR	X-ray Specular Reflectivity

Appendix II: XPS Fitting Parameters of C1s Scan

CHAPTER 4

Table for Figure 4.3 & Table 4.1

Thickness	Peak #	Peak	15°				75°			
			Pos.	Height	FWHM	Area %	Pos.	Height	FWHM	Area %
	1&2	CH / C	284.55	26126	1.46	85.99	-	-	-	-
29 nm	3	CO	285.91	3144	1.78	12.63	-	-	-	-
1.68 Lo	4	COO	289.02	508	1.20	**1.38**	-	-	-	-
	1&2	CH / C	284.63	26569	1.44	89.80	284.61	14661	1.59	90.02
22.8 nm	3	CO	286.14	2746	1.39	8.94	286.33	1376	1.37	7.28
1.32 Lo	4	COO	289.08	432	1.25	**1.26**	288.83	414	1.69	**2.70**
	1&2	CH / C	-	-	-	-	284.65	11220	1.45	83.01
21 nm	3	CO	-	-	-	-	286.02	1371	1.68	11.76
1.21 Lo	4	COO	-	-	-	**-**	289.03	606	1.69	**5.24**
	1&2	CH / C	284.54	27507	1.39	83.86	284.55	21651	1.45	92.11
18 nm	3	CO	285.72	3815	1.80	15.03	286.14	1771	1.16	6.03
1.04 Lo	4	COO	289.34	382	1.32	**1.11**	288.93	317	1.99	**1.86**

Table for Figure 4.4 & Table 4.2

Sample	Thickness (nm)	Peak	Binding Energy (BE, eV)	Height	Width	Peak Area (%)
PS	20.5	1 & 2	279.16	2968.01	1.13	100
PHBPB Homopolymer	26.1	1 & 2	279.54	2225.34	1.41	90.51
		3 (CO)	281.31	251.12	0.98	7.11
		4 (COO)	283.70	117.26	0.70	**2.38**
1/1 wt Blend	57.5	1 & 2	279.03	1785.14	1.26	93.08
		3 (CO)	280.74	111.51	1.18	5.45
		4 (COO)	283.16	47.38	0.75	**1.47**
1/1 wt Blend	30.2	1 & 2	278.99	2174.84	1.31	93.87
		3 (CO)	280.72	136.16	1.09	4.89
		4 (COO)	283.22	43.12	0.87	**1.24**

Sample	Thickness (nm)	Peak	Binding Energy (BE, eV)	Height	Width	Peak Area (%)
1/1 mol Blend	23.6	1 & 2	279.26	1644.12	1.36	92.12
		3 (CO)	280.93	131.29	1.10	5.97
		4 (COO)	283.47	59.69	0.77	**1.91**
1/1 mol Blend	22.2	1 & 2	279.07	1651.50	1.22	87.57
		3 (CO)	280.59	186.98	1.22	9.91
		4 (COO)	283.16	70.18	0.82	**2.51**

Table for Figure 4.6 & Table 4.2

Sample	Thickness (nm)	Peak	Binding Energy (BE, eV)	Width	Peak Area (%)
PS	17.4	1 & 2	278.2	1.81	-
PHBPB Homopolymer	32.0	1 & 2	278.4	1.8	84.76
		3	280.02	1.8	11.60
		4	282.42	1.8	**3.65**
H41	30.8	1 & 2	278.27	1.69	-
H41	28.6	1	278.32	1.56	92.29
		2	279.44	1.56	7.71
H41	25.0	1	278.04	1.57	92.92
		2	279.29	1.54	7.08
H41	16.1	1	278.06	1.56	91.34
		2	279.22	1.62	8.66

Table for Figure 4.16 & Table 4.4

	Thickness	Peak #	Peak	15°				75°			
				Pos.	Height	FWHM	Area %	Pos.	Height	FWHM	Area %
(I, II, III)	30.8 nm	1&2	CH / C	284.61	28639	1.50	97.07	284.59	14845	1.57	97.65
	1.78 Lo	3	CO	286.39	1082	1.20	2.93	286.25	469	1.20	2.35
(II, III)	28.6 nm	1&2	CH / C	284.59	29396	1.40	96.30	284.62	9799	1.55	96.55
	1.65 Lo	3	CO	286.19	1231	1.28	3.70	286.26	491	1.11	3.45
(I)	7.7 nm	1&2	CH / C	284.59	16901	1.42	89.82	284.64	14173	1.49	94.56
	0.44 Lo	3	CO	286.25	1877	1.45	10.18	286.35	895	1.36	5.44

CHAPTER 5:

Table for Figure 5.6 & Table 5.3

Sample	Thickness (nm)	Peak	Binding Energy (BE, eV)	Height	Width	Peak Area (%)
H85	22.7	1 & 2	278.44	7871.6	1.71	85.58
		3	279.69	1179.46	1.71	12.82
		4	282.84	146.5	1.71	1.59
H85	17.6	1 & 2	278.11	7331.38	1.6	83.33
		3	279.43	1288.01	1.6	14.64
		4	282.25	179.09	1.6	2.04
H85	14.6	1 & 2	277.83	7907.88	1.6	84.56
		3	279.26	1195.42	1.6	12.78
		4	281.98	248.34	1.6	2.66
H85	13.5	1 & 2	278.15	7641.77	1.6	81.38
		3	279.3	1587.83	1.6	16.97
		4	282.42	126.45	1.6	1.65
H85	6.2	1 & 2	277.92	6357.84	1.76	88.49
		3	279.48	695	1.76	9.67
		4	282.06	131.86	1.76	1.84

Appendix III: XSR Fitting Parameters

CHAPTER 3:

Table for Figure 3.9 & Table 3.5

	Calculated					XSR Fitted			
	Density (g/cm^3)	Thickness (nm)	SLD (ρ, $Å^{-2}$)	Reduced Density[1] (δ)	Absorptivity	Thickness (nm)	SLD (ρ, $Å^{-2}$)	Reduced Density (δ)	Absorptivity
Air	-	-	1.00E-08	3.78E-09	-3.04E-09	-	1.00E-08	3.78E-09	-3.04E-09
Interface	-	-	-	-	-	**0.32**	-	-	-
Film	1.154	**6.45**	1.05E-05	3.96E-06	-3.74E-08	**5.84**	1.16E-05	4.37E-06	-5.28E-07
Interface	-	-	-	-	-	**0.32**	-	-	-
Total Film	-	**6.45**	-	-	-	**6.48**	-	-	-
SiO_2	2.32	-	1.94E-05	7.33E-06	-2.90E-07	0.24	1.94E-05	7.33E-06	-2.90E-07
Silicon	2.328	-	2.00E-05	7.55E-06	-2.40E-08	-	2.00E-05	7.55E-06	-2.40E-08

---

[1] Reduced density = SLD * ($\lambda^2 r_e / 2\pi$). λ is 1.54 Å for X-ray and r_e is the classic radius of electron. It is dimensionless.

Table for Figure 3.10 & Table 3.6

	Calculated					XSR Fitted			
	Estimated Density (g/cm³)	Estimated Thickness (nm)	SLD (ρ, Å^{-2})	Reduced Density (δ)	Absorptivity	Thickness (nm)	SLD (ρ, Å^{-2})	Reduced Density (δ)	Absorptivity
Air	-	-	1.00E-08	3.78E-09	-3.04E-09	-	1.00E-08	3.78E-09	-3.04E-09
Interface	-	-	-	-	-	1.66	-	-	-
Homeotropic Mesogen (1)	1.154	3.5	1.05E-05	3.96E-06	-3.74E-08	0.93	5.54E-06	2.09E-06	-1.38E-07
Interface	-	-	-	-	-	0.77	-	-	-
Homeotropic Mesogen (2)	1.218	2.0	1.09E-05	4.11E-06	-4.19E-08	1.66	8.68E-06	3.28E-06	-8.00E-11
Interface	-	-	-	-	-	0.19	-	-	-
Transition (3)	1.033	2.7	9.39E-06	3.54E-06	-3.51E-08	2.92	4.84E-06	1.83E-06	-1.40E-08
Interface	-	-	-	-	-	0.63	-	-	-
Planar (4)	1.154[m]	4.5	1.05E-05	3.96E-06	-3.74E-08	2.85	1.20E-05	4.53E-06	-9.85E-08
Interface	-	-	-	-	-	0.73	-	-	-
Total	1.154	12.7[n]	-	-	-	12.34	-	-	-
SiO_2	2.32	-	1.94E-05	7.33E-06	-2.90E-07	2.43	1.94E-05	7.33E-06	-2.90E-07
Interface	-	-	-	-	-	0.21	-	-	-
Silicon	2.328	-	2.00E-05	7.55E-06	-2.40E-08	-	2.00E-05	7.55E-06	-2.40E-08

---

[m] Experimental data from samples in the bulk state

[n] The thickness obtained from the ellipsometry measurement

CHAPTER 4

Table for Figure 4.14 & Table 4.3

	Calculated				
	Estimated Density (g/cm³)	Estimated Thickness (nm)	SLD (ρ, Å^{-2})	Reduced Density (δ)	Absorptivity
Air	-	-	1.00E-08	3.78E-09	-3.04E-09
Homeotropic LC (1)	1.154	~ 3	1.05E-5	3.97E-6	-3.74E-8
PS (2)	1.074	5.28	9.82E-6	3.71E-6	-5.23E-9
Parallel LC (3)	1.154	6.75	1.05E-5	3.97E-6	-3.74E-8
PS (4)	1.074	10.55	9.82E-6	3.71E-6	-5.23E-9
Parallel LC (5)	1.154	3.37	1.05E-5	3.97E-6	-3.74E-8
Total	-	28.95	-	-	-
SiO_2	2.32	-	1.94E-5	7.33E-6	-2.90E-7
Interface	-	-	-	-	-
Silicon	2.328	-	2.00E-5	7.56E-6	-2.40E-8

	XSR Fitted Figure 4.14a				XSR Fitted Figure 4.14c			
	Thickness (nm)	SLD (ρ, Å^{-2})	Reduced Density (δ)	Absorptivity	Thickness (nm)	SLD (ρ, Å^{-2})	Reduced Density (δ)	Absorptivity
Air	-	1.00E-8	3.78E-9	-3.04E-9	-	1.00E-8	3.78E-9	-3.04E-9
Interface	0.30	-	-	-	0.30	-	-	-
Homeotropic LC (1)	1.70	2.70E-6	1.02E-6	-1.08E-8	1.63	3.39E-6	1.28E-6	-1.32E-8
Interface	0.87	-	-	-	1.01	-	-	-
PS (2)	5.51	9.34E-6	3.53E-6	-4.64E-9	24.33	1.05E-5	3.97E-6	-5.24E-9
Interface	0.32	-	-	-				
Parallel LC (3)	6.31	1.02E-5	3.86E-6	-3.21E-8				
Interface	0.28	-	-	-				
PS (4)	8.52	9.99E-6	3.78E-6	-4.97E-9				
Interface	0.09	-	-	-				
Parallel LC (5)	3.36	1.06E-5	4.01E-6	-3.35E-8				
Interface	1.21	-	-	-	1.18	-	-	-
Total	28.47	-	-	-	28.45	-	-	-
SiO_2	0	1.96E-5	7.41E-6	-1.10E-7	0	1.96E-5	7.41E-6	-1.10E-7
Interface	0	-	-	-	0	-	-	-
Silicon	-	2.00E-5	7.55E-6	-2.40E-8	-	2.00E-5	7.55E-6	-2.40E-8